ON THE ELECTROMAGNETIC FIELDS IN PLANAR LAYERED MEDIA COMPRISING ANISOTROPIC CONDUCTIVE SHEETS AT THE INTERFACES

A Dissertation

by

MAZIN MOHAMED MUSA MUSTAFA

Submitted to the Office of Graduate and Professional Studies of
Texas A&M University
in partial fulfillment of the requirements for the degree of

DOCTOR OF PHILOSOPHY

Chair of Committee,	Krzysztof A. Michalski
Committee Members,	Robert D. Nevels
	Kamran Entesari
	Andrea Bonito
Head of Department,	Miroslav Begovic

August 2019

Major Subject: Electrical Engineering

ABSTRACT

The recent revolution in two-dimensional materials, such as graphene mono-layers, has attracted many researchers to investigate their properties and potential applications in different fields. The 2D materials are usually implemented as flat surfaces of atomic thickness embedded transversely in layered structures. The EM properties of 2D materials are described by surface conductivity that can be anisotropic in general. In this work, we demonstrate a general framework to study the EM fields in planar layered media in the presence of anisotropic conductive sheets arbitrarily placed at the interfaces.

The EM problem of planar layered media has been successfully modeled by a transmission line analogy in the past. The introduction of anisotropic surface conductive sheets results in a coupled transmission lines model representing TE and TM fields decompositions. A numerically stable novel formulation is developed to solve the new problem, and applied to various EM aspects of layered structures such as fields evaluation and modal analysis. The elegant methods developed for evaluating EM fields in layered media, using the transmission line model, will be upgraded after modifying the dyadic Green's functions in order to include the effect of anisotropic surface conductivity tensor.

The study of EM modes supported by planar layered structures is of high demand in many applications from design to analysis. A reliable and robust approach for finding the EM modes in this environment is developed with new proposed dispersion relations. The Cauchy integration method is accompanied with efficient treatments to alleviate the mathematical challenges in applying this method in this problem. The coupling between TE and TM modes, resulting from the fully populated surface conductivity tensor, is handled by the new transmission line model formulation developed in this work.

ACKNOWLEDGMENTS

I would like to express my sincere gratitude to Dr. Krzysztof A. Michalski for serving as my advisor during this research. I would like to thank him for his patience and continuous motivation throughout this journey. Also, I want to take this opportunity to thank the committee members for the valuable advices and the useful comments to improve this work. Last but not least, I would like to thank Texas A&M University for the great opportunity to achieve this level of education.

CONTRIBUTORS AND FUNDING SOURCES

Contributors

This work was supported by a dissertation committee consisting of Professor Krzysztof A. Michalski (advisor), Robert D. Nevels, and Kamran Entesari of the Department of Electrical & Computer Engineering and Professor Andrea Bonito of the Department of Mathematics.

The sample data used in Figure 4.8 were provided by Professor George Hanson of the Department of Electrical Engineering at University of Wisconsin-Milwaukee, WI.

All other work conducted for the dissertation was completed by the student independently.

Funding Sources

This graduate study was supported by Graduate Teaching Assistantships in the Department of Electrical & Computer Engineering at Texas A&M University, College Station, TX.

TABLE OF CONTENTS

LIST OF FIGURES

LIST OF TABLES

1. INTRODUCTION AND LITERATURE REVIEW

This chapter is an introduction for the reader to the problems of interest that will be covered in this study. Relevant works and contributions from the literature will be highlighted along this introduction. This chapter also provides a brief problem statement to the major topics of this study.

The planar layered media problem has emerged as a natural extension to the original half-space problem first considered by Sommerfeld in 1909 [6]. This simple ideal scenario on itself has resulted in a prolonged controversy about the existence of surface waves along the interface. A thorough review for these arguments and developments is covered in [7]. Later, this half-space study has been generalized into multiple layers medium and became the subject of several notable works [8–10]. The multiple planar layered medium is an idealization to numerous scenarios commonly encountered in geophysics, Radio Frequency (RF) devices, and nano-structures. Several techniques were introduced to handle this problem, among them is the spectral domain Transmission Line (TL) analogy which is the most elegant and versatile formulation. The TL model exploits the symmetry in these structures and delivers an efficient solution. The TL model has been adopted and generalized for uniaxial media by the prominent works of Michalski [11–14].

The recent developments in 2D materials led by the introduction of graphene with promising advancements in nano-electric devices and optoelectronics has attracted many researchers and resulted in a Noble prize in 2010 [15–18]. Such a material of atomic thickness is best approximated as a 2D conductive sheet [1, 19, 20]. This category of materials includes Black Phosphorus (BP), Transition Metal Dichalcogenide (TMD) monolayers, and also may include 2DEG layers. For example, an illustration of a graphene sheet atomic structure is shown in Figure 1.1. The unique optical properties of 2D materials have po-

tential applications associated with surface wave propagations [21–25]. In addition to the electrical properties of graphene sheet, it also exhibits interesting mechanical properties such as high thermal conductivity, high electron mobility, and high modulus of elasticity [26]. The advantage of graphene over the other 2D metals is the possibility to control its optical properties by changing the electrostatic and magnetostatic bias [27].

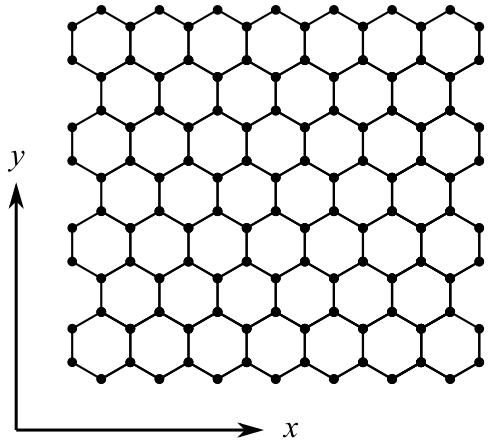

Figure 1.1: Depiction of graphene sheet atomic structure from top view. The carbon atoms are represented by circles, and the tetravalent atoms are connected to three other carbon atoms by three covalent bonds. This forms a 2D hexagonal structure [1].

Introducing the 2D materials into planar layered structures at interfaces has been considered in several practical applications. For example, Field Effect Transistors (FETs), Surface Plasmon Resonance (SPR) sensors, and antennas [28–35]. Moreover, in some 2D materials such as BP and magnetically biased graphene, the surface conductivity tensor exhibits anisotropic properties which is pertinent to some applications [36]. In addition to this, metasurfaces can be made of arrays with anisotropic light scatterers that can be approximated by homogenized conductive sheets [37–41]. The problem of half-space with anisotropic conductive sheet was investigated in few works from the literature [27, 42–44], while recent attempts to generalize the solutions for multilayered media are

limited [3, 45, 46]. The only attempt to generalize this problem was demonstrated for an electric dipole on the top layer [47]. However, these approaches are not general nor flexible for computing Electromagnetic (EM) fields due to a point source embedded at any location in the presence of multiple arbitrary anisotropic conductive sheets. Nevertheless, there is no flexibility to treat other aspects of this problem such as modal analysis, far-fields approximations, and plane-wave excitation via these solutions to the best of our knowledge.

The modal analysis is of high importance to gain insights about EM structures [48]. This makes the investigation of modes in planar layered media a continuing research topic [49–52]. For example, many RF and optical designs are based on layered structures which require eliminating the spurious waves effects [53]. In semiconductor devices, surface waves may couple to surface carriers when 2DEG inversion layer is formed. Several techniques for computing the Sommerfeld Integrals (SIs) require evaluating the poles locations accurately in the spectral domain [54–59]. Also, the excitation of Surface Plasmon Polariton (SPP) waves plays a major role in many applications which requires knowledge about this mode in layered media [60–64]. Several techniques for evaluating the modes in planar layered structure have been proposed such as Fast Fourier Transform (FFT) [65], Reflection Pole Method (RPM), and Wave-vector Density Method (WDM) [66, 67]. However, these techniques are limited to specific configurations or types of modes.

The modal analysis is performed by developing a dispersion function, where the zeros correspond to the transverse wavenumbers (eigenvalues) of the modes supported by the structure. Developing dispersion functions to accommodate the presence of 2D isotropic conductive sheet in planar layered media was discussed in the literature [69–73]. However, considering anisotropic conductive sheets is scarce [3, 74]. A reliable method for computing zeros of arbitrary function is the Cauchy Integral Method (CIM) introduced by Delves and Lyness [68]. The application of CIM in this context requires additional treatments.

Outline

This study is mainly divided into isotropic and anisotropic conductive sheets scenarios. Chapters 2 and 3, discuss all the EM problems of interest for isotropic conductive sheets. While Chapters 4 and 5 are dedicated to the anisotropic case. This approach follows the work progress during this research and provides enough background in order to handle the more general scenarios of anisotropic conductive sheets. So, the remaining chapters of this study will discuss the following. In Chapter 2, the reader will find a thorough introduction to the EM aspects of the planar layered media and the TL model. This chapter also demonstrates the EM fields computation when isotropic conductive sheets are included in a planar layered structure. Chapter 3, presents a complete discussion on the modal analysis in this environment. In Chapter 4, the introduction and treatment of anisotropic conductive sheets are demonstrated and discussed using the new TL formulation. While Chapter 5 describes the modal analysis for this environment. As stated earlier, graphene is the ideal example to illustrate our formulations and results since its optical properties were thoroughly studied and reported. Hence, several isotropic and anisotropic graphene based structures were considered in our numerical examples. This study ends with final conclusions and recommendations for future work in Chapter 6.

The numerical examples presented in this study are meant to demonstrate the application and the validation of the developed methods. Practical physical aspects were considered in the studied structures as much as possible. The physical constants were taken from [75], and the MKS system of units was used throughout this work. All the numerical results presented in this work were computed using MATLAB codes written by the author of this dissertation.

2. DYADIC GREEN'S FUNCTIONS FOR ISOTROPIC CONDUCTIVE SHEETS

2.1 Planar Layered Media Environment

A uniaxial planar layered media comprising arbitrary anisotropic conductive sheets placed at the interfaces is illustrated in Figure 2.1. A number of N planar layers are stratified against the z-axis and extend to infinity in the transverse direction. Each layer $n \in [1, N]$ occupies the space between z_{n-1} and z_n with a thickness of $d_n = z_{n-1} - z_n$. Each layer consists of a homogeneous uniaxial material with electric and magnetic constants tensors as described in (2.1) and (2.2), respectively. The unaxial media is equivalent to optic axis directed in z-axis direction [77]. The z dependency in the media parameters represents a piece-wise definition according to the structure (*i.e.*, $\underline{\underline{\boldsymbol{\mu}}}(z) = \underline{\underline{\boldsymbol{\mu}_n}} : z_n \leq z \leq z_{n-1} \quad , \forall n \in [1, N]$ and the same for $\underline{\underline{\boldsymbol{\epsilon}}}(z)$). Moreover, a number of $N - 1$ possible anisotropic conductive sheets are placed at the interfaces between layers with tensor surface conductivity as in (2.3). The top and bottom layers 1 and N, respectively, are considered of finite thicknesses. This choice allows us to terminate the configuration with boundary layers such as Perfect Electric Conductor (PEC) or Perfect Magnetic Conductor (PMC) at the top and bottom layers. It is also possible to choose any arbitrary impedance as a termination if needed. However, if the top and bottom layers are to be open (semi infinite), then z_0 and z_N, respectively, will serve as numerical boundaries for the evaluational of fields inside the layered medium. Any calumniation of the terminations mentioned above is allowed.

Scalarizing the Maxwell's equations and satisfying the boundary conditions results in a TL model analogy for this problem. The TL model has been thoroughly studied and applied to the planar layered media in the literature. The Transmission Line Green's Functions (TLGFs) are the solutions for source-free and source-excited TL inside all sections.

When the media are uniaxial, this results in two separate TLs e and h representing Transverse Magnetic (TM) and Transverse Electric (TE) modes, respectively. Moreover, the anisotropic conductive sheets between layers can be included by adding transformers coupling the two TLs. In this work, we propose solving various problems in this environment via new TL formulation and methods.

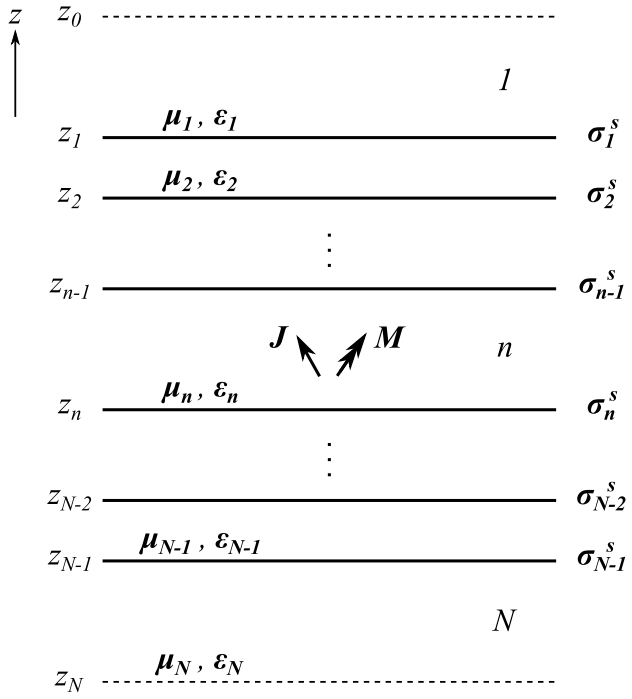

Figure 2.1: Planar layered media structure stratified against z-axis consists of N uniaxial layers with $N-1$ possible anisotropic conductive sheets at interfaces. Arbitrary electric and magnetic current sources $\boldsymbol{J}$ and $\boldsymbol{M}$, respectively, are placed inside the configuration.

$$\underline{\underline{\boldsymbol{\mu}}} = \begin{bmatrix} \mu & 0 & 0 \\ 0 & \mu & 0 \\ 0 & 0 & \mu_z \end{bmatrix} \tag{2.1}$$

$$\underline{\underline{\boldsymbol{\epsilon}}} = \begin{bmatrix} \epsilon & 0 & 0 \\ 0 & \epsilon & 0 \\ 0 & 0 & \epsilon_z \end{bmatrix} \tag{2.2}$$

$$\underline{\underline{\boldsymbol{\sigma}}}^s = \begin{bmatrix} \sigma^s_{xx} & \sigma^s_{xy} \\ \sigma^s_{yx} & \sigma^s_{yy} \end{bmatrix} \tag{2.3}$$

The treatment of the planar layered media is done for as follows. The Dyadic Green's Functions (DGFs) will be developed for layer $n \in [1, N]$ allowing the evaluation of the EM field within the layer. For this purpose, both electric and magnetic point sources are assumed to exist inside the same layer n of interest. Then, the EM fields in the other layers are computed after enforcing the boundary conditions at the interfaces. This process should take into account the terminations at top and bottom layers as well. All of this treatment will be performed using the TL analogy to be discussed in details later. Throughout this study, we assume time-harmonic fields with $e^{j\omega t}$ time convention. The Maxwell's postulates are given in (2.4) [78]. The spatial dependency $\boldsymbol{r} = x\hat{\boldsymbol{x}} + y\hat{\boldsymbol{y}} + z\hat{\boldsymbol{z}}$ is implicit in all expressions for convenience. Sometimes, we prefer to explicitly write the spatial dependency for clarification when needed. For uniaxial media, the constitutive relations are $\boldsymbol{D} = \epsilon_0 \underline{\underline{\boldsymbol{\epsilon}}} \cdot \boldsymbol{E}$ and $\boldsymbol{B} = \mu_0 \underline{\underline{\boldsymbol{\mu}}} \cdot \boldsymbol{H}$. Also, we allow the media constants components to be complex in general as $\mu = \mu' - j\mu''$ and $\epsilon = \epsilon' - j\epsilon''$.

$$\begin{aligned} \nabla \cdot \boldsymbol{D} &= q_e \\ \nabla \cdot \boldsymbol{B} &= q_m \\ \nabla \times \boldsymbol{E} &= -j\omega \boldsymbol{B} - \boldsymbol{M} \\ \nabla \times \boldsymbol{H} &= j\omega \boldsymbol{D} + \boldsymbol{J} \end{aligned} \tag{2.4}$$

The boundary conditions between layers n and $n+1$ at the interface $z = z_n$ can be expressed in general as in (2.5), where $\hat{\boldsymbol{n}} = \hat{\boldsymbol{z}}$ according to the configuration described in Figure 2.1. Here, $\boldsymbol{E}_n$ and $\boldsymbol{H}_n$ represents the fields inside layer n. Note that only the transverse fields continuity boundary conditions are needed to satisfy the physical requirements and the normal fields discontinuity boundary conditions will be automatically satisfied [59, p. 19].

$$\begin{aligned} \hat{\boldsymbol{n}} \times \big[\boldsymbol{E}_n(z_n) - \boldsymbol{E}_{n+1}(z_n)\big] &= 0 \\ \hat{\boldsymbol{n}} \times \big[\boldsymbol{H}_n(z_n) - \boldsymbol{H}_{n+1}(z_n)\big] &= \boldsymbol{J}_n^s = \underline{\underline{\boldsymbol{\sigma}_n^s}} \cdot \boldsymbol{E}_n(z_n) \end{aligned} \tag{2.5}$$

2.2 Scalarization of Maxwell's Equations

The solution for DGFs begins with scalarizing the system in (2.4). Since the planar layered media is symmetric in the transverse direction for a given z, it is possible to take advantage of this property in the structure and apply Fourier Transform (FT) for $\boldsymbol{\rho}$ and simplify the differential operators. Note that this property is not true for anisotropic conductive sheets. However, we will start our derivation from isotropic conductive sheets and then add more complexity by introducing anisotropic conductivity. So, assuming isotropic conductive sheets, this results in the spectral domain derivation presented in this section. The FT pairs[1] in (2.6) will be applied to the system in (2.4). The spectral domain can be thought of a rotation as illustrated in Figure 2.2. The orthonormal set of vectors $(\hat{\boldsymbol{u}}, \hat{\boldsymbol{v}}, \hat{\boldsymbol{z}})$ will be used to decompose the Maxwell's equations into e and h solutions, where $\boldsymbol{k}_\rho = k_\rho \hat{\boldsymbol{u}}$, the transverse wave vector.

[1]The complete FT in $\boldsymbol{r}$ and t is given in [79, p. 16].

$$\begin{aligned} \tilde{f}(\boldsymbol{k}_\rho) &= \int_{-\infty}^{\infty}\int_{-\infty}^{\infty} f(\boldsymbol{\rho}) e^{j\boldsymbol{k}_\rho\cdot\boldsymbol{\rho}} d\boldsymbol{\rho} \\ f(\boldsymbol{\rho}) &= \frac{1}{(2\pi)^2}\int_{-\infty}^{\infty}\int_{-\infty}^{\infty} \tilde{f}(\boldsymbol{k}_\rho) e^{-j\boldsymbol{k}_\rho\cdot\boldsymbol{\rho}} d\boldsymbol{k}_\rho \end{aligned} \tag{2.6}$$

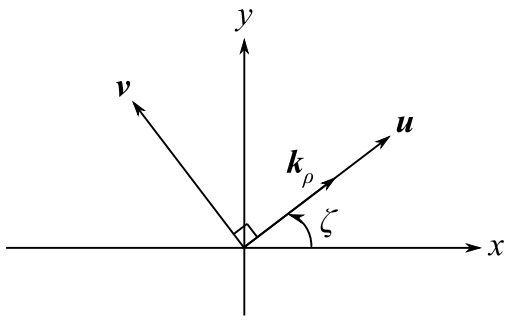

Figure 2.2: Definition of the orthonormal set of vectors $(\hat{\boldsymbol{u}}, \hat{\boldsymbol{v}}, \hat{\boldsymbol{z}})$ and $\boldsymbol{k}_\rho$ via spectral immittance [2].

The differential operator can be re-written as $\nabla = \nabla_t + \dfrac{\partial}{\partial z}\hat{\boldsymbol{z}}$, where t denotes the transverse components here. Also the fields can split into transverse and longitudinal components as in (2.7).

$$\begin{aligned} \boldsymbol{E} &= \boldsymbol{E}_t + E_z\hat{\boldsymbol{z}} \\ \boldsymbol{H} &= \boldsymbol{H}_t + H_z\hat{\boldsymbol{z}} \end{aligned} \tag{2.7}$$

After applying the FT in (2.6), ∇ becomes $\tilde{\nabla} = -j\boldsymbol{k}_\rho + \frac{\partial}{\partial z}\hat{\boldsymbol{z}}$. In all expressions, the $\boldsymbol{k}_\rho$ dependency is implicit for convenience, and this is distinguished by the tilde symbol in the components. Applying the FT in (2.6), the last two equations of (2.4) become:

$$
\begin{aligned}
(-j\boldsymbol{k}_\rho + \frac{\partial}{\partial z}\hat{\boldsymbol{z}}) \times (\tilde{\boldsymbol{E}}_t + \tilde{E}_z\hat{\boldsymbol{z}}) &= -j\omega\mu_0\mu\tilde{\boldsymbol{H}}_t - j\omega\mu_0\mu_z\tilde{H}_z\hat{\boldsymbol{z}} - \tilde{\boldsymbol{M}}_t - \tilde{M}_z\hat{\boldsymbol{z}} \\
(-j\boldsymbol{k}_\rho + \frac{\partial}{\partial z}\hat{\boldsymbol{z}}) \times (\tilde{\boldsymbol{H}}_t + \tilde{H}_z\hat{\boldsymbol{z}}) &= j\omega\epsilon_0\epsilon\tilde{\boldsymbol{E}}_t + j\omega\epsilon_0\epsilon_z\tilde{E}_z\hat{\boldsymbol{z}} + \tilde{\boldsymbol{J}}_t + \tilde{J}_z\hat{\boldsymbol{z}}
\end{aligned}
\tag{2.8}
$$

The longitudinal field components are found as in (2.9).

$$
\begin{aligned}
\tilde{E}_z &= \frac{-1}{j\omega\epsilon_0\epsilon_z}\big[j\boldsymbol{k}_\rho \cdot (\tilde{\boldsymbol{H}}_t \times \hat{\boldsymbol{z}}) + \tilde{J}_z\big] \\
\tilde{H}_z &= \frac{-1}{j\omega\mu_0\mu_z}\big[j\boldsymbol{k}_\rho \cdot (\hat{\boldsymbol{z}} \times \tilde{\boldsymbol{E}}_t) + \tilde{M}_z\big]
\end{aligned}
\tag{2.9}
$$

It is possible to reduce the equations into:

$$
\begin{aligned}
\frac{\partial}{\partial z}\tilde{\boldsymbol{E}}_t &= \frac{1}{j\omega\epsilon_0\epsilon}\big[k^2\underline{\underline{\boldsymbol{I}}}_t - \frac{1}{\nu^e}\boldsymbol{k}_\rho\boldsymbol{k}_\rho\big] \cdot (\tilde{\boldsymbol{H}}_t \times \hat{\boldsymbol{z}}) + \frac{\tilde{J}_z}{\omega\epsilon_0\epsilon_z}\boldsymbol{k}_\rho - \tilde{\boldsymbol{M}}_t \times \hat{\boldsymbol{z}} \\
\frac{\partial}{\partial z}\tilde{\boldsymbol{H}}_t &= \frac{1}{j\omega\mu_0\mu}\big[k^2\underline{\underline{\boldsymbol{I}}}_t - \frac{1}{\nu^h}\boldsymbol{k}_\rho\boldsymbol{k}_\rho\big] \cdot (\hat{\boldsymbol{z}} \times \tilde{\boldsymbol{E}}_t) + \frac{\tilde{M}_z}{\omega\mu_0\mu_z}\boldsymbol{k}_\rho + \tilde{\boldsymbol{J}}_t \times \hat{\boldsymbol{z}}
\end{aligned}
\tag{2.10}
$$

Where the wave number is defined as $k = k_0\sqrt{\mu\epsilon}$ and $k_0 = \omega\sqrt{\mu_0\epsilon_0}$. The intrinsic impedance is defined as $\eta = \eta_0\sqrt{\frac{\mu}{\epsilon}}$ and $\eta_0 = \sqrt{\frac{\mu_0}{\epsilon_0}}$.[2] Also, the axial anisotropy ratios are $\nu^e = \frac{\epsilon_z}{\epsilon}$ and $\nu^h = \frac{\mu_z}{\mu}$. Also, $\underline{\underline{\boldsymbol{I}}}_t = \hat{\boldsymbol{x}}\hat{\boldsymbol{x}} + \hat{\boldsymbol{y}}\hat{\boldsymbol{y}} = \hat{\boldsymbol{u}}\hat{\boldsymbol{u}} + \hat{\boldsymbol{v}}\hat{\boldsymbol{v}}$. The notations e, h in previous expressions indicate a TM and TE decompositions receptively with respect to the transverse x-y plane. The next step in this solution is to apply the spectral immittance. Thus, if the wave is propagating with wave vector $\boldsymbol{k} = \boldsymbol{k}_\rho + k_z\hat{\boldsymbol{z}}$, the transverse field components can be decomposed into $\hat{\boldsymbol{u}}$ and $\hat{\boldsymbol{v}}$ as in (2.11). The choice for voltages and currents symbols will become clear in the next steps where a TL equivalent can be obtained.

[2]It is possible to include Left Handed (LH) materials by implementing $k = k_0\sqrt{\mu}\sqrt{\epsilon}$ and $\eta = \eta_0\frac{\sqrt{\mu}}{\sqrt{\epsilon}}$. This choice will preserve the correct signs [80].

$$\begin{aligned}\tilde{\boldsymbol{E}}_t = V^e\hat{\boldsymbol{u}} + V^h\hat{\boldsymbol{v}} \longrightarrow \hat{\boldsymbol{z}} \times \tilde{\boldsymbol{E}}_t = -V^h\hat{\boldsymbol{u}} + V^e\hat{\boldsymbol{v}} \\ \tilde{\boldsymbol{H}}_t = -I^h\hat{\boldsymbol{u}} + I^e\hat{\boldsymbol{v}} \longrightarrow \tilde{\boldsymbol{H}}_t \times \hat{\boldsymbol{z}} = I^e\hat{\boldsymbol{u}} + I^h\hat{\boldsymbol{v}}\end{aligned} \tag{2.11}$$

Thus, introducing (2.11) into (2.10) gives the system in (2.12).

$$\begin{aligned}\frac{\partial}{\partial z}[V^e\hat{\boldsymbol{u}} + V^h\hat{\boldsymbol{v}}] &= \frac{1}{j\omega\epsilon_0\epsilon}\Big[k^2\underline{\underline{\boldsymbol{I}}}_t - \frac{k_\rho^2}{\nu^e}\hat{\boldsymbol{u}}\hat{\boldsymbol{u}}\Big] \cdot [I^e\hat{\boldsymbol{u}} + I^h\hat{\boldsymbol{v}}] + \frac{k_\rho}{\omega\epsilon_0\epsilon_z}\tilde{J}_z\hat{\boldsymbol{u}} - \tilde{\boldsymbol{M}}_t \times \hat{\boldsymbol{z}} \\ \frac{\partial}{\partial z}[-I^h\hat{\boldsymbol{u}} + I^e\hat{\boldsymbol{v}}] &= \frac{1}{j\omega\mu_0\mu}\Big[k^2\underline{\underline{\boldsymbol{I}}}_t - \frac{k_\rho^2}{\nu^h}\hat{\boldsymbol{u}}\hat{\boldsymbol{u}}\Big] \cdot [-V^h\hat{\boldsymbol{u}} + V^e\hat{\boldsymbol{v}}] + \frac{k_\rho}{\omega\mu_0\mu_z}\tilde{M}_z\hat{\boldsymbol{u}} + \tilde{\boldsymbol{J}}_t \times \hat{\boldsymbol{z}}\end{aligned} \tag{2.12}$$

The final step can be achieved by equating the $\hat{\boldsymbol{u}}$ and $\hat{\boldsymbol{v}}$ components in (2.12) and results in the TL system in (2.13).

$$\begin{aligned}\frac{dV^\alpha}{dz} &= -jk_z^\alpha Z^\alpha I^\alpha + v^\alpha \\ \frac{dI^\alpha}{dz} &= -jk_z^\alpha Y^\alpha V^\alpha + i^\alpha\end{aligned} \tag{2.13}$$

Where $k_z^\alpha = \sqrt{k^2 - \frac{k_\rho^2}{\nu^\alpha}}$, $Z^e = \frac{k_z^e}{\omega\epsilon_0\epsilon}$, and $Z^h = \frac{\omega\mu_0\mu}{k_z^h}$. Here, we let $\alpha = e, h$. The previous system represents TLs with series voltage and shut current sources excitations that can be summarized as in Table 2.1. Thus, we can separate these equations into two systems as in (2.14) and (2.15) utilizing the superposition in linear systems. Here, we observe that this treatment for Maxwell's equations results in two separate TLs, *viz.* e and h.

Table 2.1: Series voltage and shut current excitations for the TL system in (2.13).

	$\alpha = e$	$\alpha = h$
v^α	$\frac{k_\rho}{\omega\epsilon_0\epsilon_z}\tilde{J}_z - \tilde{M}_v$	$\tilde{M}_u$
i^α	$-\tilde{J}_u$	$-\frac{k_\rho}{\omega\mu_0\mu_z}\tilde{M}_z - \tilde{J}_v$

$$\begin{aligned} \frac{dV_i^\alpha}{dz} &= -jk_z^\alpha Z^\alpha I_i^\alpha \\ \frac{dI_i^\alpha}{dz} &= -jk_z^\alpha Y^\alpha V_i^\alpha + \delta(z - z') \end{aligned} \tag{2.14}$$

$$\begin{aligned} \frac{dI_v^\alpha}{dz} &= -jk_z^\alpha Y^\alpha V_v^\alpha \\ \frac{dV_v^\alpha}{dz} &= -jk_z^\alpha Z^\alpha I_v^\alpha + \delta(z - z') \end{aligned} \tag{2.15}$$

The TLGFs are kernels defined as $V_s^\alpha(k_\rho; z|z')$ and $I_s^\alpha(k_\rho; z|z')$ for $s = v, i$. Here, the subscript s represents the source type. The total voltages and currents are found via the kernels integrals in in (2.16)[3].

$$\begin{aligned} V^\alpha &= \langle V_i^\alpha, i^\alpha \rangle + \langle V_v^\alpha, v^\alpha \rangle \\ I^\alpha &= \langle I_i^\alpha, i^\alpha \rangle + \langle I_v^\alpha, v^\alpha \rangle \end{aligned} \tag{2.16}$$

[3]The kernel integrals denoted by $\langle K(\zeta, \zeta'), \phi(\zeta') \rangle \equiv \int_{-\infty}^{\infty} K(\zeta, \zeta')\phi(\zeta')d\zeta'$. The same definition is applicable to multi-dimensional kernels and functions.

2.3 Transmission Line Green's Functions

The TLGFs are the solutions for the differential equation that resulted from scalarizing the Maxwell's equations in (2.14) and (2.15). The equivalent TL model for the planar layered media is illustrated in Figure 2.3. The TL model is applicable to both e and h modes which are omitted in Figure 2.3. At the top and bottom terminations z_0 and z_N, the impedances $\overrightarrow{Z}_1$ and $\overleftarrow{Z}_N$ are used to express any possible terminations, respectively. Those terminations include PEC, PMC, open, and impedance boundary in general. The open termination means semi-infinite layer.

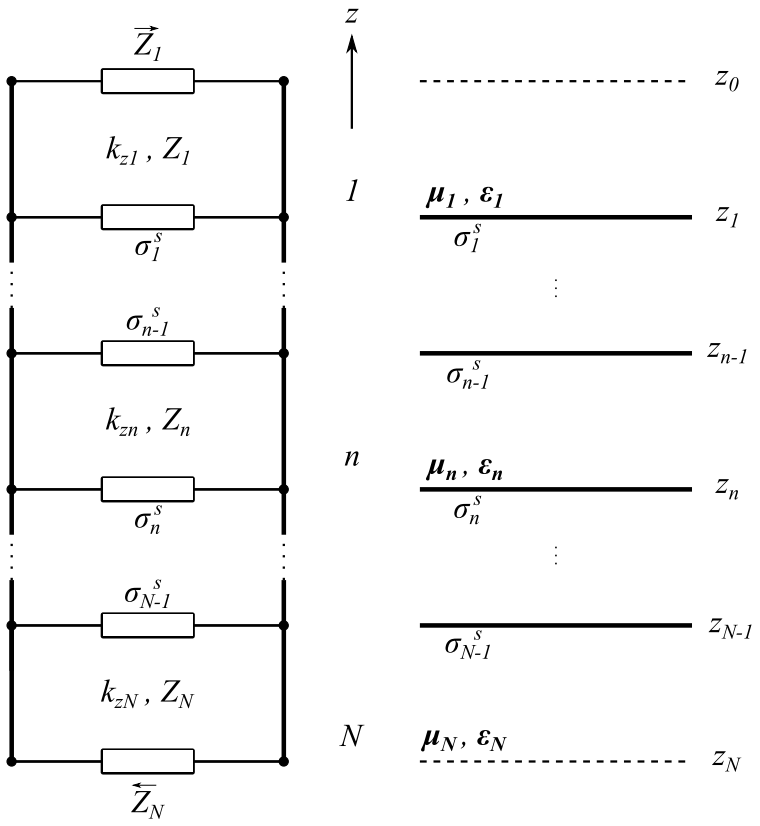

Figure 2.3: Equivalent TL model e or h (left) for the planar layered media configuration (right) for N layers with possible isotropic conductive sheets. The shut admittances represent the isotropic surface conductivities σ_n^s measured in [S].

From the boundary conditions in (2.5), in the spectral domain, the surface conductivity tensor $\underline{\underline{\boldsymbol{\sigma}}}^s$ is replaced with $\underline{\underline{\tilde{\boldsymbol{\sigma}}}}^s = \sigma^s_{uu}\hat{\boldsymbol{u}}\hat{\boldsymbol{u}}+\sigma^s_{uv}\hat{\boldsymbol{u}}\hat{\boldsymbol{v}}+\sigma^s_{vu}\hat{\boldsymbol{v}}\hat{\boldsymbol{u}}+\sigma^s_{vv}\hat{\boldsymbol{v}}\hat{\boldsymbol{v}}$.[4] Also $\tilde{\boldsymbol{E}}_t = V^e\hat{u}+V^h\hat{v}$ and $-\hat{\boldsymbol{z}} \times \tilde{\boldsymbol{H}}_t = I^e\hat{\boldsymbol{u}} + I^h\hat{\boldsymbol{v}}$. Applying these definitions in (2.13), the following boundary conditions are obtained as:

$$\begin{aligned} V^e_{n+1}(z_n) &= V^e_n(z_n) \\ V^h_{n+1}(z_n) &= V^h_n(z_n) \\ I^e_{n+1}(z_n) - I^e_n(z_n) &= \sigma^s_{uu}V^e_n(z_n) + \sigma^s_{uv}V^h_n(z_n) \\ I^h_{n+1}(z_n) - I^h_n(z_n) &= \sigma^s_{vu}V^e_n(z_n) + \sigma^s_{vv}V^h_n(z_n) \end{aligned} \tag{2.17}$$

If an isotropic conductivity is considered $\underline{\underline{\boldsymbol{\sigma}}}^s = \sigma^s(\hat{\boldsymbol{u}}\hat{\boldsymbol{u}} + \hat{\boldsymbol{v}}\hat{\boldsymbol{v}})$, this reduces (2.17) to (2.18) and (2.19). This also decouples the equations and simplifies the derivation [82].

$$V^\alpha_{n+1}(z_n) = V^\alpha_n(z_n) \tag{2.18}$$

$$\frac{I^\alpha_{n+1}(z_n) - I^\alpha_n(z_n)}{V^\alpha_n(z_n)} = \sigma^s_n \tag{2.19}$$

The complete TLGFs solutions for isotropic conductive sheets are summarized in Appendix A.

2.4 Fields Dyadic Green's Functions

In order to obtain the fields DGFs, a point source should be considered. Thus, the fields expressions allow the extraction of DGFs as presented in this section. The total field can be formed as in (2.7) and using (2.9) by combing the expressions of transverse and

[4]The symbol $\tilde{\underline{\underline{\boldsymbol{\sigma}}}}^s$ is used in order to distinguish between the spatial and spectral domain coordinates. Note that the surface conductivity is independent of $\boldsymbol{\rho}$ and hence no convolution is needed[81].

longitudinal components in (2.11). This takes the form:

$$\begin{aligned}\tilde{\boldsymbol{E}} &= V^e\hat{\boldsymbol{u}} + V^h\hat{\boldsymbol{v}} - \frac{k_\rho}{\omega\epsilon_0\epsilon_z}I^e\hat{\boldsymbol{z}} - \frac{\tilde{J}_z}{j\omega\epsilon_0\epsilon_z}\hat{\boldsymbol{z}} \\ \tilde{\boldsymbol{H}} &= -I^h\hat{\boldsymbol{u}} + I^e\hat{\boldsymbol{v}} + \frac{k_\rho}{\omega\mu_0\mu_z}V^h\hat{\boldsymbol{z}} - \frac{\tilde{M}_z}{j\omega\mu_0\mu_z}\hat{\boldsymbol{z}}\end{aligned} \tag{2.20}$$

Using the voltages and currents solutions in (2.16) and the sources in Table 2.1 and substituting the expressions into (2.20), the complete field is obtained. Considering point sources $\boldsymbol{J} = I\boldsymbol{l}\delta(\boldsymbol{\rho})\delta(z-z')$ and $\boldsymbol{M} = K\boldsymbol{l}\delta(\boldsymbol{\rho})\delta(z-z')$ which correspond to the spectral domain $\tilde{\boldsymbol{J}} = I\boldsymbol{l}\delta(z-z')$ and $\tilde{\boldsymbol{M}} = K\boldsymbol{l}\delta(z-z')$. Here, $I\boldsymbol{l}$ and $K\boldsymbol{l}$ are the electric and magnetic current moments, respectively. The fields DGFs are obtained as follows:[5]

$$\begin{aligned}\tilde{\boldsymbol{E}} &= \langle\underline{\underline{\tilde{\boldsymbol{G}}}}^{EJ};\tilde{\boldsymbol{J}}\rangle + \langle\underline{\underline{\tilde{\boldsymbol{G}}}}^{EM};\tilde{\boldsymbol{M}}\rangle \\ \tilde{\boldsymbol{H}} &= \langle\underline{\underline{\tilde{\boldsymbol{G}}}}^{HJ};\tilde{\boldsymbol{J}}\rangle + \langle\underline{\underline{\tilde{\boldsymbol{G}}}}^{HM};\tilde{\boldsymbol{M}}\rangle\end{aligned} \tag{2.21}$$

The spectral domain DGFs given in (2.22)-(2.25) can be obtained by carefully isolating the current components and moving the other terms to the kernel side.

$$\begin{aligned}\underline{\underline{\tilde{\boldsymbol{G}}}}^{EJ} &= -V_i^e\hat{\boldsymbol{u}}\hat{\boldsymbol{u}} - V_i^h\hat{\boldsymbol{v}}\hat{\boldsymbol{v}} + \frac{k_\rho}{\omega\epsilon_0\epsilon_z}I_i^e\hat{\boldsymbol{z}}\hat{\boldsymbol{u}} + \frac{k_\rho}{\omega\epsilon_0\epsilon_z'}V_v^e\hat{\boldsymbol{u}}\hat{\boldsymbol{z}} \\ &\quad - \frac{1}{j\omega\epsilon_0\epsilon_z'}\Big[\frac{jk_\rho^2}{\omega\epsilon_0\epsilon_z}I_v^e + \delta(z-z')\Big]\hat{\boldsymbol{z}}\hat{\boldsymbol{z}}\end{aligned} \tag{2.22}$$

$$\underline{\underline{\tilde{\boldsymbol{G}}}}^{EM} = -V_v^e\hat{\boldsymbol{u}}\hat{\boldsymbol{v}} + V_v^h\hat{\boldsymbol{v}}\hat{\boldsymbol{u}} + \frac{k_\rho}{\omega\epsilon_0\epsilon_z}I_v^e\hat{\boldsymbol{z}}\hat{\boldsymbol{v}} - \frac{k_\rho}{\omega\mu_0\mu_z'}V_i^h\hat{\boldsymbol{v}}\hat{\boldsymbol{z}} \tag{2.23}$$

[5]The kernel integrals $\langle\underline{\underline{\boldsymbol{K}}}(\zeta,\zeta');\boldsymbol{F}(\zeta')\rangle$ indicate the dot-product.

$$\tilde{\underline{\underline{\boldsymbol{G}}}}^{HJ} = I_i^h \hat{\boldsymbol{u}}\hat{\boldsymbol{v}} - I_i^e \hat{\boldsymbol{v}}\hat{\boldsymbol{u}} - \frac{k_\rho}{\omega\mu_0\mu_z} V_i^h \hat{\boldsymbol{z}}\hat{\boldsymbol{v}} + \frac{k_\rho}{\omega\epsilon_0\epsilon_z'} I_v^e \hat{\boldsymbol{v}}\hat{\boldsymbol{z}} \tag{2.24}$$

$$\begin{aligned}\tilde{\underline{\underline{\boldsymbol{G}}}}^{HM} = &-I_v^h \hat{\boldsymbol{u}}\hat{\boldsymbol{u}} - I_v^e \hat{\boldsymbol{v}}\hat{\boldsymbol{v}} + \frac{k_\rho}{\omega\mu_0\mu_z} V_v^h \hat{\boldsymbol{z}}\hat{\boldsymbol{u}} + \frac{k_\rho}{\omega\mu_0\mu_z'} I_i^h \hat{\boldsymbol{u}}\hat{\boldsymbol{z}} \\ &- \frac{1}{j\omega\mu_0\mu_z'}\Big[\frac{jk_\rho^2}{\omega\mu_0\mu_z} V_i^h + \delta(z-z')\Big]\hat{\boldsymbol{z}}\hat{\boldsymbol{z}}\end{aligned} \tag{2.25}$$

Where $\mu_z' = \mu_z(z')$ and $\epsilon_z' = \epsilon_z(z')$. The spatial domain DGFs require applying the inverse FT in (2.6). Figure 2.4 illustrates the relation between spatial and spectral domain unit vectors. The point sources considered in the previous derivation allow exploiting the symmetry in φ and result in Fourier Bessel Transform (FBT). Just as a reminder, the spectral domain DGFs have the dependency $\tilde{\underline{\underline{\boldsymbol{G}}}}^{PQ}(\boldsymbol{k}_\rho; z|z')$, whereas the spatial domain DGF have the dependency $\underline{\underline{\boldsymbol{G}}}^{PQ}(\boldsymbol{\rho}; z|z')$. Here, P field type is due to Q current type.

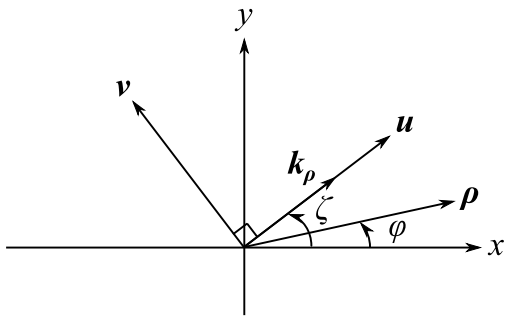

Figure 2.4: Spatial and spectral domain relation.

Consider that $\tilde{f}(\boldsymbol{k}_\rho)$ is independent of ζ, hence $\tilde{f}(\boldsymbol{k}_\rho) = \tilde{f}(k_\rho)$ and the inverse FT becomes:

$$f(\boldsymbol{\rho}) = \frac{1}{2\pi}\int_0^{\infty} \tilde{f}(k_\rho)\frac{1}{2\pi}\Big[\int_0^{2\pi} e^{-jk_\rho\rho\cos(\zeta-\varphi)}d\zeta\Big]k_\rho dk_\rho = \frac{1}{2\pi}\int_0^{\infty} \tilde{f}(k_\rho)J_0(k_\rho\rho)k_\rho dk_\rho \tag{2.26}$$

The integral in (2.26) can be re-written as in (2.27).

$$S_n\{\tilde{f}(k_\rho)\} = \frac{1}{2\pi}\int_0^{\infty} \tilde{f}(k_\rho)J_n(k_\rho\rho)k_\rho dk_\rho \tag{2.27}$$

The integral in (2.27) is referred to as Sommerfeld Integral (SI). When evaluating SIs, sometimes it is preferred to re-express the integrals from $-\infty$ to $+\infty$ under the assumption that $\tilde{f}(k_\rho)$ is even (odd) for even (odd) values of n respectively.[6]

$$S_n\{\tilde{f}(k_\rho)\} = \frac{1}{4\pi}\int_{-\infty}^{\infty} \tilde{f}(k_\rho)H_n^{(2)}(k_\rho\rho)k_\rho dk_\rho \tag{2.28}$$

Applying the definition in (2.27) and utilizing Bessel's functions properties to the spectral DGFs in (2.22)-(2.25), one can obtain the spatial domain DGFs which are listed in Appendix B.

2.5 Point Source Excitation

The evaluation of EM fields due to point sources (Hertzian dipoles) is a special case of the general arbitrary current distribution. But, it is very important to focus on this special case since it provides a lot of insights and it is applicable to many practical scenarios. An example of an arbitrary electric current point source located at $\boldsymbol{r'}$ is illustrated in Figure 2.5. Here, the point source is defined by a current moment $I\boldsymbol{l}$ and orientation angles (θ_0, φ_0).

For multiple dipoles, the superposition results in a sum of dot products for point sources as in (2.29). Where N_J and N_M are the number of electric and magnetic dipoles

[6]The Hankel relations $J_n(z) = \frac{1}{2}[H_n^{(1)}(z)+H_n^{(2)}(z)]$ and $H_n^{(1)}(ze^{j\pi}) = -e^{-jn\pi}H_n^{(2)}(z)$ are also used.

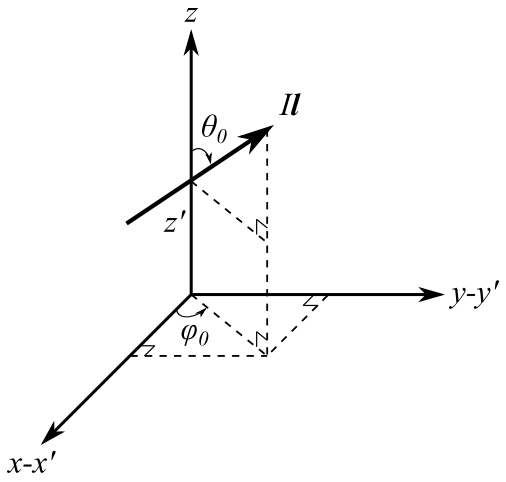

Figure 2.5: A point source of current moment $I\boldsymbol{l}$ [Am]. Note that the x and y axes are shifted by x' and y' respectively.

with arbitrary current moments $I\boldsymbol{l}_{k_J}$ and $K\boldsymbol{l}_{k_M}$, respectively. For a continuous distribution of currents, a convolution is needed.

$$\begin{aligned}\boldsymbol{E} &= \sum_{k_J=1}^{N_J} \underline{\underline{\boldsymbol{G}}}^{EJ} \cdot I\boldsymbol{l}_{k_J} + \sum_{k_M=1}^{N_M} \underline{\underline{\boldsymbol{G}}}^{EM} \cdot K\boldsymbol{l}_{k_M} \\ \boldsymbol{H} &= \sum_{k_J=1}^{N_J} \underline{\underline{\boldsymbol{G}}}^{HJ} \cdot I\boldsymbol{l}_{k_J} + \sum_{k_M=1}^{N_M} \underline{\underline{\boldsymbol{G}}}^{HM} \cdot K\boldsymbol{l}_{k_M}\end{aligned} \tag{2.29}$$

For point source excitation, we need to evaluate the SIs as mentioned in the previous section. Unfortunately, these integrals have no closed form expressions and require either an approximation or a numerical integration. These SIs as discussed earlier can be represented as infinite or semi-infinite integrals which are both equivalent. For example, the integration path is defined as in Figure 2.6 [83, p. 459], for the Hankel function definition in (2.28). Note that the Sommerfeld Integration Path (SIP) in Figure 2.6 has to avoid the influence of poles in the integrand near integration path. These poles are unique and related to the configuration resonance condition. Each pole corresponds to a special wave

type such as surface and leaky waves [84, p. 470], and will be investigated thoroughly in Chapter 3.

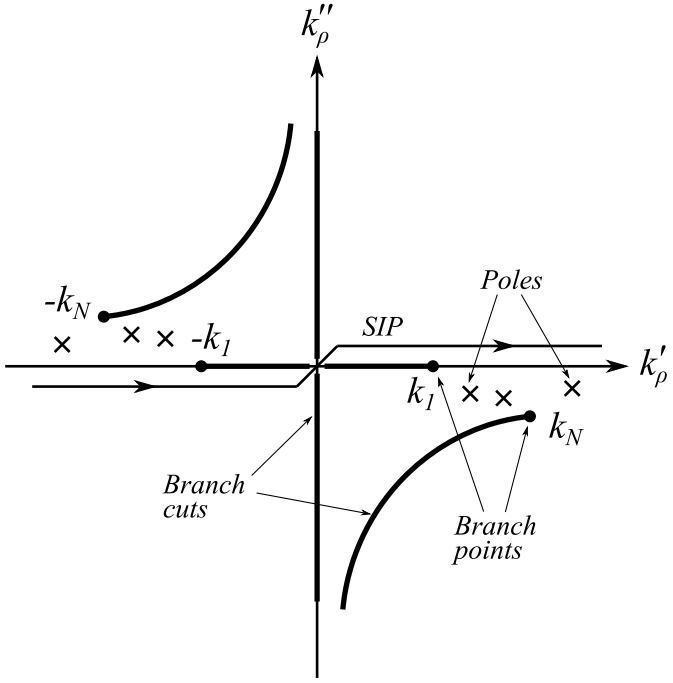

Figure 2.6: An example of the SIP. The branch cut associated with the Hankel function is not presented. In this case layer 1 is lossless and layer N is lossy.

Moreover, the definition of $k_{zn}^{\alpha} = \sqrt{k_n^2 - k_\rho^2/\nu_n^{\alpha}}$ results in two branch cuts [85] for layers 1 and N.[7] The branch cuts can be chosen arbitrarily, but the definitions at $\mathrm{Im}[k_{z1}^{\alpha}] = 0$ and $\mathrm{Im}[k_{zN}^{\alpha}] = 0$ were chosen according to [84, p. 460], as in Figure 2.6. The two branch cuts correspond to four Riemann sheets [86, p. 613], with possible transitions between the sheets through the branch cuts for k_1 and k_N as shown in Figure 2.7.

Several methods for evaluating this integral have been successfully presented such as DCIM, FHT and matrix pencil method [57, 87–95]. Nevertheless, the only method that

[7]For the layers $n = 2, 3, \ldots, N-1$ it can be shown that the definition of k_{zn} doesn't result in a branch cut [86, p. 479] This be can verified by alternating the sign of k_{zn} and we notice no change on the integrand.

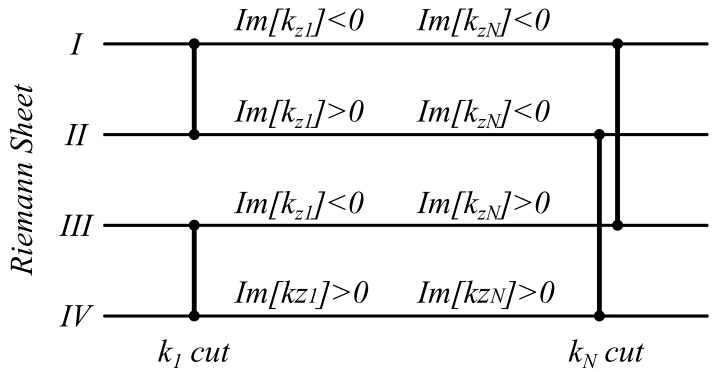

Figure 2.7: The four Riemann sheets definitions and connections between the sheets through the branch cuts associated with branch points k_1 and k_N.

provides accurate and reliable results is the real axis integration method which will be used in this work. The only disadvantage in this method is the limitation for large ρ computations and the time it takes to evaluate the integrals. When $\rho \gg \lambda_0$, the integrands become extremely highly oscillatory making it very difficult to evaluate with reasonable accuracy. Roughly, a distance of hundreds λ_0 would be the maximum range for this method. For distances beyond this, one would prefer to use the far fields approximations instead of computing the exact solution via SIs. The details of the numerical evaluation of SIs using the real axis integration are summarized in Appendix C.

2.5.1 Numerical Examples

A numerical example of isotropic graphene sheet in layered media from Simsek [96] is considered for validation. The results were computed using both the finite thickness model $\delta = 0.335$ [nm] [97] and the conductive sheet formulation developed in this chapter for validation.[8] The frequency of operation is $f = 750$ [THz]. The configuration details are summarized in Table 2.2, where the graphene sheet is at the interface between layers 1 and 2.

[8]The effective dielectric constant $\epsilon = 1 - j\dfrac{\sigma^s}{\omega\epsilon_0\delta}$.

The conductivity of thin-film of graphene is modeled by Kubo-model for surface conductivity which results in intraband and interband conductivities that can be approximated as in (2.30) [19, 27, 98]. The surface conductivity in the low THz frequency range is illustrated in Figure 2.8. The results are shown in Figure 2.9.

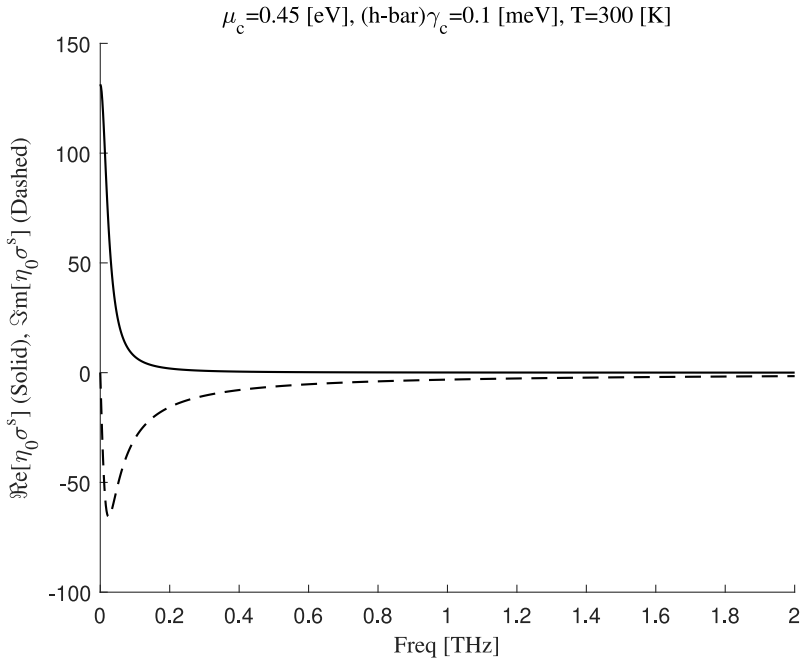

Figure 2.8: An example for the surface conductivity of isotropic graphene sheet using (2.30).

$$\begin{aligned}\sigma_{\text{intra}} &= \frac{-j2e^2k_BT}{\pi\hbar^2(\omega - j\gamma_c)}\ln\left(2\cosh\left[\frac{\mu_c}{2k_BT}\right]\right)\\ \sigma_{\text{inter}} &= \frac{e^2}{4\hbar}\left[\frac{1}{2} + \frac{1}{\pi}\tan^{-1}\left(\frac{\hbar(\omega - j\gamma_c) - 2\mu_c}{2k_BT}\right)\right.\\ &\quad\left. + \frac{j}{2\pi}\ln\left(\frac{[\hbar(\omega - j\gamma_c) + 2\mu_c]^2}{[\hbar(\omega - j\gamma_c) - 2\mu_c]^2 + (2k_BT)^2}\right)\right]\end{aligned} \tag{2.30}$$

Where e: charge of electron, k_B: Boltzmann's constant, h: Planck's constant, ω: radial

frequency, and T: absolute temperature. μ_c is the chemical potential $|\mu_c| \leq 1$ and γ_c is the phenomenological carrier scattering rate. Also, $\hbar = \dfrac{h}{2\pi}$ and $\sigma_0 = \dfrac{e^2}{\hbar}$. The total surface conductivity is evaluated as $\sigma^s = \sigma_{\text{intra}} + \sigma_{\text{inter}}$.

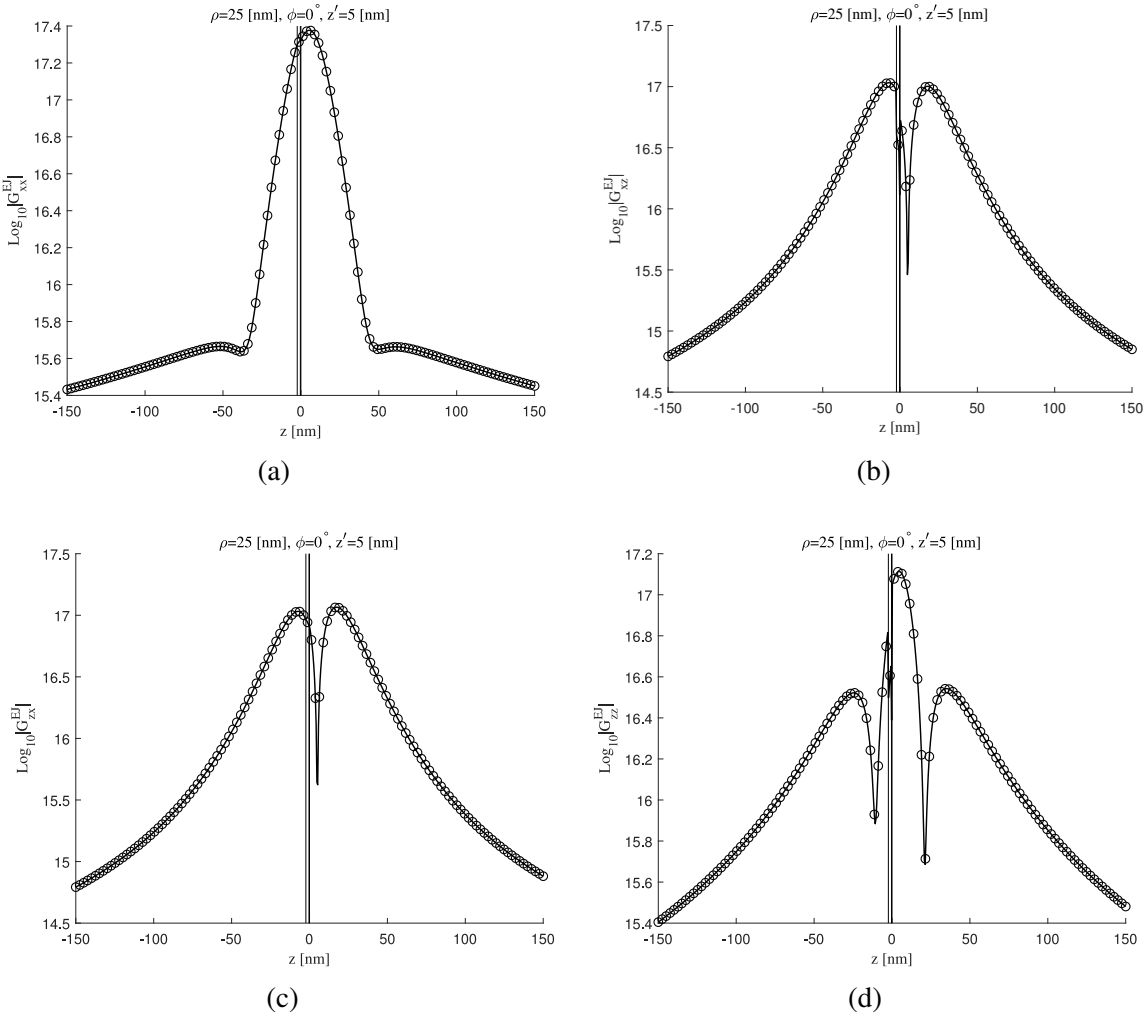

Figure 2.9: DGFs computed using the modified TL model (solid) and values computed using finite thickness model and (circles) for the configuration in Table 2.2. The graphene parameters are: $\mu_c = 0.2$ [eV], $\hbar\gamma_c = 2.7$ [meV] and $T = 300$ [K] using Kubo-model in (2.30). The frequency of operation was selected to be 750 [THz]. The surface conductivity is $\sigma^s \approx 6.0660 \times 10^{-5} - j1.9221 \times 10^{-7}$ [S].

Table 2.2: Details of Simsek configuration. A dielectric slab surrounded by air.

Layer n	z_n [nm]	ϵ_n
0	open	-
1	0	1
Graphene	-	-
2	-2	2.25
3	open	1

2.6 Plane Wave Excitation

The evaluation of the plane wave excitation in planar layered media is a very important aspect of this study. Several optical devices can be modeled by planar layered such as thin-film anti-reflection coatings, dielectric mirrors, and optical interference filters [99, p. 186]. In addition to that, the excitation of surface waves modes such as Surface Plasmon Polariton (SPP) [100] are usually achieved by laser sources which can be adequately represented in small region of interest by incident plane waves [101, p. 47]. The optical signal passing in these devices are well represented by incident plane waves. An illustration of the wave number of an incident plane wave from the top layer is shown in Figure 2.10. The plane wave is decomposed into two components E^i_θ and E^i_φ allowing the definition of TE and TM polarizations, but also circular polarizations.

The analysis of plane wave excitation can be simplified by using the surface equivalence theorem [78, 102, 103]. Thus, it is possible to define an equivalent magnetic surface current at z_0 as $\hat{\boldsymbol{n}} \times \boldsymbol{E} = \boldsymbol{M}_s$. Using image theorem, the problem in the range $z_N \leq z \leq z_0$ can be solved using magnetic currents sheet $\boldsymbol{M}_s = 2\hat{\boldsymbol{z}} \times \boldsymbol{E}^i \delta(z - z_0)$ as depicted in Figure 2.11. Also, the transverse wave number is $k^i_\rho = k_1 \sin(\theta_i)$. The incident field in $z > z_0$ is expressed in (2.31) according to Figure 2.10.

$$\boldsymbol{E}^i = \boldsymbol{E}_0 e^{j\boldsymbol{k}^i_\rho \cdot \boldsymbol{\rho}} e^{jk_1 \cos(\theta_i) z} \tag{2.31}$$

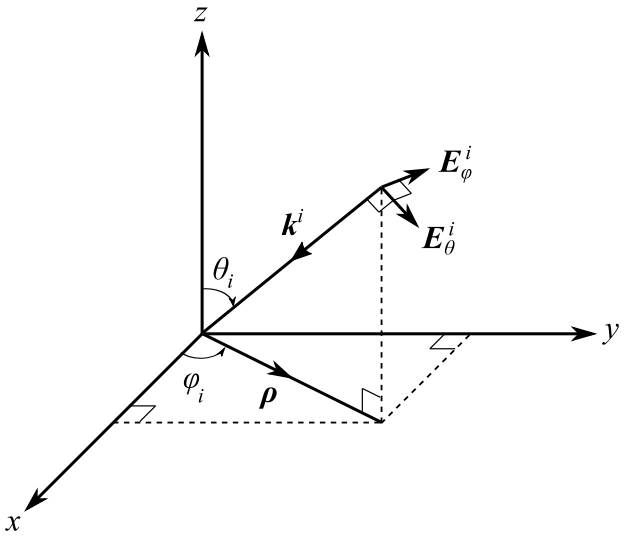

Figure 2.10: Schematic of the incident plane wave excitation from the top layer. The wave vector $\boldsymbol{k}^i$ is defined by the incidence angles (θ_i, φ_i).

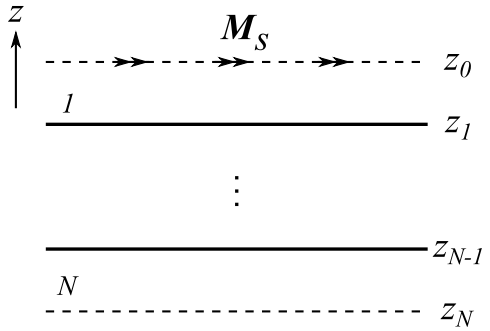

Figure 2.11: The equivalent problem of incident plane wave from the top layer. The equivalent current sheet is defined at $z = z_0$.

Where $\boldsymbol{E}_0$ is given as:

$$\boldsymbol{E}_0 = E_\theta^i \hat{\boldsymbol{\theta}}_i + E_\varphi^i \hat{\boldsymbol{\varphi}}_i \tag{2.32}$$

According to this choice, for TM excitation we set $E_\varphi^i = 0$, while and for TE excitation we set $E_\theta^i = 0$. The evaluation of the fields due to this excitation can be simplified by exploiting FT properties. Hence, the FT is applied and the evaluation is performed in the spectral domain where $\hat{\boldsymbol{\rho}}_i = \hat{\boldsymbol{u}}$ and $\hat{\boldsymbol{\varphi}}_i = \hat{\boldsymbol{v}}$. Thus, the spectral domain equivalent current $\tilde{\boldsymbol{M}}_s$ is given in (2.33).

$$\tilde{\boldsymbol{M}}_s = \left[E_\theta^i \cos(\theta_i)\hat{\boldsymbol{v}} - E_\varphi^i \hat{\boldsymbol{u}}\right] e^{jk_1 \cos(\theta_i) z_0} (2\pi)^2 \delta(\boldsymbol{k}_\rho + \boldsymbol{k}_\rho^i)\delta(z - z_0) \tag{2.33}$$

Now, the convolution integral in (2.23) and (2.25) are used to evaluate the fields in the range of interest $z_N \leq z \leq z_0$ as in (2.34). Note that these convolutions reduce into dot product because of $\delta(z - z_0)$.

$$\begin{aligned} \tilde{\boldsymbol{E}} &= \langle \underline{\underline{\tilde{\boldsymbol{G}}}}^{EM}; 2\tilde{\boldsymbol{M}}_s \rangle \\ \tilde{\boldsymbol{H}} &= \langle \underline{\underline{\tilde{\boldsymbol{G}}}}^{HM}; 2\tilde{\boldsymbol{M}}_s \rangle \end{aligned} \tag{2.34}$$

Upon applying the inverse FT to the resulting fields, this reduces to the expression in (2.35). Where the definitions $Z_1^e = \eta_1 \cos(\theta_i)$ and $Z_1^h = \dfrac{\eta_1}{\cos(\theta_i)}$ were used.

$$\begin{aligned} \boldsymbol{E} &= -2\boldsymbol{E}_0 \cdot \left[V_v^e \cos(\theta_i)\hat{\boldsymbol{\theta}}_i\hat{\boldsymbol{\rho}}_i + V_v^h \hat{\boldsymbol{\varphi}}_i\hat{\boldsymbol{\varphi}}_i - I_v^e Z_1^e \frac{\epsilon_1}{\epsilon_z} \sin(\theta_i)\hat{\boldsymbol{\theta}}_i\hat{\boldsymbol{z}}\right] e^{j\boldsymbol{k}_\rho^i \cdot \boldsymbol{\rho}} e^{jk_1 \cos(\theta_i) z_0} \\ \boldsymbol{H} &= -2\boldsymbol{E}_0 \cdot \left[- I_v^h \hat{\boldsymbol{\varphi}}_i\hat{\boldsymbol{\rho}}_i + I_v^e \cos(\theta_i)\hat{\boldsymbol{\theta}}_i\hat{\boldsymbol{\varphi}}_i + V_v^h \frac{1}{Z_1^h}\frac{\mu_1}{\mu_z} \sin(\theta_i)\hat{\boldsymbol{\varphi}}_i\hat{\boldsymbol{z}}\right] e^{j\boldsymbol{k}_\rho^i \cdot \boldsymbol{\rho}} e^{jk_1 \cos(\theta_i) z_0} \end{aligned} \tag{2.35}$$

2.6.1 Numerical Examples

In this example, a graphene based Otto configuration [20] is considered as illustrated in Figure 2.12. However, we decided to optimize this example for more practical values. The minimum reflectivity is found at $f = 1$ [THz] when $d = 20$ [μm] after tuning the setup vs μ_c. These results are evident from Figure 2.13. The advantage of introducing graphene sheet is the possibility of tuning the configuration by adjusting the electrostatic bias represented by the value of μ_c.

Table 2.3: Otto configuration with graphene details.

Layer	Thickness [μm]	$n = \sqrt{\epsilon}$
Prism	open	2.003
Air	20	1
Graphene	-	-
Dielectric	open	1.762

Note that the SPP mode can be excited only by evanescent waves beyond the critical angle, *i.e.*, $\theta_i > \theta_c$. In this case $\theta_c = \sin^{-1}\sqrt{\max(\epsilon_2, \epsilon_3)/\epsilon_1} \approx 61.6°$. Using the methods from Chapter 3, the SPP pole is found at $k_\rho/k_0 = 1.88224 - j0.00063$. Hence, the transverse incident plane wave number is $n_1 \sin(70°) = 1.8822 \approx \mathrm{Re}[k_\rho/k_0]$.

2.7 Far Fields Computation

The far field due to a point source can be evaluated using the equivalence theorem combined with image theorem in a similar way to the plane wave excitation fields. Here, the interest is on the top and bottom layers. Hence, the solution will be considered for $z > z_0$ and $z < z_N$. The solution for $z < z_N$ can be easily obtained using a similar procedure to the one used for $z > z_0$. The electric field due to equivalent magnetic current at $z = z_0$ is shown in (2.34) using free-space Green's function [104].

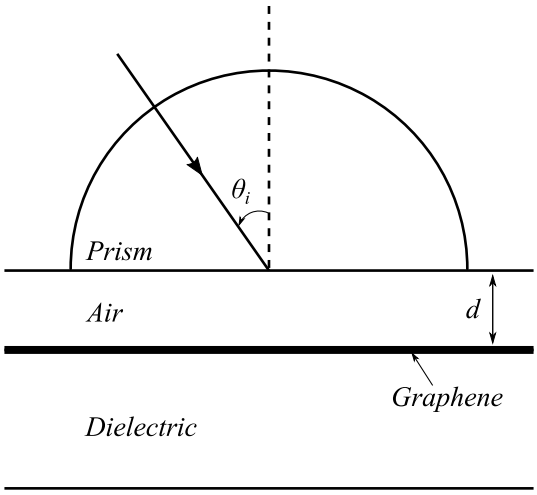

Figure 2.12: Otto configuration with graphene sheet. The graphene parameters are $\mu_c = 0.8138$ [eV], $\hbar\gamma_c = 0.1$ [meV], and $T = 300$ [K]. The configuration is designed to operate at $f = 1$ [THz] for air gap width $d = 20$ [μm].

$$\boldsymbol{E} = -\nabla \times \iiint \frac{e^{-jk_1|\boldsymbol{r}-\boldsymbol{r}'|}}{4\pi|\boldsymbol{r}-\boldsymbol{r}'|}\boldsymbol{M}(\boldsymbol{r}')d\boldsymbol{r}' \tag{2.36}$$

In the far field, it is possible to make the following approximation [105, Ch. 2]: $\nabla \sim -jk\hat{\boldsymbol{r}}$ and $|\boldsymbol{r}-\boldsymbol{r}'| \sim r - \boldsymbol{r}'\cdot\hat{\boldsymbol{r}}$. Applying these asymptotic expressions to (2.36), this results in equation (2.37).[9]

$$\begin{aligned}\boldsymbol{E} &\sim jk_1\frac{e^{-jk_1r}}{4\pi r}\int_{-\infty}^{\infty}\int_{-\infty}^{\infty}\int_{-\infty}^{\infty}\hat{\boldsymbol{r}}\times\boldsymbol{M}(\boldsymbol{r}')\delta(z'-z_0)e^{j\boldsymbol{k}_\rho\cdot\boldsymbol{\rho}'}e^{jk_1\cos(\theta)z'}d\boldsymbol{\rho}'dz' \\ &\sim jk_1\frac{e^{-jk_1r}}{4\pi r}e^{jk_1\cos(\theta)z_0}\left[\hat{\boldsymbol{r}}\times\tilde{\boldsymbol{M}}_s(\boldsymbol{k}_\rho;z_0)\right]\end{aligned} \tag{2.37}$$

Considering the magnetic currents sheet $\boldsymbol{M}_s = 2\hat{\boldsymbol{z}}\times\boldsymbol{E}\delta(z-z_0)$ as in Figure 2.11. The spectral electric field can be found using (2.21). Assuming N_J and N_M electric and magnetic dipoles respectively. For dipole k_J:

[9]Here, $k_1\boldsymbol{r}'\cdot\hat{\boldsymbol{r}} = k_1(\boldsymbol{\rho}'+z'\hat{\boldsymbol{z}})\cdot\hat{\boldsymbol{r}} = \boldsymbol{k}_\rho\cdot\boldsymbol{\rho}' + k_1\cos(\theta)z'$. Also, $\boldsymbol{k}_\rho = k_1\sin(\theta)\hat{\boldsymbol{\rho}}$.

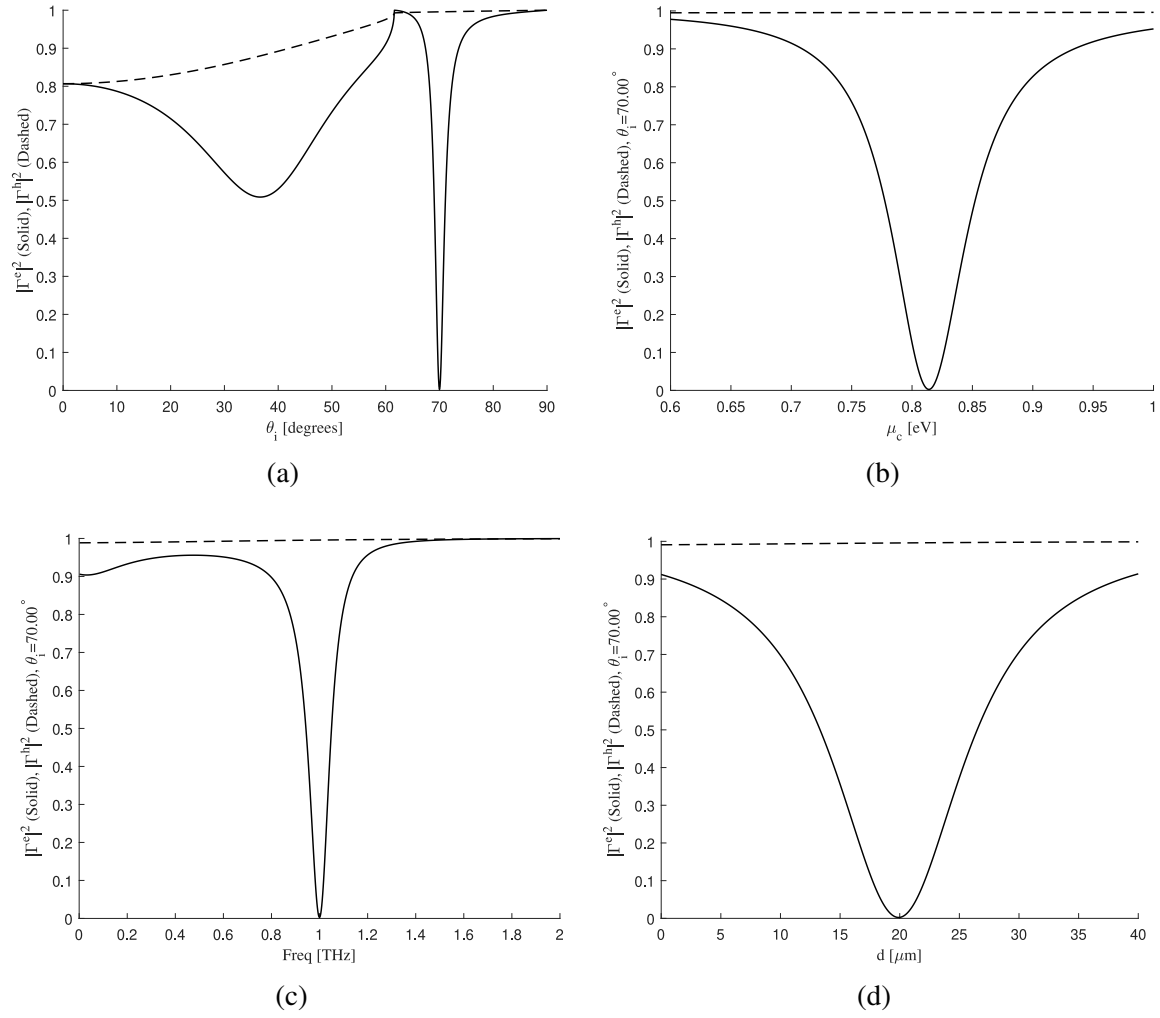

Figure 2.13: Otto configuration with graphene sheet. Default values are: $\theta_i = 70°$, $\mu_c = 0.8138$ [eV], $d = 20$ [μm] , and $f = 1$ [THz] (a) Reflectivity vs incident angle θ_i. (b) Reflectivity vs μ_c. (c) Reflectivity vs frequency f. (d) Reflectivity vs air gap thickness d.

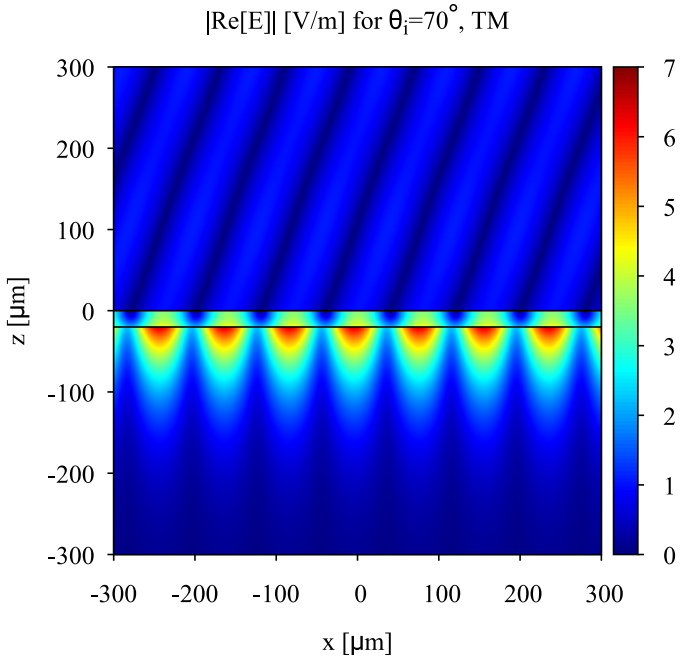

Figure 2.14: Plane wave excitation for SPP mode in Figure 2.12 Otto configuration.

$$\tilde{\boldsymbol{J}} = F\{I\boldsymbol{l}_{k_J}\delta(\boldsymbol{\rho}-\boldsymbol{\rho}_{k_J})\delta(z-z_{k_J})\} = I\boldsymbol{l}_{k_J}e^{j\boldsymbol{k}_\rho\cdot\boldsymbol{\rho}_{k_J}}\delta(z-z_{k_J}) \tag{2.38}$$

Thus, the far field for $z > z_0$ can be found using (2.38).

$$\boldsymbol{E} \sim -jk_1\frac{e^{-jk_1r}}{2\pi r}e^{jk_1\cos(\theta)z_0}\left[\hat{\boldsymbol{r}}\times\hat{\boldsymbol{z}}\times\underline{\underline{\tilde{\boldsymbol{G}}}}^{EJ}(\boldsymbol{k}_\rho;z_0|z_{k_J})\right]\cdot I\boldsymbol{l}_{k_J}e^{j\boldsymbol{k}_\rho\cdot\boldsymbol{\rho}_{k_J}} \tag{2.39}$$

Thus, for the electric and magnetic dipoles k_J and k_M respectively, it is possible to write the far field due to these dipoles for $z > z_0$ in (2.40) and (2.41). Where, the far field for $z < z_N$ is in (2.42) and (2.43).

For $z > z_0$, we substitute $k_\rho = k_1 \sin(\theta)$, and this corresponds to $0 \leq \theta \leq \pi/2$:

$$\boldsymbol{E} \sim -jk_1 \frac{e^{-jk_1 r}}{2\pi r} e^{jk_1 \cos(\theta) z_0} \left[V_i^e \hat{\boldsymbol{\theta}} \hat{\boldsymbol{\rho}} + V_i^h \cos(\theta) \hat{\boldsymbol{\varphi}} \hat{\boldsymbol{\varphi}} - V_v^e \eta_1 \frac{\epsilon_1}{\epsilon_z'} \sin(\theta) \hat{\boldsymbol{\theta}} \hat{\boldsymbol{z}} \right] \cdot I \boldsymbol{l}_{k_J} e^{j \boldsymbol{k}_\rho \cdot \boldsymbol{\rho}_{k_J}} \tag{2.40}$$

$$\boldsymbol{E} \sim jk_1 \frac{e^{-jk_1 r}}{2\pi r} e^{jk_1 \cos(\theta) z_0} \left[V_v^h \cos(\theta) \hat{\boldsymbol{\varphi}} \hat{\boldsymbol{\rho}} - V_v^h \hat{\boldsymbol{\theta}} \hat{\boldsymbol{\varphi}} - V_i^h \frac{1}{\eta_1} \frac{\mu_1}{\mu_z'} \cos(\theta) \hat{\boldsymbol{\varphi}} \hat{\boldsymbol{z}} \right] \cdot K \boldsymbol{l}_{k_M} e^{j \boldsymbol{k}_\rho \cdot \boldsymbol{\rho}_{k_M}} \tag{2.41}$$

For $z < z_N$, we substitute $k_\rho = k_N \sin(\theta)$, and this corresponds to $\pi/2 \leq \theta \leq \pi$:

$$\boldsymbol{E} \sim -jk_N \frac{e^{-jk_N r}}{2\pi r} e^{-jk_N \cos(\theta) z_N} \left[V_i^e \hat{\boldsymbol{\theta}} \hat{\boldsymbol{\rho}} + V_i^h \cos(\theta) \hat{\boldsymbol{\varphi}} \hat{\boldsymbol{\varphi}} - V_v^e \eta_N \frac{\epsilon_N}{\epsilon_z'} \sin(\theta) \hat{\boldsymbol{\theta}} \hat{\boldsymbol{z}} \right] \cdot I \boldsymbol{l}_{k_J} e^{j \boldsymbol{k}_\rho \cdot \boldsymbol{\rho}_{k_J}} \tag{2.42}$$

$$\boldsymbol{E} \sim jk_N \frac{e^{-jk_N r}}{2\pi r} e^{jk_N \cos(\theta) z_0} \left[V_v^h \cos(\theta) \hat{\boldsymbol{\varphi}} \hat{\boldsymbol{\rho}} - V_v^h \hat{\boldsymbol{\theta}} \hat{\boldsymbol{\varphi}} - V_i^h \frac{1}{\eta_N} \frac{\mu_N}{\mu_z'} \cos(\theta) \hat{\boldsymbol{\varphi}} \hat{\boldsymbol{z}} \right] \cdot K \boldsymbol{l}_{k_M} e^{j \boldsymbol{k}_\rho \cdot \boldsymbol{\rho}_{k_M}} \tag{2.43}$$

2.7.1 Numerical Examples

An example of the far fields computation is the previous Otto configuration at $f = 1$ [THz]. The formulas presented in (2.40)-(2.43) were used to obtain the far field due to Vertical Electric Dipole (VED) and Horizontal Electric Dipole (HED) as shown in Figure 2.15. Note the strong absorption at $\theta = 70^\circ$ by the VED due to the SPP excitation as discussed in the previous section.

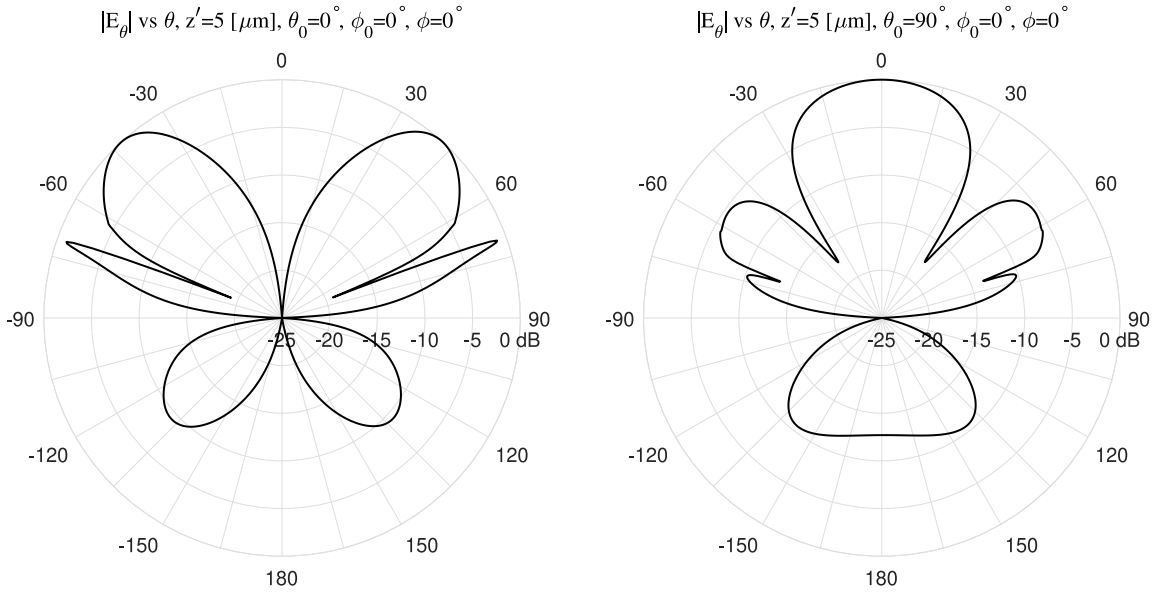

Figure 2.15: Far field due to electric dipole embedded in the Otto configuration. The dipole is located at 25 [μm] above the graphene sheet (i.e., 5 [μm] in the prism). (a) VED (b) HED.

3. MODAL ANALYSIS FOR ISOTROPIC CONDUCTIVE SHEETS

3.1 Dispersion Relation

The general approach for modal analysis is to develop a Dispersion Function (DF) that contains all the information about the configuration. The DF or $D(k_\rho)$, is a transcendental function, where the roots (zeros) represent the modes or eigenvalues k_ρ. When the DF is set to zero, it results in the dispersion relation $D(k_\rho) = 0$. Here, we will refer to the dispersion relation as the DF and both names are used interchangeably. In the planar layered media, the DF is a function of the transverse propagation constant k_ρ. The values of k_ρ solutions also allow the evaluation of the longitudinal propagation constants k_{zn}^{α}. This should be evaluated in the light of choosing the suitable Riemann sheet. In this chapter, the mode types $\alpha = e, h$ are omitted in the expressions for simplicity. This is also because the derivation here is applicable to both modes. Also, one should note that the poles of DGFs are the roots of the DF. As stated earlier, the search method for zeros is the Cauchy Integration Method (CIM) summarized in Appendix D.

From the previous discussion, one can seek spatial fields solutions with $e^{-j\boldsymbol{k}_\rho\cdot\boldsymbol{\rho}}$ dependency ($\boldsymbol{k}_\rho$ is a fixed eigenvalue) which corresponds to $\delta(\boldsymbol{k}_\rho)$ shifted by the eigenvalue in the spectral domain and reduces the source-free expressions from (2.20).[1] This leads to two possible e and h or TM and TE modes, respectively, as in (3.1) and (3.2). Hence, it is possible to study the modal analysis for planar layered media via the TL quantities directly, *i.e.*, the modal fields are voltages and currents solutions of the TL.

$$\boldsymbol{E}_t^e = V^e\hat{\boldsymbol{u}} \quad , \quad \boldsymbol{H}_t^e = I^e\hat{\boldsymbol{v}} \quad , \quad E_z^e = -\frac{k_\rho}{k_0}\frac{\eta_0 I^e}{\epsilon_z} \tag{3.1}$$

[1] Note that in the isotropic case, we are only interested in k_ρ since the symmetry in ζ.

$$\boldsymbol{E}_t^h = V^h \hat{\boldsymbol{v}} \quad , \quad \boldsymbol{H}_t^h = -I^h \hat{\boldsymbol{u}} \quad , \quad H_z^h = \frac{k_\rho}{k_0} \frac{V^h}{\eta_0 \mu_z} \tag{3.2}$$

The DF can be obtained in different ways. The easiest DF is obtained from the Transverse Resonance Condition (TRC) [106, p. 246]. In (3.3), this condition is applied for an arbitrary point source located at z' in section n. The determinant gives the non-trivial solutions.

$$\begin{bmatrix} [1 + \overrightarrow{\Gamma}' e^{j2k_{zn}(z-z')}] & [1 + \overleftarrow{\Gamma}' e^{-j2k_{zn}(z-z')}] \\ Y_n[1 - \overrightarrow{\Gamma}' e^{j2k_{zn}(z-z')}] & -Y_n[1 - \overleftarrow{\Gamma}' e^{-j2k_{zn}(z-z')}] \end{bmatrix} \begin{bmatrix} V_n^+ \\ V_n^- \end{bmatrix} = \begin{bmatrix} 0 \\ 0 \end{bmatrix} \tag{3.3}$$

At $z = z'$, the determinant reduces to (3.4).

$$\overleftarrow{\Gamma}' \overrightarrow{\Gamma}' = 1 \tag{3.4}$$

Upon the substitution of reflection coefficients definitions, the transverse resonance condition is obtained and the resulting DF is given in (3.5) in two equivalent forms.

$$\begin{aligned} \overleftarrow{Z}_n(z') + \overrightarrow{Z}_n(z') &= 0 \\ \overleftarrow{Y}_n(z') + \overrightarrow{Y}_n(z') &= 0 \end{aligned} \tag{3.5}$$

Equation (3.5) represents a DF that contains all the necessary information about the configuration in order to find the modes. The arbitrary choice of z' is permissible for $z_N \leq z' \leq z_0$. Unfortunately, there is no way to guarantee that this DF is pole-free (depends on the number of layers and the choice of n), and hence it is not possible to reliably apply the CIM. This DF is useful when treating a simple scenario of half-space or perhaps a slab surrounded with the same media. In these simple configurations, it is possible to handle the DF analytically and reach some conclusions such as SPP modes.

For instance, one can obtain the SPP k_ρ eigenvalues for conductive sheet suspended in the same medium as in [98] in (3.6).

$$k_\rho = \sqrt{\nu^\alpha}\sqrt{k^2 - (p^\alpha)^2} \tag{3.6}$$

Where $p^e = \dfrac{2\omega\epsilon_0\epsilon}{\sigma_1^s}$ and $p^h = \dfrac{\omega\mu_0\mu\sigma_1^s}{2}$. Also, for a slab suspended in the identical isotropic media, the direct application of (3.5) result in (3.7). Here, $N = 3$ and $k_1 = k_3 = k_{\text{amt}}$ and the slab is defined as $k_2 = k_{\text{slab}}$.

$$\frac{Z_{slab} - Z_{\text{amt}}}{Z_{\text{slab}} + Z_{\text{amt}}} \pm e^{j\Theta_{\text{slab}}} = 0 \tag{3.7}$$

Although it is easy to compute the DFs above, the DF of this type does not result in a systematic DF and the function may include both zeros and poles which affects the CIM and may result in spurious poles. Thus, a rigorous approach is to use T-matrix (Transfer Matrix) formulation instead [50, 107, 108]. It can be shown that treating the overall stack as a two-port network and by eliminating the incident waves, it is possible to define DFs from the equivalent T-matrix. This procedure will be demonstrated in the next section.

Before rushing into the derivation of our DFs, it is important to briefly discuss the issue of having branch points and branch cuts when applying the CIM. As mentioned earlier, the definitions of k_z result in four Riemann sheets depicted in Figure 2.7. Generally speaking, there are several methods to handle this discontinuity. One solution is to apply a k_ρ-transformation in such a way that the four Riemann sheets are mapped all together on the new domain. This approach we shall call it double transformation [109–112], in this case the two branch cuts disappear allowing direct implementation of the CIM. However, these transformations always result in numerical instability, and also the mapping change according to the configuration. A better solution is to use the Sine transformation [9, p. 462]. This transformation leads to a fixed mapping, but one would need to navigate

through two Riemann sheets as proposed by Smith [107, 113]. This approach we shall call it the single transformation. Nevertheless, a more recent technique "point-wise product of Riemann sheets", suggested by Kowalczyk [114], totally removes the branch cuts and points numerically. But, it was found that this method slows down the numerical computations even though it is the most convenient method. The last method to mention is the four loop integration, also discussed by Smith [109]. This requires navigating through the four Riemann sheets every time we want to search for roots. This technique will return all the eigenvalues on all Riemann sheets together once the region of interest is defined. In our implementation, the previous methods were studied and implemented. Our preference goes to the last two methods.

3.1.1 T-Matrix Formulation

The source-free section n solution can be written as in (3.8).

$$\begin{aligned} V_n^{\alpha}(z) &= V_n^{+} e^{-jk_{zn}^{\alpha}(z-z_n)} + V_n^{-} e^{jk_{zn}^{\alpha}(z-z_n)} \\ I_n^{\alpha}(z) &= Y_n^{\alpha}\left[V_n^{+} e^{-jk_{zn}^{\alpha}(z-z_n)} - V_n^{-} e^{jk_{zn}^{\alpha}(z-z_n)}\right] \end{aligned} \tag{3.8}$$

The boundary conditions between sections n and $n-1$ at $z = z_{n-1}$ must be enforced in order to construct the basic T-matrix relation.

$$\begin{aligned} V_n(z_{n-1}) &= V_{n-1}(z_{n-1}) \\ I_n(z_{n-1}) &= \sigma_{n-1}^{s} V_{n-1}(z_{n-1}) + I_{n-1}(z_{n-1}) \end{aligned} \tag{3.9}$$

From (3.7), it is possible to re-arrange the expressions in a convenient matrix form at the boundary z_{n-1}. This results in the expressions in (3.10) and (3.11).

$$\begin{bmatrix} V_n(z_{n-1}) \\ I_n(z_{n-1}) \end{bmatrix} = \begin{bmatrix} 1 & 1 \\ Y_n & -Y_n \end{bmatrix} \begin{bmatrix} e^{-j\Theta_n} & 0 \\ 0 & e^{j\Theta_n} \end{bmatrix} \begin{bmatrix} V_n^+ \\ V_n^- \end{bmatrix} \tag{3.10}$$

$$\begin{bmatrix} V_{n-1}(z_{n-1}) \\ I_{n-1}(z_{n-1}) \end{bmatrix} = \begin{bmatrix} 1 & 1 \\ Y_{n-1} & -Y_{n-1} \end{bmatrix} \begin{bmatrix} V_{n-1}^+ \\ V_{n-1}^- \end{bmatrix} \tag{3.11}$$

Now, it is possible to form the matrix relation in (3.12) between incident V^+ and reflected V^- voltages in sections n and $n-1$. This results in the matrix $\left[\boldsymbol{T}_n\right]$ which is the T-matrix relating sections n and $n-1$. $\left[\boldsymbol{T}_n\right]$ will become the building block for the final DF.

$$\begin{bmatrix} V_n^+ \\ V_n^- \end{bmatrix} = \left[\boldsymbol{T}_n\right] \begin{bmatrix} V_{n-1}^+ \\ V_{n-1}^- \end{bmatrix} \tag{3.12}$$

The elements of matrix $\left[\boldsymbol{T}_n\right]$ can be expressed as in (3.13) and (3.14).

$$\left[\boldsymbol{T}_n\right] = \begin{bmatrix} T_{11,n} & T_{12,n} \\ T_{21,n} & T_{22,n} \end{bmatrix} \tag{3.13}$$

$$\begin{aligned} T_{11,n} &= \frac{1}{2}\Big[1 + Q_n + Z_n\sigma_{n-1}^s\Big]e^{j\Theta_n} \\ T_{12,n} &= \frac{1}{2}\Big[1 - Q_n + Z_n\sigma_{n-1}^s\Big]e^{j\Theta_n} \\ T_{21,n} &= \frac{1}{2}\Big[1 - Q_n - Z_n\sigma_{n-1}^s\Big]e^{-j\Theta_n} \\ T_{22,n} &= \frac{1}{2}\Big[1 + Q_n - Z_n\sigma_{n-1}^s\Big]e^{-j\Theta_n} \end{aligned} \tag{3.14}$$

Where $Q_n = \dfrac{Z_n}{Z_{n-1}}$. The overall T-matrix can be defined in (3.15) by equating the contiguous sections. This is also an advantage when using T-matrix formulation.

$$\begin{bmatrix} V_N^+ \\ V_N^- \end{bmatrix} = \underbrace{\left[\boldsymbol{T}_N\right] \ldots \left[\boldsymbol{T}_2\right]}_{\left[\boldsymbol{T}\right]} \begin{bmatrix} V_1^+ \\ V_1^- \end{bmatrix} \tag{3.15}$$

The boundary impedances $\overleftarrow{Z}_N$ and $\overrightarrow{Z}_1$ will be used to represent the all possible terminations. Thus, the following relations are used to introduce these terminations in the dispersion relation:

$$\begin{bmatrix} 1 & \overleftarrow{Z}_N \end{bmatrix} \begin{bmatrix} V_N(z_N) \\ I_N(z_N) \end{bmatrix} = 0 \tag{3.16}$$

$$\begin{bmatrix} V_1(z_0) \\ I_1(z_0) \end{bmatrix} = \begin{bmatrix} \overrightarrow{Z}_1 \\ 1 \end{bmatrix} I_1(z_0) \tag{3.17}$$

The previous termination relations in (3.16) and (3.17) are given in terms of voltages and currents. This requires introducing intermediate relations to allow using (3.16) and (3.17) in (3.15). Thus, the relations in (3.18) and (3.19) are applied.

$$\begin{bmatrix} V_1^+ \\ V_1^- \end{bmatrix} = \frac{1}{2} \begin{bmatrix} e^{j\Theta_1} & Z_1 e^{j\Theta_1} \\ e^{-j\Theta_1} & -Z_1 e^{-j\Theta_1} \end{bmatrix} \begin{bmatrix} V_1(z_0) \\ I_1(z_0) \end{bmatrix} \tag{3.18}$$

$$\begin{bmatrix} V_N(z_N) \\ I_N(z_N) \end{bmatrix} = \begin{bmatrix} 1 & 1 \\ Y_N & -Y_N \end{bmatrix} \begin{bmatrix} V_N^+ \\ V_N^- \end{bmatrix} \tag{3.19}$$

The last step is to collect all the previous expressions in (3.15)-(3.19) as illustrated in (3.20) in order to obtain the final DF in (3.21).

$$\frac{1}{2}\begin{bmatrix}1 & \overleftarrow{Z}_N\end{bmatrix}\begin{bmatrix}1 & 1\\ Y_N & -Y_N\end{bmatrix}[\boldsymbol{T}]\begin{bmatrix}e^{j\Theta_1} & Z_1e^{j\Theta_1}\\ e^{-j\Theta_1} & -Z_1e^{-j\Theta_1}\end{bmatrix}\begin{bmatrix}\overrightarrow{Z}_1\\ 1\end{bmatrix}I_1(z_0)=0 \tag{3.20}$$

$$D^{\alpha}=\underbrace{\begin{bmatrix}1+\dfrac{\overleftarrow{Z}_N}{Z_N} & 1-\dfrac{\overleftarrow{Z}_N}{Z_N}\end{bmatrix}}_{\text{Termination}_N}[\boldsymbol{T}]\underbrace{\begin{bmatrix}\big[\overrightarrow{Z}_1+Z_1\big]e^{j\Theta_1}\\ \big[\overrightarrow{Z}_1-Z_1\big]e^{-j\Theta_1}\end{bmatrix}}_{\text{Termination}_1}=0 \tag{3.21}$$

The dispersion relation in (3.21) is required to be analytic. Thus, the terminations 1 and N as in Table 3.1 and 3.2 must be strictly applied. For arbitrary impedance boundary, the terminations in Table 3.3 must be applied. These terminations automatically remove the branch point singularities and make the DF pole-free. Hence, the only problem left is to navigate through the Riemann sheets.

Table 3.1: Terminations for $\alpha = e$ TL.

Termination	PEC	PMC	open
1	$\begin{bmatrix}Z_1^e e^{j\Theta_1}\\ -Z_1^e e^{-j\Theta_1}\end{bmatrix}$	$\begin{bmatrix}Z_1^e e^{j\Theta_1}\\ Z_1^e e^{-j\Theta_1}\end{bmatrix}$	$\begin{bmatrix}Z_1^e\\ 0\end{bmatrix}$
N	$\begin{bmatrix}1 & 1\end{bmatrix}$	$\begin{bmatrix}1 & -1\end{bmatrix}$	$\begin{bmatrix}1 & 0\end{bmatrix}$

The proof for the pole-free property of the DF developed in (3.21) can be understood by considering the simple scenario of half-space separated with a conductive sheet. Considering open/open terminations, the DFs are given in (3.22) and (3.23) for e and h modes respectively.

Table 3.2: Terminations for $\alpha = h$ TL.

Termination	PEC	PMC	open
1	$\begin{bmatrix} e^{j\Theta_1} \\ -e^{-j\Theta_1} \end{bmatrix}$	$\begin{bmatrix} e^{j\Theta_1} \\ e^{-j\Theta_1} \end{bmatrix}$	$\begin{bmatrix} 1 \\ 0 \end{bmatrix}$
N	$\begin{bmatrix} \frac{1}{Z_N^h} & \frac{1}{Z_N^h} \end{bmatrix}$	$\begin{bmatrix} \frac{1}{Z_N^h} & -\frac{1}{Z_N^h} \end{bmatrix}$	$\begin{bmatrix} \frac{1}{Z_N^h} & 0 \end{bmatrix}$

Table 3.3: Terminations for impedance boundary conditions.

Term.	$\alpha = e$	$\alpha = h$
1	$\begin{bmatrix} \big[Z_1^e + \overrightarrow{Z}_1\big] e^{j\Theta_1} \\ \big[Z_1^e - \overrightarrow{Z}_1\big] e^{-j\Theta_1} \end{bmatrix}$	$\begin{bmatrix} \big[\frac{\overrightarrow{Z}_1}{Z_1^h} + 1\big] e^{j\Theta_1} \\ \big[\frac{\overrightarrow{Z}_1}{Z_1^h} - 1\big] e^{-j\Theta_1} \end{bmatrix}$
N	$\begin{bmatrix} 1 + \frac{\overleftarrow{Z}_N}{Z_N^e} & 1 - \frac{\overleftarrow{Z}_N}{Z_N^e} \end{bmatrix}$	$\begin{bmatrix} \frac{\overleftarrow{Z}_N + Z_N^h}{(Z_N^h)^2} & \frac{\overleftarrow{Z}_N - Z_N^h}{(Z_N^h)^2} \end{bmatrix}$

$$\epsilon_2 k_{z1}^e + \epsilon_1 k_{z2}^e + k_{z1}^e k_{z2}^e \frac{\sigma_1^s}{\omega \epsilon_0} = 0 \tag{3.22}$$

$$\frac{k_{z1}^h}{\mu_1} + \frac{k_{z2}^h}{\mu_2} + \omega \mu_0 \sigma_1^s = 0 \tag{3.23}$$

For half-space only, if $k_1 = k_2 = k$, the above expression for e modes results in a spurious mode at $k_\rho = k$ for a suspended conductive sheets. Thus, we replace it with (3.24).

$$2 + k_z^e \frac{\sigma^s}{\omega \epsilon_0 \epsilon} = 0 \tag{3.24}$$

At the branch point $k_z = 0$, hence the DF given in (3.22) and (3.23) are pole-free. In addition to this, by alternating the signs of k_{z1} and k_{z2}, one may check for the existence of branch cuts [86, p. 479]. Another important example is the termination open/PEC which is suitable for substrate applications. The DFs for this scenario are given in (3.25) and (3.26).

$$\left[\epsilon_2 k_{z1}^e + \epsilon_1 k_{z2}^e + k_{z1}^e k_{z2}^e \frac{\sigma_1^s}{\omega \epsilon_0}\right] e^{j\Theta_2} + \left[\epsilon_2 k_{z1}^e - \epsilon_1 k_{z2}^e - k_{z1}^e k_{z2}^e \frac{\sigma_1^s}{\omega \epsilon_0}\right] e^{-j\Theta_2} = 0 \tag{3.25}$$

$$\left[\frac{k_{z1}^h}{\mu_1} + \frac{k_{z2}^h}{\mu_2} + \omega \mu_0 \sigma_1^s\right] e^{j\Theta_2} + \left[\frac{k_{z1}^h}{\mu_1} - \frac{k_{z2}^h}{\mu_2} - \omega \mu_0 \sigma_1^s\right] e^{-j\Theta_2} = 0 \tag{3.26}$$

A last example is given for PEC/PEC terminations. This is also a common scenario in layered media waveguides. The DFs for this scenario are shown in (3.27) and (3.28).

$$\Bigg[\Big[\epsilon_2 k_{z1}^e + \epsilon_1 k_{z2}^e + k_{z1}^e k_{z2}^e \frac{\sigma_1^s}{\omega\epsilon_0}\Big] e^{j\Theta_2} + \Big[\epsilon_2 k_{z1}^e - \epsilon_1 k_{z2}^e - k_{z1}^e k_{z2}^e \frac{\sigma_1^s}{\omega\epsilon_0}\Big] e^{-j\Theta_2}\Bigg] e^{j\Theta_1}$$
$$- \Bigg[\Big[\epsilon_2 k_{z1}^e - \epsilon_1 k_{z2}^e + k_{z1}^e k_{z2}^e \frac{\sigma_1^s}{\omega\epsilon_0}\Big] e^{j\Theta_2} + \Big[\epsilon_2 k_{z1}^e + \epsilon_1 k_{z2}^e - k_{z1}^e k_{z2}^e \frac{\sigma_1^s}{\omega\epsilon_0}\Big] e^{-j\Theta_2}\Bigg] e^{-j\Theta_1}$$
$$= 0 \tag{3.27}$$

$$\Bigg[\Big[\frac{k_{z1}^h}{\mu_1} + \frac{k_{z2}^h}{\mu_2} + \omega\mu_0\sigma_1^s\Big] e^{j\Theta_2} + \Big[\frac{k_{z1}^h}{\mu_1} - \frac{k_{z2}^h}{\mu_2} - \omega\mu_0\sigma_1^s\Big] e^{-j\Theta_2}\Bigg] e^{j\Theta_1}$$
$$- \Bigg[\Big[\frac{k_{z1}^h}{\mu_1} - \frac{k_{z2}^h}{\mu_2} + \omega\mu_0\sigma_1^s\Big] e^{j\Theta_2} + \Big[\frac{k_{z1}^h}{\mu_1} + \frac{k_{z2}^h}{\mu_2} - \omega\mu_0\sigma_1^s\Big] e^{-j\Theta_2}\Bigg] e^{-j\Theta_1} \tag{3.28}$$
$$= 0$$

Similarly, it is possible to give expressions for other terminations. As seen from the above, this formulation is versatile and suits several applications of interest. Again, the objective is to show that this formulation is pole-free and other scenarios of $N > 2$ will follow the same analysis.

3.1.2 S-Matrix Formulation

In the previous T-matrix formulation, growing exponentials of $e^{j\Theta_n}$ are present in some matrix elements which affects the numerical stability. In addition to this, the S-matrix (Scattering Matrix) is considered numerically more stable than the T-matrix formulation in the presence of evanescent waves [115] or very thick layers with respect to λ_0. Hence, the S-matrix formulation is introduced. The elements of $\big[\boldsymbol{T}_n\big]$ in (3.13) and (3.14) can be re-written as in (3.29).

$$\left[\boldsymbol{T}_n\right] = \frac{1}{\tau_{n-1,n}} \begin{bmatrix} \left[1+\Omega_{n-1,n}\sigma^s_{n-1}\right]e^{j\Theta_n} & \left[\Gamma_{n-1,n}+\Omega_{n-1,n}\sigma^s_{n-1}\right]e^{j\Theta_n} \\ \left[\Gamma_{n-1,n}-\Omega_{n-1,n}\sigma^s_{n-1}\right]e^{-j\Theta_n} & \left[1-\Omega_{n-1,n}\sigma^s_{n-1}\right]e^{-j\Theta_n} \end{bmatrix} \tag{3.29}$$

Where $\tau_{i,j} = 1 + \Gamma_{i,j}$. Note that $\sigma^s_n = 0$ when the conductive sheets are removed. The equivalent S-matrix $\left[\boldsymbol{S_n}\right]$ can be obtained from the relation in (3.30) [116, 117].

$$\left[\boldsymbol{S}\right] = \begin{bmatrix} T_{21}T_{11}^{-1} & T_{22} - T_{21}T_{11}^{-1}T_{12} \\ T_{11}^{-1} & -T_{11}^{-1}T_{12} \end{bmatrix} \tag{3.30}$$

Using (3.30), the equivalent $\left[\boldsymbol{S}_n\right]$ can be written as in (3.31).[2]

$$\left[\boldsymbol{S}_n\right] = \frac{1}{1+\Omega_{n-1,n}\sigma^s_{n-1}} \begin{bmatrix} \left[\Gamma_{n-1,n}-\Omega_{n-1,n}\sigma^s_{n-1}\right]e^{-j2\Theta_n} & \tau_{n,n-1}e^{-j\Theta_n} \\ \tau_{n-1,n}e^{-j\Theta_n} & \left[\Gamma_{n,n-1}-\Omega_{n-1,n}\sigma^s_{n-1}\right] \end{bmatrix} \tag{3.31}$$

It is clear from (3.31) that all the matrix elements have only decaying exponentials. According to this, the S-matrix formulation is more stable than the T-matrix. In order to utilize the S-matrix and apply it in the DF formulation, the overall S-matrix is computed using the star product [118] described in (3.32). Here, considering the overall matrix of $\left[\boldsymbol{S}\right] = \left[\boldsymbol{S}^a\right] \star \left[\boldsymbol{S}^b\right]$.

$$\left[\boldsymbol{S}\right] = \begin{bmatrix} S^a_{11} + S^a_{12}S^b_{11}(1-S^a_{22}S^b_{11})^{-1}S^a_{21} & S^a_{12}(1-S^b_{11}S^a_{22})^{-1}S^b_{12} \\ S^b_{21}(1-S^a_{22}S^b_{11})^{-1}S^a_{21} & S^b_{22} + S^b_{21}S^a_{22}(1-S^b_{11}S^a_{22})^{-1}S^b_{12} \end{bmatrix} \tag{3.32}$$

Thus, the overall S-matrix is evaluated using (3.33). Then, the T-matrix is converted

[2]Here, the relations $\Gamma_{n-1,n} = -\Gamma_{n,n-1}$ and $\tau_{n,n-1} = 1 + \Gamma_{n,n-1}$ were used.

back using (3.34).

$$\left[\boldsymbol{S}\right] = \left[\boldsymbol{S}_N\right] \star \left[\boldsymbol{S}_{N-1}\right] \star \ldots \star \left[\boldsymbol{S}_2\right] \tag{3.33}$$

$$\left[\boldsymbol{T}\right] = \begin{bmatrix} S_{21}^{-1} & -S_{21}^{-1}S_{22} \\ S_{11}S_{21}^{-1} & S_{12} - S_{11}S_{21}^{-1}S_{22} \end{bmatrix} \tag{3.34}$$

In the light of the DF described in (3.21), it is possible to re-express the DF for several terminations using the S-Matrix formulation directly. Sample DFs based on S-matrix for common terminations are summarized in Table 3.4. So, the T-matrix can be evaluated using the S-matrix stable formulation.

Table 3.4: DF based on S-matrix formulation.

Termination	$\alpha = e$	$\alpha = h$
open/open	$\frac{Z_1^e}{S_{21}}$	$\frac{1}{Z_N^h S_{21}}$
open/PEC	$\frac{Z_1^e}{S_{21}}(1 + S_{11})$	$\frac{Z_1^h}{Z_N^h S_{21}}(1 + S_{11})$
open/PMC	$\frac{1}{S_{21}}(1 - S_{11})$	$\frac{1}{Z_N^h S_{21}}(1 - S_{11})$

For parallel PEC termination one can obtain the following DFs in (3.33) and (3.34) for e and h modes respectively.

$$\frac{Z_1^e}{S_{21}}\left[(1+S_{11})(1+S_{22}e^{-j2\Theta_1})-S_{12}S_{21}e^{-j2\Theta_1}\right]=0 \tag{3.35}$$

$$\frac{1}{Z_N^h S_{21}}\left[(1+S_{11})(1+S_{22}e^{-j2\Theta_1})-S_{12}S_{21}e^{-j2\Theta_1}\right]=0 \tag{3.36}$$

It should be noted that all the terminations in Tables 3.1-3.3 are still valid. However, it can be shown that the overall S-matrix corresponds to the following:

$$\left[\boldsymbol{S}\right]=\begin{bmatrix}\overrightarrow{\Gamma} & \overleftarrow{\tau}\\ \overrightarrow{\tau} & \overleftarrow{\Gamma}\end{bmatrix} \tag{3.37}$$

Thus, we can compute the overall S-matrix components using the above expressions via our TL model.

3.2 Modal Fields Profile

The computation of modal fields profile is another important aspect of this study. This helps in visualizing the modal field. The analysis presented here is restricted to structures with open boundary on layer 1 while the termination in layer N is arbitrary. This doesn't limit the method presented here, but it is more convenient and suitable for the vast majority of practical configurations. The transverse propagation constant k_ρ eigenvalues result in $\overleftarrow{\Gamma}_1=\infty$ as indicated earlier due to resonance which results in additional precautions. In addition to this, the field in layer 1 is leaving the structure, *i.e.*, $V_1^-=0$ as shown in (3.38). Hence, the boundary conditions in the previous chapter were enforced in the first interface. Also, note that the solutions in layers $n>1$ are computed using the down-looking solutions as in (3.39).

$$
\begin{aligned}
V_1(z) &= V_1^+ e^{-jk_{z1}(z-z_1)} \\
I_1(z) &= Y_1 V_1^+ e^{-jk_{z1}(z-z_1)}
\end{aligned}
\tag{3.38}
$$

$$
\begin{aligned}
V_n(z) &= V_n^- e^{-j\Theta_n}[e^{jk_{zn}(z-z_n)} + \overleftarrow{\Gamma}_n e^{-jk_{zn}(z-z_n)}] \\
I_n(z) &= -Y_n V_n^- e^{-j\Theta_n}[e^{jk_{zn}(z-z_n)} - \overleftarrow{\Gamma}_n e^{-jk_{zn}(z-z_n)}]
\end{aligned}
\tag{3.39}
$$

The transition between layers 1 and 2 has to be carefully evaluated because two different solutions are used in the two sections and the boundary condition is not automatically satisfied as one would expect. In contrast to the conventional TL solutions, the voltages and currents solutions are separate, hence:

For voltages:

$$
V_2^- = \frac{V_1^+}{1 + \overleftarrow{\Gamma}_2 e^{-j2\Theta_2}} \tag{3.40}
$$

For currents:

$$
V_2^- = -\frac{Z_2[Y_1 + \sigma_1^s]V_1^+}{1 - \overleftarrow{\Gamma}_2 e^{-j2\Theta_2}} \tag{3.41}
$$

Thus, using (3.40) and (3.41), one can compute the voltages and currents solutions respectively for $n > 1$.

3.3 Numerical Examples

Several examples for practical structures were considered for demonstrating our methods. These configurations were taken from the literature in order to provide a validation for our results. The examples were chosen so that they will cover all possible configura-

tions and challenges that can be faced in the modal analysis. This is an illustration for the reliability and accuracy of the approach developed in this work.

3.3.1 Active Layer InGaAsP-InP Waveguide

In this example, the five-layers dielectric waveguide in [50] was considered. The details of this structure are summarized in Table 3.5. This configuration contains lossy dielectrics and an active layer sandwiched in the middle. Moreover, the top and bottom layers are both open air. The frequency of operation correspond to the free-space wavelength $\lambda_0 = 1.3$ [μm]. The Search contour was defined by the two corners $(x_1 = 0.4k_0, y_1 = -0.1k_0)$ and $(x_2 = 0.6k_0, y_2 = 0.8k_0)$ in z domain. In Table 3.6, the k_ρ solutions for TE and TM modes are listed after applying this contour. The transverse electric field profile for samples from Table 3.6 are illustrated in Figure 3.1. This is an example for the case $k_1 = k_N$ which requires no special treatment as stated previously.

Table 3.5: Details of active layer InGaAsP-InP configuration.

Layer	Thickness [nm]	$n = \sqrt{\epsilon}$
1	open	1
2	600	$3.4 - j0.002$
3	400	$3.6 + j0.01$
4	600	$3.4 - j0.002$
5	open	1

3.3.2 PEC Backed Waveguide

A configuration which includes a PEC backing is considered from [119]. The summary of this configuration in available in Table 3.7. The frequency of operation is $f = 30$ [GHz]. Notice that the k_ρ are all real as shown in Table 3.8.

Table 3.6: k_ρ values for TE and TM modes.

Mode	k_ρ/k_0
TE_0	$3.50344333295003 + j0.007103000978684$
TE_1	$3.33728685820776 - j0.000229491104012$
TE_2	$3.25168520698338 - j0.000530514779911$
TE_3	$3.10425142141457 + j0.001337986339752$
TE_4	$2.87863677988123 - j0.000173729890361$
TE_5	$2.62813932045903 + j0.001548644331148$
TE_6	$2.24395136260119 + j0.000708377958009$
TE_7	$1.76819096634077 + j0.001353217176371$
TE_8	$1.07426202652578 + j0.002457891473571$
TM_0	$3.49668379589128 + j0.006543981710984$
TM_1	$3.33069711910721 + j0.000035186422257$
TM_2	$3.22433799874652 - j0.000174482612621$
TM_3	$3.05040586521867 + j0.001170315120992$
TM_4	$2.79439777568252 + j0.000708785204484$
TM_5	$2.46292446281425 + j0.001179320064768$
TM_6	$2.00514007332263 + j0.001602922029295$
TM_7	$1.35099878658162 + j0.002314049514967$
TM_8	$1.00143843982593 + j0.000046694123539$

Table 3.7: Layered media details of the PEC backed waveguide.

Layer	Thickness [mm]	ϵ
1	open	1
2	1.5	2.1
3	1	12.5
4	1.5	9.8
5	1.5	8.6
-	PEC	-

Table 3.8: k_ρ values for TE and TM modes.

Mode	k_ρ/k_0
TE_0	3.04424283140817
TE_1	2.35900516800964
TE_2	1.00029607180535
TM_0	3.00016000121686
TM_1	2.57078112913698
TM_2	1.36810357278679

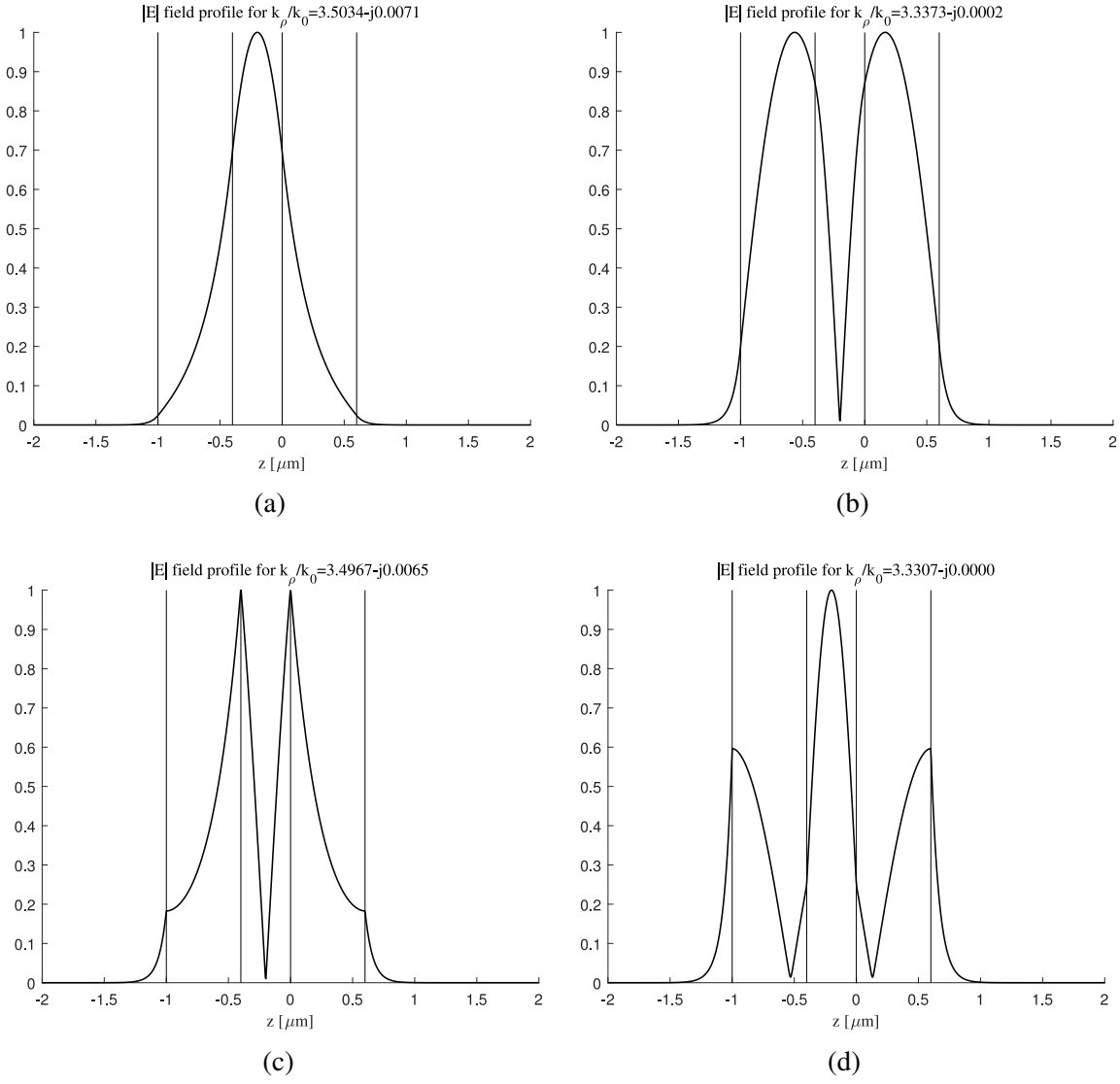

Figure 3.1: Transverse electric field profile for modes from Table 3.6 (normalized to 1). (a) TE_0. (b) TE_1. (c) TM_0. (d) TM_1.

3.3.3 Uniaxial Media Metal-Clad Waveguide

This example considers uniaxial media metal-clad waveguide structure for surface-plasmon to guided-mode coupling reported in [120]. In this example $\lambda_0 = 632.8$ [nm]. The summary of this configuration is found in Table 3.5. This configuration has possible device applications because of the strong coupling between layers.

Table 3.9: Layered media details of the Metal-Clad waveguide with uniaxial media.

Layer	Medium	Thickness [nm]	$n = \sqrt{\epsilon}$	$n_z = \sqrt{\epsilon_z}$
1	Air	open	1	1
2	Ag	126.56	$0.067 - j4.05$	$0.067 - j4.05$
3	ZnO	341.712	1.99	2.007
4	PE:$LiNbO_3$	841.624	2.2465	2.3266
5	$LiNbO_3$	open	2.2865	2.2026

Table 3.10: k_ρ values for TM modes.

Mode	k_ρ/k_0
TM_0	$2.30556713927974 - j0.011864664172497$
TM_1	$2.30555961890282 - j0.000256272937491$
TM_2	$2.24499542019970 - j0.000063137358457$
TM_3	$1.03192473691726 - j0.001104799491271$

3.3.4 Isotropic Graphene

Here, several scenarios that include a graphene sheet in a planar layered media are considered. First, the method is validated by computing the SPP transverse propagation constant for a graphene ribbon in free-space. In this case, a closed form for SPP k_ρ values is available as in (3.42) [98]. It can be shown for this case that graphene ribbon supports

TM mode if $\mathrm{Im}[\sigma^s] < 0$ and TE mode if $\mathrm{Im}[\sigma^s] > 0$ assuming $\mathrm{Re}[\sigma^s] \sim 0$. Thus, a comparison of the results obtained using CIM with the closed form values at several frequencies is shown in Figure 3.2.

$$k_\rho = \sqrt{\nu^\alpha}\sqrt{k^2 - (p^\alpha)^2} \tag{3.42}$$

Where $p^e = \dfrac{2\omega\epsilon_0\epsilon}{\sigma_1^s}$ and $p^h = \dfrac{\omega\mu_0\mu\sigma_1^s}{2}$.

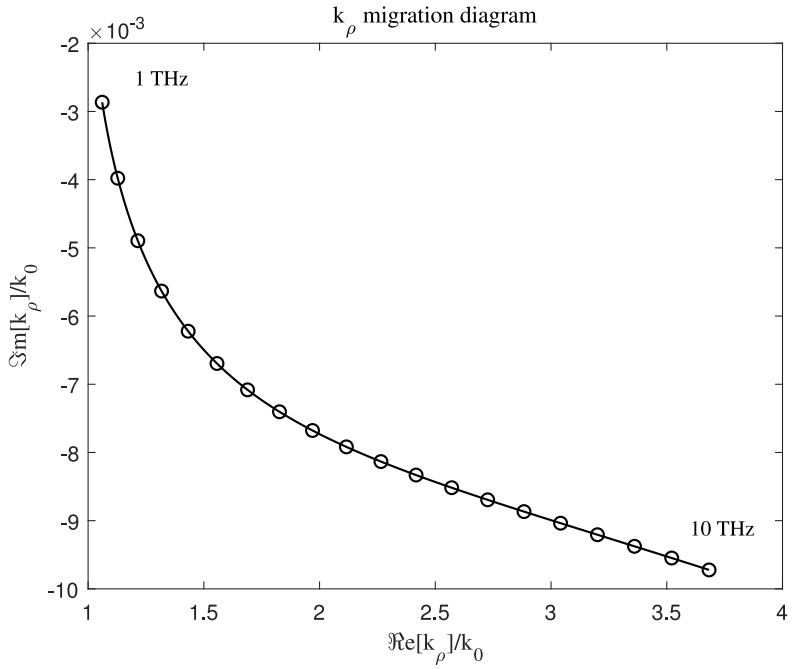

Figure 3.2: k_ρ migration diagram for SPP (TM mode). Frequency range from 1 [THz] to 10 [THz]. (Solid) using the formula in (3.42). (Circles) values computed using the CIM described here.

Next, the interesting scenario of a graphene based Otto configuration in Table 2.3 from the Chapter 2 is considered again at frequency of operation 1 [THz]. The SPP mode was found using the methods developed here and the transverse fields are presented in Figure 3.3 for the TM mode $k_\rho/k_0 = 1.88224222918665 - j0.00063471402154$.

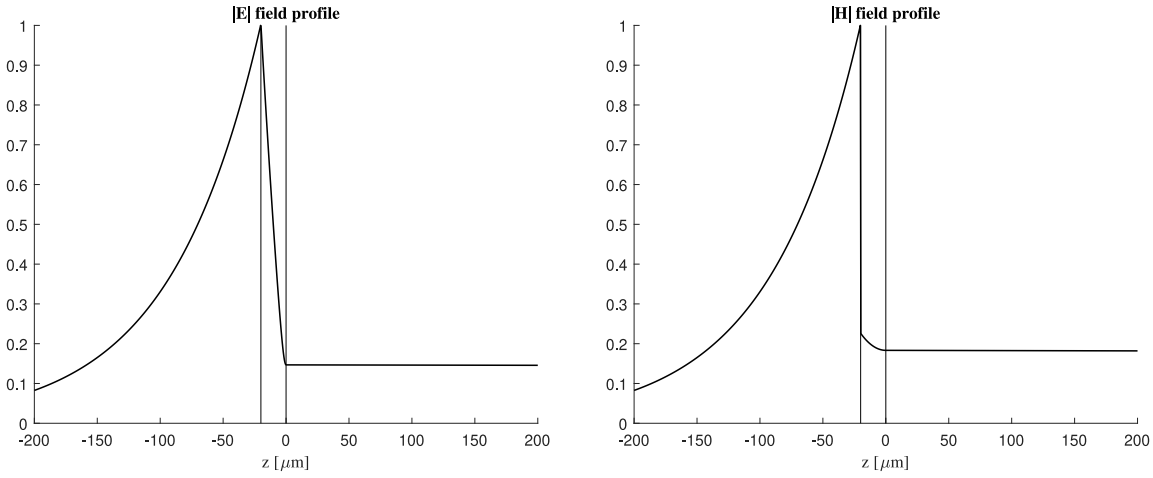

(a) (b)

Figure 3.3: Transverse fields profile for TM mode (normalized to 1). (a) Electric field. (b) Magnetic field.

The last example is a half-space with graphene sheet of spatial dispersion taken from [121] and illustrated in Figure 3.4. In this case the interband contribution is ignored in σ^s as in [70] since the frequency of interest in relatively lower than the optical range. The surface conductively is replaced with σ_d^s as given in (3.43).

$$\begin{aligned} \sigma^s &= \frac{2e^2\tau_s k_B T}{\pi\hbar^2(1+j\omega\tau_s)} \ln\left[2\cosh\left(\frac{\mu_c}{2k_BT}\right)\right] \\ \sigma_d^s &= \sigma^s\left[1+\left(\frac{k_\rho \tau_s v_F}{1+j\omega\tau_s}\right)^2\right] \end{aligned} \tag{3.43}$$

As seen from the results in Figure 3.5, one of the modes is non-physical at frequencies beyond 4 [GHz] [70]. This problem is due to limitations in the spatially dispersive graphene expression in (3.43). A modified expression was introduced in [122] as given in (3.44). This expression is examined in Otto configuration again with the parameters: $\tau_s = 0.5$ [ps], $\mu_c = 50$ [meV], $v_F = 10^6$ [ms^{-1}] and $T = 300$ [K]. The media parameters are also modified as in Table 3.11. The results illustrated in Figure 3.6 represent physical

Figure 3.4: The graphene parameters are $\tau_s = \dfrac{\hbar}{\gamma_c} = 0.135$ [ps], $\mu_c = 50$ [meV], $v_F = 10^6$ [ms^{-1}] and $T = 300$ [K]. The dielectric is layer permittivity is $\epsilon = 11.9$.

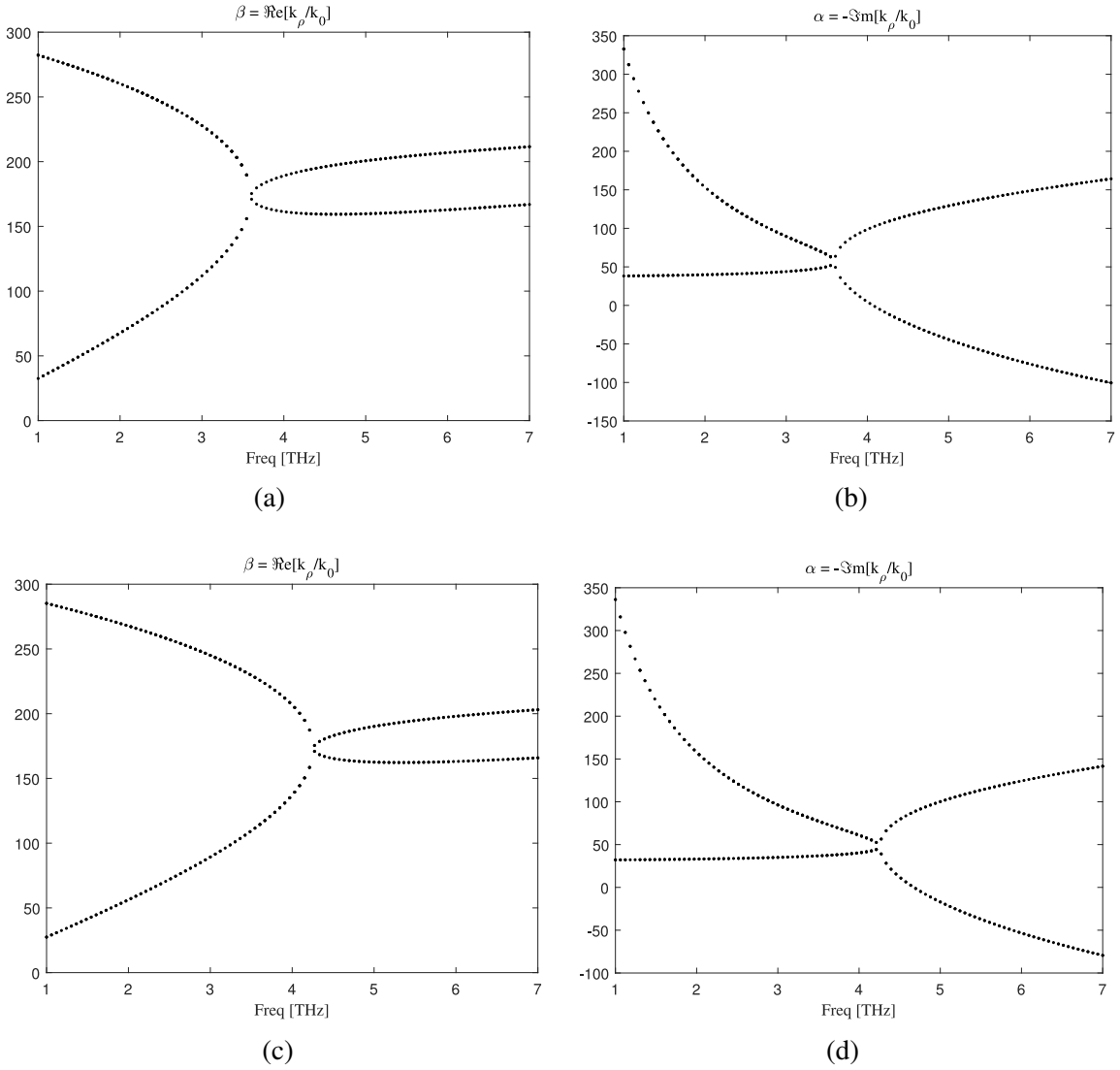

Figure 3.5: TM modes for the graphene half-space configuration. Transverse propagation constant $k_\rho = \beta - j\alpha$. (a) and (b) Results on Sheet I. (c) and (d) Results on Sheet II.

modes.

Table 3.11: Otto configuration with graphene details for results in Figure 3.6.

Layer	Thickness [μm]	ϵ
Prism	open	11.9
Air	20	1
Graphene	-	-
Dielectric	open	3.9

$$\sigma^s = \Big[\frac{-je^2k_BT}{\pi\hbar^2}\Big]\frac{\ln\Big[2\Big[1+\cosh\Big(\frac{\mu_c}{2k_BT}\Big)\Big]\Big]}{\sqrt{(\omega - j\tau_s^{-1})^2 - v_F^2k_\rho^2}} \tag{3.44}$$

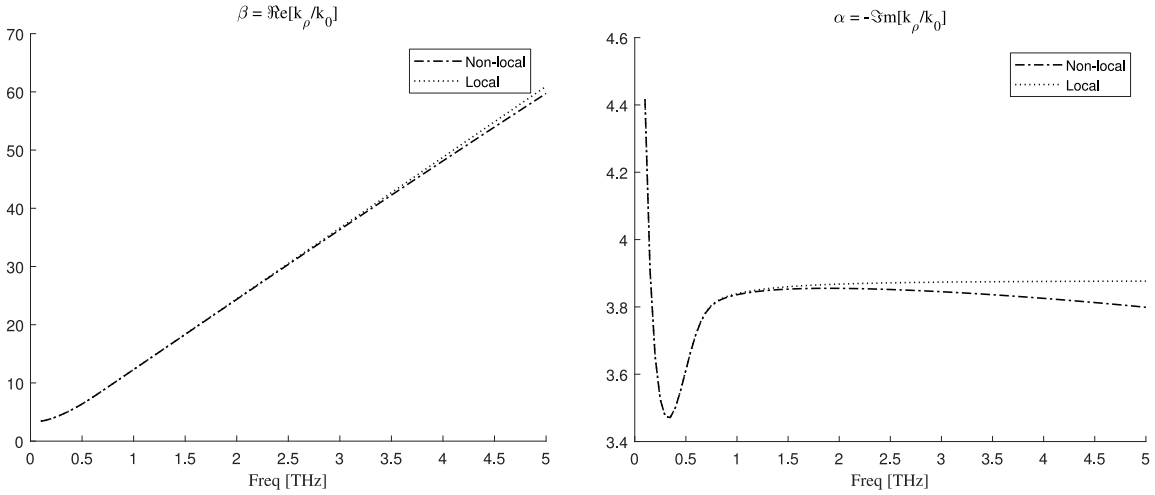

(a) (b)

Figure 3.6: TM modes for the Otto configuration with graphene vs frequency. The interband effects were ignored in the local conductivity. The non-local conductivity is given in (3.44).

3.3.5 Metamaterial Multilayered Waveguide

In this example a 63 layers stack suspended in air is considered [123] forming a Metamaterial Multilayered (ML) with effective hyperbolic uniaxial media parameters [124]. The frequency of operation corresponds to $\lambda_0 = 422$ [nm]. A dielectric-metal bi-layers [3] are repeated 32 times. The media parameters are $\epsilon_D = 6.76$ and $\epsilon_M = -5.637 - j0.214$ where $d_D = 11.7788$ [nm] and $d_M = 10.2212$ [nm]. In order to make the configuration symmetric, the top dielectric layer is halved and the other half is placed below the bottom layer of the 63 layers. The stack corresponds to an effective medium which exhibits strong anisotropy [124–127]. The TM modes are listed in Table 3.12. In this example the computation was done by inserting PEC and PMC for even and odd modes respectively splitting the waveguide. This simplifies the computations as shown in Figure 3.7 and 3.8.

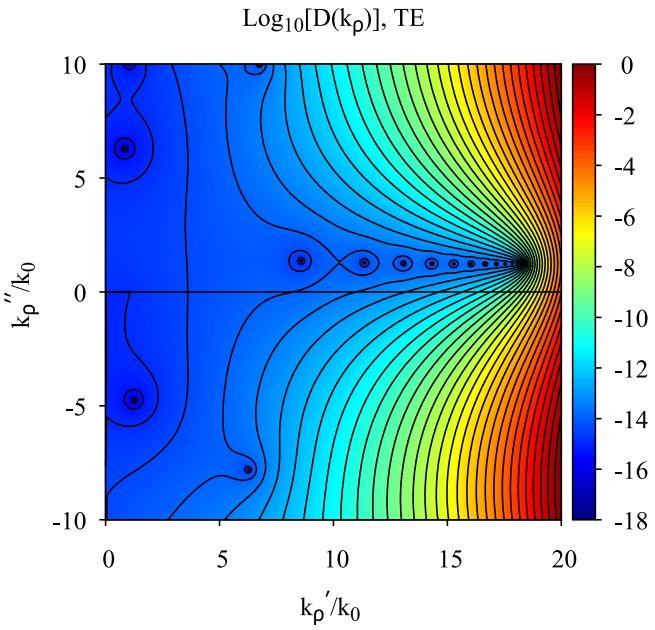

Figure 3.7: The DF for TE modes of the metamaterial ML configuration with boundary placed in the middle of the configuration with PEC.

[3] Dielectric on top of the metal bi-layer.

Table 3.12: k_ρ values for TM modes.

Mode	k_ρ/k_0
TM_s	$1.0664873335033 - j0.11115261799855$
TM_0	$5.8854156233753 + j1.60530790786940$
TM_1	$8.5910378082737 + j1.36679486975981$
TM_2	$10.189888644414 + j1.30745983161466$
TM_3	$11.364387201748 + j1.27929330849708$
TM_4	$12.301163846515 + j1.26292683965598$
TM_5	$13.081187277157 + j1.25240279413208$
TM_6	$13.747811945725 + j1.24520640975688$
TM_7	$14.327311972078 + j1.24007712164205$
TM_8	$14.836968577866 + j1.23631023876062$
TM_9	$15.288826322046 + j1.23348082771745$
TM_{10}	$15.691648389941 + j1.23131793168107$
TM_{11}	$16.052023705706 + j1.22964117627636$
TM_{12}	$16.375035755902 + j1.22832629234286$
TM_{13}	$16.664688046716 + j1.22728521449809$
TM_{14}	$16.924186492410 + j1.22645402676158$
TM_{15}	$17.156133781086 + j1.22578536272484$
TM_{16}	$17.362667652078 + j1.22524344730243$
TM_{17}	$17.545562597890 + j1.22480076497879$
TM_{18}	$17.706307590974 + j1.22443576788610$
TM_{19}	$17.846168527505 + j1.22413128554099$
TM_{20}	$17.966241842029 + j1.22387346298643$
TM_{21}	$18.067504237722 + j1.22365118954974$
TM_{22}	$18.150861548331 + j1.22345610723103$
TM_{23}	$18.217195461406 + j1.22328335549243$
TM_{24}	$18.267397577562 + j1.22313301155693$
TM_{25}	$18.302366070888 + j1.22301138946613$
TM_{26}	$18.322932478830 + j1.22293014603284$

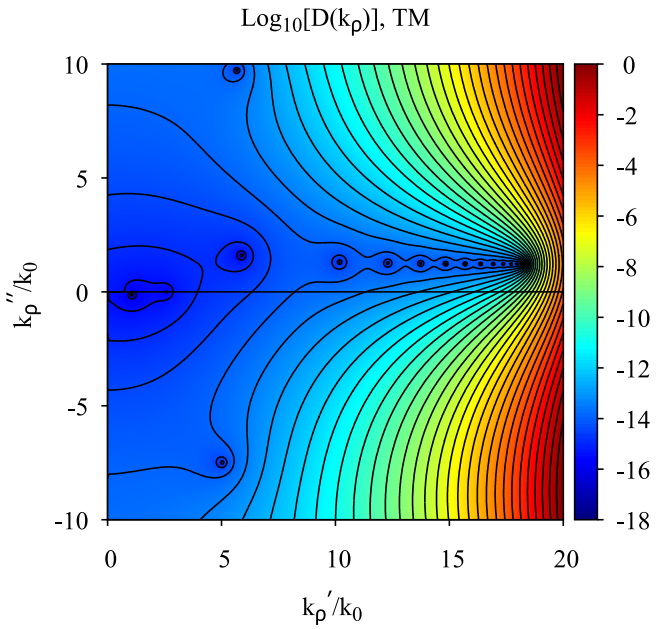

Figure 3.8: The DF for TM modes of the metamaterial ML configuration with boundary placed in the middle of the configuration with PMC.

The hyperbolic properties of this structure are explained via the Effective Medium Theory (EMT) [128–130]. In this case, the effective media parameters are $\epsilon \approx 1.0004 - j0.0994$ and $\epsilon_z \approx -160.0240 - j161.2890$ according to (3.45). The anisotropy ratio would be $\nu^e \approx -142.5347 - j175.3984$ which indicates that the effective media is uniaxial but also hyperbolic because of the negative sign on the real part.

$$\begin{aligned} \epsilon &= p\epsilon_M + (1-p)\epsilon_D \\ \epsilon_z &= \frac{\epsilon_M \epsilon_D}{p\epsilon_D + (1-p)\epsilon_M} \end{aligned} \tag{3.45}$$

Where the filling ratio $p = \dfrac{d_M}{d_M + d_D}$.

3.3.6 9-Layers ARROW Waveguide

This example is a 9-layer Anti-Resonant Reflecting Optical Waveguide (ARROW) in [108] summarized in Table 3.13 with operating frequency corresponds to $\lambda_0 = 632.8$ [nm]. The transverse magnetic fields for the modes: TM_0 for $k_\rho/k_0 = 1.45792542304 - j4.58804880738 \times 10^{-6}$ and TM_1 for $k_\rho/k_0 = 1.45778277326 - j5.71632735529 \times 10^{-6}$ are illustrated in Figure 3.9.

Table 3.13: Layered media details of 9-layer ARROW waveguide.

Layer	Thickness [μm]	$n = \sqrt{\epsilon}$
1	open	1
2	2	1.46
3	0.448	1.5
4	4	1.46
5	0.448	1.5
6	2	1.46
7	0.448	1.5
8	4	1.46
9	0.448	1.5
10	2	1.46
11	open	3.5

3.3.7 4-Layers Leaky Waves

Finally, in this configuration is $k_1 \neq k_N$ as described in [131] and summarized in Table 3.14 where $\lambda_0 = 632.8$ [nm]. The first propagating and leaky TE modes are listed in Table 3.15 and 3.16 respectively.

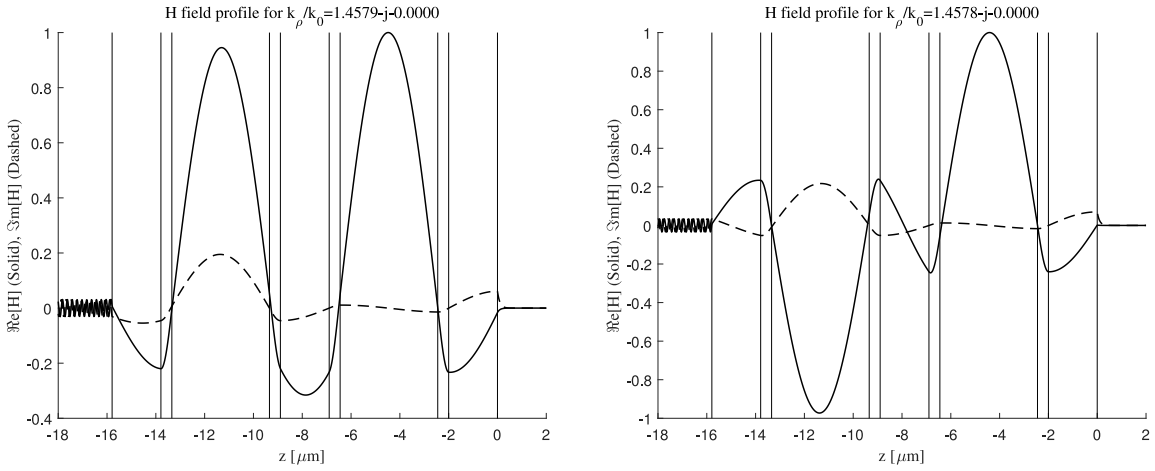

(a) (b)

Figure 3.9: The transverse magnetic field profile for TM modes (normalized by the complex value of H that corresponds to $\max(|H|)$).

Table 3.14: Layered media details of 4-layers waveguide.

Layer	Thickness [nm]	$n = \sqrt{\epsilon}$
1	open	1
2	500	1.66
3	500	1.53
4	500	1.46
5	500	1.6
6	500	1.66
7	open	1.5

Table 3.15: k_ρ values for TE propagating modes on sheet I.

Mode	k_ρ/k_0
TE_0	1.62272868232444
TE_1	1.60527569809455
TE_2	1.55713615229412
TE_3	1.50358711202272

Table 3.16: k_ρ values for TE leaky modes on sheet III.

Mode	k_ρ/k_0
TE_4	$1.46185664144564 - j0.007155870648894$
TE_5	$1.38248922303422 - j0.018165877364415$
TE_6	$1.28136443614803 - j0.035877392160044$
TE_7	$1.14231446246756 - j0.052876075117094$
TE_8	$1.00303701888735 - j0.070770941090572$

4.1 Transmission Line Model

Anisotropic conductive sheets are distinguished by tensor surface conductivity as mentioned earlier (4.1). The equivalent circuit of anisotropic conductive sheet in the TL model has been suggested as in Figure 4.1 [45, 46]. This model resembles the coupling between the TM and TE TLs, and it is derived directly from the boundary conditions in (2.17).

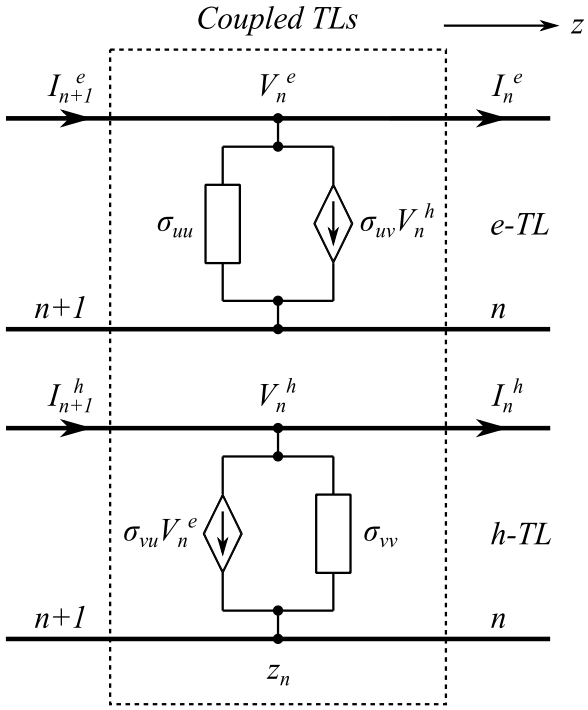

Figure 4.1: Coupled TLs at the junction $z = z_n$ circuit model representing the boundary condition arising from anisotropic conductive sheet placed between layers n and $n + 1$.

$$\underline{\underline{\boldsymbol{\sigma}}}^s = \begin{bmatrix} \sigma^s_{xx} & \sigma^s_{xy} \\ \sigma^s_{yx} & \sigma^s_{yy} \end{bmatrix} \tag{4.1}$$

The tensor surface conductivity can be expressed in the spectral domain as in (4.2) [24, 132].

$$\underline{\underline{\tilde{\boldsymbol{\sigma}}}}^s = \underline{\underline{\boldsymbol{R}}}^T \cdot \underline{\underline{\boldsymbol{\sigma}}}^s \cdot \underline{\underline{\boldsymbol{R}}} = \begin{bmatrix} \sigma^s_{uu} & \sigma^s_{uv} \\ \sigma^s_{vu} & \sigma^s_{vv} \end{bmatrix} \tag{4.2}$$

Where the rotation matrix $\underline{\underline{\boldsymbol{R}}}$ is defined as in (4.3), and $\underline{\underline{\boldsymbol{R}}}^T$ is the transpose. This is a similarity transformation which preserves the matrix properties: rank, determinant, and eigenvalues invariant under rotation [133, p. 181].

$$\underline{\underline{\boldsymbol{R}}} = \frac{1}{k_\rho} \begin{bmatrix} k_x & -k_y \\ k_y & k_x \end{bmatrix} \tag{4.3}$$

One can write the spectral domain components as follows:

$$\begin{aligned}
\sigma^s_{uu} &= \frac{1}{k_\rho^2}\left[k_x^2\sigma^s_{xx} + k_y^2\sigma^s_{yy} + k_xk_y(\sigma^s_{xy} + \sigma^s_{yx})\right] \\
\sigma^s_{uv} &= \frac{1}{k_\rho^2}\left[k_x^2\sigma^s_{xy} - k_y^2\sigma^s_{yx} - k_xk_y(\sigma^s_{xx} - \sigma^s_{yy})\right] \\
\sigma^s_{vu} &= \frac{1}{k_\rho^2}\left[k_x^2\sigma^s_{yx} - k_y^2\sigma^s_{xy} - k_xk_y(\sigma^s_{xx} - \sigma^s_{yy})\right] \\
\sigma^s_{vv} &= \frac{1}{k_\rho^2}\left[k_x^2\sigma^s_{yy} + k_y^2\sigma^s_{xx} - k_xk_y(\sigma^s_{xy} + \sigma^s_{yx})\right]
\end{aligned} \tag{4.4}$$

One should note that $\frac{k_x}{k_\rho} = \cos(\zeta)$ and $\frac{k_y}{k_\rho} = \sin(\zeta)$ which uses the definition of the spectral angle ζ. Also, we can define the isotropic case as $\underline{\underline{\boldsymbol{\sigma}}}^s = \sigma^s \underline{\underline{\boldsymbol{I}}}$ if needed. In a special case such as anisotropic graphene, the tensor surface conductivity results in no change in

the elements under rotation [134].

$$\underline{\underline{\boldsymbol{\sigma}}}^s = \begin{bmatrix} \sigma_d^s & -\sigma_h^s \\ \sigma_h^s & \sigma_d^s \end{bmatrix} = \underline{\underline{\tilde{\boldsymbol{\sigma}}}}^s \tag{4.5}$$

The coupling between both TLs requires that we solve both TLs simultaneously. This means that we need a different approach to solve for TL quantities. The following definitions will be used:

$$\left[\boldsymbol{V}_n(z)\right] = \begin{bmatrix} V_n^e(z) \\ V_n^h(z) \end{bmatrix} \quad , \quad \left[\boldsymbol{I}_n(z)\right] = \begin{bmatrix} I_n^e(z) \\ I_n^h(z) \end{bmatrix} \tag{4.6}$$

$$\left[\boldsymbol{V}_n^+\right] = \begin{bmatrix} V_n^{e+} \\ V_n^{h+} \end{bmatrix} \quad , \quad \left[\boldsymbol{V}_n^-\right] = \begin{bmatrix} V_n^{e-} \\ V_n^{h-} \end{bmatrix} \tag{4.7}$$

$$\left[\boldsymbol{P}_n^+(z)\right] = \begin{bmatrix} e^{-jk_{zn}^e(z-z_n)} & 0 \\ 0 & e^{-jk_{zn}^h(z-z_n)} \end{bmatrix} \quad , \quad \left[\boldsymbol{P}_n^-(z)\right] = \begin{bmatrix} e^{jk_{zn}^e(z-z_n)} & 0 \\ 0 & e^{jk_{zn}^h(z-z_n)} \end{bmatrix} \tag{4.8}$$

$$\left[\boldsymbol{\Theta}_n^+\right] = \begin{bmatrix} e^{-j\Theta_n^e} & 0 \\ 0 & e^{-j\Theta_n^h} \end{bmatrix} = \left[\boldsymbol{P}_n^+(z_{n-1})\right] \quad , \quad \left[\boldsymbol{\Theta}_n^-\right] = \begin{bmatrix} e^{j\Theta_n^e} & 0 \\ 0 & e^{j\Theta_n^h} \end{bmatrix} = \left[\boldsymbol{P}_n^-(z_{n-1})\right] \tag{4.9}$$

$$\left[\boldsymbol{Z}_n\right] = \begin{bmatrix} Z_n^e & 0 \\ 0 & Z_n^h \end{bmatrix} \quad , \quad \left[\boldsymbol{Y}_n\right] = \begin{bmatrix} Y_n^e & 0 \\ 0 & Y_n^h \end{bmatrix} \tag{4.10}$$

Also, note the relations $\left[\boldsymbol{P}_n^+(z)\right] = \left[\boldsymbol{P}_n^-(z)\right]^{-1}$, $\left[\boldsymbol{\Theta}_n^+\right] = \left[\boldsymbol{\Theta}_n^-\right]^{-1}$, and $\left[\boldsymbol{Z}_n\right] =$

$\big[\boldsymbol{Y}_n\big]^{-1}$.

In this solution, one should note that the symbol $\big[\quad\big]$ represents a matrix. This notation reduces the mathematical expressions and make them more readable. It is possible to define the boundary conditions in (2.5) as in (4.11) using the new notation. This is in agreement with [135]:[1]

$$\begin{bmatrix} \big[\boldsymbol{V}_{n+1}(z_n)\big] \\ \big[\boldsymbol{I}_{n+1}(z_n)\big] \end{bmatrix} = \begin{bmatrix} \big[\mathbf{1}\big] & \big[\mathbf{0}\big] \\ \big[\tilde{\boldsymbol{\sigma}}_n^s\big] & \big[\mathbf{1}\big] \end{bmatrix} \begin{bmatrix} \big[\boldsymbol{V}_n(z_n)\big] \\ \big[\boldsymbol{I}_n(z_n)\big] \end{bmatrix} \tag{4.11}$$

The next step is to write a solution to this TLs system. Here, we follow a similar approach to what we have done in Appendix A by splitting the solutions into source-free and source-excited. In addition, in the source-free regions we have up-looking and down-looking solutions. In the following, the source is assume to be located in section m.

4.1.1 Source-Free Solution $(n \neq m)$

A source-free section is illustrated in Figure 4.2. Here, we follow the same approach for finding the solutions in both TLs simultaneously due to the coupling of anisotropic conductive sheets.

4.1.1.1 Down-Looking Case $(n > m)$

Considering the following down-looking solution:

$$\begin{aligned} \big[\boldsymbol{V}_n(z)\big] &= \Big[\big[\boldsymbol{P}_n^-(z)\big] + \big[\boldsymbol{P}_n^+(z)\big]\big[\overleftarrow{\boldsymbol{\Gamma}}_n\big]\Big]\big[\boldsymbol{\Theta}_n^+\big]\big[\boldsymbol{V}_n^-\big] \\ \big[\boldsymbol{I}_n(z)\big] &= -\big[\boldsymbol{Y}_n\big]\Big[\big[\boldsymbol{P}_n^-(z)\big] - \big[\boldsymbol{P}_n^+(z)\big]\big[\overleftarrow{\boldsymbol{\Gamma}}_n\big]\Big]\big[\boldsymbol{\Theta}_n^+\big]\big[\boldsymbol{V}_n^-\big] \end{aligned} \tag{4.12}$$

Here, initially we postulate this type of reflection coefficient definition which will be-

[1] Where $\big[\mathbf{1}\big]$ is the identity matrix.

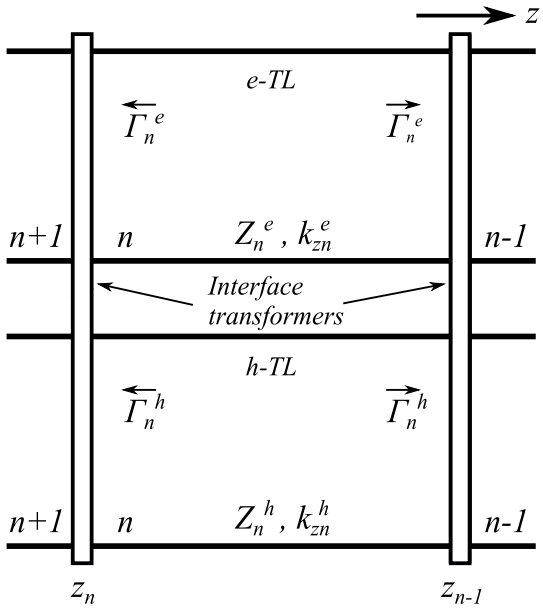

Figure 4.2: A source-free section n for coupled e and h TLs. The coupling is generally represented by junctions at interfaces.

come clear as we proceed:

$$\left[\overleftarrow{\mathbf{\Gamma}}_n\right] = \begin{bmatrix} \overleftarrow{\Gamma}_n^{ee} & \overleftarrow{\Gamma}_n^{eh} \\ \overleftarrow{\Gamma}_n^{he} & \overleftarrow{\Gamma}_n^{hh} \end{bmatrix} \tag{4.13}$$

The incident and reflected waves definitions are:

$$\begin{aligned} \left[\boldsymbol{w}_n^+(z)\right] &= \left[\boldsymbol{P}_n^+(z)\right]\left[\overleftarrow{\mathbf{\Gamma}}_n\right]\left[\mathbf{\Theta}_n^+\right]\left[\boldsymbol{V}_n^-\right] \\ \left[\boldsymbol{w}_n^-(z)\right] &= \left[\boldsymbol{P}_n^-(z)\right]\left[\mathbf{\Theta}_n^+\right]\left[\boldsymbol{V}_n^-\right] \end{aligned} \tag{4.14}$$

The reflection coefficients are defined based on the wave relations: $\left[\boldsymbol{w}_n^+(z_n)\right] = \left[\overleftarrow{\mathbf{\Gamma}}_n\right]\left[\boldsymbol{w}_n^-(z_n)\right]$. This can be re-written as follows:

$$\begin{bmatrix} [\boldsymbol{V}_n(z)] \\ [\boldsymbol{I}_n(z)] \end{bmatrix} = \begin{bmatrix} [\mathbf{1}] & [\mathbf{1}] \\ -[\boldsymbol{Y}_n] & [\boldsymbol{Y}_n] \end{bmatrix} \begin{bmatrix} [\boldsymbol{P}_n^-(z)] & [\mathbf{0}] \\ [\mathbf{0}] & [\boldsymbol{P}_n^+(z)][\overleftarrow{\boldsymbol{\Gamma}}_n] \end{bmatrix} \begin{bmatrix} [\boldsymbol{\Theta}_n^+][\boldsymbol{V}_n^-] \\ [\boldsymbol{\Theta}_n^+][\boldsymbol{V}_n^-] \end{bmatrix} \tag{4.15}$$

The solution in (4.15) at $z = z_n$ becomes:

$$\begin{bmatrix} [\boldsymbol{V}_n(z_n)] \\ [\boldsymbol{I}_n(z_n)] \end{bmatrix} = \begin{bmatrix} [\mathbf{1}] & [\mathbf{1}] \\ -[\boldsymbol{Y}_n] & [\boldsymbol{Y}_n] \end{bmatrix} \begin{bmatrix} [\boldsymbol{\Theta}_n^+][\boldsymbol{V}_n^-] \\ [\overleftarrow{\boldsymbol{\Gamma}}_n][\boldsymbol{\Theta}_n^+][\boldsymbol{V}_n^-] \end{bmatrix} \tag{4.16}$$

And the same for section $n+1$ solution:

$$\begin{bmatrix} [\boldsymbol{V}_{n+1}(z_n)] \\ [\boldsymbol{I}_{n+1}(z_n)] \end{bmatrix} = \begin{bmatrix} [\mathbf{1}] & [\mathbf{1}] \\ -[\boldsymbol{Y}_{n+1}] & [\boldsymbol{Y}_{n+1}] \end{bmatrix} \begin{bmatrix} [\boldsymbol{V}_{n+1}^-] \\ [\boldsymbol{\Theta}_{n+1}^+][\overleftarrow{\boldsymbol{\Gamma}}_{n+1}][\boldsymbol{\Theta}_{n+1}^+][\boldsymbol{V}_{n+1}^-] \end{bmatrix} \tag{4.17}$$

Using the boundary conditions in (4.11), we obtain the following relation:

$$\begin{bmatrix} [\boldsymbol{V}_{n+1}^-] \\ [\boldsymbol{\Theta}_{n+1}^+][\overleftarrow{\boldsymbol{\Gamma}}_{n+1}][\boldsymbol{\Theta}_{n+1}^+][\boldsymbol{V}_{n+1}^-] \end{bmatrix} = \begin{bmatrix} [\boldsymbol{M}_{11,n}] & [\boldsymbol{M}_{12,n}] \\ [\boldsymbol{M}_{21,n}] & [\boldsymbol{M}_{22,n}] \end{bmatrix} \begin{bmatrix} [\boldsymbol{\Theta}_n^+][\boldsymbol{V}_n^-] \\ [\overleftarrow{\boldsymbol{\Gamma}}_n][\boldsymbol{\Theta}_n^+][\boldsymbol{V}_n^-] \end{bmatrix} \tag{4.18}$$

Where,

$$
\begin{aligned}
\left[\boldsymbol{M}_{11,n}\right] &= \frac{1}{2}\left[\left[\mathbf{1}\right] + \left[\boldsymbol{Z}_{n+1}\right]\left[\left[\boldsymbol{Y}_n - \left[\tilde{\boldsymbol{\sigma}}_n^s\right]\right]\right]\right] \\
\left[\boldsymbol{M}_{12,n}\right] &= \frac{1}{2}\left[\left[\mathbf{1}\right] - \left[\boldsymbol{Z}_{n+1}\right]\left[\left[\boldsymbol{Y}_n + \left[\tilde{\boldsymbol{\sigma}}_n^s\right]\right]\right]\right] \\
\left[\boldsymbol{M}_{21,n}\right] &= \frac{1}{2}\left[\left[\mathbf{1}\right] - \left[\boldsymbol{Z}_{n+1}\right]\left[\left[\boldsymbol{Y}_n - \left[\tilde{\boldsymbol{\sigma}}_n^s\right]\right]\right]\right] \\
\left[\boldsymbol{M}_{22,n}\right] &= \frac{1}{2}\left[\left[\mathbf{1}\right] + \left[\boldsymbol{Z}_{n+1}\right]\left[\left[\boldsymbol{Y}_n + \left[\tilde{\boldsymbol{\sigma}}_n^s\right]\right]\right]\right]
\end{aligned}
\tag{4.19}
$$

Note that the inverse matrix in (4.20) was applied in (4.19).

$$
\begin{bmatrix} \left[\mathbf{1}\right] & \left[\mathbf{1}\right] \\ -\left[\boldsymbol{Y}_{n+1}\right] & \left[\boldsymbol{Y}_{n+1}\right] \end{bmatrix}^{-1} = \frac{1}{2}\begin{bmatrix} \left[\mathbf{1}\right] & -\left[\boldsymbol{Z}_{n+1}\right] \\ \left[\mathbf{1}\right] & \left[\boldsymbol{Z}_{n+1}\right] \end{bmatrix}
\tag{4.20}
$$

Allowing the next definitions which are extensions to previous relations:

$$
\left[\boldsymbol{\Gamma}_{i,j}\right] = \begin{bmatrix} \Gamma_{i,j}^e & 0 \\ 0 & \Gamma_{i,j}^h \end{bmatrix}
\tag{4.21}
$$

$$
\left[\boldsymbol{\tau}_{i,j}\right] = \left[\mathbf{1}\right] + \left[\boldsymbol{\Gamma}_{i,j}\right] = \begin{bmatrix} \tau_{i,j}^e & 0 \\ 0 & \tau_{i,j}^h \end{bmatrix}
\tag{4.22}
$$

Using the previous definitions and the relations in (4.18), It is possible to show that:

$$
\begin{aligned}
\left[\boldsymbol{V}_{n+1}^-\right] &= \left[\left[\boldsymbol{M}_{11,n}\right] + \left[\boldsymbol{M}_{12,n}\right]\left[\overleftarrow{\boldsymbol{\Gamma}}_n\right]\right]\left[\boldsymbol{\Theta}_n^+\right]\left[\boldsymbol{V}_n^-\right] \\
\left[\overleftarrow{\boldsymbol{D}}_{n+1}\right]\left[\boldsymbol{V}_{n+1}^-\right] &= \left[\left[\boldsymbol{M}_{21,n}\right] + \left[\boldsymbol{M}_{22,n}\right]\left[\overleftarrow{\boldsymbol{\Gamma}}_n\right]\right]\left[\boldsymbol{\Theta}_n^+\right]\left[\boldsymbol{V}_n^-\right]
\end{aligned}
\tag{4.23}
$$

Where,

$$\left[\overleftarrow{\boldsymbol{D}}_{n+1}\right] = \left[\boldsymbol{\Theta}^{+}_{n+1}\right]\left[\overleftarrow{\boldsymbol{\Gamma}}_{n+1}\right]\left[\boldsymbol{\Theta}^{+}_{n+1}\right] \tag{4.24}$$

Also, $\left[\boldsymbol{\Omega}_{i,j}\right] = \Big[\left[\boldsymbol{Y}_i\right] + \left[\boldsymbol{Y}_j\right]\Big]^{-1}$. Using (4.23) and rearranging the terms, one can obtain:

$$\left[\left[\boldsymbol{M}_{22,n}\right] - \left[\overleftarrow{\boldsymbol{D}}_{n+1}\right]\left[\boldsymbol{M}_{12,n}\right]\right]\left[\overleftarrow{\boldsymbol{\Gamma}}_{n}\right] = \left[-\left[\boldsymbol{M}_{21,n}\right] + \left[\overleftarrow{\boldsymbol{D}}_{n+1}\right]\left[\boldsymbol{M}_{11,n}\right]\right] \tag{4.25}$$

The matrix elements in (4.19) can be re-written as in (4.26):[2]

$$\begin{aligned}
\left[\boldsymbol{M}_{11,n}\right] &= \left[\boldsymbol{\tau}_{n,n+1}\right]^{-1}\left[\left[\mathbf{1}\right] - \left[\boldsymbol{\Omega}_{n+1,n}\right]\left[\tilde{\boldsymbol{\sigma}}^{s}_{n}\right]\right] \\
-\left[\boldsymbol{M}_{12,n}\right] &= \left[\boldsymbol{\tau}_{n,n+1}\right]^{-1}\left[\left[\boldsymbol{\Gamma}_{n+1,n}\right] + \left[\boldsymbol{\Omega}_{n+1,n}\right]\left[\tilde{\boldsymbol{\sigma}}^{s}_{n}\right]\right] \\
-\left[\boldsymbol{M}_{21,n}\right] &= \left[\boldsymbol{\tau}_{n,n+1}\right]^{-1}\left[\left[\boldsymbol{\Gamma}_{n+1,n}\right] - \left[\boldsymbol{\Omega}_{n+1,n}\right]\left[\tilde{\boldsymbol{\sigma}}^{s}_{n}\right]\right] \\
\left[\boldsymbol{M}_{22,n}\right] &= \left[\boldsymbol{\tau}_{n,n+1}\right]^{-1}\left[\left[\mathbf{1}\right] + \left[\boldsymbol{\Omega}_{n+1,n}\right]\left[\tilde{\boldsymbol{\sigma}}^{s}_{n}\right]\right]
\end{aligned} \tag{4.26}$$

Thus, the reflection coefficient is given in (4.27) and the voltages are related by (4.32).

$$\left[\overleftarrow{\boldsymbol{\Gamma}}_{n}\right] = \Big(\left[\boldsymbol{A}\right] + \left[\boldsymbol{B}\right]\Big)^{-1}\Big(\left[\boldsymbol{C}\right] + \left[\boldsymbol{D}\right]\Big) \tag{4.27}$$

Where,

[2]Note that $\left[\boldsymbol{\Gamma}_{n,n+1}\right] = -\left[\boldsymbol{\Gamma}_{n+1,n}\right]$ was used.

$$
\begin{aligned}
\big[\boldsymbol{A}\big] &= \big[\boldsymbol{\tau}_{n,n+1}\big]^{-1}\Big(\big[\mathbf{1}\big] + \big[\boldsymbol{\Omega}_{n+1,n}\big]\big[\tilde{\boldsymbol{\sigma}}_n^s\big]\Big) \\
\big[\boldsymbol{B}\big] &= \big[\overleftarrow{\boldsymbol{D}}_{n+1}\big]\big[\boldsymbol{\tau}_{n,n+1}\big]^{-1}\Big(\big[\boldsymbol{\Gamma}_{n+1,n}\big] + \big[\boldsymbol{\Omega}_{n+1,n}\big]\big[\tilde{\boldsymbol{\sigma}}_n^s\big]\Big) \\
\big[\boldsymbol{C}\big] &= \big[\boldsymbol{\tau}_{n,n+1}\big]^{-1}\Big(\big[\boldsymbol{\Gamma}_{n+1,n}\big] - \big[\boldsymbol{\Omega}_{n+1,n}\big]\big[\tilde{\boldsymbol{\sigma}}_n^s\big]\Big) \\
\big[\boldsymbol{D}\big] &= \big[\overleftarrow{\boldsymbol{D}}_{n+1}\big]\big[\boldsymbol{\tau}_{n,n+1}\big]^{-1}\Big(\big[\mathbf{1}\big] - \big[\boldsymbol{\Omega}_{n+1,n}\big]\big[\tilde{\boldsymbol{\sigma}}_n^s\big]\Big)
\end{aligned}
\tag{4.28}
$$

For $n = N$, we start with:

$$
\big[\overleftarrow{\boldsymbol{\Gamma}}_N\big] = \begin{bmatrix} \overleftarrow{\Gamma}_N^{ee} & 0 \\ 0 & \overleftarrow{\Gamma}_N^{hh} \end{bmatrix}
\tag{4.29}
$$

Note that the overall reflection coefficient $\big[\overleftarrow{\boldsymbol{\Gamma}}_1\big]$ takes the form in (4.30) in the presence of anisotropic sheet(s) embedded in the stack. Hence, the coupling between the TLs is observed explicitly.

$$
\big[\overleftarrow{\boldsymbol{\Gamma}}_1\big] = \begin{bmatrix} \overleftarrow{\Gamma}_1^{ee} & \overleftarrow{\Gamma}_1^{eh} \\ \overleftarrow{\Gamma}_1^{he} & \overleftarrow{\Gamma}_1^{hh} \end{bmatrix}
\tag{4.30}
$$

Also, using the first boundary condition: $\big[\boldsymbol{V}_{n+1}(z_n)\big] = \big[\boldsymbol{V}_n(z_n)\big]$:

$$
\Big[\big[\mathbf{1}\big] + \big[\overleftarrow{\boldsymbol{D}}_{n+1}\big]\Big]\big[\boldsymbol{V}_{n+1}^-\big] = \Big[\big[\mathbf{1}\big] + \big[\overleftarrow{\boldsymbol{\Gamma}}_n\big]\Big]\big[\boldsymbol{\Theta}_n^+\big]\big[\boldsymbol{V}_n^-\big]
\tag{4.31}
$$

Thus, we obtain:

$$
\big[\boldsymbol{V}_{n+1}^-\big] = \Big[\big[\mathbf{1}\big] + \big[\overleftarrow{\boldsymbol{D}}_{n+1}\big]\Big]^{-1}\Big[\big[\mathbf{1}\big] + \big[\overleftarrow{\boldsymbol{\Gamma}}_n\big]\Big]\big[\boldsymbol{\Theta}_n^+\big]\big[\boldsymbol{V}_n^-\big] = \big[\overleftarrow{\boldsymbol{\tau}}_n\big]\big[\boldsymbol{V}_n^-\big]
\tag{4.32}
$$

The overall $\left[\overleftarrow{\boldsymbol{\tau}}\right] = \prod_{n=N-1}^{1}\left[\overleftarrow{\boldsymbol{\tau}}_n\right]$. Notice that these relations simplify to the uncoupled TL formulation presented previously. If $n = m+1$, then we define $\left[\boldsymbol{V}_n^-\right]$ as follows:

$$\left[\boldsymbol{V}_n^-\right] = \left[\left[\boldsymbol{1}\right] + \left[\overleftarrow{\boldsymbol{D}}_n\right]\right]^{-1}\left[\boldsymbol{V}_m(z_m)\right] \tag{4.33}$$

4.1.1.2 Up-Looking Case $(n < m)$

Similar to what we have done for isotropic scenario, the proposed solution is:

$$\begin{aligned}\left[\boldsymbol{V}_n(z)\right] &= \left[\left[\boldsymbol{P}_n^+(z)\right] + \left[\boldsymbol{P}_n^-(z)\right]\left[\overrightarrow{\boldsymbol{\Gamma}}_n\right]\right]\left[\boldsymbol{\Theta}_n^+\right]\left[\boldsymbol{V}_n^+\right] \\ \left[\boldsymbol{I}_n(z)\right] &= \left[\boldsymbol{Y}_n\right]\left[\left[\boldsymbol{P}_n^+(z)\right] - \left[\boldsymbol{P}_n^-(z)\right]\left[\overrightarrow{\boldsymbol{\Gamma}}_n\right]\right]\left[\boldsymbol{\Theta}_n^+\right]\left[\boldsymbol{V}_n^+\right]\end{aligned} \tag{4.34}$$

Where the definitions of $\left[\boldsymbol{P}_n^+(z)\right]$ and $\left[\boldsymbol{P}_n^-(z)\right]$ are replaced with (4.35).

$$\begin{aligned}\left[\boldsymbol{P}_n^+(z)\right] &= \begin{bmatrix} e^{-jk_{zn}^e(z-z_{n-1})} & 0 \\ 0 & e^{-jk_{zn}^h(z-z_{n-1})}\end{bmatrix} \\ \left[\boldsymbol{P}_n^-(z)\right] &= \begin{bmatrix} e^{jk_{zn}^e(z-z_{n-1})} & 0 \\ 0 & e^{jk_{zn}^h(z-z_{n-1})}\end{bmatrix}\end{aligned} \tag{4.35}$$

The reflection coefficients are defined based on the wave relation: $\left[\boldsymbol{w}_n^-(z_{n-1})\right] = \left[\overrightarrow{\boldsymbol{\Gamma}}_n\right]\left[\boldsymbol{w}_n^+(z_{n-1})\right]$. The reflection coefficient is given in (4.36).

$$\left[\overrightarrow{\boldsymbol{\Gamma}}_n\right] = \Big(\left[\boldsymbol{A}\right] + \left[\boldsymbol{B}\right]\Big)^{-1}\Big(\left[\boldsymbol{C}\right] + \left[\boldsymbol{D}\right]\Big) \tag{4.36}$$

Where,

$$
\begin{aligned}
\left[\boldsymbol{A}\right] &= \left[\boldsymbol{\tau}_{n,n-1}\right]^{-1}\Big(\left[\mathbf{1}\right] + \left[\boldsymbol{\Omega}_{n-1,n}\right]\left[\tilde{\boldsymbol{\sigma}}^{s}_{n-1}\right]\Big) \\
\left[\boldsymbol{B}\right] &= \left[\overrightarrow{\boldsymbol{D}}_{n-1}\right]\left[\boldsymbol{\tau}_{n,n-1}\right]^{-1}\Big(\left[\boldsymbol{\Gamma}_{n-1,n}\right] + \left[\boldsymbol{\Omega}_{n-1,n}\right]\left[\tilde{\boldsymbol{\sigma}}^{s}_{n-1}\right]\Big) \\
\left[\boldsymbol{C}\right] &= \left[\boldsymbol{\tau}_{n,n-1}\right]^{-1}\Big(\left[\boldsymbol{\Gamma}_{n-1,n}\right] - \left[\boldsymbol{\Omega}_{n-1,n}\right]\left[\tilde{\boldsymbol{\sigma}}^{s}_{n-1}\right]\Big) \\
\left[\boldsymbol{D}\right] &= \left[\overrightarrow{\boldsymbol{D}}_{n-1}\right]\left[\boldsymbol{\tau}_{n,n-1}\right]^{-1}\Big(\left[\mathbf{1}\right] - \left[\boldsymbol{\Omega}_{n-1,n}\right]\left[\tilde{\boldsymbol{\sigma}}^{s}_{n-1}\right]\Big)
\end{aligned}
\tag{4.37}
$$

For $n = 1$, we start with:

$$
\left[\overrightarrow{\boldsymbol{\Gamma}}_{1}\right] = \begin{bmatrix} \overrightarrow{\Gamma}^{ee}_{1} & 0 \\ 0 & \overrightarrow{\Gamma}^{hh}_{1} \end{bmatrix}
\tag{4.38}
$$

The voltages are related by (4.39).

$$
\left[\boldsymbol{V}^{+}_{n-1}\right] = \left[\left[\mathbf{1}\right] + \left[\overrightarrow{\boldsymbol{D}}_{n-1}\right]\right]^{-1}\left[\left[\mathbf{1}\right] + \left[\overrightarrow{\boldsymbol{\Gamma}}_{n}\right]\right]\left[\boldsymbol{\Theta}^{+}_{n}\right]\left[\boldsymbol{V}^{+}_{n}\right] = \left[\overrightarrow{\boldsymbol{\tau}}_{n}\right]\left[\boldsymbol{V}^{+}_{n}\right]
\tag{4.39}
$$

Where,

$$
\left[\overrightarrow{\boldsymbol{D}}_{n-1}\right] = \left[\boldsymbol{\Theta}^{+}_{n-1}\right]\left[\overrightarrow{\boldsymbol{\Gamma}}_{n-1}\right]\left[\boldsymbol{\Theta}^{+}_{n-1}\right]
\tag{4.40}
$$

The overall $\left[\overrightarrow{\boldsymbol{\tau}}\right] = \prod_{n=2}^{N}\left[\overrightarrow{\boldsymbol{\tau}}_{\boldsymbol{n}}\right]$. Also, if $n = m-1$, then we define $\left[\boldsymbol{V}^{+}_{n}\right]$ as follows:

$$
\left[\boldsymbol{V}^{+}_{n}\right] = \left[\left[\mathbf{1}\right] + \left[\overrightarrow{\boldsymbol{D}}_{n}\right]\right]^{-1}\left[\boldsymbol{V}_{m}(z_{m-1})\right]
\tag{4.41}
$$

Similarly, the overall reflection coefficient is given below:

$$
\left[\overrightarrow{\boldsymbol{\Gamma}}_{N}\right] = \begin{bmatrix} \overrightarrow{\Gamma}^{ee}_{N} & \overrightarrow{\Gamma}^{eh}_{N} \\ \overrightarrow{\Gamma}^{he}_{N} & \overrightarrow{\Gamma}^{hh}_{N} \end{bmatrix}
\tag{4.42}
$$

This completes the solution for source-free sections.

4.1.2 Source-Excited Solution $(n = m)$

A source-excited section is illustrated in Figure 4.3. Notice that we distinguish the excitations from each TL using the notation e and h. Considering section n where the source is place in z', we introduce the definitions:

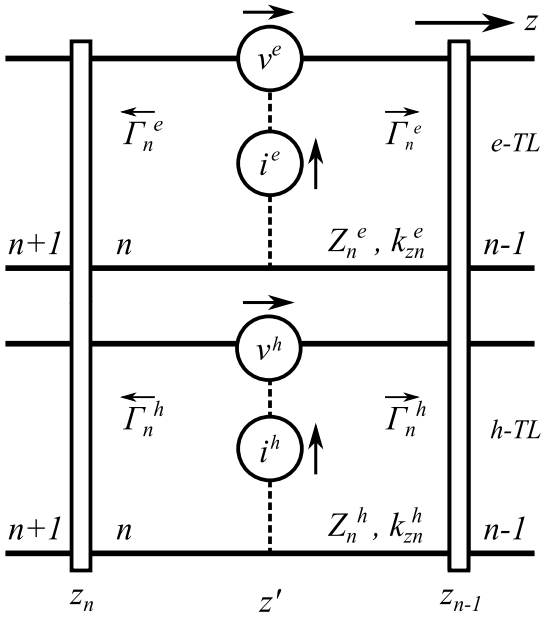

Figure 4.3: A source-excited section n for coupled e and h TLs. The coupling is generally represented by junctions at interfaces.

$$\left[\acute{\boldsymbol{P}}_n^{+}(z)\right] = \begin{bmatrix} e^{-jk_{zn}^{e}(z-z')} & 0 \\ 0 & e^{-jk_{zn}^{h}(z-z')} \end{bmatrix} \quad , \quad \left[\acute{\boldsymbol{P}}_n^{-}(z)\right] = \begin{bmatrix} e^{jk_{zn}^{e}(z-z')} & 0 \\ 0 & e^{jk_{zn}^{h}(z-z')} \end{bmatrix} \tag{4.43}$$

Similar to the isotropic case, the proposed solutions are:

$$\big[\boldsymbol{V}_n(z)\big] = \begin{cases} \big[\boldsymbol{V}_n^{+}(z)\big] = \Big[\big[\acute{\boldsymbol{P}}_n^{+}(z)\big] + \big[\acute{\boldsymbol{P}}_n^{-}(z)\big]\big[\overrightarrow{\boldsymbol{\Gamma}}'\big]\Big]\big[\boldsymbol{V}_n^{+}\big], & z > z' \\ \big[\boldsymbol{V}_n^{-}(z)\big] = \Big[\big[\acute{\boldsymbol{P}}_n^{-}(z)\big] + \big[\acute{\boldsymbol{P}}_n^{+}(z)\big]\big[\overleftarrow{\boldsymbol{\Gamma}}'\big]\Big]\big[\boldsymbol{V}_n^{-}\big], & z < z' \end{cases} \tag{4.44}$$

$$\big[\boldsymbol{I}_n(z)\big] = \begin{cases} \big[\boldsymbol{I}_n^{+}(z)\big] = \big[\boldsymbol{Y}_n\big]\Big[\big[\acute{\boldsymbol{P}}_n^{+}(z)\big] - \big[\acute{\boldsymbol{P}}_n^{-}(z)\big]\big[\overrightarrow{\boldsymbol{\Gamma}}'\big]\Big]\big[\boldsymbol{V}_n^{+}\big], & z > z' \\ \big[\boldsymbol{I}_n^{-}(z)\big] = -\big[\boldsymbol{Y}_n\big]\Big[\big[\acute{\boldsymbol{P}}_n^{-}(z)\big] - \big[\acute{\boldsymbol{P}}_n^{+}(z)\big]\big[\overleftarrow{\boldsymbol{\Gamma}}'\big]\Big]\big[\boldsymbol{V}_n^{-}\big], & z < z' \end{cases} \tag{4.45}$$

Notice that the reflection coefficients definitions are based on the following waves relations:

$$\begin{aligned} \big[\boldsymbol{w}_n^{+}(z')\big] &= \big[\overleftarrow{\boldsymbol{\Gamma}}'\big]\big[\boldsymbol{w}_n^{-}(z')\big] \quad , \quad z < z' \\ \big[\boldsymbol{w}_n^{-}(z')\big] &= \big[\overrightarrow{\boldsymbol{\Gamma}}'\big]\big[\boldsymbol{w}_n^{+}(z')\big] \quad , \quad z > z' \end{aligned} \tag{4.46}$$

From the definitions in (4.46), we can obtain:

$$\begin{aligned} \big[\boldsymbol{w}_n^{+}(z_n)\big] &= \big[\overleftarrow{\boldsymbol{\Gamma}}_n\big]\big[\boldsymbol{w}_n^{-}(z_n)\big] \quad , \quad z < z' \\ \big[\boldsymbol{w}_n^{-}(z_{n-1})\big] &= \big[\overrightarrow{\boldsymbol{\Gamma}}_n\big]\big[\boldsymbol{w}_n^{+}(z_{n-1})\big] \quad , \quad z > z' \end{aligned} \tag{4.47}$$

From the previous, we introduce the following relations in (4.48) and (4.49).

$$\begin{aligned} \big[\acute{\boldsymbol{P}}_n^{+}(z_n)\big]\big[\boldsymbol{w}_n^{+}(z')\big] &= \big[\overleftarrow{\boldsymbol{\Gamma}}_n\big]\big[\acute{\boldsymbol{P}}_n^{-}(z_n)\big]\big[\boldsymbol{w}_n^{-}(z')\big] \\ \big[\acute{\boldsymbol{P}}_n^{-}(z_{n-1})\big]\big[\boldsymbol{w}_n^{-}(z')\big] &= \big[\overrightarrow{\boldsymbol{\Gamma}}_n\big]\big[\acute{\boldsymbol{P}}_n^{+}(z_{n-1})\big]\big[\boldsymbol{w}_n^{+}(z')\big] \end{aligned} \tag{4.48}$$

$$\begin{aligned}\left[\overleftarrow{\boldsymbol{\Gamma}}'\right] &= \left[\acute{\boldsymbol{P}}_n^-(z_n)\right]\left[\overleftarrow{\boldsymbol{\Gamma}}_n\right]\left[\acute{\boldsymbol{P}}_n^-(z_n)\right] \\ \left[\overrightarrow{\boldsymbol{\Gamma}}'\right] &= \left[\acute{\boldsymbol{P}}_n^+(z_{n-1})\right]\left[\overrightarrow{\boldsymbol{\Gamma}}_n\right]\left[\acute{\boldsymbol{P}}_n^+(z_{n-1})\right]\end{aligned} \tag{4.49}$$

Here, the following definitions will be used for the excitations $\left[\boldsymbol{v}\right]$ and $\left[\boldsymbol{i}\right]$ as in (4.50). Note that only one type of excitation will be used while the other values are set to zeros.

$$\left[\boldsymbol{v}\right] = \begin{bmatrix} v^e \\ \\ v^h \end{bmatrix} \quad , \quad \left[\boldsymbol{i}\right] = \begin{bmatrix} i^e \\ \\ i^h \end{bmatrix} \tag{4.50}$$

The jump condition can be expressed as:

$$\begin{aligned}\left[\boldsymbol{V}_n^+(z')\right] - \left[\boldsymbol{V}_n^-(z')\right] &= \left[\boldsymbol{v}\right] \\ \left[\boldsymbol{I}_n^+(z')\right] - \left[\boldsymbol{I}_n^-(z')\right] &= \left[\boldsymbol{i}\right]\end{aligned} \tag{4.51}$$

Substituting the corresponding expressions from (4.44) and (4.45) into (4.51) we obtain:

$$\begin{bmatrix} \overbrace{\left[\left[\mathbf{1}\right] + \left[\overrightarrow{\boldsymbol{\Gamma}}'\right]\right]}^{\left[\boldsymbol{A}\right]} & \overbrace{-\left[\left[\mathbf{1}\right] + \left[\overleftarrow{\boldsymbol{\Gamma}}'\right]\right]}^{\left[\boldsymbol{B}\right]} \\ \underbrace{\left[\boldsymbol{Y}_n\right]\left[\left[\mathbf{1}\right] - \left[\overrightarrow{\boldsymbol{\Gamma}}'\right]\right]}_{\left[\boldsymbol{C}\right]} & \underbrace{\left[\boldsymbol{Y}_n\right]\left[\left[\mathbf{1}\right] - \left[\overleftarrow{\boldsymbol{\Gamma}}'\right]\right]}_{\left[\boldsymbol{D}\right]} \end{bmatrix} \begin{bmatrix} \left[\boldsymbol{V}_n^+\right] \\ \left[\boldsymbol{V}_n^-\right] \end{bmatrix} = \begin{bmatrix} \left[\boldsymbol{v}\right] \\ \left[\boldsymbol{i}\right] \end{bmatrix} \tag{4.52}$$

The system above in (4.52) can be solved as in (4.53).

$$
\begin{aligned}
\left[\boldsymbol{V}_n^{+}\right] &= \left[\left[\boldsymbol{B}\right]^{-1}\left[\boldsymbol{A}\right] - \left[\boldsymbol{D}\right]^{-1}\left[\boldsymbol{C}\right]\right]^{-1}\left[\left[\boldsymbol{B}\right]^{-1}\left[\boldsymbol{v}\right] - \left[\boldsymbol{D}\right]^{-1}\left[\boldsymbol{i}\right]\right] \\
\left[\boldsymbol{V}_n^{-}\right] &= \left[\left[\boldsymbol{A}\right]^{-1}\left[\boldsymbol{B}\right] - \left[\boldsymbol{C}\right]^{-1}\left[\boldsymbol{D}\right]\right]^{-1}\left[\left[\boldsymbol{A}\right]^{-1}\left[\boldsymbol{v}\right] - \left[\boldsymbol{C}\right]^{-1}\left[\boldsymbol{i}\right]\right]
\end{aligned}
\tag{4.53}
$$

Hence, the expressions in (4.53) will be substituted in (4.44) and (4.45) and give the complete solutions inside section n where the source is embedded.

For computing the components $V_{s\beta}^{\alpha}(z|z')$ and $I_{s\beta}^{\alpha}(z|z')$ we apply (4.50). In the previous notation, we defined the voltage on $\alpha = e, h$ TL excited by source type $s = v, i$ located on $\beta = e, h$ TL. Note that the coupling between TLs via interface transformers result in exciting both TLs due to any source. The expressions in (4.54)-(4.55) illustrates this concept.

$$
\begin{aligned}
V^{\alpha}(z) = &\langle V_{ie}^{\alpha}(z|z'), i^{e}(z')\rangle + \langle V_{ih}^{\alpha}(z|z'), i^{h}(z')\rangle \\
&+ \langle V_{ve}^{\alpha}(z|z'), v^{e}(z')\rangle + \langle V_{vh}^{\alpha}(z|z'), v^{h}(z')\rangle
\end{aligned}
\tag{4.54}
$$

$$
\begin{aligned}
I^{\alpha}(z) = &\langle I_{ie}^{\alpha}(z|z'), i^{e}(z')\rangle + \langle I_{ih}^{\alpha}(z|z'), i^{h}(z')\rangle \\
&+ \langle I_{ve}^{\alpha}(z|z'), v^{e}(z')\rangle + \langle I_{vh}^{\alpha}(z|z'), v^{h}(z')\rangle
\end{aligned}
\tag{4.55}
$$

4.1.3 Numerical Examples

Here, we study an example of planar layered structure that includes an anisotropic conductive sheet. The idea is to validate the TL implementation discussed above against the literatures before we proceed with our DGFs development. The magnetically biased graphene surface conductivity model was presented in [27, 136–140]. This model will be used in the following examples for demonstrating our solution on anisotropic graphene.

The surface conductivity tensor components are given in (4.57)-(4.59). Under magnetic bias, the Hall conductivities are introduced and hence the tensor conductivity takes the form defined in (4.56). In Figure 4.4, an example of the surface conductivity of magnetically biased graphene values vs frequency are shown.

$$\underline{\underline{\boldsymbol{\sigma}}}^s = \begin{bmatrix} \sigma_d^s & -\sigma_h^s \\ \sigma_h^s & \sigma_d^s \end{bmatrix} = \underline{\underline{\tilde{\boldsymbol{\sigma}}}}^s \tag{4.56}$$

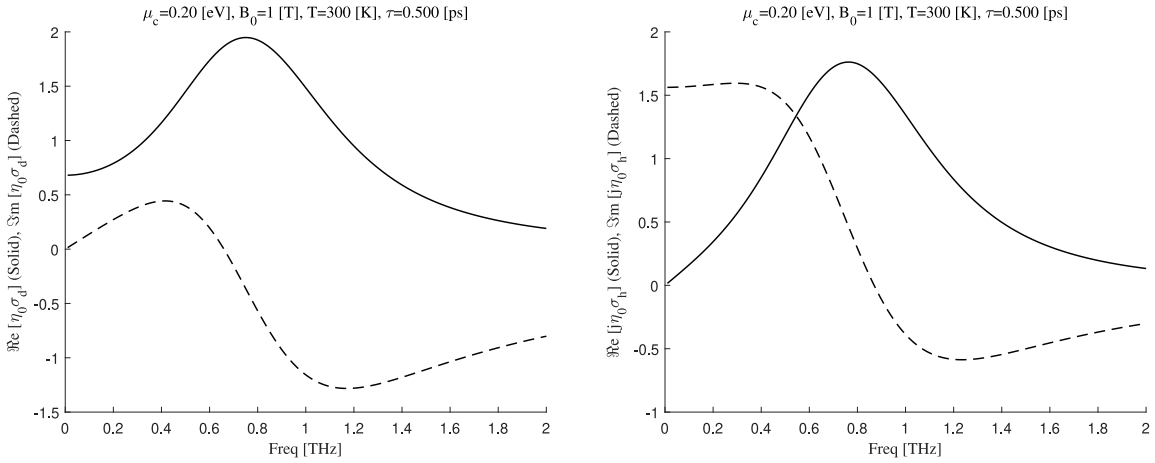

(a) (b)

Figure 4.4: Tensor surface conductivity components vs frequency. The graphene parameters are: $B_0 = 1$ [T], $\mu_c = 0.2$ [eV], $\tau = 0.5$ [ps], $v_F = 10^6$ [ms^{-1}] and $T = 300$ [K].

$$\begin{aligned} \sigma_d = j\frac{2\sigma_0}{\pi}L^2\varpi \sum_{n=0}^{\infty} \Bigg[& \frac{n_F(M_n) - n_F(M_{n+1}) - n_F(-M_n) + n_F(-M_{n+1})}{(M_{n+1} - M_n)\big[(M_{n+1} - M_n)^2 - \varpi^2\big]} \\ & + \frac{n_F(-M_n) - n_F(M_{n+1}) - n_F(M_n) + n_F(-M_{n+1})}{(M_{n+1} + M_n)\big[(M_{n+1} + M_n)^2 - \varpi^2\big]} \Bigg] \end{aligned} \tag{4.57}$$

$$\sigma_h = \mathrm{sgn}(B_0)\frac{2\sigma_0}{\pi}L^2\sum_{n=0}^{\infty}\Big[n_F(M_n) - n_F(M_{n+1}) + n_F(-M_n) - n_F(-M_{n+1})\Big] \times \left[\frac{1}{(M_{n+1}-M_n)^2 - \varpi^2} + \frac{1}{(M_{n+1}+M_n)^2 - \varpi^2}\right] \tag{4.58}$$

Where:

$$\begin{aligned} \varpi = (\omega - j2\Gamma)\hbar \quad &, \quad M_n = \sqrt{n}L \\ L = \sqrt{(2|eB_0|\hbar)}v_F \quad &, \quad n_F(E) = \frac{1}{1 + e^{(E-\mu_c)/(k_BT)}} \end{aligned} \tag{4.59}$$

In the above, $\sigma_0 = \dfrac{e^2}{4\hbar} \approx 6.085337 \times 10^{-5}$ [S], $\Gamma = \dfrac{1}{2\tau}$ is the phenomenological scattering rate ($\hbar\gamma_c$), M_n is the Landau level energy with index n, n_F is the Fermi-Dirac distribution.

4.1.3.1 Otto Configuration with Graphene

This configuration is an extension to the Otto configuration studied in Chapter 2. The effect of magnetic bias on this configuration was highlighted in [136]. The graphene parameters are: $B_0 = 1$ [T], $\mu_c = 0.5$ [eV], $\tau = 3$ [ps], $v_F = 10^6$ [ms^{-1}] and $T = 300$ [K]. The reflectivity components were computed using the methods above and compared using the T-matrix definitions found in [3] for validation. This comparison is illustrated in Figure 4.5.

Another comparison for various magnetic bias is demonstrated in Figure 4.6. It should be understood that in all these results, the incident angle φ_i was ignored since the tensor conductivity is invariant under rotation.

Table 4.1: Otto configuration with magnetically biased graphene details.

Layer	Thickness	ϵ
Prism	open	12
Air	5 [μm]	1
Graphene	-	-
Dielectric	open	4

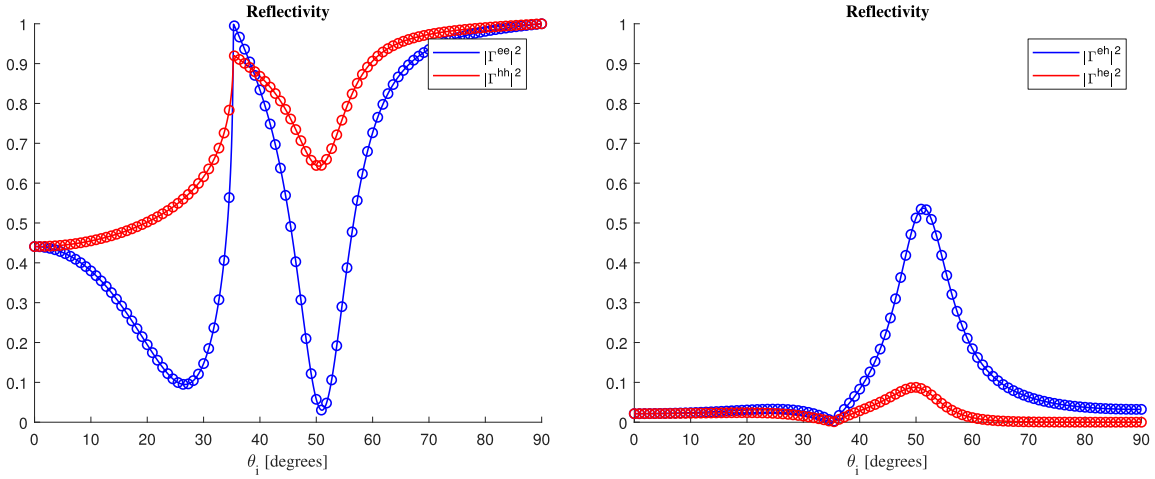

(a) (b)

Figure 4.5: Reflectivity for Otto configuration with graphene sheet at $f = 1$ [THz]. Results obtained using the expression in (4.27). Results obtained using the formulation given in [3] (Circles).

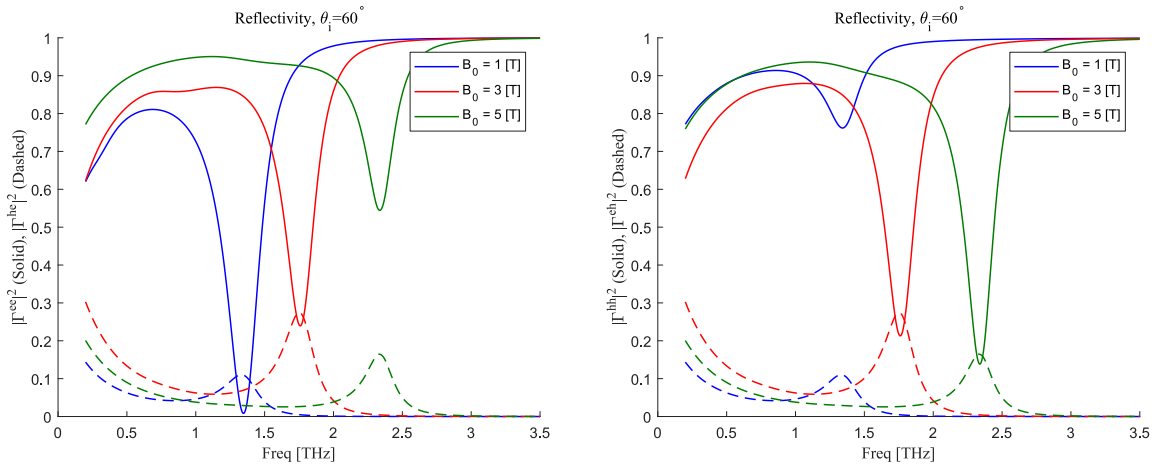

(a) (b)

Figure 4.6: Reflectivity vs frequency at angle $\theta_i = 60°$. Note that Γ^{eh} and Γ^{he} were multiplied and divided by a factor of 2 respectively for comparison with reference results.

4.2 Point Source Excitation

It is interesting to evaluate the fields due to point source in the presence of anisotropic conductive sheets. The spectral domain DGFs can be extended for this scenario as in (4.60)-(4.63) using the solution discussed above. These expressions were obtained by considering that both TLs are excited simultaneously.

$$\begin{aligned}\tilde{\underline{\underline{G}}}^{EJ} &= -V_{ie}^{e}\hat{\boldsymbol{u}}\hat{\boldsymbol{u}} - V_{ih}^{e}\hat{\boldsymbol{u}}\hat{\boldsymbol{v}} + \frac{\eta_0 k_\rho}{k_0\epsilon_z'}V_{ve}^{e}\hat{\boldsymbol{u}}\hat{\boldsymbol{z}} - V_{ie}^{h}\hat{\boldsymbol{v}}\hat{\boldsymbol{u}} - V_{ih}^{h}\hat{\boldsymbol{v}}\hat{\boldsymbol{v}} + \frac{\eta_0 k_\rho}{k_0\epsilon_z'}V_{ve}^{h}\hat{\boldsymbol{v}}\hat{\boldsymbol{z}} \\ &+ \frac{\eta_0 k_\rho}{k_0\epsilon_z}I_{ie}^{e}\hat{\boldsymbol{z}}\hat{\boldsymbol{u}} + \frac{\eta_0 k_\rho}{k_0\epsilon_z}I_{ih}^{e}\hat{\boldsymbol{z}}\hat{\boldsymbol{v}} - \frac{\eta_0^2 k_\rho^2}{k_0^2\epsilon_z\epsilon_z'}I_{ve}^{e}\hat{\boldsymbol{z}}\hat{\boldsymbol{z}} - \frac{\eta_0}{jk_0\epsilon_z'}\delta(z-z')\hat{\boldsymbol{z}}\hat{\boldsymbol{z}}\end{aligned} \tag{4.60}$$

$$\begin{aligned}\tilde{\underline{\underline{G}}}^{HJ} &= I_{ie}^{h}\hat{\boldsymbol{u}}\hat{\boldsymbol{u}} + I_{ih}^{h}\hat{\boldsymbol{u}}\hat{\boldsymbol{v}} - \frac{\eta_0 k_\rho}{k_0\epsilon_z'}I_{ve}^{h}\hat{\boldsymbol{u}}\hat{\boldsymbol{z}} - I_{ie}^{e}\hat{\boldsymbol{v}}\hat{\boldsymbol{u}} - I_{ih}^{e}\hat{\boldsymbol{v}}\hat{\boldsymbol{v}} + \frac{\eta_0 k_\rho}{k_0\epsilon_z'}I_{ve}^{e}\hat{\boldsymbol{v}}\hat{\boldsymbol{z}} \\ &- \frac{k_\rho}{\eta_0 k_0\mu_z}V_{ie}^{h}\hat{\boldsymbol{z}}\hat{\boldsymbol{u}} - \frac{k_\rho}{\eta_0 k_0\mu_z}V_{ih}^{h}\hat{\boldsymbol{z}}\hat{\boldsymbol{v}} + \frac{k_\rho^2}{k_0^2\mu_z\epsilon_z'}V_{ve}^{h}\hat{\boldsymbol{z}}\hat{\boldsymbol{z}}\end{aligned} \tag{4.61}$$

$$\begin{aligned}\tilde{\underline{\underline{G}}}^{EM} &= V_{vh}^{e}\hat{\boldsymbol{u}}\hat{\boldsymbol{u}} - V_{ve}^{e}\hat{\boldsymbol{u}}\hat{\boldsymbol{v}} - \frac{k_\rho}{\eta_0 k_0\mu_z'}V_{ih}^{e}\hat{\boldsymbol{u}}\hat{\boldsymbol{z}} + V_{vh}^{h}\hat{\boldsymbol{v}}\hat{\boldsymbol{u}} - V_{ve}^{h}\hat{\boldsymbol{v}}\hat{\boldsymbol{v}} - \frac{k_\rho}{\eta_0 k_0\mu_z'}V_{ih}^{h}\hat{\boldsymbol{v}}\hat{\boldsymbol{z}} \\ &- \frac{\eta_0 k_\rho}{k_0\epsilon_z}I_{vh}^{e}\hat{\boldsymbol{z}}\hat{\boldsymbol{u}} + \frac{\eta_0 k_\rho}{k_0\epsilon_z}I_{ve}^{e}\hat{\boldsymbol{z}}\hat{\boldsymbol{v}} + \frac{k_\rho^2}{k_0^2\mu_z'\epsilon_z}I_{ih}^{e}\hat{\boldsymbol{z}}\hat{\boldsymbol{z}}\end{aligned} \tag{4.62}$$

$$\begin{aligned}\tilde{\underline{\underline{G}}}^{HM} &= -I_{vh}^{h}\hat{\boldsymbol{u}}\hat{\boldsymbol{u}} + I_{ve}^{h}\hat{\boldsymbol{u}}\hat{\boldsymbol{v}} + \frac{k_\rho}{\eta_0 k_0\mu_z'}I_{ih}^{h}\hat{\boldsymbol{u}}\hat{\boldsymbol{z}} + I_{vh}^{e}\hat{\boldsymbol{v}}\hat{\boldsymbol{u}} - I_{ve}^{e}\hat{\boldsymbol{v}}\hat{\boldsymbol{v}} - \frac{k_\rho}{\eta_0 k_0\mu_z'}I_{ih}^{e}\hat{\boldsymbol{v}}\hat{\boldsymbol{z}} \\ &+ \frac{k_\rho}{\eta_0 k_0\mu_z}V_{vh}^{h}\hat{\boldsymbol{z}}\hat{\boldsymbol{u}} - \frac{k_\rho}{\eta_0 k_0\mu_z}V_{ve}^{h}\hat{\boldsymbol{z}}\hat{\boldsymbol{v}} - \frac{k_\rho^2}{\eta_0^2 k_0^2\mu_z\mu_z'}V_{ih}^{h}\hat{\boldsymbol{z}}\hat{\boldsymbol{z}} - \frac{\delta(z-z')}{j\eta_0 k_0\mu_z'}\hat{\boldsymbol{z}}\hat{\boldsymbol{z}}\end{aligned} \tag{4.63}$$

In general, the spatial domain DGFs should be computed using the 2D inverse FT given in (4.64). Unfortunately, this type of integrals can't be simplified using 1D SIs as for the isotropic conductive sheets case generally. Similar 2D integrals were approximated in

literature using techniques such as Spectral Domain Approximation (SDA) [141–145].

$$G_{\alpha\beta}^{PQ}(\boldsymbol{\rho}; z|z') = \frac{1}{(2\pi)^2}\int_0^{2\pi}\int_0^{\infty}\tilde{G}_{\alpha\beta}^{PQ}(k_\rho, \zeta; z|z')e^{-jk_\rho\rho\cos(\zeta-\varphi)}k_\rho dk_\rho d\zeta \tag{4.64}$$

However, our recommended method is to discretize the angular integral over ζ and then treat the radial integral over k_ρ as SIs. Note that in this case, $q = \dfrac{\pi}{\rho\cos(\zeta-\varphi)}$ (see appendix C). The integral in ζ can be performed using Romberg integration to accelerate the convergence [27]. This is shown more explicitly as in (4.65).

$$\begin{aligned} G_{\alpha\beta}^{PQ}(\boldsymbol{\rho}; z|z') &= \int_0^{2\pi} F_{\alpha\beta}^{PQ}(\zeta; z|z')d\zeta \\ F_{\alpha\beta}^{PQ}(\zeta; z|z') &= \frac{1}{(2\pi)^2}\int_0^{\infty}\tilde{G}_{\alpha\beta}^{PQ}(k_\rho, \zeta; z|z')e^{-jk_\rho\rho\cos(\zeta-\varphi)}k_\rho dk_\rho \end{aligned} \tag{4.65}$$

However, in the case of conductivity tensor invariant under rotation, the integrand function $\tilde{G}_{\alpha\beta}^{PQ}(k_\rho, \zeta; z|z')$ becomes independent from the spectral angle ζ, *i.e.*, $\tilde{G}_{\alpha\beta}^{PQ}(k_\rho; z|z')$, except for the simple vector relations in Table B.1. Note that when using the expression in (4.64), the Cartesian spectral DGFs take the forms in (B.7)-(B.15) with the spectral domain components from (4.60)-(4.63). Fortunately, the anisotropic graphene surface conductivity tensor obeys this invariance property and hence the spatial DGFs can be reduced into 1D SIs. These new spatial domain DGFs are listed in (4.66)-(4.101).

$$G_{xx}^{EJ}(\boldsymbol{\rho}; z|z') = -\frac{1}{2}S_0\{V_{ie}^e + V_{ih}^h\} + \frac{\cos(2\varphi)}{2}S_2\{V_{ie}^e - V_{ih}^h\} - \frac{\sin(2\varphi)}{2}S_2\{V_{ih}^e + V_{ie}^h\} \tag{4.66}$$

$$G_{xy}^{EJ}(\boldsymbol{\rho}; z|z') = -\frac{1}{2}S_0\{V_{ih}^e - V_{ie}^h\} + \frac{\cos(2\varphi)}{2}S_2\{V_{ih}^e + V_{ie}^h\} + \frac{\sin(2\varphi)}{2}S_2\{V_{ie}^e - V_{ih}^h\} \quad (4.67)$$

$$G_{yx}^{EJ}(\boldsymbol{\rho}; z|z') = \frac{1}{2}S_0\{V_{ih}^e - V_{ie}^h\} + \frac{\cos(2\varphi)}{2}S_2\{V_{ih}^e + V_{ie}^h\} + \frac{\sin(2\varphi)}{2}S_2\{V_{ie}^e - V_{ih}^h\} \quad (4.68)$$

$$G_{yy}^{EJ}(\boldsymbol{\rho}; z|z') = -\frac{1}{2}S_0\{V_{ie}^e + V_{ih}^h\} - \frac{\cos(2\varphi)}{2}S_2\{V_{ie}^e - V_{ih}^h\} + \frac{\sin(2\varphi)}{2}S_2\{V_{ih}^e + V_{ie}^h\} \quad (4.69)$$

$$G_{xz}^{EJ}(\boldsymbol{\rho}; z|z') = \frac{\eta_0}{jk_0\epsilon_z'}\cos(\varphi)S_1\{k_\rho V_{ve}^e\} - \frac{\eta_0}{jk_0\epsilon_z'}\sin(\varphi)S_1\{k_\rho V_{ve}^h\} \quad (4.70)$$

$$G_{yz}^{EJ}(\boldsymbol{\rho}; z|z') = \frac{\eta_0}{jk_0\epsilon_z'}\sin(\varphi)S_1\{k_\rho V_{ve}^e\} + \frac{\eta_0}{jk_0\epsilon_z'}\cos(\varphi)S_1\{k_\rho V_{ve}^h\} \quad (4.71)$$

$$G_{zx}^{EJ}(\boldsymbol{\rho}; z|z') = \frac{\eta_0}{jk_0\epsilon_z}\cos(\varphi)S_1\{k_\rho I_{ie}^e\} - \frac{\eta_0}{jk_0\epsilon_z}\sin(\varphi)S_1\{k_\rho I_{ih}^e\} \quad (4.72)$$

$$G_{zy}^{EJ}(\boldsymbol{\rho}; z|z') = \frac{\eta_0}{jk_0\epsilon_z}\sin(\varphi)S_1\{k_\rho I_{ie}^e\} + \frac{\eta_0}{jk_0\epsilon_z}\cos(\varphi)S_1\{k_\rho I_{ih}^e\} \quad (4.73)$$

$$G_{zz}^{EJ}(\boldsymbol{\rho}; z|z') = -\frac{\eta_0^2}{k_0^2\epsilon_z\epsilon_z'}S_0\{k_\rho^2 I_{ve}^e\} - \frac{\eta_0}{jk_0\epsilon_z}\delta(\rho)\delta(z - z') \quad (4.74)$$

$$G_{xx}^{HJ}(\boldsymbol{\rho};z|z') = \frac{1}{2}S_0\{I_{ie}^h - I_{ih}^e\} - \frac{\cos(2\varphi)}{2}S_2\{I_{ie}^h + I_{ih}^e\} + \frac{\sin(2\varphi)}{2}S_2\{I_{ih}^h - I_{ie}^e\} \quad (4.75)$$

$$G_{xy}^{HJ}(\boldsymbol{\rho};z|z') = \frac{1}{2}S_0\{I_{ih}^h + I_{ie}^e\} - \frac{\cos(2\varphi)}{2}S_2\{I_{ih}^h - I_{ie}^e\} - \frac{\sin(2\varphi)}{2}S_2\{I_{ie}^h + I_{ih}^e\} \quad (4.76)$$

$$G_{yx}^{HJ}(\boldsymbol{\rho};z|z') = -\frac{1}{2}S_0\{I_{ih}^h + I_{ie}^e\} - \frac{\cos(2\varphi)}{2}S_2\{I_{ih}^h - I_{ie}^e\} - \frac{\sin(2\varphi)}{2}S_2\{I_{ie}^h + I_{ih}^e\} \quad (4.77)$$

$$G_{yy}^{HJ}(\boldsymbol{\rho};z|z') = \frac{1}{2}S_0\{I_{ie}^h - I_{ih}^e\} + \frac{\cos(2\varphi)}{2}S_2\{I_{ie}^h + I_{ih}^e\} - \frac{\sin(2\varphi)}{2}S_2\{I_{ih}^h - I_{ie}^e\} \quad (4.78)$$

$$G_{xz}^{HJ}(\boldsymbol{\rho};z|z') = -\frac{\eta_0}{jk_0\epsilon_z'}\cos(\varphi)S_1\{k_\rho I_{ve}^h\} - \frac{\eta_0}{jk_0\epsilon_z'}\sin(\varphi)S_1\{k_\rho I_{ve}^e\} \quad (4.79)$$

$$G_{yz}^{HJ}(\boldsymbol{\rho};z|z') = -\frac{\eta_0}{jk_0\epsilon_z'}\sin(\varphi)S_1\{k_\rho I_{ve}^h\} + \frac{\eta_0}{jk_0\epsilon_z'}\cos(\varphi)S_1\{k_\rho I_{ve}^e\} \quad (4.80)$$

$$G_{zx}^{HJ}(\boldsymbol{\rho};z|z') = \frac{1}{j\eta_0 k_0\mu_z}\sin(\varphi)S_1\{k_\rho V_{ih}^h\} - \frac{1}{j\eta_0 k_0\mu_z}\cos(\varphi)S_1\{k_\rho V_{ie}^h\} \quad (4.81)$$

$$G_{zy}^{HJ}(\boldsymbol{\rho}; z|z') = -\frac{1}{j\eta_0 k_0 \mu_z}\cos(\varphi)S_1\{k_\rho V_{ih}^h\} - \frac{1}{j\eta_0 k_0 \mu_z}\sin(\varphi)S_1\{k_\rho V_{ie}^h\} \tag{4.82}$$

$$G_{zz}^{HJ}(\boldsymbol{\rho}; z|z') = \frac{1}{k_0^2 \mu_z \epsilon_z'} S_0\{k_\rho^2 V_{ve}^h\} \tag{4.83}$$

$$G_{xx}^{EM}(\boldsymbol{\rho}; z|z') = \frac{1}{2}S_0\{V_{vh}^e - V_{ve}^h\} - \frac{\cos(2\varphi)}{2}S_2\{V_{vh}^e + V_{ve}^h\} - \frac{\sin(2\varphi)}{2}S_2\{V_{ve}^e - V_{vh}^h\} \tag{4.84}$$

$$G_{xy}^{EM}(\boldsymbol{\rho}; z|z') = -\frac{1}{2}S_0\{V_{ve}^e + V_{vh}^h\} + \frac{\cos(2\varphi)}{2}S_2\{V_{ve}^e - V_{vh}^h\} - \frac{\sin(2\varphi)}{2}S_2\{V_{vh}^e + V_{ve}^h\} \tag{4.85}$$

$$G_{yx}^{EM}(\boldsymbol{\rho}; z|z') = \frac{1}{2}S_0\{V_{ve}^e + V_{vh}^h\} + \frac{\cos(2\varphi)}{2}S_2\{V_{ve}^e - V_{vh}^h\} - \frac{\sin(2\varphi)}{2}S_2\{V_{vh}^e + V_{ve}^h\} \tag{4.86}$$

$$G_{yy}^{EM}(\boldsymbol{\rho}; z|z') = \frac{1}{2}S_0\{V_{vh}^e - V_{ve}^h\} + \frac{\cos(2\varphi)}{2}S_2\{V_{vh}^e + V_{ve}^h\} + \frac{\sin(2\varphi)}{2}S_2\{V_{ve}^e - V_{vh}^h\} \tag{4.87}$$

$$G_{xz}^{EM}(\boldsymbol{\rho}; z|z') = \frac{1}{j\eta_0 k_0 \mu_z'}\sin(\varphi)S_1\{k_\rho V_{ih}^h\} - \frac{1}{j\eta_0 k_0 \mu_z'}\cos(\varphi)S_1\{k_\rho V_{ih}^e\} \tag{4.88}$$

$$G_{yz}^{EM}(\boldsymbol{\rho}; z|z') = -\frac{1}{j\eta_0 k_0 \mu_z'} \cos(\varphi) S_1\{k_\rho V_{ih}^h\} - \frac{1}{j\eta_0 k_0 \mu_z'} \sin(\varphi) S_1\{k_\rho V_{ih}^e\} \tag{4.89}$$

$$G_{zx}^{EM}(\boldsymbol{\rho}; z|z') = \frac{j\eta_0}{k_0 \epsilon_z} \sin(\varphi) S_1\{k_\rho I_{ve}^e\} + \frac{j\eta_0}{k_0 \epsilon_z} \cos(\varphi) S_1\{k_\rho I_{vh}^e\} \tag{4.90}$$

$$G_{zy}^{EM}(\boldsymbol{\rho}; z|z') = -\frac{j\eta_0}{k_0 \epsilon_z} \cos(\varphi) S_1\{k_\rho I_{ve}^e\} + \frac{j\eta_0}{k_0 \epsilon_z} \sin(\varphi) S_1\{k_\rho I_{vh}^e\} \tag{4.91}$$

$$G_{zz}^{EM}(\boldsymbol{\rho}; z|z') = \frac{1}{k_0^2 \mu_z' \epsilon_z} S_0\{k_\rho^2 I_{ih}^e\} \tag{4.92}$$

$$G_{xx}^{HM}(\boldsymbol{\rho}; z|z') = -\frac{1}{2} S_0\{I_{vh}^h + I_{ve}^e\} + \frac{\cos(2\varphi)}{2} S_2\{I_{vh}^h - I_{ve}^e\} + \frac{\sin(2\varphi)}{2} S_2\{I_{ve}^h + I_{vh}^e\} \tag{4.93}$$

$$G_{xy}^{HM}(\boldsymbol{\rho}; z|z') = \frac{1}{2} S_0\{I_{ve}^h - V_{vh}^e\} - \frac{\cos(2\varphi)}{2} S_2\{I_{ve}^h + I_{vh}^e\} + \frac{\sin(2\varphi)}{2} S_2\{I_{vh}^h - I_{ve}^e\} \tag{4.94}$$

$$G_{yx}^{HM}(\boldsymbol{\rho}; z|z') = -\frac{1}{2} S_0\{I_{ve}^h - I_{vh}^e\} - \frac{\cos(2\varphi)}{2} S_2\{I_{ve}^{he} + I_{vh}^e\} + \frac{\sin(2\varphi)}{2} S_2\{I_{vh}^h - I_{ve}^e\} \tag{4.95}$$

$$G_{yy}^{HM}(\boldsymbol{\rho}; z|z') = -\frac{1}{2}S_0\{I_{vh}^h + I_{ve}^e\} - \frac{\cos(2\varphi)}{2}S_2\{I_{vh}^h - I_{ve}^e\} - \frac{\sin(2\varphi)}{2}S_2\{I_{ve}^h + I_{vh}^e\} \quad (4.96)$$

$$G_{xz}^{HM}(\boldsymbol{\rho}; z|z') = \frac{1}{j\eta_0 k_0 \mu_z'}\cos(\varphi)S_1\{k_\rho I_{ih}^h\} + \frac{1}{j\eta_0 k_0 \mu_z'}\sin(\varphi)S_1\{k_\rho I_{ih}^e\} \quad (4.97)$$

$$G_{yz}^{HM}(\boldsymbol{\rho}; z|z') = \frac{1}{j\eta_0 k_0 \mu_z'}\sin(\varphi)S_1\{k_\rho I_{ih}^h\} - \frac{1}{j\eta_0 k_0 \mu_z'}\cos(\varphi)S_1\{k_\rho I_{ih}^e\} \quad (4.98)$$

$$G_{zx}^{HM}(\boldsymbol{\rho}; z|z') = \frac{1}{j\eta_0 k_0 \mu_z}\cos(\varphi)S_1\{k_\rho V_{vh}^h\} + \frac{1}{j\eta_0 k_0 \mu_z}\sin(\varphi)S_1\{k_\rho V_{ve}^h\} \quad (4.99)$$

$$G_{zy}^{HM}(\boldsymbol{\rho}; z|z') = \frac{1}{j\eta_0 k_0 \mu_z}\sin(\varphi)S_1\{k_\rho V_{vh}^h\} - \frac{1}{j\eta_0 k_0 \mu_z}\cos(\varphi)S_1\{k_\rho V_{ve}^h\} \quad (4.100)$$

$$G_{zz}^{HM}(\boldsymbol{\rho}; z|z') = -\frac{1}{\eta_0^2 k_0^2 \mu_z \mu_z'}S_0\{k_\rho^2 V_{ih}^h\} - \frac{1}{j\eta_0 k_0 \mu_z}\delta(\rho)\delta(z - z') \quad (4.101)$$

Also, it is possible to obtain alternative form for the transverse components as follows:

$$\begin{aligned} G_{xx}^{EJ}(\boldsymbol{\rho}; z|z') = &-\cos^2(\varphi)S_0\{V_{ie}^e\} - \sin^2(\varphi)S_0\{V_{ih}^h\} + \frac{\cos(2\varphi)}{\rho}S_1\{\frac{V_{ie}^e - V_{ih}^h}{k_\rho}\} \\ &+ \frac{\sin(2\varphi)}{2}S_0\{V_{ih}^e + V_{ie}^h\} - \frac{\sin(2\varphi)}{\rho}S_1\{\frac{V_{ih}^e + V_{ie}^h}{k_\rho}\} \end{aligned} \quad (4.102)$$

$$G_{xy}^{EJ}(\boldsymbol{\rho};z|z') = -\frac{\sin(2\varphi)}{2}S_0\{V_{ie}^e - V_{ih}^h\} + \frac{\sin(2\varphi)}{\rho}S_1\{\frac{V_{ie}^e - V_{ih}^h}{k_\rho}\} \\ - \cos^2(\varphi)S_0\{V_{ih}^e\} + \sin^2(\varphi)S_0\{V_{ie}^h\} + \frac{\cos(2\varphi)}{\rho}S_1\{\frac{V_{ih}^e + V_{ie}^h}{k_\rho}\} \tag{4.103}$$

$$G_{yx}^{EJ}(\boldsymbol{\rho};z|z') = -\frac{\sin(2\varphi)}{2}S_0\{V_{ie}^e - V_{ih}^h\} + \frac{\sin(2\varphi)}{\rho}S_1\{\frac{V_{ie}^e - V_{ih}^h}{k_\rho}\} \\ + \sin^2(\varphi)S_0\{V_{ih}^e\} - \cos^2(\varphi)S_0\{V_{ie}^h\} + \frac{\cos(2\varphi)}{\rho}S_1\{\frac{V_{ih}^e + V_{ie}^h}{k_\rho}\} \tag{4.104}$$

$$G_{yy}^{EJ}(\boldsymbol{\rho};z|z') = -\sin^2(\varphi)S_0\{V_{ie}^e\} - \cos^2(\varphi)S_0\{V_{ih}^h\} - \frac{\cos(2\varphi)}{\rho}S_1\{\frac{V_{ie}^e - V_{ih}^h}{k_\rho}\} \\ -\frac{\sin(2\varphi)}{2}S_0\{V_{ih}^e + V_{ie}^h\} + \frac{\sin(2\varphi)}{\rho}S_1\{\frac{V_{ie}^e + V_{ie}^h}{k_\rho}\} \tag{4.105}$$

$$G_{xx}^{HJ}(\boldsymbol{\rho};z|z') = -\frac{\sin(2\varphi)}{2}S_0\{I_{ih}^h - I_{ie}^e\} + \frac{\sin(2\varphi)}{\rho}S_1\{\frac{I_{ih}^h - I_{ie}^e}{k_\rho}\} \\ + \cos^2(\varphi)S_0\{I_{ie}^h\} - \sin^2(\varphi)S_0\{I_{ih}^e\} - \frac{\cos(2\varphi)}{\rho}S_1\{\frac{I_{ie}^h + I_{ih}^e}{k_\rho}\} \tag{4.106}$$

$$G_{xy}^{HJ}(\boldsymbol{\rho};z|z') = \cos^2(\varphi)S_0\{I_{ih}^h\} + \sin^2(\varphi)S_0\{I_{ie}^e\} - \frac{\cos(2\varphi)}{\rho}S_1\{\frac{I_{ih}^h - I_{ie}^e}{k_\rho}\} \\ + \frac{\sin(2\varphi)}{2}S_0\{I_{ie}^h + I_{ih}^e\} - \frac{\sin(2\varphi)}{\rho}S_1\{\frac{I_{ie}^h + I_{ih}^e}{k_\rho}\} \tag{4.107}$$

$$G_{yx}^{HJ}(\boldsymbol{\rho};z|z') = -\sin^2(\varphi)S_0\{I_{ih}^h\} - \cos^2(\varphi)S_0\{I_{ie}^e\} - \frac{\cos(2\varphi)}{\rho}S_1\{\frac{I_{ih}^h - I_{ie}^e}{k_\rho}\} + \frac{\sin(2\varphi)}{2}S_0\{I_{ie}^h + I_{ih}^e\} - \frac{\sin(2\varphi)}{\rho}S_1\{\frac{I_{ie}^h + I_{ih}^e}{k_\rho}\} \tag{4.108}$$

$$G_{yy}^{HJ}(\boldsymbol{\rho};z|z') = \frac{\sin(2\varphi)}{2}S_0\{I_{ih}^h - I_{ie}^e\} - \frac{\sin(2\varphi)}{\rho}S_1\{\frac{I_{ih}^h - I_{ie}^e}{k_\rho}\} + \sin^2(\varphi)S_0\{I_{ie}^h\} - \cos^2(\varphi)S_0\{I_{ih}^e\} + \frac{\cos(2\varphi)}{\rho}S_1\{\frac{I_{ie}^h + I_{ih}^e}{k_\rho}\} \tag{4.109}$$

$$G_{xx}^{EM}(\boldsymbol{\rho};z|z') = \frac{\sin(2\varphi)}{2}S_0\{V_{ve}^e - V_{vh}^h\} - \frac{\sin(2\varphi)}{\rho}S_1\{\frac{V_{ve}^e - V_{vh}^h}{k_\rho}\} + \cos^2(\varphi)S_0\{V_{vh}^e\} - \sin^2(\varphi)S_0\{V_{ve}^h\} - \frac{\cos(2\varphi)}{\rho}S_1\{\frac{V_{vh}^e + V_{ve}^h}{k_\rho}\} \tag{4.110}$$

$$G_{xy}^{EM}(\boldsymbol{\rho};z|z') = -\cos^2(\varphi)S_0\{V_{ve}^e\} - \sin^2(\varphi)S_0\{V_{vh}^h\} + \frac{\cos(2\varphi)}{\rho}S_1\{\frac{V_{ve}^e - V_{vh}^h}{k_\rho}\} + \frac{\sin(2\varphi)}{2}S_0\{V_{vh}^e + I_{ve}^h\} - \frac{\sin(2\varphi)}{\rho}S_1\{\frac{V_{vh}^e + V_{ve}^h}{k_\rho}\} \tag{4.111}$$

$$G_{yx}^{EM}(\boldsymbol{\rho};z|z') = \sin^2(\varphi)S_0\{V_{ve}^e\} + \cos^2(\varphi)S_0\{V_{vh}^h\} + \frac{\cos(2\varphi)}{\rho}S_1\{\frac{V_{ve}^e - V_{vh}^h}{k_\rho}\} + \frac{\sin(2\varphi)}{2}S_0\{V_{vh}^e + V_{ve}^h\} - \frac{\sin(2\varphi)}{\rho}S_1\{\frac{V_{vh}^e + V_{ve}^h}{k_\rho}\} \tag{4.112}$$

$$G_{yy}^{EM}(\boldsymbol{\rho};z|z') = -\frac{\sin(2\varphi)}{2}S_0\{V_{ve}^e - V_{vh}^h\} + \frac{\sin(2\varphi)}{\rho}S_1\{\frac{V_{ve}^e - V_{vh}^h}{k_\rho}\} \\ + \sin^2(\varphi)S_0\{V_{vh}^e\} - \cos^2(\varphi)S_0\{V_{ve}^h\} + \frac{\cos(2\varphi)}{\rho}S_1\{\frac{V_{vh}^e + V_{ve}^h}{k_\rho}\} \tag{4.113}$$

$$G_{xx}^{HM}(\boldsymbol{\rho};z|z') = -\cos^2(\varphi)S_0\{I_{vh}^h\} - \sin^2(\varphi)S_0\{I_{ve}^e\} + \frac{\cos(2\varphi)}{\rho}S_1\{\frac{I_{vh}^h - I_{ve}^e}{k_\rho}\} \\ - \frac{\sin(2\varphi)}{2}S_0\{I_{ve}^h + I_{vh}^e\} + \frac{\sin(2\varphi)}{\rho}S_1\{\frac{I_{ve}^h + I_{vh}^e}{k_\rho}\} \tag{4.114}$$

$$G_{xy}^{HM}(\boldsymbol{\rho};z|z') = \frac{\sin(2\varphi)}{2}S_0\{I_{vh}^h - I_{ve}^e\} - \frac{\sin(2\varphi)}{\rho}S_1\{\frac{I_{vh}^h - I_{ve}^e}{k_\rho}\} \\ + \cos^2(\varphi)S_0\{I_{ve}^h\} - \sin^2(\varphi)S_0\{I_{vh}^e\} - \frac{\cos(2\varphi)}{\rho}S_1\{\frac{I_{ve}^h + I_{vh}^e}{k_\rho}\} \tag{4.115}$$

$$G_{yx}^{HM}(\boldsymbol{\rho};z|z') = -\frac{\sin(2\varphi)}{2}S_0\{I_{vh}^h - I_{ve}^e\} + \frac{\sin(2\varphi)}{\rho}S_1\{\frac{I_{vh}^h - I_{ve}^e}{k_\rho}\} \\ - \sin^2(\varphi)S_0\{I_{ve}^h\} + \cos^2(\varphi)S_0\{I_{vh}^e\} - \frac{\cos(2\varphi)}{\rho}S_1\{\frac{I_{ve}^h + I_{vh}^e}{k_\rho}\} \tag{4.116}$$

$$G_{yy}^{HM}(\boldsymbol{\rho};z|z') = -\sin^2(\varphi)S_0\{I_{vh}^h\} - \cos^2(\varphi)S_0\{I_{ve}^e\} - \frac{\cos(2\varphi)}{\rho}S_1\{\frac{I_{vh}^h - I_{ve}^e}{k_\rho}\} \\ -\frac{\sin(2\varphi)}{2}S_0\{I_{ve}^h + I_{vh}^e\} - \frac{\sin(2\varphi)}{\rho}S_1\{\frac{I_{ve}^h + I_{vh}^e}{k_\rho}\} \tag{4.117}$$

Note that the above spatial domain DGFs reduce to the isotropic case when removing

the coupling between the TLs.

4.2.1 Numerical Examples

4.2.1.1 Half-Space with Graphene

In this example, we provide a validation for our implementation from the results in [27]. A half-space of free-space with a graphene ribbon is considered. Assuming the graphene sheet is placed at $z = 0$ [cm]. At frequency of $f = 10$ [GHz], we compute the DGFs from a $\boldsymbol{J}$ source located at $z' = 5$ [cm] along the graphene surface from the top layer $z = 0^+$ [cm]. The graphene parameters are: $\mu_c = 0.1$ [eV], $\tau = 3$ [ps], $v_F = 10^6$ [ms^{-1}], and $T = 300$ [K]. The surface conductivity vs the magneto-static bias is presented in Figure 4.7. The DGFs results are shown in Figure 4.8.

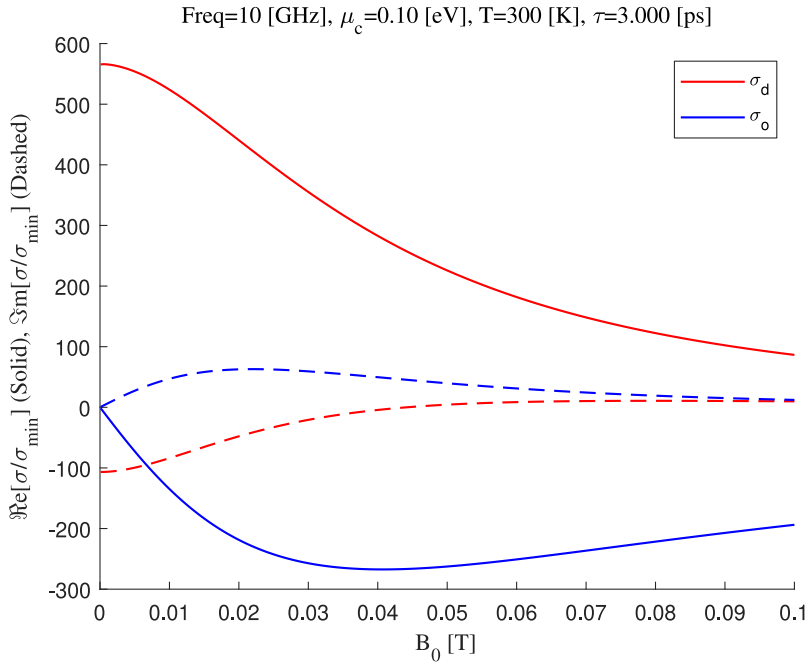

Figure 4.7: Graphene surface conductivity vs B_0, where $\sigma_{\text{min}} = \dfrac{e}{4\hbar}$. Notice that $\sigma_o = -\sigma_h$ for the sake of comparison with reference results.

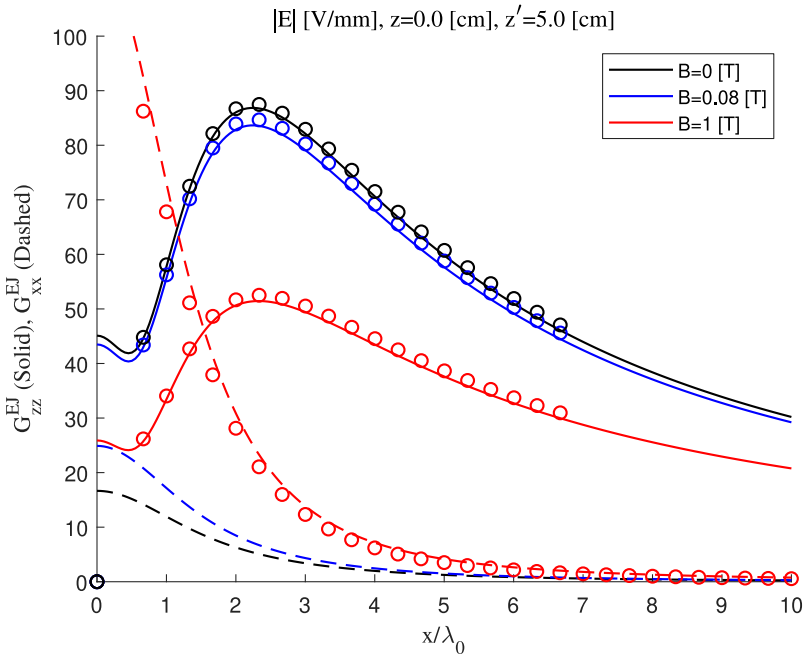

Figure 4.8: Electric fields DGFs for Hanson's half-space configuration for various magnetic bias values. Results were validated against Hanson's data samples (circles).

Another example is considered with different parameters. Here, the half-space media are free-space and dielectric $\epsilon = 4$ for top and bottom layers respectively. The frequency of operation is $f = 1$ [THz] and the electric point source $\boldsymbol{J}$ is place at $z' = 0.5$ [mm] above the surface, *i.e.*, in the free-space layer. The orientation of this $Il = 1$ [Am] electric dipole is defined by the angles $(30°, 60°)$. The observation is a vertical cut distant by $\rho = 4$ [mm] from the source point. The vertical cut is ranged between -10 [mm] and 10 [mm]. We have chosen two angles $\varphi = 35°$ and $125°$ for the observation cuts. The electric fields Cartesian components are illustrated in Figure 4.9.

4.2.1.2 Half-Space with Hyperbolic Graphene Metasurface

In this example, we consider a hyperbolic metasurface based on graohene ribbons surrounded by air. The complete model for evaluating this structure is given in (5.33) and (5.34). However, the values for the surface conductivity tensor were chosen according to

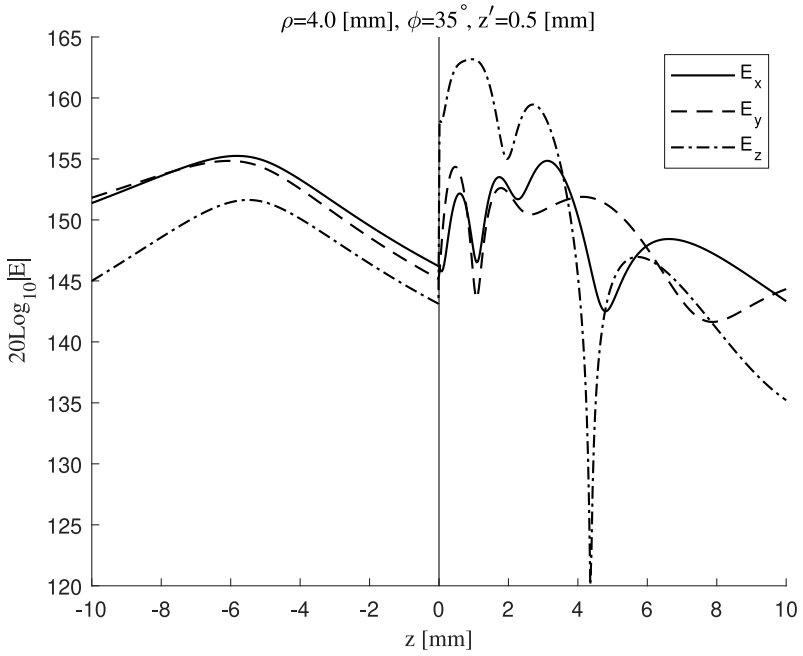

(a)

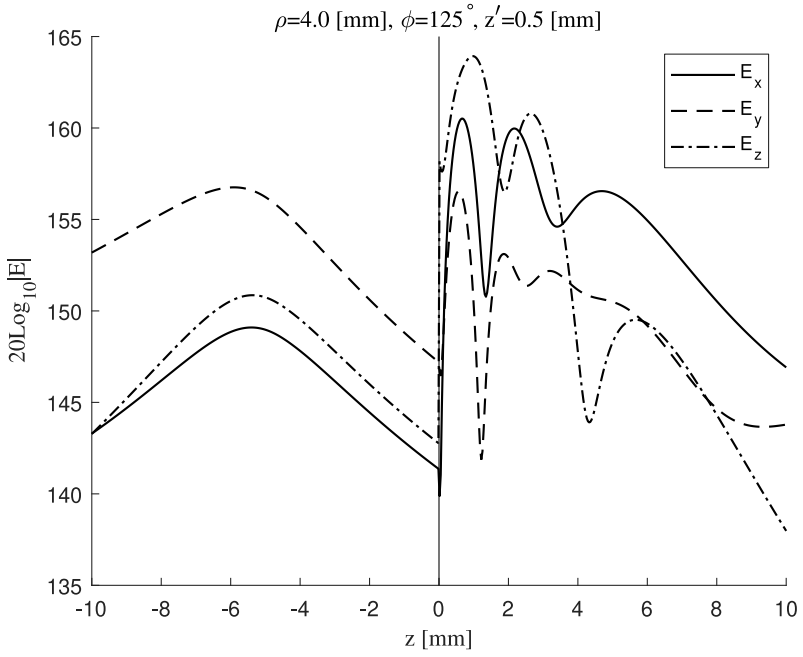

(b)

Figure 4.9: Electric fields in half-space due to $\boldsymbol{J}$ dipole above anisotropic graphene (a) $\varphi = 35°$. (b) $\varphi = 125°$. The graphene parameters are the same as Figure 4.4.

[146] for comparison. For $\mu_c = 0.33$ [eV]: $\sigma_{xx} = 0.02 + j0.57$ [mS] and $\sigma_{yy} = 0.02 - j0.57$ [mS]. For $\mu_c = 0.45$ [eV]: $\sigma^s_{xx} = 0.0103 + j0.4558$ [mS] and $\sigma^s_{yy} = 0.0353 - j0.7756$ [mS]. The frequency of operation is $f = 10$ [THz]. The results consider a Vertical Electric Dipole (VED) at $z' = \lambda_0/50$, while the observation is made at $z = \lambda_0/200$ and $\rho = \lambda_0/5$ against the azimuth angle φ. The DGF $|G^{EJ}_{zz}|$ results are shown in Figure 4.10 vs φ. Results were computed for the first quadrant and mirrored.

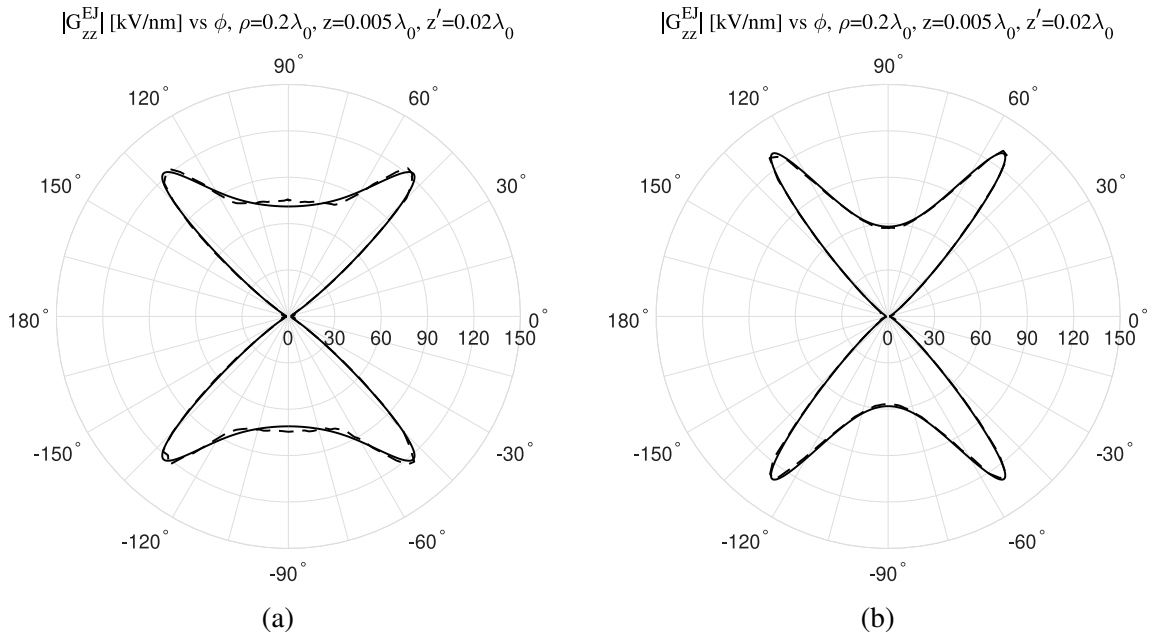

Figure 4.10: Electric fields vs φ due to VED above a hyperbolic metasurface. Solid lines are the results computed using (4.64) and dashed lines are result obtained using COMSOL. The parameters are: (a) $\mu_c = 0.33$ [eV] and (b) $\mu_c = 0.45$ [eV].

4.3 Plane Wave Excitation

In general, for spectral domain dyadic function $\underline{\underline{\tilde{\boldsymbol{f}}}}$, the field type $\boldsymbol{F}$ will take the following form in (4.118). Where $\boldsymbol{E}_0 = E^i_\theta \hat{\boldsymbol{\theta}}_i + E^i_\varphi \hat{\boldsymbol{\varphi}}_i$, using the definitions in Chapter 2.

$$\boldsymbol{F} = -2\boldsymbol{E}_0 \cdot \Bigg[\left(\tilde{f}_{uu}\hat{\boldsymbol{\varphi}}_i - \tilde{f}_{uv}\cos(\theta_i)\hat{\boldsymbol{\theta}}_i \right)\hat{\boldsymbol{\rho}}_i + \left(\tilde{f}_{vu}\hat{\boldsymbol{\varphi}}_i - \tilde{f}_{vv}\cos(\theta_i)\hat{\boldsymbol{\theta}}_i \right)\hat{\boldsymbol{\varphi}}_i + \left(\tilde{f}_{zu}\hat{\boldsymbol{\varphi}}_i - \tilde{f}_{zv}\cos(\theta_i)\hat{\boldsymbol{\theta}}_i \right)\hat{\boldsymbol{z}} \Bigg] \tag{4.118}$$

For incident field from the top layer and using the above definitions, one can obtain the fields as in (4.119) and (4.120). Note that for plane wave excitation $\zeta = \varphi_i$. This means that for ζ dependent anisotropic conductive sheets, the solution depends on the azimuth incident angle φ_i. However, this might not be present for ansiotropic graphene sheets due to the properties discussed previously in the tensor surface conductivity.

$$\boldsymbol{E} = -2\boldsymbol{E}_0 \cdot \Bigg[\left(V^e_{vh}\hat{\boldsymbol{\varphi}}_i + V^e_{ve}\cos(\theta_i)\hat{\boldsymbol{\theta}}_i \right)\hat{\boldsymbol{\rho}}_i + \left(V^h_{vh}\hat{\boldsymbol{\varphi}}_i + V^h_{ve}\cos(\theta_i)\hat{\boldsymbol{\theta}}_i \right)\hat{\boldsymbol{\varphi}}_i - \eta_1\frac{\epsilon_1}{\epsilon_z}\sin(\theta_i)\left(I^e_{vh}\hat{\boldsymbol{\varphi}}_i + I^e_{ve}\cos(\theta_i)\hat{\boldsymbol{\theta}}_i \right)\hat{\boldsymbol{z}} \Bigg] \tag{4.119}$$

$$\boldsymbol{H} = -2\boldsymbol{E}_0 \cdot \Bigg[-\left(I^h_{vh}\hat{\boldsymbol{\varphi}}_i + I^h_{ve}\cos(\theta_i)\hat{\boldsymbol{\theta}}_i \right)\hat{\boldsymbol{\rho}}_i + \left(I^e_{vh}\hat{\boldsymbol{\varphi}}_i + I^e_{ve}\cos(\theta_i)\hat{\boldsymbol{\theta}}_i \right)\hat{\boldsymbol{\varphi}}_i + \frac{1}{\eta_1}\frac{\mu_1}{\mu_z}\sin(\theta_i)\left(V^h_{vh}\hat{\boldsymbol{\varphi}}_i + V^h_{ve}\cos(\theta_i)\hat{\boldsymbol{\theta}}_i \right)\hat{\boldsymbol{z}} \Bigg] \tag{4.120}$$

4.3.1 Numerical Examples

For this scenario, we present the Otto configuration excited by both TM and TE incident plane waves using the formulations described here. The SPP mode is clear as shown in Figure 4.11.

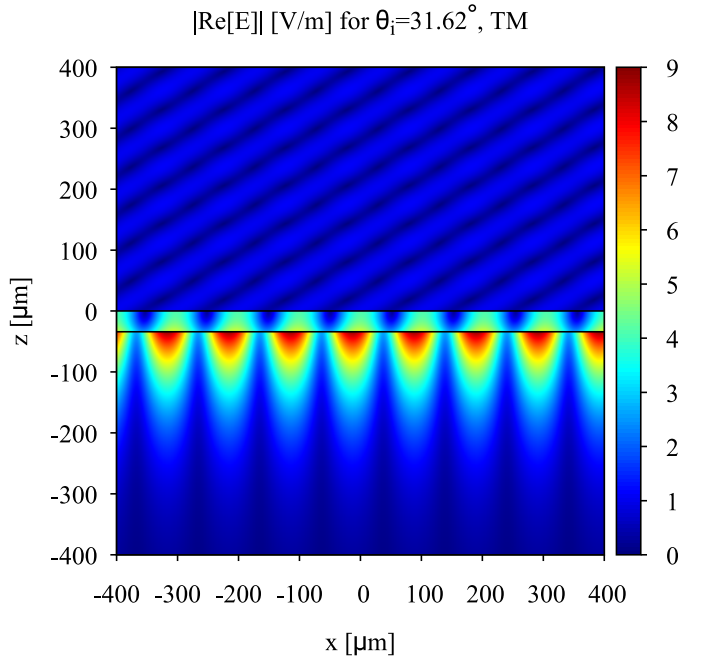

(a)

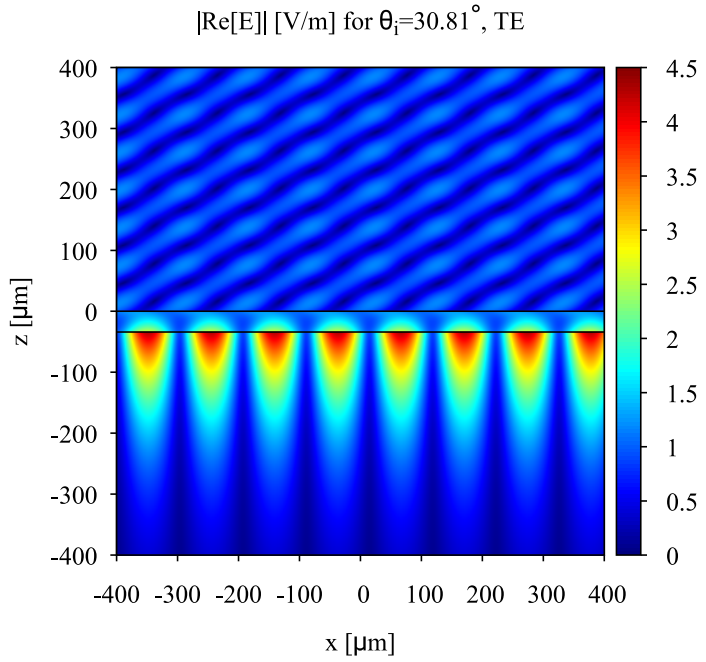

(b)

Figure 4.11: Plane wave excitation for SPP mode in the Otto configuration. The media parameters are listed in Table 4.2 and the frequency of operation is $f = 1$ [THz]. The graphene parameters are: $\tau = 0.5$ [ps], $v_F = 10^6$ [ms^{-1}] and $T = 300$ [K]. (a) $B_0 = 1.6$ [T] and $\mu_c = 0.8$ [eV] (b) $B_0 = 2.9$ [T] and $\mu_c = 0.34$ [eV].

Table 4.2: Otto configuration with graphene details.

Layer	Thickness [μm]	ϵ
Prism	open	8
Air	34	1
Graphene	-	-
Dielectric	open	2

4.4 Far Fields Computation

The far fields computations are very important as mentioned previously. Here, we will use the far fields to compare with the DGFs exact solution. This can be considered a dependent validation for our results. Following the same procedure for isotropic case and noticing the relations in Appendix B. This solution is given in (4.121)-(4.124). Also, we set $\zeta = \varphi$.

For $z > z_0$ which corresponds to $0 \leq \theta \leq \pi/2$

$$\boldsymbol{E} \sim -jk_1 \frac{e^{-jk_1 r}}{2\pi r} e^{jk_1 \cos(\theta) z_0} \Bigg[\Big(V_{ie}^e \hat{\boldsymbol{\theta}} + V_{ie}^h \cos(\theta) \hat{\boldsymbol{\varphi}} \Big) \hat{\boldsymbol{\rho}} + \Big(V_{ih}^e \hat{\boldsymbol{\theta}} + V_{ih}^h \cos(\theta) \hat{\boldsymbol{\varphi}} \Big) \hat{\boldsymbol{\varphi}} - \eta_1 \frac{\epsilon_1}{\epsilon_z'} \sin(\theta) \Big(V_{ve}^e \hat{\boldsymbol{\theta}} + V_{ve}^h \cos(\theta) \hat{\boldsymbol{\varphi}} \Big) \hat{\boldsymbol{z}} \Bigg] \cdot I \boldsymbol{l}_{k_J} e^{j \boldsymbol{k}_\rho \cdot \boldsymbol{\rho}_{k_J}} \tag{4.121}$$

$$\boldsymbol{E} \sim jk_1 \frac{e^{-jk_1 r}}{2\pi r} e^{jk_1 \cos(\theta) z_0} \Bigg[\Big(V_{vh}^e \hat{\boldsymbol{\theta}} + V_{vh}^h \cos(\theta) \hat{\boldsymbol{\varphi}} \Big) \hat{\boldsymbol{\rho}} - \Big(V_{ve}^e \hat{\boldsymbol{\theta}} + V_{ve}^h \cos(\theta) \hat{\boldsymbol{\varphi}} \Big) \hat{\boldsymbol{\varphi}} - \frac{1}{\eta_1} \frac{\mu_1}{\mu_z'} \sin(\theta) \Big(V_{ih}^e \hat{\boldsymbol{\theta}} + V_{ih}^h \cos(\theta) \hat{\boldsymbol{\varphi}} \Big) \hat{\boldsymbol{z}} \Bigg] \cdot K \boldsymbol{l}_{k_M} e^{j \boldsymbol{k}_\rho \cdot \boldsymbol{\rho}_{k_M}} \tag{4.122}$$

For $z < z_N$ which corresponds to $\pi/2 \leq \theta \leq \pi$

$$\boldsymbol{E} \sim -jk_N \frac{e^{-jk_N r}}{2\pi r} e^{jk_N \cos(\theta) z_N} \Bigg[\left(V_{ie}^e \hat{\boldsymbol{\theta}} + V_{ie}^h \cos(\theta) \hat{\boldsymbol{\varphi}} \right) \hat{\boldsymbol{\rho}} + \left(V_{ih}^e \hat{\boldsymbol{\theta}} + V_{ih}^h \cos(\theta) \hat{\boldsymbol{\varphi}} \right) \hat{\boldsymbol{\varphi}} - \eta_N \frac{\epsilon_N}{\epsilon_z'} \sin(\theta) \left(V_{ve}^e \hat{\boldsymbol{\theta}} + V_{ve}^h \cos(\theta) \hat{\boldsymbol{\varphi}} \right) \hat{\boldsymbol{z}} \Bigg] \cdot I \boldsymbol{l}_{k_J} e^{j \boldsymbol{k}_\rho \cdot \boldsymbol{\rho}_{k_J}} \tag{4.123}$$

$$\boldsymbol{E} \sim jk_N \frac{e^{-jk_N r}}{2\pi r} e^{jk_N \cos(\theta) z_N} \Bigg[\left(V_{vh}^e \hat{\boldsymbol{\theta}} + V_{vh}^h \cos(\theta) \hat{\boldsymbol{\varphi}} \right) \hat{\boldsymbol{\rho}} - \left(V_{ve}^e \hat{\boldsymbol{\theta}} + V_{ve}^h \cos(\theta) \hat{\boldsymbol{\varphi}} \right) \hat{\boldsymbol{\varphi}} - \frac{1}{\eta_N} \frac{\mu_N}{\mu_z'} \sin(\theta) \left(V_{ih}^e \hat{\boldsymbol{\theta}} + V_{ih}^h \cos(\theta) \hat{\boldsymbol{\varphi}} \right) \hat{\boldsymbol{z}} \Bigg] \cdot K \boldsymbol{l}_{k_M} e^{j \boldsymbol{k}_\rho \cdot \boldsymbol{\rho}_{k_M}} \tag{4.124}$$

4.4.1 Numerical Examples

In this example, the details of this configuration are described in Table 4.3 and illustrated in Figure 4.12. First, the far-fields were computed using (4.121)-(4.124). Then, the exact fields were computed using (4.66)-(4.101) at distance $r = 150\lambda_0$ from the sources vs θ at two fixed cuts $\varphi = 0^\circ$ and 90°. The results were computed by removing the r dependency and normalized by k_0. In Figure 4.13, the far fields due to excitation of electric and magnetic dipoles were compared with the exact DGFs respectively using SIs.

Table 4.3: 5-layers separated by magnetically biased graphene details. All materials are non-magnetic.

Layer	z_n [μm]	ϵ
0	open	-
1	75	1
2	50	4
3	-50	6
4	-75	2
5	open	1

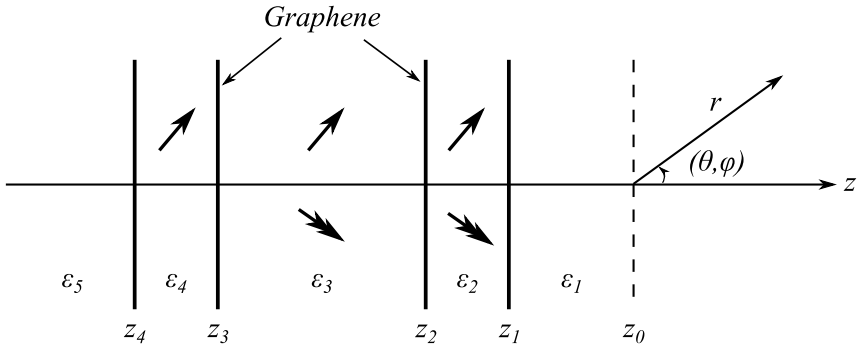

Figure 4.12: Illustration of the configuration in Table 4.3. The graphene parameters are the same as in Figure 4.4.

Table 4.4: Details of 5-layers separated by magnetically biased graphene. All materials are non-magnetic.

Layer	Type	Moment	x' [μm]	y' [μm]	z' [μm]	θ_0 [°]	φ_0 [°]
4	$\boldsymbol{J}$	1 [Am]	100	0	-60	60	30
3	$\boldsymbol{J}$	1 [Am]	50	150	30	45	45
3	$\boldsymbol{M}$	150 [Vm]	100	100	-30	45	45
2	$\boldsymbol{M}$	200 [Vm]	0	-100	60	45	-45
2	$\boldsymbol{J}$	1 [Am]	100	0	60	60	0

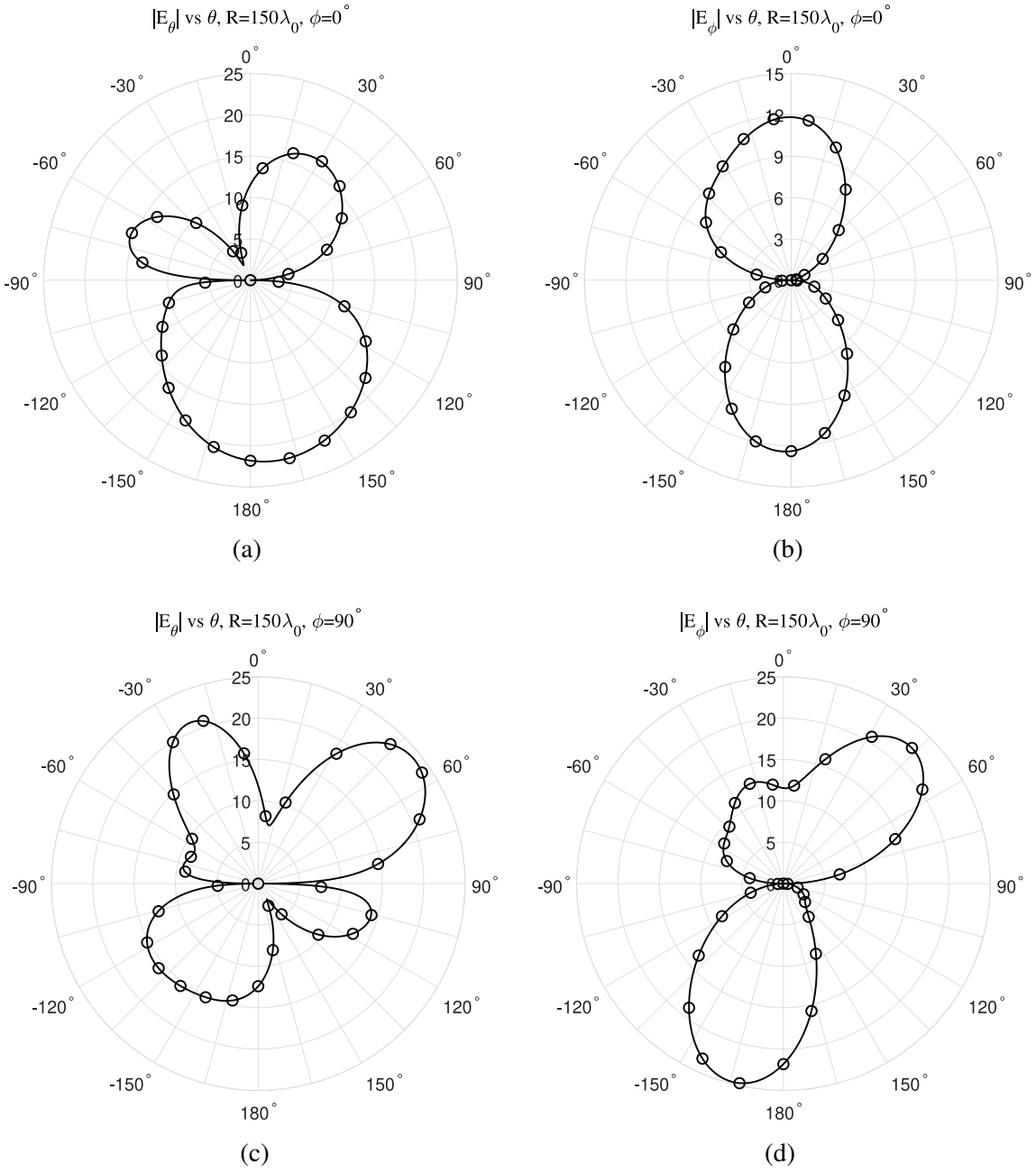

Figure 4.13: Far fields approximation (solid) vs exact SIs (circles) for the dipoles distribution in Table 4.4 at $f = 1$ [THz].

5. MODAL ANALYSIS FOR ANISOTROPIC CONDUCTIVE SHEETS

The modal analysis can be carried out by developing a DF similar to Chapter 3. In contrast to the isotropic conductive sheets case, here the TLs are coupled and so the modes. This means that the DF is one for all modes. Nevertheless, the DF and methods developed for the anisotropic sheets case are more general and can be easily downgraded to the simpler case discussed thoroughly for isotropic case. The CIM will be deployed in a similar fashion to what was presented previously. Another important thing to mention is the search in the complex domain. Here, DF is no longer a function of k_ρ only as in isotropic case. But, when anisotropic conductive sheets are introduced, the DF is a function of k_ρ and ζ. For this problem, we fix ζ and perform the same procedure for searching k_ρ eigenvalues (zeros) using the CIM in complex k_ρ complex domain. One should note that for anisotropic graphene surface conductivity tensor, DF is independent of ζ as a special case. This will be emphasized in the numerical examples for this sections.

5.1 Dispersion Function

Following a similar approach to the one illustrated in Chapter 4, considering the following source-free solutions:

$$\begin{aligned} \left[\boldsymbol{V}_n(z)\right] &= \left[\boldsymbol{P}_n^{+}(z)\right]\left[\boldsymbol{V}_n^{+}\right] + \left[\boldsymbol{P}_n^{-}(z)\right]\left[\boldsymbol{V}_n^{-}\right] \\ \left[\boldsymbol{I}_n(z)\right] &= \left[\boldsymbol{Y}_n\right]\left[\left[\boldsymbol{P}_n^{+}(z)\right]\left[\boldsymbol{V}_n^{+}\right] - \left[\boldsymbol{P}_n^{-}(z)\right]\left[\boldsymbol{V}_n^{-}\right]\right] \end{aligned} \tag{5.1}$$

Hence, it is possible to re-write these equations in the matrix form as:

$$\begin{bmatrix}[\boldsymbol{V}_n(z)]\\ [\boldsymbol{I}_n(z)]\end{bmatrix} = \begin{bmatrix}[\mathbf{1}] & [\mathbf{1}]\\ [\boldsymbol{Y}_n] & -[\boldsymbol{Y}_n]\end{bmatrix} \begin{bmatrix}[\boldsymbol{P}_n^{+}(z)] & [\mathbf{0}]\\ [\mathbf{0}] & [\boldsymbol{P}_n^{-}(z)]\end{bmatrix} \begin{bmatrix}[\boldsymbol{V}_n^{+}]\\ [\boldsymbol{V}_n^{-}]\end{bmatrix} \tag{5.2}$$

Using the boundary conditions at $z = z_{n-1}$, the T-matrix formulation becomes:

$$\begin{bmatrix}[\boldsymbol{V}_n^{+}]\\ [\boldsymbol{V}_n^{-}]\end{bmatrix} = \begin{bmatrix}[\boldsymbol{T}_{11,n}] & [\boldsymbol{T}_{12,n}]\\ [\boldsymbol{T}_{21,n}] & [\boldsymbol{T}_{22,n}]\end{bmatrix} \begin{bmatrix}[\boldsymbol{V}_{n-1}^{+}]\\ [\boldsymbol{V}_{n-1}^{-}]\end{bmatrix} \tag{5.3}$$

Where the matrix elements are given in (5.4).

$$\begin{aligned}
[\boldsymbol{T}_{11,n}] &= \frac{1}{2}[\boldsymbol{\Theta}_n^{-}]\left[[\mathbf{1}] + [\boldsymbol{Q}_n] + [\boldsymbol{Z}_n][\tilde{\boldsymbol{\sigma}}_{n-1}^{s}]\right]\\
[\boldsymbol{T}_{12,n}] &= \frac{1}{2}[\boldsymbol{\Theta}_n^{-}]\left[[\mathbf{1}] - [\boldsymbol{Q}_n] + [\boldsymbol{Z}_n][\tilde{\boldsymbol{\sigma}}_{n-1}^{s}]\right]\\
[\boldsymbol{T}_{21,n}] &= \frac{1}{2}[\boldsymbol{\Theta}_n^{+}]\left[[\mathbf{1}] - [\boldsymbol{Q}_n] - [\boldsymbol{Z}_n][\tilde{\boldsymbol{\sigma}}_{n-1}^{s}]\right]\\
[\boldsymbol{T}_{22,n}] &= \frac{1}{2}[\boldsymbol{\Theta}_n^{+}]\left[[\mathbf{1}] + [\boldsymbol{Q}_n] - [\boldsymbol{Z}_n][\tilde{\boldsymbol{\sigma}}_{n-1}^{s}]\right]
\end{aligned} \tag{5.4}$$

Where $[\boldsymbol{Q}_n] = [\boldsymbol{Z}_n][\boldsymbol{Y}_{n-1}]$. This can take the classical T-matrix form also as follows:

$$\begin{aligned}
[\boldsymbol{T}_{11,n}] &= \frac{1}{2}[\boldsymbol{\tau}_{n-1,n}]^{-1}[\boldsymbol{\Theta}_{\boldsymbol{n}}^{-}]\left[[\mathbf{1}] + [\boldsymbol{\Omega}_{n-1,n}][\tilde{\boldsymbol{\sigma}}_{n-1}^{s}]\right]\\
[\boldsymbol{T}_{12,n}] &= \frac{1}{2}[\boldsymbol{\tau}_{n-1,n}]^{-1}[\boldsymbol{\Theta}_n^{-}]\left[[\boldsymbol{\Gamma}_{n-1,n}] + [\boldsymbol{\Omega}_{n-1,n}][\tilde{\boldsymbol{\sigma}}_{n-1}^{s}]\right]\\
[\boldsymbol{T}_{21,n}] &= \frac{1}{2}[\boldsymbol{\tau}_{n-1,n}]^{-1}[\boldsymbol{\Theta}_n^{+}]\left[[\boldsymbol{\Gamma}_{n-1,n}] - [\boldsymbol{\Omega}_{n-1,n}][\tilde{\boldsymbol{\sigma}}_{n-1}^{s}]\right]\\
[\boldsymbol{T}_{22,n}] &= \frac{1}{2}[\boldsymbol{\tau}_{n-1,n}]^{-1}[\boldsymbol{\Theta}_n^{+}]\left[[\mathbf{1}] - [\boldsymbol{\Omega}_{n-1,n}][\tilde{\boldsymbol{\sigma}}_{n-1}^{s}]\right]
\end{aligned} \tag{5.5}$$

The overall T-matrix for the N-layers can be written as follows:

$$\begin{bmatrix} [\boldsymbol{V}_N^+] \\ [\boldsymbol{V}_N^-] \end{bmatrix} = \underbrace{[\boldsymbol{T}_N] \dots [\boldsymbol{T}_2]}_{[\boldsymbol{T}]} \begin{bmatrix} [\boldsymbol{V}_1^+] \\ [\boldsymbol{V}_1^-] \end{bmatrix} \tag{5.6}$$

In this case, we would like to apply the notations in (5.7) to identify the T-matrix elements. These notations will be used in this section to describe various DFs.

$$\begin{bmatrix} [\boldsymbol{V}_N^+] \\ [\boldsymbol{V}_N^-] \end{bmatrix} = \begin{bmatrix} [\boldsymbol{\alpha}] & [\boldsymbol{\gamma}] \\ [\boldsymbol{\delta}] & [\boldsymbol{\beta}] \end{bmatrix} \begin{bmatrix} [\boldsymbol{V}_1^+] \\ [\boldsymbol{V}_1^-] \end{bmatrix} \tag{5.7}$$

5.2 S-Matrix Formulation

As stated previously, the stable S-matrix formulation can be applied in order to compute the overall T-matrix [147]. Thus, it can be shown that:

$$[\boldsymbol{S}] = \begin{bmatrix} [\overrightarrow{\boldsymbol{\Gamma}}] & [\overleftarrow{\boldsymbol{\tau}}] \\ [\overrightarrow{\boldsymbol{\tau}}] & [\overleftarrow{\boldsymbol{\Gamma}}] \end{bmatrix} \tag{5.8}$$

Hence, the equivalent T-matrix elements might be computed using the numerically stable S-matrix elements with the TL solution described above.

$$\begin{bmatrix} [\boldsymbol{\alpha}] & [\boldsymbol{\gamma}] \\ [\boldsymbol{\delta}] & [\boldsymbol{\beta}] \end{bmatrix} = \begin{bmatrix} [\overrightarrow{\boldsymbol{\tau}}]^{-1} & -[\overrightarrow{\boldsymbol{\tau}}]^{-1}[\overleftarrow{\boldsymbol{\Gamma}}] \\ [\overrightarrow{\boldsymbol{\Gamma}}][\overrightarrow{\boldsymbol{\tau}}] & [\overleftarrow{\boldsymbol{\tau}}] - [\overrightarrow{\boldsymbol{\Gamma}}][\overrightarrow{\boldsymbol{\tau}}]^{-1}[\overleftarrow{\boldsymbol{\Gamma}}] \end{bmatrix} \tag{5.9}$$

In contrast to the isotropic case, each type of termination requires a special treatment to satisfy the boundary conditions associated with it. The following examples explain this process and covers the most common case.

5.2.1 Open/Open Structures

In this case, $\left[\boldsymbol{V}_N^+\right] = \left[\boldsymbol{V}_1^-\right] = \left[\boldsymbol{0}\right]$. This results in:

$$\begin{aligned} \left[\boldsymbol{0}\right] &= \left[\boldsymbol{\alpha}\right]\left[\boldsymbol{V}_1^+\right] \\ \left[\boldsymbol{V}_N^-\right] &= \left[\boldsymbol{\delta}\right]\left[\boldsymbol{V}_1^+\right] \end{aligned} \tag{5.10}$$

Hence, the proposed DF is given in (5.11).

$$Y_N^h Z_1^e \det\Big(\left[\boldsymbol{\alpha}\right]\Big) = 0 \tag{5.11}$$

An important example is the half-space. In this case, the explicit expression for the DF becomes:

$$\left[Z_1^e + Z_2^e + Z_1^e Z_2^e \tilde{\sigma}_{uu}^s\right]\left[Y_1^h + Y_2^h + \tilde{\sigma}_{vv}^s\right] - Z_1^e Z_2^e \tilde{\sigma}_{uv}^s \tilde{\sigma}_{vu}^s = 0 \tag{5.12}$$

This agrees with the expressions found in [27, 132]. However, we note that for the half-space scenario if $k_1 = k_2 = k$, one should use the expressions in (5.13) to avoid a spurious zero at $k_\rho = k$.

$$\left[2 + Z^e \tilde{\sigma}_{uu}^s\right]\left[2Y^h + \tilde{\sigma}_{vv}^s\right] - Z^e \tilde{\sigma}_{uv}^s \tilde{\sigma}_{vu}^s = 0 \tag{5.13}$$

Note that from (5.10) the solutions for $\left[\boldsymbol{V}_1^+\right]$ are defined once k_ρ value has been defined since $\left[\boldsymbol{\alpha}\right]$ is defined. Thus, by choosing suitable value for either V_1^{e+} or V_1^{h+} allows computing the corresponding modal field profile from (5.1). The solution for $\left[\boldsymbol{V}_1^+\right]$ is simply the null-space $N\Big(\left[\boldsymbol{\alpha}\right]\Big)$ [148, p. 94].

$$\left[\boldsymbol{\alpha}\right]\left[\boldsymbol{V}_1^+\right] = \left[\boldsymbol{0}\right] \tag{5.14}$$

In the case of free-space surrounding an anisotropic conductive sheet, it is possible to derive the following dispersion relation from (5.13).

$$\begin{aligned} k_0 k_z \Big[4+\eta_0^2\big(\sigma_{xx}^s\sigma_{yy}^s - \sigma_{xy}^s\sigma_{yx}^s\big)\Big] + 2\eta_0 k_0^2\big(\sigma_{xx}^s + \sigma_{yy}^s\big) \\ - 2\eta_0\Big[k_x^2\sigma_{xx}^s + k_y^2\sigma_{yy}^s + k_x k_y\big(\sigma_{xy}^s + \sigma_{yx}^s\big)\Big] = 0 \end{aligned} \tag{5.15}$$

We demonstrate this expression since it has appeared in the literature for comparison [24, 132, 149]. The disadvantage of the DF in (5.15) is that it is based on k_x and k_y, which over complicates the search in the complex domain in contrast to k_ρ and ζ domain. However, it is possible to specialize this DF for anisotropic graphene tensor conductivity $\underline{\underline{\boldsymbol{\sigma}}}^s = \sigma_d(\hat{\boldsymbol{x}}\hat{\boldsymbol{x}} + \hat{\boldsymbol{y}}\hat{\boldsymbol{y}}) - \sigma_h(\hat{\boldsymbol{x}}\hat{\boldsymbol{y}} - \hat{\boldsymbol{y}}\hat{\boldsymbol{x}})$ as in (5.16).

$$Ak_\rho^4 + Bk_0^2k_\rho^2 - Bk_0^4 = 0 \tag{5.16}$$

Where,

$$\begin{aligned} A &= 4\eta_0^2\sigma_d^2 \\ B &= \Big[4 + \eta_0^2\big(\sigma_d^2 + \sigma_h^2\big)\Big]^2 - 4A \end{aligned} \tag{5.17}$$

Hence, the k_ρ solutions are:

$$k_\rho = k_0\sqrt{\frac{-B \pm \sqrt{B^2 + 4AB}}{2A}} \tag{5.18}$$

In (5.18), the square roots are defined to reflect k_ρ on the required Riemann sheet.[1] Another special case is the hyperbolic metasurface with surface conductivity tensor of

[1]Modern computer languages default is $\mathrm{Re}[\sqrt{z}] \geq 0$.

$\underline{\underline{\boldsymbol{\sigma}}}^s = \sigma^s_{xx}\hat{\boldsymbol{x}}\hat{\boldsymbol{x}} + \sigma^s_{yy}\hat{\boldsymbol{y}}\hat{\boldsymbol{y}}$. In this case, the DF is a function of k_ρ and ζ as in (5.19).

$$Ak_\rho^4 + Bk_0^2k_\rho^2 + Ck_0^4 = 0 \tag{5.19}$$

Where,

$$\begin{aligned} A &= 4\eta_0^2 b^2 \\ B &= a^2 - 8\eta_0^2 bc \\ C &= 4\eta_0^2 c^2 - a^2 \\ a &= 4 + \eta_0^2 \sigma^s_{xx}\sigma^s_{yy} \\ b &= \sigma^s_{xx}\cos^2(\zeta) + \sigma^s_{yy}\sin^2(\zeta) \\ c &= \sigma^s_{xx} + \sigma^s_{yy} \end{aligned} \tag{5.20}$$

Hence, for fixed ζ, the k_ρ solutions are:

$$k_\rho = k_0\sqrt{\frac{-B \pm \sqrt{B^2 - 4AC}}{2A}} \tag{5.21}$$

5.2.2 Open/PEC Structures

In this case, $\left[\boldsymbol{V}_N^+\right] = -\left[\boldsymbol{V}_N^-\right]$. Also, $\left[\boldsymbol{V}_1^-\right] = \left[\boldsymbol{0}\right]$. This results in:

$$\begin{aligned} \left[\boldsymbol{V}_N^+\right] &= \left[\boldsymbol{\alpha}\right]\left[\boldsymbol{V}_1^+\right] \\ -\left[\boldsymbol{V}_N^+\right] &= \left[\boldsymbol{\delta}\right]\left[\boldsymbol{V}_1^+\right] \end{aligned} \tag{5.22}$$

Hence, the proposed DF is given in (5.23).

$$Y_N^h Z_1^e \det\Big(\big[\boldsymbol{\alpha}\big] + \big[\boldsymbol{\delta}\big]\Big) = 0 \tag{5.23}$$

Similarly, one can compute $\big[\boldsymbol{V}_1^+\big]$ as the null-space of $N\Big(\big[\boldsymbol{\alpha}\big] + \big[\boldsymbol{\delta}\big]\Big)$:

$$\Big(\big[\boldsymbol{\alpha}\big] + \big[\boldsymbol{\delta}\big]\Big)\big[\boldsymbol{V}_1^+\big] = \big[\boldsymbol{0}\big] \tag{5.24}$$

An important example is the half-space. In this case, the DF becomes:

$$\begin{aligned}&\big[Z_1^e \cos(\Theta_2^e) + jZ_2^e(1 + Z_1^e\tilde{\sigma}_{uu}^s)\sin(\Theta_2^e)\big]\big[Y_2^h \cos(\Theta_2^h) + j(Y_1^h + \sigma_{vv}^s)\sin(\Theta_2^h)\big] \\ &+ Z_1^e Z_2^e \tilde{\sigma}_{uv}^s \tilde{\sigma}_{vu}^s \sin(\Theta_2^e)\sin(\Theta_2^h) = 0\end{aligned} \tag{5.25}$$

5.2.3 Open/PMC Structures

In this case, $\big[\boldsymbol{V}_N^+\big] = \big[\boldsymbol{V}_N^-\big]$. Also, $\big[\boldsymbol{V}_1^-\big] = \big[\boldsymbol{0}\big]$. The results in:

$$\begin{aligned}\big[\boldsymbol{V}_N^+\big] &= \big[\boldsymbol{\alpha}\big]\big[\boldsymbol{V}_1^+\big] \\ \big[\boldsymbol{V}_N^+\big] &= \big[\boldsymbol{\delta}\big]\big[\boldsymbol{V}_1^+\big]\end{aligned} \tag{5.26}$$

Hence, the proposed DF is given in (5.27).

$$Y_N^h Z_1^e \det\Big(\big[\boldsymbol{\alpha}\big] - \big[\boldsymbol{\delta}\big]\Big) = 0 \tag{5.27}$$

Similarly, one can compute $\big[\boldsymbol{V}_1^+\big]$ as the null-space of $N\Big(\big[\boldsymbol{\alpha}\big] - \big[\boldsymbol{\delta}\big]\Big)$:

$$\Big(\big[\boldsymbol{\alpha}\big] - \big[\boldsymbol{\delta}\big]\Big)\big[\boldsymbol{V}_1^+\big] = \big[\boldsymbol{0}\big] \tag{5.28}$$

An important example is the half-space. In this case, the DF becomes:

$$\begin{aligned}&\left[jZ_1^e\sin(\Theta_2^e)+Z_2^e(1+Z_1^e\tilde{\sigma}_{uu}^s)\cos(\Theta_2^e)\right]\left[jY_2^h\sin(\Theta_2^h)+(Y_1^h+\tilde{\sigma}_{vv}^s)\cos(\Theta_2^h)\right]\\&-Z_1^eZ_2^e\tilde{\sigma}_{uv}^s\tilde{\sigma}_{vu}^s\cos(\Theta_2^e)\cos(\Theta_2^h)=0\end{aligned}\tag{5.29}$$

5.3 Modal Fields Profile

The field distribution can be computed using the solution above down-looking and up-looking. Here, the following procedure is recommended for its simplicity, but without excluding the other approaches. In layer 1, only leaving waves are allowed. From these relations, one can evidently find $\left[\boldsymbol{V}_1^+\right]$ while $\left[\boldsymbol{V}_1^+\right]=\left[\boldsymbol{0}\right]$. Note that, in practical implementation it is not possible to numerically compute the null space because the corresponding k_ρ eigenvalues won't lead to exactly 0 determinant. For example, consider the open/open structure where $\det\left(\left[\boldsymbol{\alpha}\right]\right)=0$. Hence, it is possible to assign a non-zero value for V_1^{e+} and then $V_1^{h+}=-\dfrac{\alpha_{11}}{\alpha_{12}}V_1^{e+}$ is assigned. After computing the fields profile, one can normalize the total field with a suitable choice. Thus, the solutions in layer 1 are given in (5.30).

$$\begin{aligned}\left[\boldsymbol{V_1}(z)\right]&=\left[\boldsymbol{P_1^+}(z)\right]\left[\boldsymbol{V_1^+}\right]\\\left[\boldsymbol{I_1}(z)\right]&=\left[\boldsymbol{Y_1}\right]\left[\boldsymbol{P_1^+}(z)\right]\left[\boldsymbol{V_1^+}\right]\end{aligned}\tag{5.30}$$

For the layers below layer 1 ($n>1$), the down-looking solutions are applied. By enforcing the boundary condition in (4.11) at the interface $z=z_1$, the value of $\left[\boldsymbol{V}_2^-\right]$ is given as in (5.31) and (5.32). Where $\left[\overleftarrow{\boldsymbol{D}}_2\right]=\left[\boldsymbol{\Theta}_2^+\right]\left[\overleftarrow{\boldsymbol{\Gamma}}_2\right]\left[\boldsymbol{\Theta}_2^+\right]$ for clarity. As discussed in Chapter 3, the voltages and currents solutions are separate.

For voltages:

$$\left[\boldsymbol{V}_2^-\right] = \left[\left[\boldsymbol{1}\right] + \left[\overleftarrow{\boldsymbol{D}}_2\right]\right]^{-1}\left[\boldsymbol{V}_1^+\right] \tag{5.31}$$

For currents:

$$\left[\boldsymbol{V}_2^-\right] = -\left[\left[\boldsymbol{1}\right] - \left[\overleftarrow{\boldsymbol{D}}_2\right]\right]^{-1}\left[\left[\boldsymbol{Z}_2\right]\left(\left[\boldsymbol{Y}_1\right] + \left[\tilde{\boldsymbol{\sigma}}_1^s\right]\right)\right]\left[\boldsymbol{V}_1^+\right] \tag{5.32}$$

Given the value of $\left[\boldsymbol{V}_2^-\right]$, the down-looking solution can be used as described earlier for the remaining layers $n > 1$.

5.4 Numerical Examples

5.4.1 Parallel Plate Waveguide (PPWG)

The configuration illustrated in Figure 5.1 [74, 150] is to be studied for modal analysis using the methods developed in this chapter. The CIM will be applied to new DFs developed here. In this example, the graphene parameters were taken from Figure 4.4.

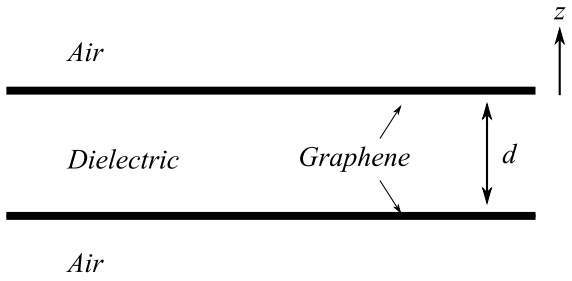

Figure 5.1: A PPWG filled with a dielectric. In this example SiO_2 has been chosen where the spacing is $d = 100$ [nm]. The external magnetic field bias is applied in the z direction in addition to the external electric field bias indicated by μ_c.

The modes found at $f = 1$ [THz] are presented in Table 5.1. Note that all modes are coupled TM and TE. Also, regardless of the symmetry in this structure, using PEC and PMC bisections in order to detect even and odd modes, respectively, is not applicable.

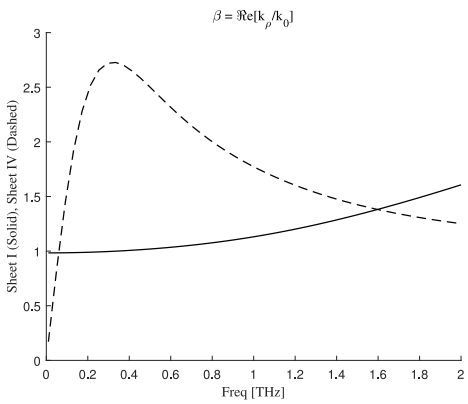

(a)

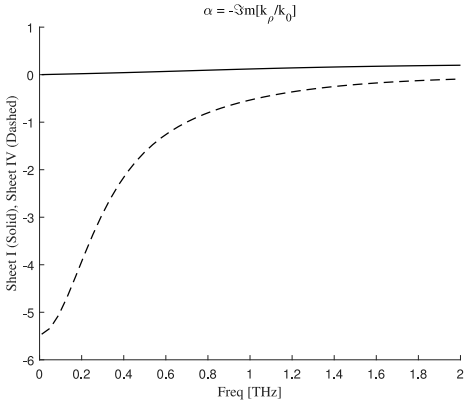

(b)

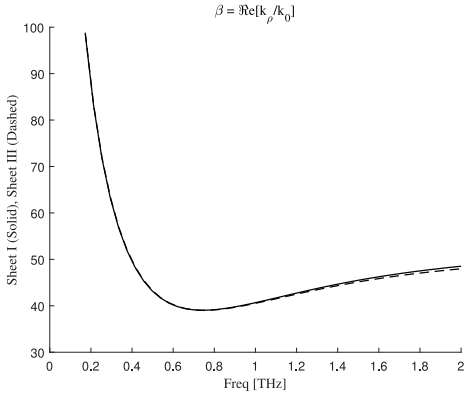

(c)

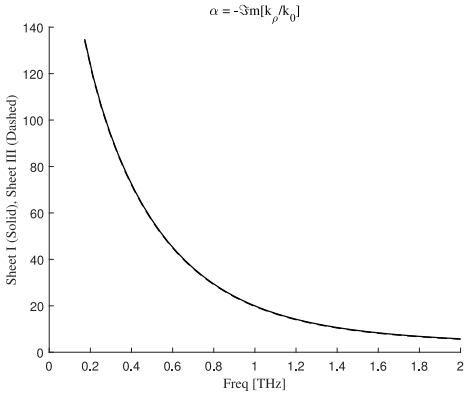

(d)

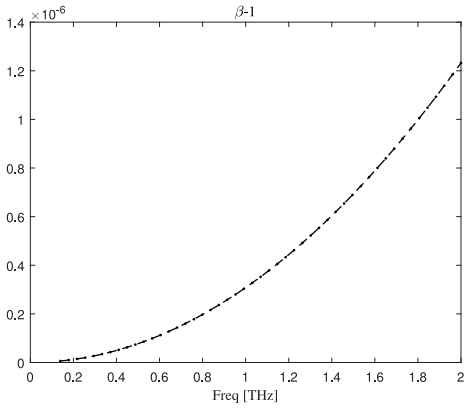

(e)

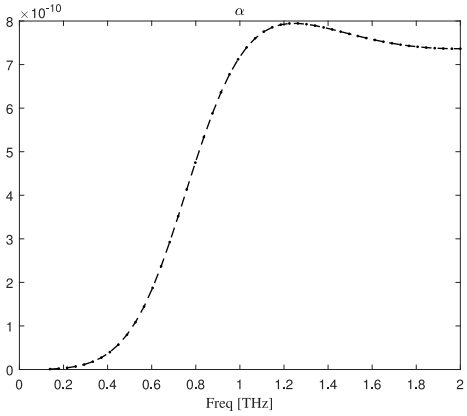

(f)

Figure 5.2: k_ρ eigenvalues vs frequency for modes in the PPWG configuration with $\epsilon = 4$. (a) and (b) Proper and improper slow waves. (c) and (d) Lossy proper and leaky waves are almost identical. (e) and (f) Proper mode very close to free-space wavenumber.

This is observed by the two modes in Table 5.1, since improper modes on sheets II and III only leak into substrate or cladding layers but not both at the same time. The third proper mode is very close to the free-space wavenumber which demonstrates the reliability of CIM.[2]

Table 5.1: k_ρ values for PPWG in Figure 5.1 for $\epsilon = 3.9$.

Mode	Sheet	Symmetry	k_ρ/k_0
1	I	PEC	$40.16214062233 - j19.69890451728$
2	I	PMC	$1.131049672685 - j0.119504968174$
3	I	PEC	$1.000000303047 - j0.000000000700$
4	II,III	N/A	$40.02117391407 - j19.49162447793$
5	II,III	N/A	$1.000274565367 - j0.000098059060$
6	IV	PEC	$39.83786798739 - j19.27844230550$
7	IV	PMC	$1.772139187042 + j0.534064618718$

5.4.2 Otto Configuration with Graphene

Here, we simply present the modes associated with the configuration from Chapter 4 in Table 4.2. The slow waves associated wit the SPP mode are listed in Table 5.2 and the modal field distributions are illustrated in Figure 5.3.

Table 5.2: k_ρ values for Otto configuration SPP modes with graphene biasing (a) and (b) from Figure 4.11.

Sheet	Parameters	k_ρ/k_0
I	(a)	$1.4824055875891 - j0.0000362410786$
II	(a)	$1.4801298442195 - j0.0174223787339$
I	(b)	$1.4512217625886 - j0.0002372631349$
II	(b)	$1.4331753377130 - j0.0535973672169$

[2]For computations near branch point, double loop integrals through the four Riemanns sheets were applied rather than point-wise product.

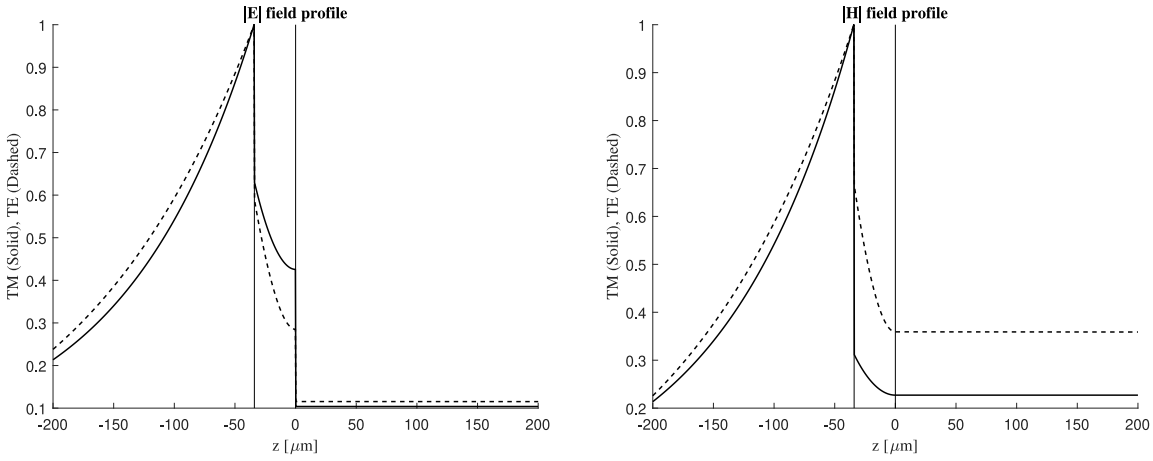

(a) (b)

Figure 5.3: Modal field distributions for proper modes from Table 5.2. The TM and TE modal fields are results that correspond to parameters sets (a) and (b), respectively, from Figure 4.11. TM (TE) mode means that SPP mode can be excited by incident TM (TE) plane wave as discussed in Chapter 4.

5.4.3 6-Layers with Graphene

In this example we analyze the 6-layers configuration shown in Figure 5.4 [151]. Here, we are not interested in the functionality of this configuration, but rather we want to use it for demonstrating our modal analysis method. The configuration consists of five graphene sheets in air with equal spacings. The graphene parameters are the same as in the previous example. A list of modes on sheet I where $\beta > 1$ is given in Table 5.3. In Figure 5.5, the modal fields distributions are presented for mode 2 from Table 5.3. Notice that in this mode, the current in the middle sheet is zeros since the mode is odd. Such a modal distribution is prone to numerical stability issues which our formulation doesn't suffer from.

In addition to the previous results, we present the modes migration curves vs frequency in Figure 5.6. Also, some modal fields distributions for higher modes are illustrated in Figure 5.7 and 5.8.

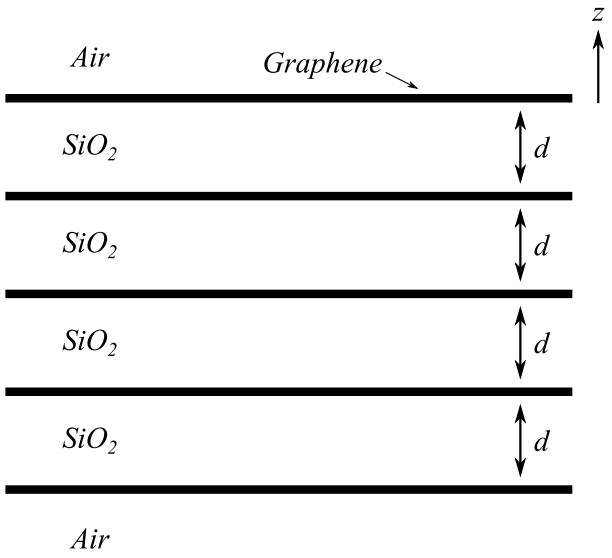

Figure 5.4: Configuration of five graphene sheets in SiO_2 and separated equally by $d = 25$ [μm].

Table 5.3: k_ρ values for the 6-layers configuration in Figure 5.4 on sheet I.

Mode	k_ρ/k_0
1	$1.063104622058 - j11.09915363510$
2	$1.123738389711 - j0.082692335335$
3	$1.729012984730 - j0.458318070691$
4	$1.982696873515 - j4.765645228475$
5	$2.188960952399 - j0.656805485873$
6	$2.768029748582 - j4.872998511452$
7	$2.847667872106 - j1.380227152956$
8	$3.492139379646 - j1.860936644723$
9	$3.975620626139 - j2.075321163496$

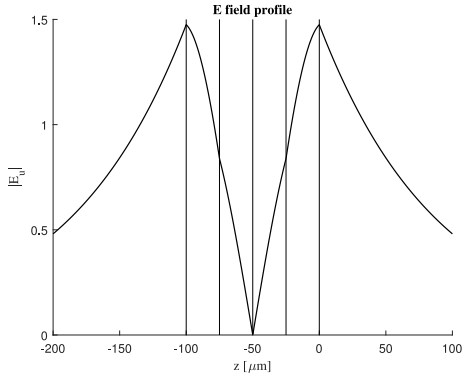

(a)

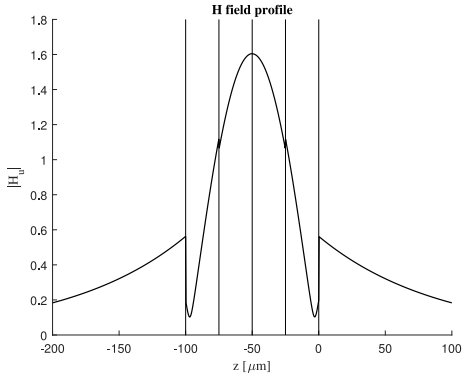

(b)

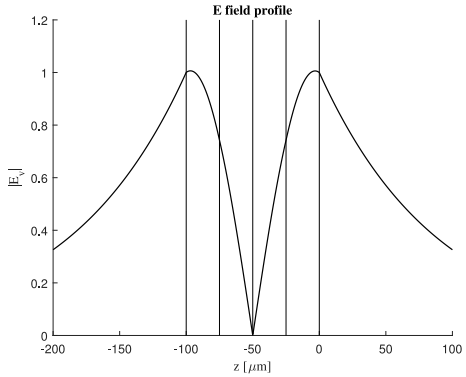

(c)

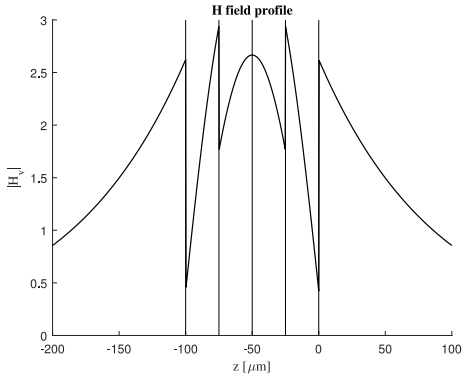

(d)

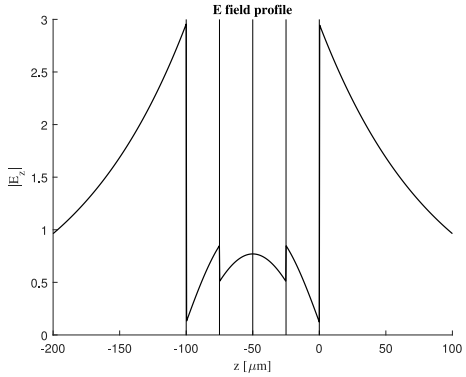

(e)

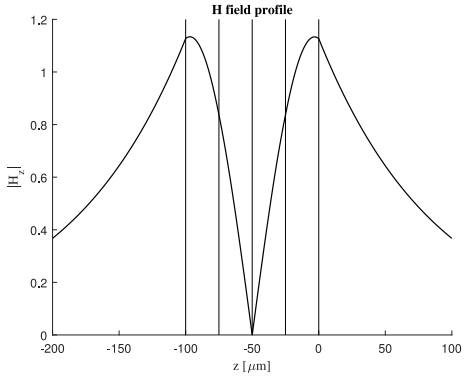

(f)

Figure 5.5: Modal fields profiles for the odd mode $k_\rho/k_0 = 1.123738389711 - j0.082692335335$ on Sheet I. Results were normalized to the maximum magnitude of the total field while H-fields were multiplied by η_0. (a), (c) & (e) E-fields. (b), (d) & (f) H-fields.

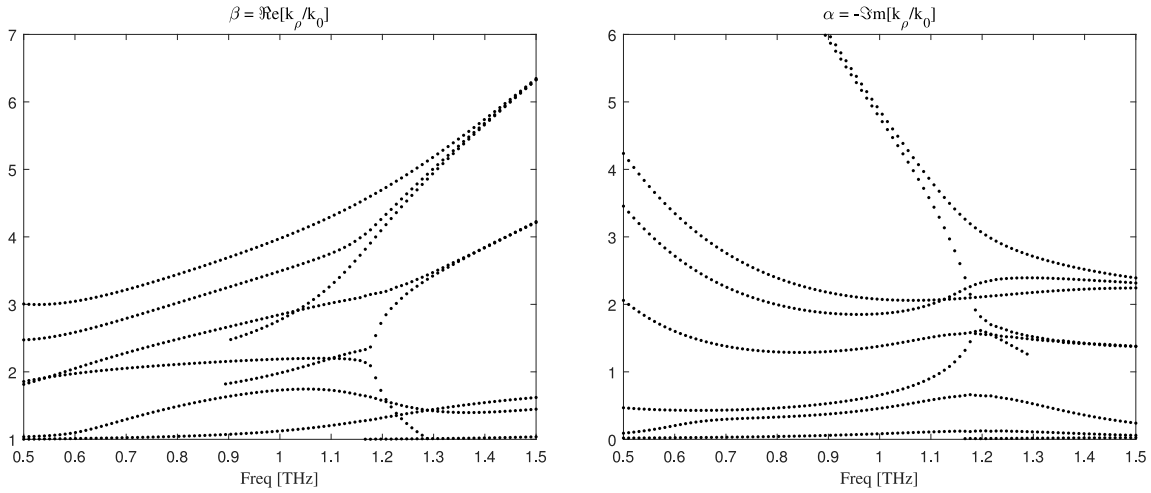

(a) (b)

Figure 5.6: Dispersion curves for the modes in between $f = 0.5$ [THz] and 1.5 [THz] in the Figure 5.4 configuration.

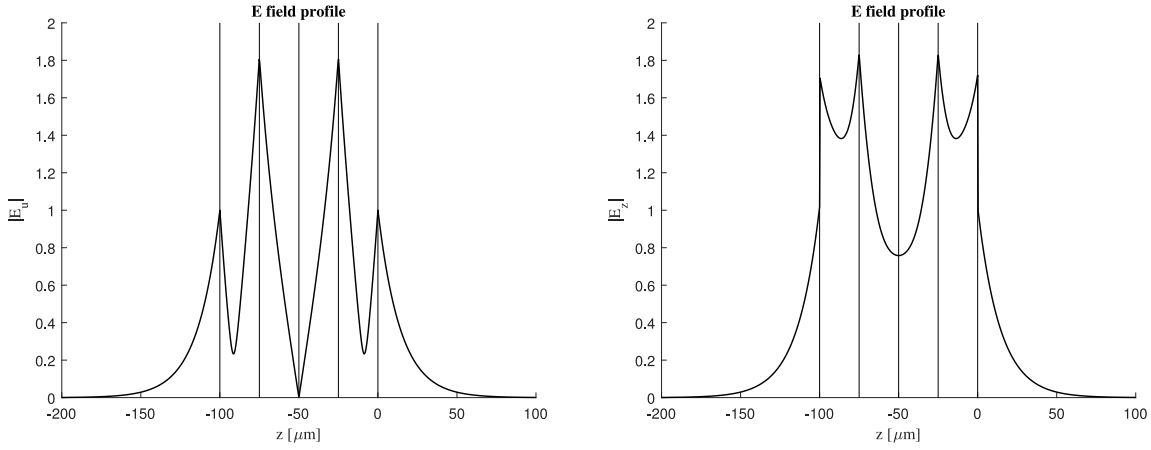

(a) (b)

Figure 5.7: Modal field distributions for mode 8 from Table 5.3.

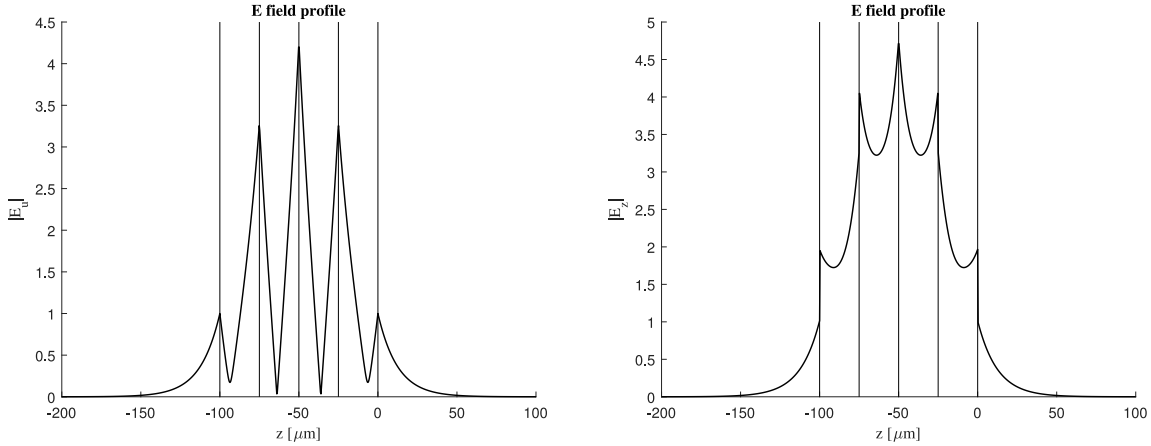

(a) (b)

Figure 5.8: Modal field distributions for mode 9 from Table 5.3.

5.4.4 Graphene Hyperbolic Metasurface

Another example is metasurface based on isotropic graphene periodic ribbons of width W and period L in the x direction. The overall behavior of this structure corresponds to anisotropic conductive sheet using the EMT [132, 149, 152]. This results in the following diagonal surface conductivity tensor:

$$\underline{\underline{\boldsymbol{\sigma}}}^{s} = \begin{bmatrix} \sigma^{s}_{xx} & 0 \\ 0 & \sigma^{s}_{yy} \end{bmatrix} \tag{5.33}$$

$$\sigma^{s}_{xx} = \frac{\sigma_g \sigma_c L}{W\sigma_c + g\sigma} \quad , \quad \sigma^{s}_{yy} = \frac{\sigma_g W}{L} \tag{5.34}$$

Where, $\sigma_c = \dfrac{j\omega\epsilon_0\epsilon_{\text{eff}}L}{\pi} \ln\left[\csc\left(\dfrac{\pi g}{2L}\right)\right]$ and $g = L - W$. Also, σ_g is the isotropic graphene surface conductivity in (2.30). In our example, the surrounding media are free-space and hence the effective dielectric constant $\epsilon_{\text{eff}} = 1$. From Figure 5.9, it is clear that this structure exhibits a hyperbolic behavior indicated by the sign difference between σ^{s}_{xx}

and σ^s_{yy}. In this example, the DF is dependent on the spectral angle ζ which corresponds to the transverse direction of propagation, *i.e.*, $\zeta = \varphi$. This means that each mode transverse propagation constant is dependent on the angle ζ and for that reason, we may apply the search vs ζ. This metasurface supports SPP mode as shown in the results from applying our method as illustrated in Figure 5.10. These results resemble isofrequency contours of the quasi-TM SPP mode.

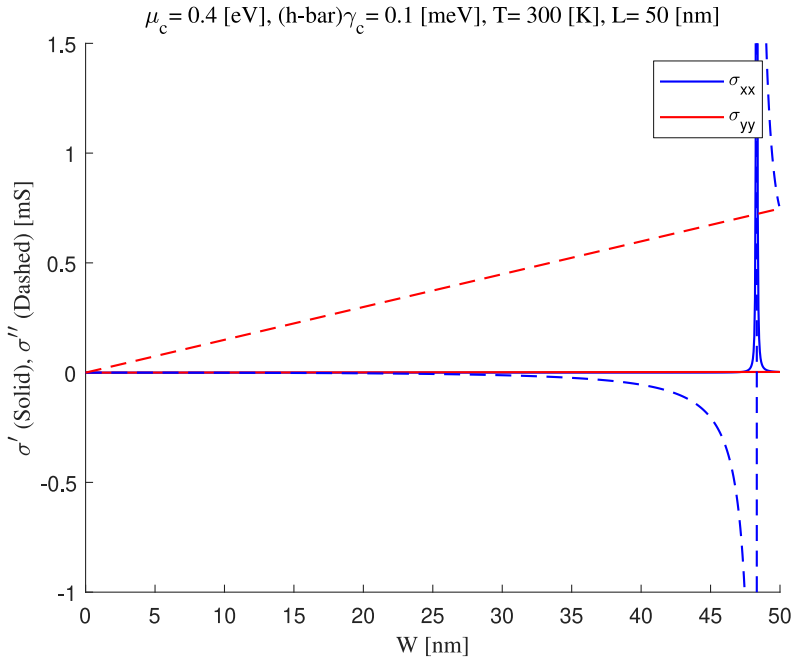

Figure 5.9: Effective anisotropic surface conductivity components vs W for graphene metasurface at $f = 10$ [THz].

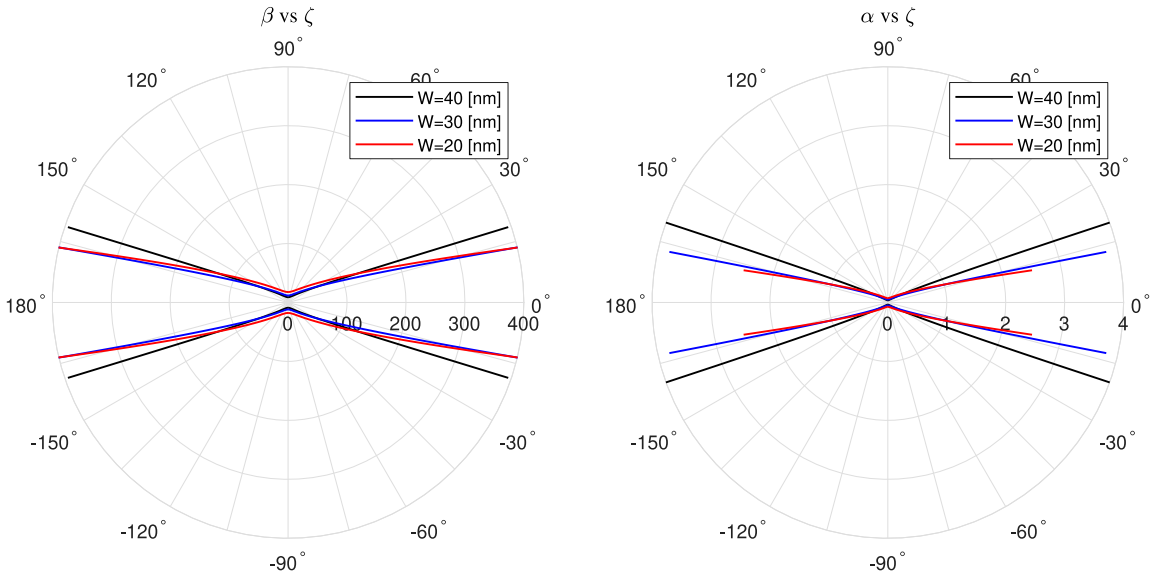

(a) (b)

Figure 5.10: SPP transverse wave number $k_\rho = \beta - j\alpha$ vs ζ for the graphene hyperbolic metasurface (normalized by k_0), at $f = 10$ [THz] and $L = 50$ [nm]. The transverse propagation angle is represented by ζ.

6. CONCLUSIONS AND RECOMMENDATIONS FOR FUTURE WORK

6.1 Conclusions

In this work, we have demonstrated a systematic solution for the EM problem of planar layered media comprising multiple anisotropic 2D conductive sheets at the interfaces. The work was mainly divided into two major topics, namely fields evaluation and modal analysis. The problem was treated through the TL analogy of stratified media by implementing the coupling effect between TM and TE fields due to the anisotropic sheets. The methods developed here were demonstrated in plenty of numerical examples for practical planar layered structures. The scientific contributions from this work were published in the following papers [153–156].

6.2 Recommendations For Future Work

The journey of scientific research is endless, and the current answers only lead to new questions and quests. Thus, we can summarize our recommendations for future works on this topic in the following points:

- This work only focused on developing the necessary tools to study planar layered structures that include anisotropic conductive sheets. But on the other hand, less attention was given to the practical applications that can be utilized from the extraordinary optical properties of the 2D materials. This can be another research objective for future works.

- Another problem that was encountered during this study is the evaluation of the 2D integrals that appeared in (4.64). This integral was computed using Romberg integration, but this treatment is computationally expensive. Further research on this topic is needed in the light of the spectral domain poles using the modal analysis

techniques from this work.

- An important topic that was not covered here is the formulation of scattering problem in this environment. Many practical structures consist of a scattering problem and require solving an integral equation. Hence, it is required to present a suitable integral equation associated with our new TL solution even though it may not be too difficult to obtain.

- Another interesting problem for future research is the excitation of 1D or 2D periodic structures made of conductive sheets. Such a structure was mentioned as a hyperbolic metasurface in Chapter 5, and it was handled using the effective homogenized surface conductivity tensor. This problem can be treated by extending the TL model into infinite TLs spaced equally in the spectral domain. This results in infinite sums to represent the TL quantities and solutions. One aspect of this problem is the evaluation of EM fields due to aperiodic dipole excitation.

- Finally, we suggest extending this work for general anisotropic media. The biaxial media with principal axes rotated in the transverse direction as in (6.1) can be treated by coupled TLs with an eigenvalue problem to determine the vertical propagation constants k_z. The TL approach is more powerful than other techniques and this topic deserves more investigation. This special case of general anisotropy is still applicable in many practical structure, e.g., the excitation of Dyakonov waves [157].

$$\underline{\underline{\boldsymbol{\mu}}} = \begin{bmatrix} \mu_{xx} & \mu_{xy} & 0 \\ \mu_{yx} & \mu_{yy} & 0 \\ 0 & 0 & \mu_{zz} \end{bmatrix} \quad , \quad \underline{\underline{\boldsymbol{\epsilon}}} = \begin{bmatrix} \epsilon_{xx} & \epsilon_{xy} & 0 \\ \epsilon_{yx} & \epsilon_{yy} & 0 \\ 0 & 0 & \epsilon_{zz} \end{bmatrix} \tag{6.1}$$

REFERENCES

[1] M. Aliofkhazraei, W. I. Milne, C. S. Ozkan, S. Mitura, J. L. Gervasoni, and N. Ali, *Graphene science handbook: electrical and optical properties*. CRC press, 2016.

[2] T. Itoh, "Spectral domain immitance approach for dispersion characteristics of generalized printed transmission lines," *IEEE transactions on Microwave Theory and Techniques*, vol. 28, no. 7, pp. 733–736, 1980.

[3] A. G. Ardakani, Z. Ghasemi, and M. M. Golshan, "A new transfer matrix for investigation of surface plasmon modes in multilayer structures containing anisotropic graphene layers," *The European Physical Journal Plus*, vol. 132, no. 5, p. 206, 2017.

[4] P. Kravanja and M. Van Barel, "Zeros of analytic functions," in *Computing the Zeros of Analytic Functions*, pp. 1–59, Springer, 2000.

[5] T. Johnson and W. Tucker, "Enclosing all zeros of an analytic function—a rigorous approach," *Journal of Computational and Applied Mathematics*, vol. 228, no. 1, pp. 418–423, 2009.

[6] A. Sommerfeld, "Über die ausbreitung der wellen in der drahtlosen telegraphie," *Annalen der Physik*, vol. 333, no. 4, pp. 665–736, 1909.

[7] R. E. Collin, "Hertzian dipole radiating over a lossy earth or sea: Some early and late 20th-century controversies," *IEEE Antennas and Propagation Magazine*, vol. 46, no. 2, pp. 64–79, 2004.

[8] W. C. Chew, *Waves and fields in inhomogeneous media*, vol. 522. IEEE press New York, 1995.

[9] L. B. Felsen and N. Marcuvitz, *Radiation and scattering of waves*, vol. 31. John Wiley & Sons, 1994.

[10] J. R. Wait, *Electromagnetic Waves in Stratified Media: Revised Edition Including Supplemented Material*, vol. 3. Elsevier, 2013.

[11] K. Michalski, "On the scalar potential of a point charge associated with a time-harmonic dipole in a layered medium," *IEEE transactions on antennas and propagation*, vol. 35, no. 11, pp. 1299–1301, 1987.

[12] K. A. Michalski and J. R. Mosig, "Multilayered media green's functions in integral equation formulations," *IEEE Transactions on Antennas and Propagation*, vol. 45, no. 3, pp. 508–519, 1997.

[13] K. A. Michalski, "Electromagnetic field computation in planar multilayers," *Encyclopedia of RF and microwave engineering*, 2005.

[14] K. Michalski and J. Mosig, "The sommerfeld half-space problem revisited: from radio frequencies and zenneck waves to visible light and fano modes," *Journal of Electromagnetic Waves and Applications*, vol. 30, no. 1, pp. 1–42, 2016.

[15] K. S. Novoselov, A. K. Geim, S. Morozov, D. Jiang, M. Katsnelson, I. Grigorieva, S. Dubonos, Firsov, and AA, "Two-dimensional gas of massless dirac fermions in graphene," *nature*, vol. 438, no. 7065, p. 197, 2005.

[16] A. K. Geim and K. S. Novoselov, "The rise of graphene," in *Nanoscience and Technology: A Collection of Reviews from Nature Journals*, pp. 11–19, World Scientific, 2010.

[17] A. K. Geim, "Graphene: status and prospects," *science*, vol. 324, no. 5934, pp. 1530–1534, 2009.

[18] A. C. Neto, F. Guinea, N. M. Peres, K. S. Novoselov, and A. K. Geim, "The electronic properties of graphene," *Reviews of modern physics*, vol. 81, no. 1, p. 109, 2009.

[19] R. A. Depine, *Graphene Optics: Electromagnetic solution of canonical problems*. Morgan & Claypool Publishers, 2017.

[20] Y. V. Bludov, A. Ferreira, N. Peres, and M. Vasilevskiy, "A primer on surface plasmon-polaritons in graphene," *International Journal of Modern Physics B*, vol. 27, no. 10, p. 1341001, 2013.

[21] W. Choi, N. Choudhary, G. H. Han, J. Park, D. Akinwande, and Y. H. Lee, "Recent development of two-dimensional transition metal dichalcogenides and their applications," *Materials Today*, 2017.

[22] L. Wu, J. Guo, Q. Wang, S. Lu, X. Dai, Y. Xiang, and D. Fan, "Sensitivity enhancement by using few-layer black phosphorus-graphene/tmdcs heterostructure in surface plasmon resonance biochemical sensor," *Sensors and Actuators B: Chemical*, vol. 249, pp. 542–548, 2017.

[23] D. Correas-Serrano, J. Gomez-Diaz, A. A. Melcon, and A. Alù, "Black phosphorus plasmonics: anisotropic elliptical propagation and nonlocality-induced canalization," *Journal of Optics*, vol. 18, no. 10, p. 104006, 2016.

[24] J. Gomez-Diaz and A. Alu, "Flatland optics with hyperbolic metasurfaces," *ACS Photonics*, vol. 3, no. 12, pp. 2211–2224, 2016.

[25] M. Nakayama, "Theory of surface waves coupled to surface carriers," *Journal of the Physical Society of Japan*, vol. 36, no. 2, pp. 393–398, 1974.

[26] D. G. Papageorgiou, I. A. Kinloch, and R. J. Young, "Mechanical properties of graphene and graphene-based nanocomposites," *Progress in Materials Science*,

vol. 90, pp. 75–127, 2017.

[27] G. W. Hanson, "Dyadic green's functions for an anisotropic, non-local model of biased graphene," *IEEE Transactions on Antennas and Propagation*, vol. 56, no. 3, pp. 747–757, 2008.

[28] Y.-M. Lin, C. Dimitrakopoulos, K. A. Jenkins, D. B. Farmer, H.-Y. Chiu, A. Grill, and P. Avouris, "100-ghz transistors from wafer-scale epitaxial graphene," *Science*, vol. 327, no. 5966, pp. 662–662, 2010.

[29] X. Li, W. Cai, J. An, S. Kim, J. Nah, D. Yang, R. Piner, A. Velamakanni, I. Jung, E. Tutuc, *et al.*, "Large-area synthesis of high-quality and uniform graphene films on copper foils," *Science*, vol. 324, no. 5932, pp. 1312–1314, 2009.

[30] L. Li, Y. Yu, G. J. Ye, Q. Ge, X. Ou, H. Wu, D. Feng, X. H. Chen, and Y. Zhang, "Black phosphorus field-effect transistors," *Nature nanotechnology*, vol. 9, no. 5, p. 372, 2014.

[31] T. Srivastava and R. Jha, "Black phosphorus: A new platform for gaseous sensing based on surface plasmon resonance," *IEEE Photonics Technology Letters*, 2018.

[32] Y. Yuan, X. Yu, Q. Ouyang, Y. Shao, J. Song, J. Qu, and K.-T. Yong, "Highly anisotropic black phosphorous-graphene hybrid architecture for ultrassensitive plasmonic biosensing: Theoretical insight," *2D Materials*, vol. 5, no. 2, p. 025015, 2018.

[33] M. Tamagnone, J. Gomez-Diaz, J. R. Mosig, and J. Perruisseau-Carrier, "Reconfigurable terahertz plasmonic antenna concept using a graphene stack," *Applied Physics Letters*, vol. 101, no. 21, p. 214102, 2012.

[34] M. Tamagnone and J. R. Mosig, "Theoretical limits on the efficiency of reconfigurable and nonreciprocal graphene antennas," *IEEE Antennas and Wireless Propa-*

gation Letters, vol. 15, pp. 1549–1552, 2016.

[35] Z. Fang, Z. Liu, Y. Wang, P. M. Ajayan, P. Nordlander, and N. J. Halas, "Graphene-antenna sandwich photodetector," *Nano letters*, vol. 12, no. 7, pp. 3808–3813, 2012.

[36] F. Xia, H. Wang, and Y. Jia, "Rediscovering black phosphorus as an anisotropic layered material for optoelectronics and electronics," *Nature communications*, vol. 5, p. 4458, 2014.

[37] S. Tretyakov, *Analytical modeling in applied electromagnetics*. Artech House, 2003.

[38] C. Caloz and T. Itoh, *Electromagnetic metamaterials: transmission line theory and microwave applications*. John Wiley & Sons, 2005.

[39] N. Yu and F. Capasso, "Flat optics with designer metasurfaces," *Nature materials*, vol. 13, no. 2, p. 139, 2014.

[40] F. Aieta, P. Genevet, N. Yu, M. A. Kats, Z. Gaburro, and F. Capasso, "Out-of-plane reflection and refraction of light by anisotropic optical antenna metasurfaces with phase discontinuities," *Nano letters*, vol. 12, no. 3, pp. 1702–1706, 2012.

[41] M. Veysi, C. Guclu, O. Boyraz, and F. Capolino, "Thin anisotropic metasurfaces for simultaneous light focusing and polarization manipulation," *JOSA B*, vol. 32, no. 2, pp. 318–323, 2015.

[42] J. R. Wait, "The electromagnetic fields of a dipole in the presence of a thin plasma sheet," *Applied Scientific Research, Section B*, vol. 8, no. 1, pp. 397–417, 1960.

[43] A. Lakhtakia, "Green's functions and brewster condition for a halfspace bounded by an anisotropic impedance plane," *International journal of infrared and millimeter waves*, vol. 13, no. 2, pp. 161–170, 1992.

[44] H. J. Bilow, "Guided waves on a planar tensor impedance surface," *IEEE Transactions on Antennas and Propagation*, vol. 51, no. 10, pp. 2788–2792, 2003.

[45] J. Gómez-Díaz and J. Perruisseau-Carrier, "Propagation of hybrid transverse magnetic-transverse electric plasmons on magnetically biased graphene sheets," *Journal of Applied Physics*, vol. 112, no. 12, p. 124906, 2012.

[46] G. Lovat, "Equivalent circuit for electromagnetic interaction and transmission through graphene sheets," *IEEE Transactions on Electromagnetic Compatibility*, vol. 54, no. 1, pp. 101–109, 2012.

[47] S. Inampudi, M. Nazari, A. Forouzmand, and H. Mosallaei, "Manipulation of surface plasmon polariton propagation on isotropic and anisotropic two-dimensional materials coupled to boron nitride heterostructures," *Journal of Applied Physics*, vol. 119, no. 2, p. 025301, 2016.

[48] K. Okamoto, *Fundamentals of optical waveguides*. Academic press, 2010.

[49] T. Tamir and A. A. Oliner, "The spectrum of electromagnetic waves guided by a plasma layer," *Proceedings of the IEEE*, vol. 51, no. 2, pp. 317–332, 1963.

[50] T. D. Visser, H. Blok, and D. Lenstra, "Modal analysis of a planar waveguide with gain and losses," *IEEE journal of quantum electronics*, vol. 31, no. 10, pp. 1803–1810, 1995.

[51] K.-H. Schlereth and M. Tacke, "The complex propagation constant of multilayer waveguides: an algorithm for a personal computer," *IEEE journal of quantum electronics*, vol. 26, no. 4, pp. 627–630, 1990.

[52] M. J. Neve and R. Paknys, "A technique for approximating the location of surface- and leaky-wave poles for a lossy dielectric slab," *IEEE transactions on antennas and propagation*, vol. 54, no. 1, pp. 115–120, 2006.

[53] G. Valerio, D. R. Jackson, and A. Galli, "Fundamental properties of surface waves in lossless stratified structures," in *Proceedings of the Royal Society of London A: Mathematical, Physical and Engineering Sciences*, vol. 466, pp. 2447–2469, The Royal Society, 2010.

[54] K. Michalski, "On the efficient evaluation of integral arising in the sommerfeld half-space problem," in *IEE Proceedings H (Microwaves, Antennas and Propagation)*, vol. 132, pp. 312–318, IET, 1985.

[55] S. Barkeshli, "Efficient asymptotic closed form approximation for dyadic green's function for anisotropic substrates," tech. rep., SABBAGH ASSOCIATES INC BLOOMINGTON IN, 1992.

[56] A. G. Polimeridis, T. V. Yioultsis, and T. D. Tsiboukis, "A robust method for the computation of green's functions in stratified media," *IEEE transactions on antennas and propagation*, vol. 55, no. 7, pp. 1963–1969, 2007.

[57] A. Alparslan, M. I. Aksun, and K. A. Michalski, "Closed-form green's functions in planar layered media for all ranges and materials," *IEEE Transactions on Microwave Theory and Techniques*, vol. 58, no. 3, pp. 602–613, 2010.

[58] S.-A. Teo, S.-T. Chew, and M.-S. Leong, "Error analysis of the discrete complex image method and pole extraction," *IEEE transactions on microwave theory and techniques*, vol. 51, no. 2, pp. 406–413, 2003.

[59] R. Collin, "Field the ory of guided waves," 1991.

[60] G. Kovacs and G. Scott, "Optical excitation of surface plasma waves in layered media," *Physical Review B*, vol. 16, no. 4, p. 1297, 1977.

[61] D. Mills and E. Burstein, "Polaritons: the electromagnetic modes of media," *Reports on Progress in Physics*, vol. 37, no. 7, p. 817, 1974.

[62] J. Homola, S. S. Yee, and G. Gauglitz, "Surface plasmon resonance sensors," *Sensors and Actuators B: Chemical*, vol. 54, no. 1, pp. 3–15, 1999.

[63] R. Wan, F. Liu, and Y. Huang, "Ultrathin layer sensing based on hybrid coupler with short-range surface plasmon polariton and dielectric waveguide," *Optics letters*, vol. 35, no. 2, pp. 244–246, 2010.

[64] E. Le Ru and P. Etchegoin, *Principles of Surface-Enhanced Raman Spectroscopy: and related plasmonic effects*. Elsevier, 2008.

[65] L. Knockaert, H. Rogier, and D. De Zutter, "An fft-based signal identification approach for obtaining the propagation constants of the leaky modes in layered media," *AEU-International Journal of Electronics and Communications*, vol. 59, no. 4, pp. 230–238, 2005.

[66] E. Anemogiannis, E. N. Glytsis, and T. K. Gaylord, "Determination of guided and leaky modes in lossless and lossy planar multilayer optical waveguides: reflection pole method and wavevector density method," *Journal of lightwave technology*, vol. 17, no. 5, p. 929, 1999.

[67] E. Anemogiannis and E. N. Glytsis, "Multilayer waveguides: efficient numerical analysis of general structures," *Journal of Lightwave Technology*, vol. 10, no. 10, pp. 1344–1351, 1992.

[68] L. Delves and J. Lyness, "A numerical method for locating the zeros of an analytic function," *Mathematics of computation*, vol. 21, no. 100, pp. 543–560, 1967.

[69] T. Zhan, X. Shi, Y. Dai, X. Liu, and J. Zi, "Transfer matrix method for optics in graphene layers," *Journal of Physics: Condensed Matter*, vol. 25, no. 21, p. 215301, 2013.

[70] J. S. Gomez-Diaz, J. R. Mosig, and J. Perruisseau-Carrier, "Effect of spatial dispersion on surface waves propagating along graphene sheets," *IEEE Transactions on Antennas and Propagation*, vol. 61, no. 7, pp. 3589–3596, 2013.

[71] S. Khorasani and B. Rashidian, "Modified transfer matrix method for conducting interfaces," *Journal of Optics A: Pure and Applied Optics*, vol. 4, no. 3, p. 251, 2002.

[72] Y. V. Bludov, N. M. Peres, and M. I. Vasilevskiy, "Unusual reflection of electromagnetic radiation from a stack of graphene layers at oblique incidence," *Journal of Optics*, vol. 15, no. 11, p. 114004, 2013.

[73] D. Dietze, J. Darmo, and K. Unterrainer, "Guided modes in layered semiconductor terahertz structures," *IEEE Journal of Quantum Electronics*, vol. 46, no. 5, pp. 618–625, 2010.

[74] A. Malekabadi, S. A. Charlebois, and D. Deslandes, "Parallel plate waveguide with anisotropic graphene plates: Effect of electric and magnetic biases," *Journal of Applied Physics*, vol. 113, no. 11, p. 113708, 2013.

[75] P. J. Mohr, D. B. Newell, and B. N. Taylor, "Codata recommended values of the fundamental physical constants: 2014," *Journal of Physical and Chemical Reference Data*, vol. 45, no. 4, p. 043102, 2016.

[76] M. N. Polyanskiy, "Refractive index database." `https://refractiveindex.info`. Accessed on 2019-04-29.

[77] J. A. Kong, *Electromagnetic wave theory*. John Wiley & Sons, Inc., 1986.

[78] R. Harrington, "Time-harmonic electromagnetic fields," 2001.

[79] A. Zangwill, *Modern electrodynamics*. Cambridge University Press, 2013.

[80] D. Sarid and W. A. Challener, *Modern introduction to surface plasmons: theory, Mathematica modeling, and applications*. Cambridge University Press, 2010.

[81] B. R. Kusse and E. A. Westwig, *Mathematical physics: applied mathematics for scientists and engineers*. John Wiley & Sons, 2006.

[82] I. D. Koufogiannis, M. Mattes, and J. R. Mosig, "On the development and evaluation of spatial-domain green's functions for multilayered structures with conductive sheets," *IEEE Transactions on Microwave Theory and Techniques*, vol. 63, no. 1, pp. 20–29, 2015.

[83] J. G. Van Bladel, *Electromagnetic fields*, vol. 19. John Wiley & Sons, 2007.

[84] L. B. Felsen, M. Mongiardo, and P. Russer, *Electromagnetic field computation by network methods*. Springer Science & Business Media, 2009.

[85] P. Dennery and A. Krzywicki, *Mathematics for physicists*. Courier Corporation, 2012.

[86] A. Ishimaru, *Electromagnetic Wave Propagation, Radiation, and Scattering*. Prentice Hall, 1991.

[87] K. Key, "Is the fast hankel transform faster than quadrature?," *Geophysics*, vol. 77, no. 3, pp. F21–F30, 2012.

[88] J. L.-W. Li, P.-P. Ding, S. Zouhdi, and S.-P. Yeo, "An accurate and efficient evaluation of planar multilayered green's functions using modified fast hankel transform method," *IEEE Transactions on Microwave Theory and Techniques*, vol. 59, no. 11, pp. 2798–2807, 2011.

[89] T. K. Sarkar and O. Pereira, "Using the matrix pencil method to estimate the parameters of a sum of complex exponentials," *IEEE Antennas and Propagation Magazine*, vol. 37, no. 1, pp. 48–55, 1995.

[90] M. Yuan and T. K. Sarkar, "Computation of the sommerfeld integral tails using the matrix pencil method," *IEEE Transactions on Antennas and Propagation*, vol. 54, no. 4, pp. 1358–1362, 2006.

[91] W. L. Anderson, "Numerical integration of related hankel transforms of orders 0 and 1 by adaptive digital filtering," *Geophysics*, vol. 44, no. 7, pp. 1287–1305, 1979.

[92] R. G. Niciforovic, A. G. Polimeridis, and J. R. Mosig, "Fast computation of sommerfeld integral tails via direct integration based on double exponential-type quadrature formulas," *IEEE Transactions on Antennas and Propagation*, vol. 59, no. 2, pp. 694–699, 2011.

[93] R. Golubovic, A. G. Polimeridis, and J. R. Mosig, "Efficient algorithms for computing sommerfeld integral tails," *IEEE Transactions on Antennas and Propagation*, vol. 60, no. 5, pp. 2409–2417, 2012.

[94] K. A. Michalski, "Extrapolation methods for sommerfeld integral tails," *IEEE Transactions on Antennas and Propagation*, vol. 46, no. 10, pp. 1405–1418, 1998.

[95] K. A. Michalski and J. R. Mosig, "Efficient computation of sommerfeld integral tails–methods and algorithms," *Journal of Electromagnetic Waves and Applications*, vol. 30, no. 3, pp. 281–317, 2016.

[96] E. Simsek, "Graphene in layered medium applications," *Microwave and Optical Technology Letters*, vol. 55, no. 10, pp. 2293–2296, 2013.

[97] Y. Huang, J. Wu, and K.-C. Hwang, "Thickness of graphene and single-wall carbon nanotubes," *Physical review B*, vol. 74, no. 24, p. 245413, 2006.

[98] G. W. Hanson, "Dyadic green's functions and guided surface waves for a surface conductivity model of graphene," *Journal of Applied Physics*, vol. 103, no. 6, p. 064302, 2008.

[99] S. J. Orfanidis, *Electromagnetic waves and antennas*. Rutgers University New Brunswick, NJ, 2002.

[100] S. A. Maier, *Plasmonics: fundamentals and applications*. Springer Science & Business Media, 2007.

[101] L. Novotny and B. Hecht, *Principles of nano-optics*. Cambridge university press, 2012.

[102] C. A. Balanis, *Advanced engineering electromagnetics*. John Wiley & Sons, 1989.

[103] K. A. Michalski and D. R. Wilton, "On the computation of plane-wave impressed fields and far-zone fields of arbitrary current sources in planar multilayer dielectric and plasmonic media," *Journal of Electromagnetic Waves and Applications*, vol. 31, no. 11-12, pp. 1177–1193, 2017.

[104] C. A. Balanis, "Antenna theory: A review," *Proceedings of the IEEE*, vol. 80, no. 1, pp. 7–23, 1992.

[105] R. E. Collin, *Antennas and radiowave propagation*. McGraw-Hill, 1985.

[106] W. L. Weeks, *Electromagnetic theory for engineering applications*. Wiley, 1964.

[107] R. E. Smith, S. Houde-Walter, and G. Forbes, "Mode determination for planar waveguide using the four-sheeted dispersion relation," *IEEE journal of quantum electronics*, vol. 28, no. 6, pp. 1520–1526, 1992.

[108] C. Chen, P. Berini, D. Feng, S. Tanev, and V. P. Tzolov, "Efficient and accurate numerical analysis of multilayer planar optical waveguides in lossy anisotropic media," *Optics Express*, vol. 7, no. 8, pp. 260–272, 2000.

[109] R. Smith, *Modal Expansions in Transparent and Nontransparent Planar Waveguides*. PhD thesis, University of Rochester, 1993.

[110] R. Smith and S. N. Houde-Walter, "The migration of bound and leaky solutions to the waveguide dispersion relation," *Journal of lightwave technology*, vol. 11, no. 11, pp. 1760–1768, 1993.

[111] A. Bakhtazad, H. Abiri, and R. Ghayour, "A general transform for regularizing planar open waveguide dispersion relation," *Journal of lightwave technology*, vol. 15, no. 2, pp. 383–390, 1997.

[112] R. Rodríguez-Berral, F. Mesa, and F. Medina, "Appropriate formulation of the characteristic equation for open nonreciprocal layered waveguides with different upper and lower half-spaces," *IEEE Transactions on Microwave Theory and Techniques*, vol. 53, no. 5, pp. 1613–1623, 2005.

[113] R. Smith, S. N. Houde-Walter, and G. Forbes, "Numerical determination of planar waveguide modes using the analyticity of the dispersion relation," *Optics letters*, vol. 16, no. 17, pp. 1316–1318, 1991.

[114] P. Kowalczyk, "On root finding algorithms for complex functions with branch cuts," *Journal of Computational and Applied Mathematics*, vol. 314, pp. 1–9, 2017.

[115] D. Whittaker and I. Culshaw, "Scattering-matrix treatment of patterned multilayer photonic structures," *Physical Review B*, vol. 60, no. 4, p. 2610, 1999.

[116] R. Collin, "Theory and design of wide-band multisection quarter-wave transformers," *Proceedings of the IRE*, vol. 43, no. 2, pp. 179–185, 1955.

[117] G. Gonzalez, *Microwave Transistor Amplifiers Analysis and Design, 2nd*. Prentice hall, 1997.

[118] M. C. Pease, "Methods of matrix algebra," tech. rep., 1965.

[119] A. Polimeridis, T. Yioultsis, and T. Tsiboukis, "An efficient pole extraction technique for the computation of green's functions in stratified media using a sine

transformation," *IEEE Transactions on Antennas and Propagation*, vol. 55, no. 1, pp. 227–229, 2007.

[120] J. F. Offersgaard, "Waveguides formed by multiple layers of dielectric, semiconductor, or metallic media with optical loss and anisotropy," *JOSA A*, vol. 12, no. 10, pp. 2122–2128, 1995.

[121] P. Kowalczyk and W. Marynowski, "Efficient complex root tracing algorithm for propagation and radiation problems," *IEEE Transactions on Antennas and Propagation*, vol. 65, no. 5, pp. 2540–2546, 2017.

[122] D. Correas-Serrano, J. S. Gomez-Diaz, J. Perruisseau-Carrier, and A. Álvarez-Melcón, "Spatially dispersive graphene single and parallel plate waveguides: Analysis and circuit model," *IEEE Transactions on Microwave Theory and Techniques*, vol. 61, no. 12, pp. 4333–4344, 2013.

[123] K. A. Michalski and J. R. Mosig, "Analysis of a plane wave-excited subwavelength circular aperture in a planar conducting screen illuminating a multilayer uniaxial sample," *IEEE Transactions on Antennas and Propagation*, vol. 63, no. 5, pp. 2054–2063, 2015.

[124] R. Kotyński, T. Stefaniuk, and A. Pastuszczak, "Sub-wavelength diffraction-free imaging with low-loss metal-dielectric multilayers," *Applied Physics A: Materials Science & Processing*, vol. 103, no. 3, pp. 905–909, 2011.

[125] P. A. Belov and Y. Hao, "Subwavelength imaging at optical frequencies using a transmission device formed by a periodic layered metal-dielectric structure operating in the canalization regime," *Physical Review B*, vol. 73, no. 11, p. 113110, 2006.

[126] S. A. Ramakrishna, "Physics of negative refractive index materials," *Reports on progress in physics*, vol. 68, no. 2, p. 449, 2005.

[127] M. Liu and C. Jin, "Image quality deterioration due to phase fluctuation in layered superlens," *Optik-International Journal for Light and Electron Optics*, vol. 121, no. 21, pp. 1966–1975, 2010.

[128] L. Alekseyev, E. Narimanov, T. Tumkur, H. Li, Y. A. Barnakov, and M. Noginov, "Uniaxial epsilon-near-zero metamaterial for angular filtering and polarization control," *Applied Physics Letters*, vol. 97, no. 13, p. 131107, 2010.

[129] L. Ferrari, C. Wu, D. Lepage, X. Zhang, and Z. Liu, "Hyperbolic metamaterials and their applications," *Progress in Quantum Electronics*, vol. 40, pp. 1–40, 2015.

[130] P. Shekhar, J. Atkinson, and Z. Jacob, "Hyperbolic metamaterials: fundamentals and applications," *Nano convergence*, vol. 1, no. 1, p. 14, 2014.

[131] J. Chilwell and I. Hodgkinson, "Thin-films field-transfer matrix theory of planar multilayer waveguides and reflection from prism-loaded waveguides," *JOSA A*, vol. 1, no. 7, pp. 742–753, 1984.

[132] J. Gomez-Diaz, M. Tymchenko, and A. Alù, "Hyperbolic metasurfaces: surface plasmons, light-matter interactions, and physical implementation using graphene strips," *Optical Materials Express*, vol. 5, no. 10, pp. 2313–2329, 2015.

[133] A. D. Polyanin and A. V. Manzhirov, *Handbook of mathematics for engineers and scientists*. CRC Press, 2006.

[134] G. Lovat, G. W. Hanson, R. Araneo, and P. Burghignoli, "Semiclassical spatially dispersive intraband conductivity tensor and quantum capacitance of graphene," *Physical Review B*, vol. 87, no. 11, p. 115429, 2013.

[135] D. L. Sounas and C. Caloz, "Gyrotropy and nonreciprocity of graphene for microwave applications," *IEEE Transactions on Microwave Theory and Techniques*, vol. 60, no. 4, pp. 901–914, 2012.

[136] L. G. Melo, "Theory of magnetically controlled low-terahertz surface plasmon-polariton modes in graphene–dielectric structures," *JOSA B*, vol. 32, no. 12, pp. 2467–2477, 2015.

[137] V. Gusynin, S. Sharapov, and J. Carbotte, "Magneto-optical conductivity in graphene," *Journal of Physics: Condensed Matter*, vol. 19, no. 2, p. 026222, 2006.

[138] V. Gusynin, S. Sharapov, and J. Carbotte, "On the universal ac optical background in graphene," *New Journal of Physics*, vol. 11, no. 9, p. 095013, 2009.

[139] V. Gusynin and S. Sharapov, "Transport of dirac quasiparticles in graphene: Hall and optical conductivities," *Physical Review B*, vol. 73, no. 24, p. 245411, 2006.

[140] V. Gusynin, S. Sharapov, and J. Carbotte, "Anomalous absorption line in the magneto-optical response of graphene," *Physical review letters*, vol. 98, no. 15, p. 157402, 2007.

[141] M. Bailey and M. Deshpande, "Integral equation formulation of microstrip antennas," *IEEE Transactions on Antennas and Propagation*, vol. 30, no. 4, pp. 651–656, 1982.

[142] J. Damiano, "Computation of input impedance in microstrip antennas. graphic representation and numerical integration of oscillating functions," in *IEE Proceedings H-Microwaves, Antennas and Propagation*, vol. 134, pp. 456–466, IET, 1987.

[143] D. Pozar, "Input impedance and mutual coupling of rectangular microstrip antennas," *IEEE Transactions on Antennas and Propagation*, vol. 30, no. 6, pp. 1191–1196, 1982.

[144] E. Newman and D. Forrai, "Scattering from a microstrip patch," *IEEE Transactions on Antennas and Propagation*, vol. 35, no. 3, pp. 245–251, 1987.

[145] S. Nam and T. Itoh, "Calculation of accurate complex resonant frequency of an open microstrip resonator using the spectral domain method," *Journal of electromagnetic waves and applications*, vol. 2, no. 7, pp. 635–651, 1988.

[146] S. A. H. Gangaraj, T. Low, A. Nemilentsau, and G. W. Hanson, "Directive surface plasmons on tunable two-dimensional hyperbolic metasurfaces and black phosphorus: Green's function and complex plane analysis," *IEEE Transactions on Antennas and Propagation*, vol. 65, no. 3, pp. 1174–1186, 2017.

[147] K. A. Michalski, "Modal transmission line theory of plane wave excited layered media with multiple conductive anisotropic sheets at the interfaces," *Journal of Quantitative Spectroscopy and Radiative Transfer*, 2019.

[148] D. S. Bernstein, *Matrix mathematics: Theory, facts, and formulas with application to linear systems theory*, vol. 41. Princeton University Press Princeton, 2005.

[149] J. S. Gomez-Diaz, M. Tymchenko, and A. Alù, "Hyperbolic plasmons and topological transitions over uniaxial metasurfaces," *Physical review letters*, vol. 114, no. 23, p. 233901, 2015.

[150] G. W. Hanson, "Quasi-transverse electromagnetic modes supported by a graphene parallel-plate waveguide," *Journal of Applied Physics*, vol. 104, no. 8, p. 084314, 2008.

[151] C. S. Kaipa, A. B. Yakovlev, G. W. Hanson, Y. R. Padooru, F. Medina, and F. Mesa, "Enhanced transmission with a graphene-dielectric microstructure at low-terahertz frequencies," *Physical Review B*, vol. 85, no. 24, p. 245407, 2012.

[152] F. Liang, G. W. Hanson, A. B. Yakovlev, G. Lovat, P. Burghignoli, R. Araneo, and S. A. H. Gangaraj, "Dyadic green's functions for dipole excitation of homogenized metasurfaces," *IEEE Transactions on Antennas and Propagation*, vol. 64, no. 1, pp. 167–178, 2016.

[153] M. M. Mustafa, "Modal analysis in planar layered structures with conductive sheets using cauchy integration method," in *2018 Texas Symposium on Wireless and Microwave Circuits and Systems (WMCS)*, IEEE, 2018.

[154] K. A. Michalski and M. M. Mustafa, "Numerically stable and reliable computation of electromagnetic modes in multilayered waveguides using the cauchy integration method with automatic differentiation," *IEEE Transactions on Microwave Theory and Techniques*, no. 99, pp. 1–12, 2018.

[155] K. Michalski and M. Mustafa, "On the computation of hybrid modes in planar layered waveguides with multiple anisotropic conductive sheets," *Proceedings of the Royal Society A: Mathematical, Physical and Engineering Sciences*, vol. 474, no. 2218, p. 20180288, 2018.

[156] K. A. Michalski and M. M. Mustafa, "Dyadic green functions for planar uniaxial multilayers with multiple anisotropic conductive sheets at the interfaces," *Journal of Applied Physics*, vol. 125, no. 5, p. 055302, 2019.

[157] J. Polo, T. Mackay, and A. Lakhtakia, *Electromagnetic surface waves: a modern perspective*. Newnes, 2013.

[158] M. Abramowitz, I. A. Stegun, *et al.*, "Handbook of mathematical functions," *Applied mathematics series*, vol. 55, no. 62, p. 39, 1966.

[159] J. McMahon, "On the roots of the bessel and certain related functions," *The Annals of Mathematics*, vol. 9, no. 1/6, pp. 23–30, 1894.

[160] A. R. Krommer and C. W. Ueberhuber, *Computational integration*. SIAM, 1998.

[161] E. J. Weniger, "Nonlinear sequence transformations for the acceleration of convergence and the summation of divergent series," *Computer Physics Reports*, vol. 10, no. 5-6, pp. 189–371, 1989.

[162] A. Sidi, *Practical extrapolation methods: Theory and applications*, vol. 10. Cambridge University Press, 2003.

[163] K. A. Michalski, "Extrapolation methods for sommerfeld integral tails," *IEEE Transactions on Antennas and Propagation*, vol. 46, no. 10, pp. 1405–1418, 1998.

[164] J. Mosig, "The weighted averages algorithm revisited," *IEEE Transactions on Antennas and Propagation*, vol. 60, no. 4, pp. 2011–2018, 2012.

[165] A. Quarteroni, R. Sacco, and F. Saleri, *Numerical mathematics*, vol. 37. Springer Science & Business Media, 2010.

[166] A. D. Chave, *Computational Statistics in the Earth Sciences: With Applications in MATLAB*. Cambridge University Press, 2017.

[167] A. D. Chave, "Numerical integration of related hankel transforms by quadrature and continued fraction expansion," *Geophysics*, vol. 48, no. 12, pp. 1671–1686, 1983.

[168] S. Lucas and H. Stone, "Evaluating infinite integrals involving bessel functions of arbitrary order," *Journal of Computational and Applied Mathematics*, vol. 64, no. 3, pp. 217–231, 1995.

[169] F. J. Flanigan, *Complex variables: harmonic and analytic functions*. Courier Corporation, 1972.

[170] C. J. Gillan, A. Schuchinsky, and I. Spence, "Computing zeros of analytic functions in the complex plane without using derivatives," *Computer physics communications*, vol. 175, no. 4, pp. 304–313, 2006.

[171] U. Reif, "AutoDiff R2015b." Updated 03 Mar 2017.

[172] S. Agarwal, M. Povolotskyi, T. Kubis, and G. Klimeck, "Adaptive quadrature for sharply spiked integrands," *Journal of computational electronics*, vol. 9, no. 3, pp. 252–255, 2010.

[173] L. Botten, M. Craig, and R. McPhedran, "Complex zeros of analytic functions," *Computer Physics Communications*, vol. 35, pp. C–878, 1984.

[174] A. P. Austin, P. Kravanja, and L. N. Trefethen, "Numerical algorithms based on analytic function values at roots of unity," *SIAM Journal on Numerical Analysis*, vol. 52, no. 4, pp. 1795–1821, 2014.

[175] F. W. Olver, *NIST handbook of mathematical functions hardback and CD-ROM*. Cambridge University Press, 2010.

[176] P. Kravanja and M. Van Barel, "Zeros of analytic functions," in *Computing the Zeros of Analytic Functions*, pp. 1–59, Springer, 2000.

[177] T. Sakurai, P. Kravanja, H. Sugiura, and M. Van Barel, "An error analysis of two related quadrature methods for computing zeros of analytic functions," *Journal of computational and applied mathematics*, vol. 152, no. 1, pp. 467–480, 2003.

APPENDIX A

TRANSMISSION LINE SOLUTION

The complete TL solution is obtained via TLGFs and should include a source embedded in the TLs. Assuming the source in section m, our solution consists of two types: source-free for sections $n \neq m$ and source-excited for section $n = m$. In addition to that, the source-free solution is divided into down-looking $n > m$ and up-looking $n < m$ solutions. The benefit of this approach will become clear as we proceed in the solution.

A.0.1 Source-Free Solution $(n \neq m)$

According to the problems in (2.13), it is possible to postulate the solutions in (A.1) and (A.2) inside section $n \in [1, N]$. This solution assumes that section n is source-free as illustrated in Figure A.1. Also, the TL type α symbol is omitted for simplicity.

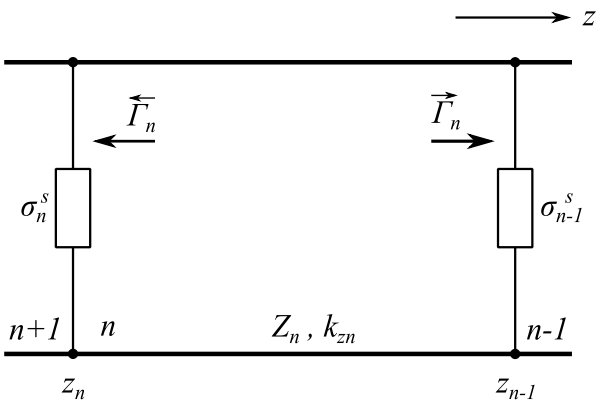

Figure A.1: A source-free section n, where $z_n \leq z \leq z_{n-1}$.

$$V_n(z) = \begin{cases} V_n^+(z) = V_n^+[e^{-jk_{zn}(z-z')} + \overrightarrow{\Gamma}' e^{jk_{zn}(z-z')}] & , z > z' \\ V_n^-(z) = V_n^-[e^{jk_{zn}(z-z')} + \overleftarrow{\Gamma}' e^{-jk_{zn}(z-z')}] & , z < z' \end{cases} \tag{A.1}$$

$$I_n(z) = \begin{cases} I_n^+(z) = Y_n V_n^+[e^{-jk_{zn}(z-z')} - \overrightarrow{\Gamma}' e^{jk_{zn}(z-z')}] & , z > z' \\ I_n^-(z) = -Y_n V_n^-[e^{jk_{zn}(z-z')} - \overleftarrow{\Gamma}' e^{-jk_{zn}(z-z')}] & , z < z' \end{cases} \tag{A.2}$$

Where $z_n \leq z' \leq z_{n-1}$ and $Z_n = Y_n^{-1}$. Also $\overrightarrow{\Gamma}_n = \overrightarrow{\Gamma}(z_{n-1})$ and $\overleftarrow{\Gamma}_n = \overleftarrow{\Gamma}(z_n)$. The relations in (A.3) and (A.4) will be used in the next sections.

$$\begin{aligned} \overrightarrow{\Gamma}(z) &= \overrightarrow{\Gamma}' e^{j2k_{zn}(z-z')} \\ \overleftarrow{\Gamma}(z) &= \overleftarrow{\Gamma}' e^{j2k_{zn}(z'-z)} \end{aligned} \tag{A.3}$$

And

$$\begin{aligned} \overrightarrow{\Gamma}' &= \overrightarrow{\Gamma}_n e^{-j2k_{zn}(z_{n-1}-z')} \\ \overleftarrow{\Gamma}' &= \overleftarrow{\Gamma}_n e^{-j2k_{zn}(z'-z_n)} \end{aligned} \tag{A.4}$$

A.0.1.1 Down-Looking Case $(n > m)$

In this case, we choose $z' = z_{n-1}$. Thus, for $z > z_n$, the following solution is considered:

$$\begin{aligned} V_n(z) &= V_n^- e^{-j\Theta_n}[e^{jk_{zn}(z-z_n)} + \overleftarrow{\Gamma}_n e^{-jk_{zn}(z-z_n)}] \\ Z_n I_n(z) &= -V_n^- e^{-j\Theta_n}[e^{jk_{zn}(z-z_n)} - \overleftarrow{\Gamma}_n e^{-jk_{zn}(z-z_n)}] \end{aligned} \tag{A.5}$$

Also, the impedance definition can be expressed as (A.6).

$$\overleftarrow{Z}_n(z) = -\frac{V_n(z)}{I_n(z)} = Z_n \frac{1 + \overleftarrow{\Gamma}_n e^{-j2k_{zn}(z-z_n)}}{1 - \overleftarrow{\Gamma}_n e^{-j2k_{zn}(z-z_n)}} \tag{A.6}$$

The reflection coefficient $\overleftarrow{\Gamma}_n$ can be obtained from the definition in (A.7), where $Z_n^s = \frac{1}{\sigma_n^s}$.

$$\overleftarrow{\Gamma}_n = \frac{\left[\overleftarrow{Z}_{n+1}(z_n)||Z_n^s\right] - Z_n(z_n)}{\left[\overleftarrow{Z}_{n+1}(z_n)||Z_n^s\right] + Z_n(z_n)} \tag{A.7}$$

Applying the conditions in (2.18) and (2.19), the following relations are obtained:

$$V_{n+1}^- = \frac{[1 + \overleftarrow{\Gamma}_n]e^{-j\Theta_n}}{[1 + \overleftarrow{\Gamma}_{n+1}e^{-j2\Theta_{n+1}}]} V_n^- = \overleftarrow{\tau}_n V_n^- \tag{A.8}$$

Note that the overall transmission coefficient $\overleftarrow{\tau} = \prod_{n=1}^{N-1} \overleftarrow{\tau}_n$.

$$\overleftarrow{\Gamma}_n = \frac{[\Gamma_{n+1,n} - \Omega_{n+1,n}\sigma_n^s] + [1 - \Omega_{n+1,n}\sigma_n^s]\overleftarrow{\Gamma}_{n+1}e^{-j2\Theta_{n+1}}}{[1 + \Omega_{n+1,n}\sigma_n^s] + [\Gamma_{n+1,n} + \Omega_{n+1,n}\sigma_n^s]\overleftarrow{\Gamma}_{n+1}e^{-j2\Theta_{n+1}}} \tag{A.9}$$

Where $\Theta_n = k_{zn}d_n = k_{zn}(z_{n-1} - z_n)$, $\Gamma_{i,j} = \frac{Z_i - Z_j}{Z_i + Z_j}$, and $\Omega_{i,j} = [Y_i + Y_j]^{-1}$. So, we start with $\overleftarrow{\Gamma}_N = \frac{\overleftarrow{Z}_N - Z_N}{\overleftarrow{Z}_N + Z_N}$ and then compute $\overleftarrow{\Gamma}_{N-1}, \ldots, \overleftarrow{\Gamma}_1$. Where $\overleftarrow{Z}_N = \overleftarrow{Z}_N(z_N)$. Typical values for $\overleftarrow{\Gamma}_N$ are 0, -1, and 1 for open, PEC, and PMC terminations, respectively.

Also, note that $V_n(z_n)$ can be obtained from (A.8) if $n > m + 1$. If $n = m + 1$, assuming the source at section m, thus $V_n^- = \frac{V_m(z_m)}{1 + \overleftarrow{\Gamma}_n e^{-j2\Theta_n}}$. The reflection coefficient relation in (A.9) can be derived directly from (A.6) which is more convenient.

A.0.1.2 Up-Looking Case $(n < m)$

For this case, we choose $z' = z_n$. Thus, for $z < z_{n-1}$, the following solution is considered:

$$
\begin{aligned}
V_n(z) &= V_n^+ e^{-j\Theta_n}[e^{-jk_{zn}(z-z_{n-1})} + \overrightarrow{\Gamma}_n e^{jk_{zn}(z-z_{n-1})}] \\
Z_n I_n(z) &= V_n^+ e^{-j\Theta_n}[e^{-jk_{zn}(z-z_{n-1})} - \overrightarrow{\Gamma}_n e^{jk_{zn}(z-z_{n-1})}]
\end{aligned}
\tag{A.10}
$$

Similarly, the impedance and reflection coefficient relations are given in (A.11) and (A.12) respectively.

$$
\overrightarrow{Z}_n(z) = \frac{V_n(z)}{I_n(z)} = Z_n \frac{1 + \overrightarrow{\Gamma}_n e^{j2k_{zn}(z-z_{n-1})}}{1 - \overrightarrow{\Gamma}_n e^{j2k_{zn}(z-z_{n-1})}} \tag{A.11}
$$

$$
\overrightarrow{\Gamma}_n = \frac{\left[\overrightarrow{Z}_{n-1}(z_{n-1}) || Z_{n-1}^s\right] - Z_n(z_{n-1})}{\left[\overrightarrow{Z}_{n-1}(z_{n-1}) || Z_{n-1}^s\right] + Z_n(z_{n-1})} \tag{A.12}
$$

Similarly, applying the conditions in (2.18) and (2.19), and following the procedure for $n > m$, the voltage and reflection coefficient relations are obtained in (A.13) and (A.14).

$$
V_{n-1}^+ = \frac{[1 + \overrightarrow{\Gamma}_n]e^{-j\Theta_n}}{[1 + \overrightarrow{\Gamma}_{n-1} e^{-j2\Theta_{n-1}}]} V_n^+ = \overrightarrow{\tau}_n V_n^+ \tag{A.13}
$$

Note that the overall transmission coefficient $\overrightarrow{\tau} = \prod_{n=2}^{N} \overrightarrow{\tau}_n$.

$$
\overrightarrow{\Gamma}_n = \frac{[\Gamma_{n-1,n} - \Omega_{n-1,n}\sigma_{n-1}^s] + [1 - \Omega_{n-1,n}\sigma_{n-1}^s]\overrightarrow{\Gamma}_{n-1} e^{-j2\Theta_{n-1}}}{[1 + \Omega_{n-1,n}\sigma_{n-1}^s] + [\Gamma_{n-1,n} + \Omega_{n-1,n}\sigma_{n-1}^s]\overrightarrow{\Gamma}_{n-1} e^{-j2\Theta_{n-1}}} \tag{A.14}
$$

We start with $\overrightarrow{\Gamma}_1 = \dfrac{\overrightarrow{Z}_1 - Z_1}{\overrightarrow{Z}_1 + Z_1}$ and then compute $\overrightarrow{\Gamma}_2, \ldots, \overrightarrow{\Gamma}_N$. Where $\overrightarrow{Z}_1 = \overrightarrow{Z}_1(z_0)$. Typical values for $\overrightarrow{\Gamma}_1$ are 0, -1, and 1 for open, PEC, and PMC terminations respectively.

Note that $V_n(z_{n-1})$ can be obtained from (A.13) if $n < m-1$. If $n = m-1$, assuming the source at section m, thus $V_n^+ = \dfrac{V_m(z_{m-1})}{1 + \overrightarrow{\Gamma}_n e^{-j2\Theta_n}}$. The previous expressions reduce into the simple TL relations after applying $\sigma^s = 0$.

A.0.2 Source-Excited Solution $(n = m)$

The differential equations in (2.13) suggest two types of sources: series voltage and shunt current sources as depicted in Figure A.2. The procedure for obtaining a solution inside the section which contains a point source at z' is taken from [106, p. 107]. Here, the voltages and currents take the forms given in (A.1) and (A.2). The jump conditions at $z = z'$ are then enforced as in (A.15) in order to obtain the complete solution defined by V_n^+ and V_n^-.

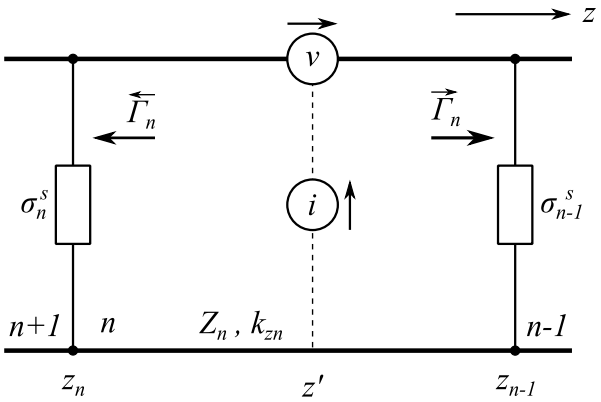

Figure A.2: A source-excited section n. Where $z_n \leq z' \leq z_{n-1}$ represents the source location.

$$\begin{aligned} V_n^+(z') - V_n^-(z') &= v \\ I_n^+(z') - I_n^-(z') &= i \end{aligned} \tag{A.15}$$

After enforcing the jump condition, we obtain:

$$\begin{bmatrix} [1+\overrightarrow{\Gamma}_n e^{-j2k_{zn}(z_{n-1}-z')}] & -[1+\overleftarrow{\Gamma}_n e^{-j2k_{zn}(z'-z_n)}] \\ Y_n[1-\overrightarrow{\Gamma}_n e^{-j2k_{zn}(z_{n-1}-z')}] & Y_n[1-\overleftarrow{\Gamma}_n e^{-j2k_{zn}(z'-z_n)}] \end{bmatrix} \begin{bmatrix} V_n^+ \\ V_n^- \end{bmatrix} = \begin{bmatrix} v \\ i \end{bmatrix} \tag{A.16}$$

Which results in the definitions of V_n^+ and V_n^- in (A.17). Where we defined $D_n = 1 - \overleftarrow{\Gamma}_n \overrightarrow{\Gamma}_n e^{-j2\Theta_n}$.

$$\begin{aligned} V_n^+ &= \frac{1}{2D_n}\Big[\big(1-\overleftarrow{\Gamma}_n e^{-j2k_{zn}(z'-z_n)}\big)v + \big(1+\overleftarrow{\Gamma}_n e^{-j2k_{zn}(z'-z_n)}\big)iZ_n\Big] \\ V_n^- &= \frac{1}{2D_n}\Big[\big(1-\overrightarrow{\Gamma}_n e^{-j2k_{zn}(z_{n-1}-z')}\big)v + \big(1+\overrightarrow{\Gamma}_n e^{-j2k_{zn}(z_{n-1}-z')}\big)iZ_n\Big] \end{aligned} \tag{A.17}$$

In our solutions, only one excitation will exist in the TL. So, either $v = 1$ and $i = 0$ for series voltage source or $v = 0$ and $i = 1$ for shunt current source. Thus, for arbitrary voltage and current sources $v(z)$ and $i(z)$, it is possible to define the convolution integral in (A.18) in order to obtain the voltage and current in the TL.

$$\begin{aligned} V(z) &= \langle V_i(z|z'), i(z')\rangle + \langle V_v(z|z'), v(z')\rangle \\ I(z) &= \langle I_i(z|z'), i(z')\rangle + \langle I_v(z|z'), v(z')\rangle \end{aligned} \tag{A.18}$$

Finally, the TL differential equation solutions in the source-excited section are summarized in (A.19) after some algebraic manipulations.

$$
\begin{aligned}
V_v(z|z') &= \frac{1}{2}[\pm e^{-jk_{zn}|z-z'|} + \frac{1}{D_n}\sum_{r=1}^{4}(-1)^r R_n^{(r)} e^{-jk_{zn}\zeta_n^{(r)}}] \\
I_v(z|z') &= \frac{Y_n}{2}[e^{-jk_{zn}|z-z'|} - \frac{1}{D_n}\sum_{r=1}^{4} R_n^{(r)} e^{-jk_{zn}\zeta_n^{(r)}}] \\
V_i(z|z') &= \frac{Z_n}{2}[e^{-jk_{zn}|z-z'|} + \frac{1}{D_n}\sum_{r=1}^{4} R_n^{(r)} e^{-jk_{zn}\zeta_n^{(r)}}] \\
I_i(z|z') &= \frac{1}{2}[\pm e^{-jk_{zn}|z-z'|} - \frac{1}{D_n}\sum_{r=1}^{4}(-1)^r R_n^{(r)} e^{-jk_{zn}\zeta_n^{(r)}}]
\end{aligned}
\tag{A.19}
$$

Where the coefficients $R_n^{(r)}$ and $\zeta_n^{(r)}$ [1] are defined in (A.20)-(A.23).

$$
\begin{aligned}
R_n^{(1)} &= \overleftarrow{\Gamma}_n \\
R_n^{(2)} &= \overrightarrow{\Gamma}_n \\
R_n^{(3)} &= \overleftarrow{\Gamma}_n \overrightarrow{\Gamma}_n \\
R_n^{(4)} &= \overleftarrow{\Gamma}_n \overrightarrow{\Gamma}_n
\end{aligned}
\tag{A.20}
$$

$$
\begin{aligned}
\zeta_n^{(1)} &= (z + z') - 2z_n \\
\zeta_n^{(2)} &= 2z_{n-1} - (z + z')
\end{aligned}
\tag{A.21}
$$

For a shunt current source:

$$
\begin{aligned}
\zeta_n^{(3)} &= 2d_n + (z - z') \\
\zeta_n^{(4)} &= 2d_n - (z - z')
\end{aligned}
\tag{A.22}
$$

[1] The symbol r was used to indicate ray number. This solution can be visualized as multiple rays including direct and reflected rays [13].

For a series voltage source:

$$\begin{aligned} \zeta_n^{(3)} &= 2d_n - (z - z') \\ \zeta_n^{(4)} &= 2d_n + (z - z') \end{aligned} \tag{A.23}$$

Also, the following reciprocity relations are evident as in (A.24).

$$\begin{aligned} V_i(z|z') &= V_i(z'|z) \\ I_v(z|z') &= I_v(z'|z) \\ V_v(z|z') &= -I_i(z'|z) \end{aligned} \tag{A.24}$$

APPENDIX B

CARTESIAN COMPONENTS FOR SPATIAL DGFS

In this appendix we present some useful general expressions used to derive DGFs and far-filed components.

B.1 Spectral to Spatial Domain Conversions

Considering the following relations:

$$\begin{aligned}\frac{1}{2\pi}\int_{-\pi}^{\pi}\cos(n\xi)e^{-jk_\rho\rho\cos(\xi-\varphi)}d\xi &= (-j)^n J_n(k_\rho\rho)\cos(n\varphi)\\ \frac{1}{2\pi}\int_{-\pi}^{\pi}\sin(n\xi)e^{-jk_\rho\rho\cos(\xi-\varphi)}d\xi &= (-j)^n J_n(k_\rho\rho)\sin(n\varphi)\end{aligned} \tag{B.1}$$

Thus, the inverse FT can be expressed in terms of SIs.

$$\begin{aligned}F^{-1}\{\cos(n\xi)\tilde{f}(k_\rho)\} &= (-j)^n\cos(n\varphi)S_n\{\tilde{f}(k_\rho)\}\\ F^{-1}\{\sin(n\xi)\tilde{f}(k_\rho)\} &= (-j)^n\sin(n\varphi)S_n\{\tilde{f}(k_\rho)\}\end{aligned} \tag{B.2}$$

$$S_2\{\tilde{f}(k_\rho)\} = \frac{2}{\rho}S_1\{k_\rho^{-1}\tilde{f}(k_\rho)\} - S_0\{\tilde{f}(k_\rho)\} \tag{B.3}$$

In order to express the DGFs in Cartesian coordinates system, the vector relations in Figure 2.2 are used to obtain the expressions in (B.4). Where $\cos(\zeta) = \dfrac{kx}{k_\rho}$ and $\sin(\zeta) = \dfrac{ky}{k_\rho}$.

$$\begin{aligned}\hat{\boldsymbol{u}} &= \cos(\zeta)\hat{\boldsymbol{x}} + \sin(\zeta)\hat{\boldsymbol{y}} \\ \hat{\boldsymbol{v}} &= -\sin(\zeta)\hat{\boldsymbol{x}} + \cos(\zeta)\hat{\boldsymbol{y}}\end{aligned} \tag{B.4}$$

Thus, combining all the previous properties and the vector definitions into (2.22)-(2.25), we obtain the relations in (B.5) and the inverse FTs can be summarized as in Table B.1. The computation of SIs is discussed in Appendix C.

$$\begin{aligned}F^{-1}\{\cos^2(\zeta)\tilde{f}(k_\rho)\} &= \frac{1}{2}S_0\{\tilde{f}(k_\rho)\} - \frac{\cos(2\varphi)}{2}S_2\{\tilde{f}(k_\rho)\} \\ F^{-1}\{\sin^2(\zeta)\tilde{f}(k_\rho)\} &= \frac{1}{2}S_0\{\tilde{f}(k_\rho)\} + \frac{\cos(2\varphi)}{2}S_2\{\tilde{f}(k_\rho)\} \\ F^{-1}\{\sin(\zeta)\cos(\zeta)\tilde{f}(k_\rho)\} &= \frac{\sin(2\varphi)}{2}S_2\{\tilde{f}(k_\rho)\}\end{aligned} \tag{B.5}$$

The previous derivation considered a point source at $\rho = 0$. For arbitrary location of source, the following replacements can be applied: $\rho \longrightarrow \varrho = \sqrt{(x-x')^2 + (y-y')^2}$ and $\varphi \longrightarrow \phi = \tan^{-1}\left[\dfrac{y-y'}{x-x'}\right]$. The reader is reminded that the previous treatment is subject to boundary conditions between layers which has not been presented yet. The analysis of the spectral domain dyadic components are summarized below:

Table B.1: Summary of inverse FT properties using SI expressions.

$\tilde{f}(\boldsymbol{k}_\rho)$	$F^{-1}\{\tilde{f}(\boldsymbol{k}_\rho)\}$
$\tilde{f}(k_\rho)$	$S_0\{\tilde{f}(k_\rho)\}$
$\cos(\zeta)\tilde{f}(k_\rho)$	$-j\cos(\varphi)S_1\{\tilde{f}(k_\rho)\}$
$\sin(\zeta)\tilde{f}(k_\rho)$	$-j\sin(\varphi)S_1\{\tilde{f}(k_\rho)\}$
$\cos^2(\zeta)\tilde{f}(k_\rho)$	$\cos^2(\varphi)S_0\{\tilde{f}(k_\rho)\} - \rho^{-1}\cos(2\varphi)S_1\{k_\rho^{-1}\tilde{f}(k_\rho)\}$
$\sin^2(\zeta)\tilde{f}(k_\rho)$	$\sin^2(\varphi)S_0\{\tilde{f}(k_\rho)\} + \rho^{-1}\cos(2\varphi)S_1\{k_\rho^{-1}\tilde{f}(k_\rho)\}$
$\sin(\zeta)\cos(\zeta)\tilde{f}(k_\rho)$	$\frac{1}{2}\sin(2\varphi)S_0\{\tilde{f}(k_\rho)\} - \rho^{-1}\sin(2\varphi)S_1\{k_\rho^{-1}\tilde{f}(k_\rho)\}$

$$
\begin{aligned}
\hat{\boldsymbol{u}}\hat{\boldsymbol{u}} &= \cos^2(\zeta)\hat{\boldsymbol{x}}\hat{\boldsymbol{x}} + \sin(\zeta)\cos(\zeta)(\hat{\boldsymbol{x}}\hat{\boldsymbol{y}} + \hat{\boldsymbol{y}}\hat{\boldsymbol{x}}) + \sin^2(\zeta)\hat{\boldsymbol{y}}\hat{\boldsymbol{y}} \\
\hat{\boldsymbol{u}}\hat{\boldsymbol{v}} &= \sin(\zeta)\cos(\zeta)(-\hat{\boldsymbol{x}}\hat{\boldsymbol{x}} + \hat{\boldsymbol{y}}\hat{\boldsymbol{y}}) + \cos^2(\zeta)\hat{\boldsymbol{x}}\hat{\boldsymbol{y}} - \sin^2(\zeta)\hat{\boldsymbol{y}}\hat{\boldsymbol{x}} \\
\hat{\boldsymbol{v}}\hat{\boldsymbol{u}} &= \sin(\zeta)\cos(\zeta)(-\hat{\boldsymbol{x}}\hat{\boldsymbol{x}} + \hat{\boldsymbol{y}}\hat{\boldsymbol{y}}) - \sin^2(\zeta)\hat{\boldsymbol{x}}\hat{\boldsymbol{y}} + \cos^2(\zeta)\hat{\boldsymbol{y}}\hat{\boldsymbol{x}} \\
\hat{\boldsymbol{v}}\hat{\boldsymbol{v}} &= \sin^2(\zeta)\hat{\boldsymbol{x}}\hat{\boldsymbol{x}} - \sin(\zeta)\cos(\zeta)(\hat{\boldsymbol{x}}\hat{\boldsymbol{y}} + \hat{\boldsymbol{y}}\hat{\boldsymbol{x}}) + \cos^2(\zeta)\hat{\boldsymbol{y}}\hat{\boldsymbol{y}} \\
\hat{\boldsymbol{u}}\hat{\boldsymbol{z}} &= \cos(\zeta)\hat{\boldsymbol{x}}\hat{\boldsymbol{z}} + \sin(\zeta)\hat{\boldsymbol{y}}\hat{\boldsymbol{z}} \\
\hat{\boldsymbol{v}}\hat{\boldsymbol{z}} &= -\sin(\zeta)\hat{\boldsymbol{x}}\hat{\boldsymbol{z}} + \cos(\zeta)\hat{\boldsymbol{y}}\hat{\boldsymbol{z}} \\
\hat{\boldsymbol{v}}\hat{\boldsymbol{u}} &= \cos(\zeta)\hat{\boldsymbol{z}}\hat{\boldsymbol{x}} + \sin(\zeta)\hat{\boldsymbol{z}}\hat{\boldsymbol{y}} \\
\hat{\boldsymbol{z}}\hat{\boldsymbol{v}} &= -\sin(\zeta)\hat{\boldsymbol{z}}\hat{\boldsymbol{x}} + \cos(\zeta)\hat{\boldsymbol{z}}\hat{\boldsymbol{y}}
\end{aligned}
\tag{B.6}
$$

The Cartesian components of spectral domain dyadic function $\underline{\underline{\tilde{\boldsymbol{f}}}}$ can be expressed as

follows:

$$\tilde{f}_{xx} = \tilde{f}_{uu}\cos^2(\zeta) + \tilde{f}_{vv}\sin^2(\zeta) - \sin(\zeta)\cos(\zeta)(\tilde{f}_{uv} + \tilde{f}_{vu}) \tag{B.7}$$

$$\tilde{f}_{xy} = \tilde{f}_{uv}\cos^2(\zeta) - \tilde{f}_{vu}\sin^2(\zeta) + \sin(\zeta)\cos(\zeta)(\tilde{f}_{uu} - \tilde{f}_{vv}) \tag{B.8}$$

$$\tilde{f}_{yx} = \tilde{f}_{vu}\cos^2(\zeta) - \tilde{f}_{uv}\sin^2(\zeta) + \sin(\zeta)\cos(\zeta)(\tilde{f}_{uu} - \tilde{f}_{vv}) \tag{B.9}$$

$$\tilde{f}_{yy} = \tilde{f}_{uu}\sin^2(\zeta) + \tilde{f}_{vv}\cos^2(\zeta) + \sin(\zeta)\cos(\zeta)(\tilde{f}_{uv} + \tilde{f}_{vu}) \tag{B.10}$$

$$\tilde{f}_{xz} = \tilde{f}_{uz}\cos(\zeta) - \tilde{f}_{vz}\sin(\zeta) \tag{B.11}$$

$$\tilde{f}_{yz} = \tilde{f}_{uz}\sin(\zeta) + \tilde{f}_{vz}\cos(\zeta) \tag{B.12}$$

$$\tilde{f}_{zx} = \tilde{f}_{zu}\cos(\zeta) - \tilde{f}_{zv}\sin(\zeta) \tag{B.13}$$

$$\tilde{f}_{zy} = \tilde{f}_{zu}\sin(\zeta) + \tilde{f}_{zv}\cos(\zeta) \tag{B.14}$$

$$\tilde{f}_{zz} = \tilde{f}_{zz} \tag{B.15}$$

Assuming the dyadic $\underline{\underline{\boldsymbol{f}}}$ independent of the spectral angle ζ. After applying the inverse FT properties $\underline{\underline{\boldsymbol{f}}}$ becomes:

$$f_{xx} = \frac{1}{2}S_0\{\tilde{f}_{uu} + \tilde{f}_{vv}\} - \frac{\cos(2\varphi)}{2}S_2\{\tilde{f}_{uu} - \tilde{f}_{vv}\} + \frac{\sin(2\varphi)}{2}S_2\{\tilde{f}_{uv} + \tilde{f}_{vu}\} \quad \text{(B.16)}$$

$$f_{xy} = \frac{1}{2}S_0\{\tilde{f}_{uv} - \tilde{f}_{vu}\} - \frac{\cos(2\varphi)}{2}S_2\{\tilde{f}_{uv} + \tilde{f}_{vu}\} - \frac{\sin(2\varphi)}{2}S_2\{\tilde{f}_{uu} - \tilde{f}_{vv}\} \quad \text{(B.17)}$$

$$f_{yx} = \frac{1}{2}S_0\{\tilde{f}_{vu} - \tilde{f}_{uv}\} - \frac{\cos(2\varphi)}{2}S_2\{\tilde{f}_{uv} + \tilde{f}_{vu}\} - \frac{\sin(2\varphi)}{2}S_2\{\tilde{f}_{uu} - \tilde{f}_{vv}\} \quad \text{(B.18)}$$

$$f_{yy} = \frac{1}{2}S_0\{\tilde{f}_{uu} + \tilde{f}_{vv}\} + \frac{\cos(2\varphi)}{2}S_2\{\tilde{f}_{uu} - \tilde{f}_{vv}\} - \frac{\sin(2\varphi)}{2}S_2\{\tilde{f}_{uv} + \tilde{f}_{vu}\} \quad \text{(B.19)}$$

$$f_{xz} = -j\cos(\varphi)S_1\{\tilde{f}_{uz}\} + j\sin(\varphi)S_1\{\tilde{f}_{vz}\} \quad \text{(B.20)}$$

$$f_{yz} = -j\sin(\varphi)S_1\{\tilde{f}_{uz}\} - j\cos(\varphi)S_1\{\tilde{f}_{vz}\} \quad \text{(B.21)}$$

$$f_{zx} = -j\cos(\varphi)S_1\{\tilde{f}_{zu}\} + j\sin(\varphi)S_1\{\tilde{f}_{zv}\} \quad \text{(B.22)}$$

$$f_{zy} = -j\sin(\varphi)S_1\{\tilde{f}_{zu}\} - j\cos(\varphi)S_1\{\tilde{f}_{zv}\} \quad \text{(B.23)}$$

$$f_{zz} = S_0\{\tilde{f}_{zz}\} \tag{B.24}$$

Alternative expressions for transverse components in terms of S_0 and S_1 only are given below:

$$\begin{aligned} f_{xx} = {} & \cos^2(\varphi) S_0\{\tilde{f}_{uu}\} + \sin^2(\varphi) S_0\{\tilde{f}_{vv}\} - \frac{\cos(2\varphi)}{\rho} S_1\{\frac{\tilde{f}_{uu} - \tilde{f}_{vv}}{k_\rho}\} \\ & + \frac{\sin(2\varphi)}{\rho} S_1\{\frac{\tilde{f}_{uv} + \tilde{f}_{vu}}{k_\rho}\} - \frac{\sin(2\varphi)}{2} S_0\{\tilde{f}_{uv} + \tilde{f}_{vu}\} \end{aligned} \tag{B.25}$$

$$\begin{aligned} f_{xy} = {} & \cos^2(\varphi) S_0\{\tilde{f}_{uv}\} - \sin^2(\varphi) S_0\{\tilde{f}_{vu}\} - \frac{\cos(2\varphi)}{\rho} S_1\{\frac{\tilde{f}_{uv} + \tilde{f}_{vu}}{k_\rho}\} \\ & - \frac{\sin(2\varphi)}{\rho} S_1\{\frac{\tilde{f}_{uu} - \tilde{f}_{vv}}{k_\rho}\} + \frac{\sin(2\varphi)}{2} S_0\{\tilde{f}_{uu} - \tilde{f}_{vv}\} \end{aligned} \tag{B.26}$$

$$\begin{aligned} f_{yx} = {} & \cos^2(\varphi) S_0\{\tilde{f}_{vu}\} - \sin^2(\varphi) S_0\{\tilde{f}_{uv}\} - \frac{\cos(2\varphi)}{\rho} S_1\{\frac{\tilde{f}_{vu} + \tilde{f}_{uv}}{k_\rho}\} \\ & - \frac{\sin(2\varphi)}{\rho} S_1\{\frac{\tilde{f}_{uu} - \tilde{f}_{vv}}{k_\rho}\} + \frac{\sin(2\varphi)}{2} S_0\{\tilde{f}_{uu} - \tilde{f}_{vv}\} \end{aligned} \tag{B.27}$$

$$\begin{aligned} f_{yy} = {} & \sin^2(\varphi) S_0\{\tilde{f}_{uu}\} + \cos^2(\varphi) S_0\{\tilde{f}_{vv}\} + \frac{\cos(2\varphi)}{\rho} S_1\{\frac{\tilde{f}_{uu} - \tilde{f}_{vv}}{k_\rho}\} \\ & - \frac{\sin(2\varphi)}{\rho} S_1\{\frac{\tilde{f}_{uv} + \tilde{f}_{vu}}{k_\rho}\} + \frac{\sin(2\varphi)}{2} S_0\{\tilde{f}_{uv} + \tilde{f}_{vu}\} \end{aligned} \tag{B.28}$$

B.2 Spatial Domain DGFs for Isotropic Sheets

The explicit expressions for the space-domain DGFs for isotropic conductive sheets were derived using the methods in Chapter 2 are listed below:

$$G_{xx}^{EJ}(\boldsymbol{\rho}; z|z') = -\cos^2(\varphi)S_0\{V_i^e\} - \sin^2(\varphi)S_0\{V_i^h\} + \frac{\cos(2\varphi)}{\rho}S_1\{\frac{V_i^e - V_i^h}{k_\rho}\} \quad \text{(B.29)}$$

$$G_{xy}^{EJ}(\boldsymbol{\rho}; z|z') = G_{yx}^{EJ}(\boldsymbol{\rho}; z|z') = -\frac{\sin(2\varphi)}{2}S_0\{V_i^e - V_i^h\} + \frac{\sin(2\varphi)}{\rho}S_1\{\frac{V_i^e - V_i^h}{k_\rho}\} \quad \text{(B.30)}$$

$$G_{xz}^{EJ}(\boldsymbol{\rho}; z|z') = \frac{\eta_0}{jk_0\epsilon_z'}\cos(\varphi)S_1\{k_\rho V_v^e\} \quad \text{(B.31)}$$

$$G_{yy}^{EJ}(\boldsymbol{\rho}; z|z') = -\sin^2(\varphi)S_0\{V_i^e\} - \cos^2(\varphi)S_0\{V_i^h\} - \frac{\cos(2\varphi)}{\rho}S_1\{\frac{V_i^e - V_i^h}{k_\rho}\} \quad \text{(B.32)}$$

$$G_{yz}^{EJ}(\boldsymbol{\rho}; z|z') = \frac{\eta_0}{jk_0\epsilon_z'}\sin(\varphi)S_1\{k_\rho V_v^e\} \quad \text{(B.33)}$$

$$G_{zx}^{EJ}(\boldsymbol{\rho}; z|z') = \frac{\eta_0}{jk_0\epsilon_z}\cos(\varphi)S_1\{k_\rho I_i^e\} \quad \text{(B.34)}$$

$$G_{zy}^{EJ}(\boldsymbol{\rho}; z|z') = \frac{\eta_0}{jk_0\epsilon_z}\sin(\varphi)S_1\{k_\rho I_i^e\} \quad \text{(B.35)}$$

$$G_{zz}^{EJ}(\boldsymbol{\rho}; z|z') = -\frac{\eta_0^2}{k_0^2 \epsilon_z \epsilon_z'} S_0\{k_\rho^2 I_v^e\} - \frac{\eta_0}{jk_0\epsilon_z}\delta(\rho)\delta(z-z') \tag{B.36}$$

$$G_{xx}^{EM}(\boldsymbol{\rho}; z|z') = -G_{yy}^{EM}(\boldsymbol{\rho}; z|z') = \frac{\sin(2\varphi)}{2} S_0\{V_v^e - V_v^h\} - \frac{\sin(2\varphi)}{\rho} S_1\{\frac{V_v^e - V_v^h}{k_\rho}\} \tag{B.37}$$

$$G_{xy}^{EM}(\boldsymbol{\rho}; z|z') = \cos^2(\varphi) S_0\{V_v^h\} + \sin^2(\varphi) S_0\{V_v^e\} + \frac{\cos(2\varphi)}{\rho} S_1\{\frac{V_v^e - V_v^h}{k_\rho}\} \tag{B.38}$$

$$G_{xz}^{EM}(\boldsymbol{\rho}; z|z') = \frac{1}{jk_0\eta_0\mu_z'} \sin(\varphi) S_1\{k_\rho V_i^h\} \tag{B.39}$$

$$G_{yx}^{EM}(\boldsymbol{\rho}; z|z') = \cos^2(\varphi) S_0\{V_v^e\} + \sin^2(\varphi) S_0\{V_v^h\} - \frac{\cos(2\varphi)}{\rho} S_1\{\frac{V_v^e - V_v^h}{k_\rho}\} \tag{B.40}$$

$$G_{yz}^{EM}(\boldsymbol{\rho}; z|z') = -\frac{1}{jk_0\eta_0\mu_z'} \cos(\varphi) S_1\{k_\rho V_i^h\} \tag{B.41}$$

$$G_{zx}^{EM}(\boldsymbol{\rho}; z|z') = -\frac{\eta_0}{jk_0\epsilon_z} \sin(\varphi) S_1\{k_\rho I_v^e\} \tag{B.42}$$

$$G_{zy}^{EM}(\boldsymbol{\rho}; z|z') = \frac{\eta_0}{jk_0\epsilon_z} \cos(\varphi) S_1\{k_\rho I_v^e\} \tag{B.43}$$

$$G_{xx}^{HJ}(\boldsymbol{\rho};z|z') = -G_{yy}^{HJ}(\boldsymbol{\rho};z|z') = -\frac{\sin(2\varphi)}{2}S_0\{I_i^h - I_i^e\} + \frac{\sin(2\varphi)}{\rho}S_1\{\frac{I_i^h - I_v^i}{k_\rho}\} \quad \text{(B.44)}$$

$$G_{xy}^{HJ}(\boldsymbol{\rho};z|z') = \cos^2(\varphi)S_0\{I_i^h\} + \sin^2(\varphi)S_0\{I_i^e\} - \frac{\cos(2\varphi)}{\rho}S_1\{\frac{I_i^h - I_i^e}{k_\rho}\} \quad \text{(B.45)}$$

$$G_{xz}^{HJ}(\boldsymbol{\rho};z|z') = -\frac{\eta_0}{jk_0\epsilon_z'}\sin(\varphi)S_1\{k_\rho I_v^e\} \quad \text{(B.46)}$$

$$G_{yx}^{HJ}(\boldsymbol{\rho};z|z') = -\cos^2(\varphi)S_0\{I_i^e\} - \sin^2(\varphi)S_0\{I_i^h\} - \frac{\cos(2\varphi)}{\rho}S_1\{\frac{I_i^e - I_i^h}{k_\rho}\} \quad \text{(B.47)}$$

$$G_{yz}^{HJ}(\boldsymbol{\rho};z|z') = \frac{\eta_0}{jk_0\epsilon_z'}\cos(\varphi)S_1\{k_\rho I_v^e\} \quad \text{(B.48)}$$

$$G_{zx}^{HJ}(\boldsymbol{\rho};z|z') = \frac{1}{jk_0\eta_0\mu_z}\sin(\varphi)S_1\{k_\rho V_i^h\} \quad \text{(B.49)}$$

$$G_{zy}^{HJ}(\boldsymbol{\rho};z|z') = -\frac{1}{jk_0\eta_0\mu_z}\cos(\varphi)S_1\{k_\rho V_i^h\} \quad \text{(B.50)}$$

$$G_{xx}^{HM}(\boldsymbol{\rho};z|z') = -\cos^2(\varphi)S_0\{I_v^h\} - \sin^2(\varphi)S_0\{I_v^e\} + \frac{\cos(2\varphi)}{\rho}S_1\{\frac{I_v^h - I_v^e}{k_\rho}\} \quad \text{(B.51)}$$

$$G_{xy}^{HM}(\boldsymbol{\rho}; z|z') = G_{yx}^{HM}(\boldsymbol{\rho}; z|z') = -\frac{\sin(2\varphi)}{2} S_0\{I_v^h - I_v^e\} + \frac{\sin(2\varphi)}{\rho} S_1\{\frac{I_v^h - I_v^e}{k_\rho}\} \quad \text{(B.52)}$$

$$G_{xz}^{HM}(\boldsymbol{\rho}; z|z') = \frac{1}{jk_0\eta_0\mu_z'} \cos(\varphi) S_1\{k_\rho I_i^h\} \quad \text{(B.53)}$$

$$G_{yy}^{HM}(\boldsymbol{\rho}; z|z') = -\sin^2(\varphi) S_0\{I_v^h\} - \cos^2(\varphi) S_0\{I_v^e\} - \frac{\cos(2\varphi)}{\rho} S_1\{\frac{I_v^h - I_v^e}{k_\rho}\} \quad \text{(B.54)}$$

$$G_{yz}^{HM}(\boldsymbol{\rho}; z|z') = \frac{1}{jk_0\eta_0\mu_z'} \sin(\varphi) S_1\{k_\rho I_i^h\} \quad \text{(B.55)}$$

$$G_{zx}^{HM}(\boldsymbol{\rho}; z|z') = \frac{1}{jk_0\eta_0\mu_z} \cos(\varphi) S_1\{k_\rho V_v^h\} \quad \text{(B.56)}$$

$$G_{zy}^{HM}(\boldsymbol{\rho}; z|z') = \frac{1}{jk_0\eta_0\mu_z} \sin(\varphi) S_1\{k_\rho V_v^h\} \quad \text{(B.57)}$$

$$G_{zz}^{HM}(\boldsymbol{\rho}; z|z') = -\frac{1}{k_0^2\eta_0^2\mu_z\mu_z'} S_0\{k_\rho^2 V_i^h\} - \frac{1}{jk_0\eta_0\mu_z}\delta(\boldsymbol{\rho})\delta(z - z') \quad \text{(B.58)}$$

B.3 Far Field Relation

For far field computations, we need to evaluate the expression $\hat{\boldsymbol{r}} \times \hat{\boldsymbol{z}} \times \underline{\underline{\tilde{\boldsymbol{f}}}}$.

$$\hat{\boldsymbol{z}} \times \underline{\underline{\tilde{\boldsymbol{f}}}} = \begin{bmatrix} -\tilde{f}_{vu} & -\tilde{f}_{vv} & -\tilde{f}_{vz} \\ \tilde{f}_{uu} & \tilde{f}_{uv} & \tilde{f}_{uz} \\ 0 & 0 & 0 \end{bmatrix} \quad \text{(B.59)}$$

Since, $\hat{\boldsymbol{u}} = \sin(\theta)\hat{\boldsymbol{r}} + \cos(\theta)\hat{\boldsymbol{\theta}} = \hat{\boldsymbol{\rho}}$ and $\hat{\boldsymbol{v}} = \hat{\boldsymbol{\varphi}}$, we can conclude that:

$$\begin{aligned}\hat{\boldsymbol{r}} \times \hat{\boldsymbol{z}} \times \underline{\underline{\tilde{\boldsymbol{f}}}} = &- \left(\tilde{f}_{uu}\hat{\boldsymbol{\theta}} + \tilde{f}_{vu}\cos(\theta)\hat{\boldsymbol{\varphi}}\right)\hat{\boldsymbol{\rho}} - \left(\tilde{f}_{uv}\hat{\boldsymbol{\theta}} + \tilde{f}_{vv}\cos(\theta)\hat{\boldsymbol{\varphi}}\right)\hat{\boldsymbol{\varphi}} \\ &- \left(\tilde{f}_{uz}\hat{\boldsymbol{\theta}} + \tilde{f}_{vz}\cos(\theta)\hat{\boldsymbol{\varphi}}\right)\hat{\boldsymbol{z}}\end{aligned} \tag{B.60}$$

APPENDIX C

SOMMERFELD INTEGRAL EVALUATION

The SI defined in (2.27) can be evaluated numerically. This appendix illustrates this computation procedure. A complete review on this topic can be found in [95]. In general, the SI can be defined on the real axis as in (C.1). But, this integral can be spitted into three parts as in (C.2).

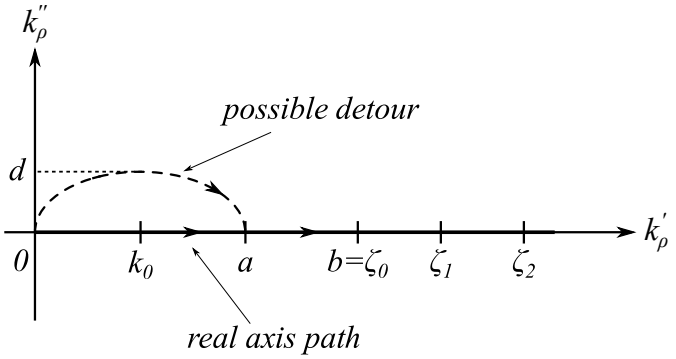

Figure C.1: The real axis integral defined with a detour into the first quadrant for I_a.

$$I = \int_0^\infty \tilde{G}(k_\rho; z|z') J_n(k_\rho \rho) k_\rho dk_\rho \tag{C.1}$$

$$\left(\int_0^a + \int_a^b + \int_b^\infty \right) \tilde{G}(k_\rho; z|z') J_n(k_\rho \rho) k_\rho dk_\rho = I_a + I_b + I_\infty \tag{C.2}$$

Where $a = k_0 \max(\sqrt{\mu_n \epsilon_n})$ [8, p. 114] and $d = 0.001 k_0$ (arbitrary choice). Those are typical choices for this integral. Since $\tilde{G}(k_\rho; z|z')$ has a singularity at branch points $k_\rho = k_1, k_N$ and may contain poles on the real axis, we have to indent the integration

path as shown in Figure C.1. The detour can be parameterized using the real variable t as follows:

$$\begin{aligned} k_\rho &= t + jd\sin(\frac{\pi t}{a}) \\ dk_\rho &= \left[1 + j\frac{\pi d}{a}\cos(\frac{\pi t}{a})\right]dt \end{aligned} \tag{C.3}$$

Where t takes the real values $0 \leq t \leq a$. For $k_\rho > a$, we simply return to the real axis with $k_\rho = t$. The Bessel's zeros are at ζ_i for $i = 0, 1, 2, \ldots,$ *etc*. The Bessel's zeros can be found from exact values tables in [158] or McMahon approximation for higher zeros [159]. Thus, I_a and I_b are defined and can be computed using any suitable quadrature, *e.g.*, Clenshaw-Curtis [160]. The tail integral I_∞ can be approximated with bounded error using the extrapolation:

$$I_\infty = \sum_{n=0}^{\infty} u_n \tag{C.4}$$

$$u_n = \int_{x_n}^{x_{n+1}} \tilde{G}(k_\rho; z|z')J_n(k_\rho\rho)k_\rho dk_\rho \tag{C.5}$$

This can be extrapolated by sequence acceleration techniques such Levin Sidi [161, 162] or Weighted Averages (WA) by Mosig and Michalski [95, 163, 164]. The extrapolation scheme (recursive formula) is given in (C.6) which is based on Richardson's extrapolation [165]. Alternatives to the WA such as Padé approximants [166, 167] were also investigated, but the accuracy is much lower than the method described here.

$$S_n^{k+1} = \frac{S_{n+1}^{(k)} - \eta_n^{(k)} S_n^{(k)}}{1 - \eta_n^{(k)}}, \quad n, k \geq 0 \tag{C.6}$$

Considering $q = \dfrac{\pi}{\rho}$ and $x_n = b + nq$. These parameters are extracted from the asymptotic behavior of the Bessel's functions. Also, $\eta_n = \dfrac{\omega_{n+1}}{\omega_n}$. A typical value for μ is 2.

$$\eta_n^{(k)} = \eta_n \Big(\frac{x_n}{x_{n+1}} \Big)^{\mu k} \tag{C.7}$$

Several transformations can be used as in (C.8). And the final value is $I_\infty = S_n^{(0)}$.

$$\omega_n = \begin{cases} u_n & \text{, t-transformation} \\ u_{n+1} & \text{, d-transformation} \\ x_n u_n & \text{, u-transformation} \\ \dfrac{u_n u_{n+1}}{u_n - u_{n+1}} & \text{, v-transformation} \end{cases} \tag{C.8}$$

C.1 Numerical Examples

The following examples from [95] are presented in Figure C.2-C.4 for demonstration. The examples in (C.9) of semi-infinite integrals from [168] which include Bessel's functions integrands are evaluated numerically via WA method using t-transformation. The numerical results are listed in Table C.1.

$$\begin{aligned} \int_0^\infty x^2 J_0(x) dx &= -1 \\ \int_0^\infty \ln \sqrt{(1+x^2)} J_1(x) dx &\simeq 0.421024438240708333 \\ \int_0^\infty \frac{1 - e^{-x}}{x \ln(1+\sqrt{2})} J_0(x) dx &= 1 \end{aligned} \tag{C.9}$$

The final example to demonstrate here is the famous Sommerfeld identity in (C.10) [8, p. 66] which is a typical example of SIs. Where $k_z = \sqrt{k^2 - k_\rho^2}$ defined on the top Riemman sheet from Figure 2.7.

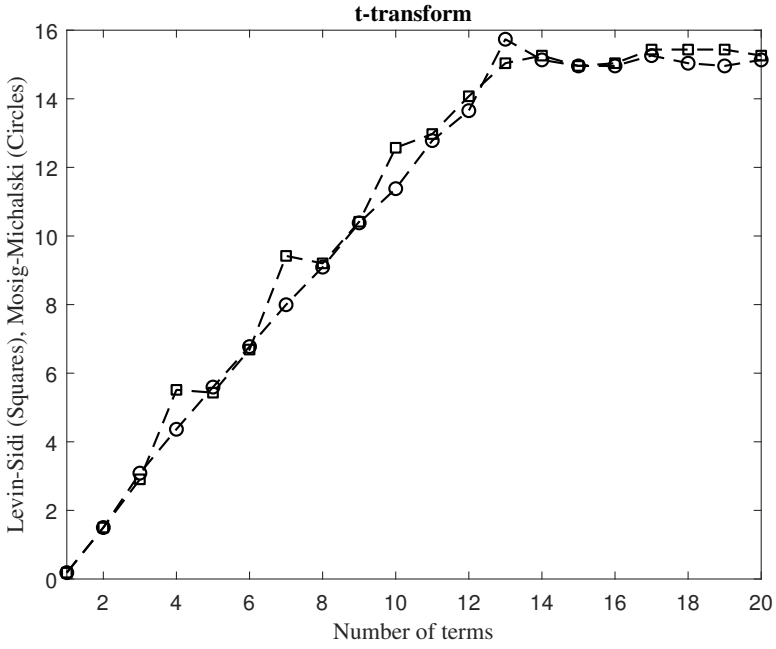

Figure C.2: Relative error for the sum $\sum_{i=0}^{\infty} \dfrac{(-1)^i}{\sqrt{i+1}} \simeq 0.604898643421630$, where $\mu = 2$.

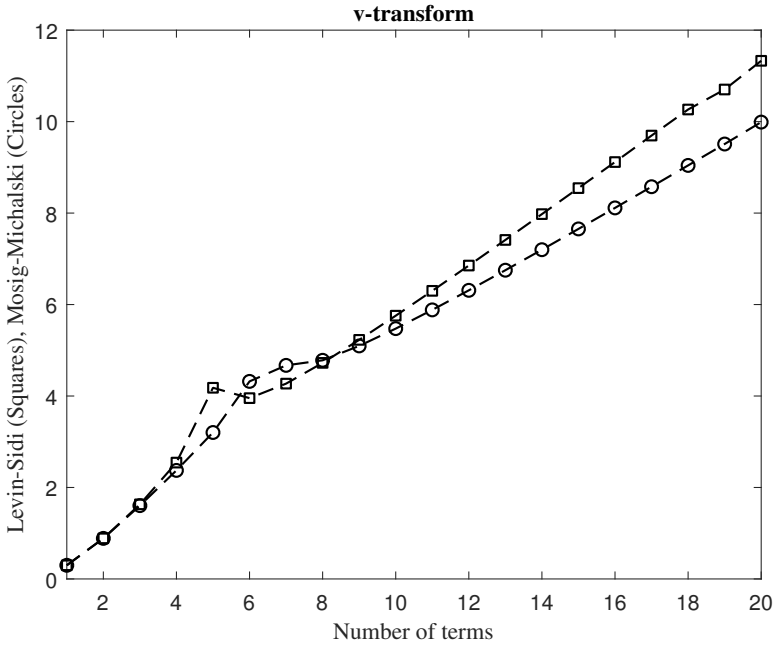

Figure C.3: Relative error for the sum $\sum_{i=0}^{\infty} \dfrac{(4/5)^{i+1}}{i+1} = \ln(5)$, where $\mu = 2$.

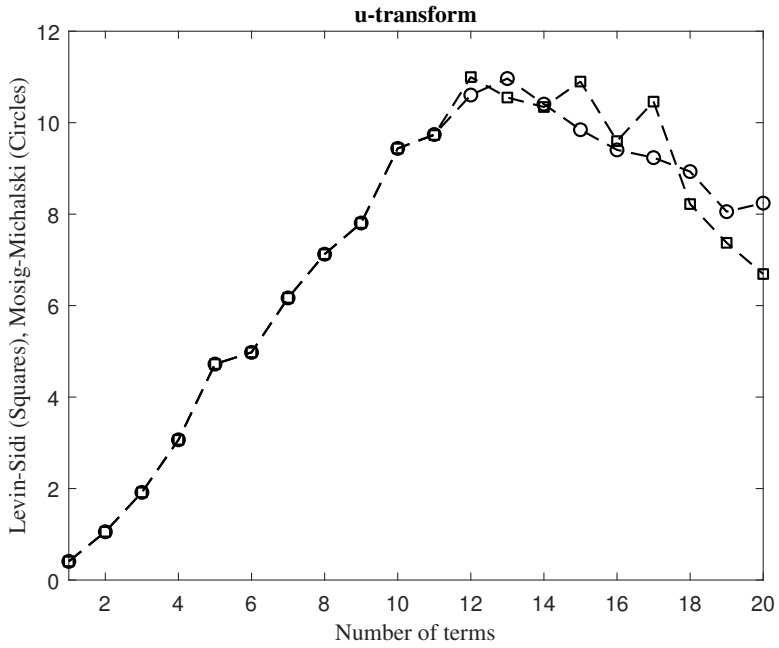

Figure C.4: Relative error for the sum $\sum_{i=0}^{\infty} \frac{1}{(i+1)^2} = \frac{\pi^2}{6}$, where $\mu = 1$.

Table C.1: Comparison of the numerically evaluated answers for the integrals in (C.9).

Integral	Numerical approximation	No. of iterations
1	-0.999999999999925	15
2	0.421024438240708	18
3	1.000000000000000	15

$$\frac{e^{-jkr}}{r} = \int_0^\infty e^{-jk_z|z|} J_0(k_\rho \rho) \frac{k_\rho}{jk_z} dk_\rho \tag{C.10}$$

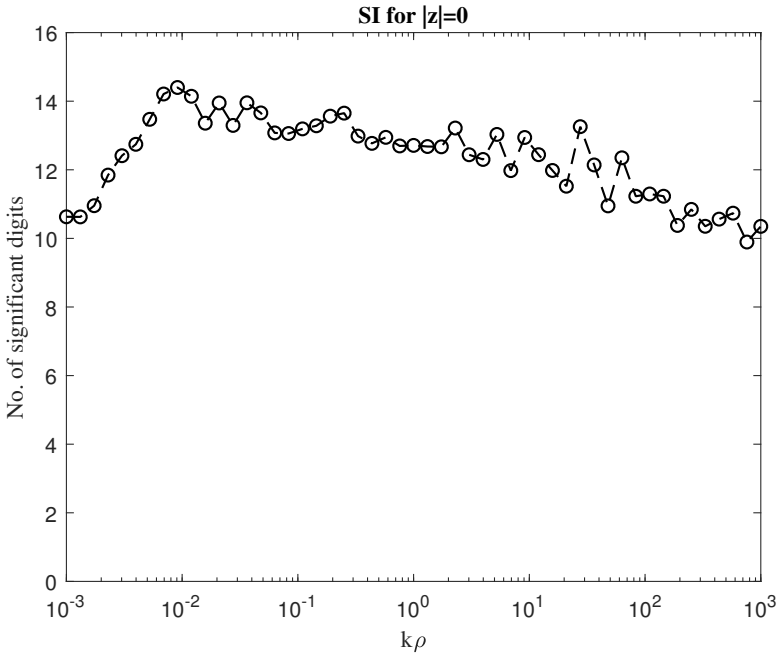

Figure C.5: Relative error for the Sommerfeld identity in (C.10).

APPENDIX D

CAUCHY INTEGRATION METHOD

The analytic function $f(z)$ with N roots inside a simple contour C can be defined using a polynomial $P_N(z)$ and an analytic function $g(z)$ that has no zeros inside the contour C. Thus, we define:

$$f(z) = P_N(z)g(z) \tag{D.1}$$

From the method developed by Delves and Lyness [68] it is possible to define $P_N(z)$ as follows:

$$P_N(z) = \sum_{k=0}^{N} \sigma_{N-k} z^k \tag{D.2}$$

This can be proven using Newton's identities. In order to evaluate the coefficients, we first define the moments μ_k as follows:

$$\mu_k = \frac{1}{2\pi j} \oint_c z^k \frac{f'(z)}{f(z)} dz \quad , k = 0, \ldots, N \tag{D.3}$$

It can be shown that $\mu_0 = N$ using argument principle [169, p. 268]. Then, It is possible to compute the coefficients σ_k as follows:

$$\sigma_k = \frac{-1}{k} \Big[\mu_k + \sum_{j=1}^{k-1} \sigma_{k-j} \mu_j \Big] \quad , k = 1, \ldots, N \tag{D.4}$$

Where $\sigma_0 = 1$ and the zeros of $f(z)$ are the roots of the polynomial $P_N(z)$ given in (D.2) after computing the coefficients from (D.4). The search contour must be simple, bounded and shouldn't cross any zero. An example for the search strategy in illustrated in

Figure D.1 must be applied in computer implementation [170].

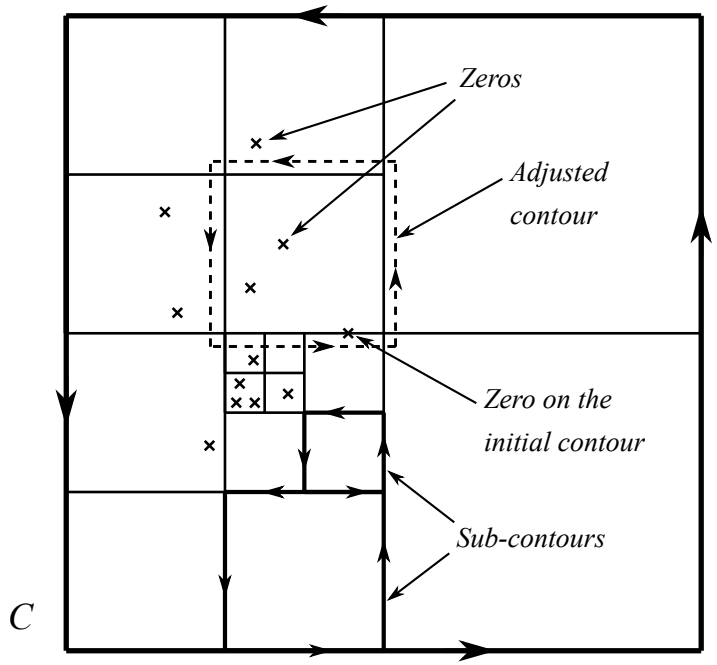

Figure D.1: Search strategy for contour C. In this illustration, the maximum number of zeros $N_{\max} = 4$. This algorithm is applied in order to improve the accuracy of computations [4, 5].

The derivative of $f(z)$ can be computed exactly using the `AutoDiff_R2015b` package available in MATLAB [171]. The final step is to polish the results using the Newton– Raphson or Muller method [165, Chapter. 6] in order to obtain machine accuracy as in (D.4).[1] We highly recommend Muller method over Newton-Raphson since it is derivative-free with a guaranteed convergence. The numerical integral can performed using adaptive quadrature such as `quadgk` from MATLAB. As stated previously, the contour C shouldn't cross any zeros in order for this method to work. Hence, a spike detection is needed when applying the contour integral such as the technique in [172]. Nevertheless, the MATLAB

[1]The initial guess would be the values obrained from CIM.

`quadgk` has a built-in detection for unbounded integrals which sends a warning. In this case, the original size of the contour C is increased by a small percentage in all directions. General guidelines are found in [4, 109, 173, 174]. Note that for $N \leq 4$, the roots are exactly known [175, p. 23].

D.1 Numerical Examples

An example is considered from [176, p. 58] for the following function $f(z) = z^2(z-2)^2[e^{2z}\cos(z) + z^3 - 1 - \sin(z)]$. The results of this example are listed in Table D.1 where $\gamma = \{z \in \mathbb{C} : |z| = 3\}$. Note that the trivial solution 0 was included for the sake of completeness.

Table D.1: Zeros for example 1 after applying Muller method for polishing the initial results.

z_1	$-0.46071411972897 + j0.62542776934777$
z_2	$-0.46071411972897 - j0.62542776934777$
z_3	$0.00000000000000 + j0.00000000000000$
z_4	$1.66468286974552 + j0.00000000000000$
z_5	$2.00000000000000 + j0.00000000000000$

Another example is taken from [177]. Here, the transcendental equation $f(z) = P_N(z)g(z)$ is given in (D.5). The search contour was chosen as a circle $\gamma = \{z \in \mathbb{C} : |z| = 6\}$. The results after applying Muller method for polishing are summarized in Table D.2 where the repeated roots are removed.

$$\begin{aligned} P_N(z) &= (z-0.2)^3(z-0.2+j0.5)(z-0.2-j0.5)(z-0.9)^2 \\ g(z) &= (z-2)(z-3)(z-4)(z-5)e^{5z^3+2z^4+z^5} \end{aligned} \tag{D.5}$$

Table D.2: Zeros for example 2 . The growing exponential $e^{5z^3+2z^4+z^5}$ was omitted.

z_0	$5.00000000000000 + j0.00000000000000$
z_1	$4.00000000000000 + j0.00000000000000$
z_2	$3.00000000000000 + j0.00000000000000$
z_3	$2.00000000000000 + j0.00000000000000$
z_4	$0.90000000000000 + j0.00000000000000$
z_5	$0.90000000000000 - j0.00000000000000$
z_6	$0.20000000000000 - j0.50000000000000$
z_7	$0.20000000000000 + j0.50000000000000$
z_8	$0.20000000000000 + j0.00000000000000$

D.2 Double Loop Integral

In this part, we explain how a double loop integral used in Cauchy Integration Method (CIM) around a branch point will not result in a spurious zero if the function of interest $f(z)$ doesn't become zero at the branch point z_b. First, we illustrate the double loop integral for a function with two Riemann sheets, *e.g.*, $f(z) = \sqrt{z}$ where $z_b = 0$. Then, we demonstrate the argument principle on two types of functions: $f(z_b) = 0$ and $f(z_b) \neq 0$. The latter is expected to produce the correct results. The argument principle given in (D.6) computes the number of zeros N surrounded by a simple contour C in the complex domain [169, p. 268].

$$N = \frac{1}{2\pi j} \oint_C \frac{f'(z)}{f(z)} dz \tag{D.6}$$

Considering the integrals I_1 and I_2 defined in Figure D.2. Note that the double loop integral is equivalent to $I_1 + I_2 - \big(B_1 + B_2\big)$. If the branch point is not included, the double loop is equivalent to $I_1 + I_2$.

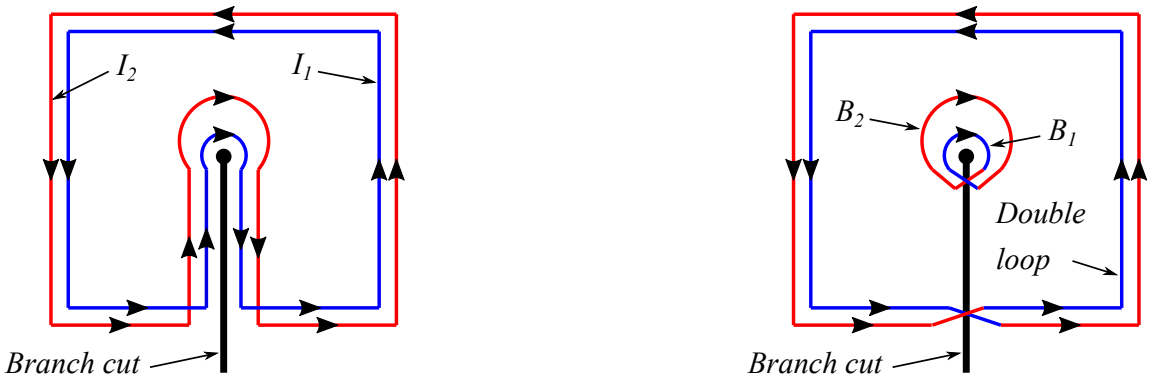

Figure D.2: The definition of double loop integral from the integrals $I_1 + I_2$. For example, I_1 is performed on the top Riemann sheet while I_2 on the bottom sheet. (b) The equivalent integral.

D.3 Computing The Double Loop Integral

Here, we demonstrate the result of applying the double loop integral defined above when the contour C surrounds the branch point on two scenarios: $f(z) = \sqrt{z}$ and $f(z) = \sqrt{z} + g(z)$ where $g(0) \neq 0$. Thus, we compute the integrals B_1 and B_2 illustrated in Figure D.2. Hence, we substitute $z = \delta e^{j\theta}$ and then we take $\lim_{\delta \to 0}\{B_1 + B_2\}$. Moreover, crossing the branch cut corresponds to replacing $\sqrt{z}$ with $-\sqrt{z}$.

D.3.1 Scenario I: $f(z) = \sqrt{z}$

For top sheet:

$$N = \frac{1}{2\pi j} \lim_{\delta \to 0} \oint_C \frac{1/2}{(\sqrt{z})(\sqrt{z})} dz = \frac{1}{2} \tag{D.7}$$

For bottom sheet:

$$N = \frac{1}{2\pi j} \lim_{\delta \to 0} \oint_C \frac{1/2}{(-\sqrt{z})(-\sqrt{z})} dz = \frac{1}{2} \tag{D.8}$$

Hence, from (D.7) and (D.8) we obtain $N = \frac{1}{2} + \frac{1}{2} = 1$ which indicates a spurious zero.

D.3.2 Scenario II: $f(z) = \sqrt{z} + g(z)$

Here, we have $f(0) \neq 0$ since $g(0) \neq 0$, but also the branch cut discontinuity from $\sqrt{z}$ still exist.

For top sheet:

$$N = \frac{1}{2\pi j} \lim_{\delta \to 0} \int_0^{2\pi} \left[\frac{\frac{1}{2\sqrt{\delta e^{j\theta}}} + g'(\delta e^{j\theta})}{\sqrt{\delta e^{j\theta}} + g(\delta e^{j\theta})} j\delta e^{j\theta} \right] d\theta = 0 \tag{D.9}$$

For bottom sheet:

$$N = \frac{1}{2\pi j} \lim_{\delta \to 0} \int_0^{2\pi} \left[\frac{\frac{-1}{2\sqrt{\delta e^{j\theta}}} + g'(\delta e^{j\theta})}{-\sqrt{\delta e^{j\theta}} + g(\delta e^{j\theta})} j\delta e^{j\theta} \right] d\theta = 0 \tag{D.10}$$

Hence, from (D.9) and (D.10) we obtain $N = 0$ which indicates no spurious zero. A generalization for this results can be done for the following form:

$$f(z) = z^p + g(z) \tag{D.11}$$

In this case, the number of zeros becomes:

$$N = \begin{cases} 0, & p \geq 0 \\ 2p, & p < 0 \end{cases} \tag{D.12}$$

The above argument was suggested by Prof. David R. Jackson from the University of Houston, TX.

D.4 Dispersion Function

The Dispersion Function (DF) for the simplest planar layered structure is the half-space in given (D.13). Where $k_{z1} = \sqrt{k_1^2 - k_\rho^2}$ and $k_{z2} = \sqrt{k_2^2 - k_\rho^2}$.

$$f(k_\rho) = \frac{k_{z1}}{\epsilon_1} + \frac{k_{z2}}{\epsilon_2} \tag{D.13}$$

Since $k_1 \neq k_2$, we expect $k_{z1}(k_1) \neq k_{z2}(k_1)$ and vice versa, this means that our DF will behave like $f(z)$ in scenario II discussed above. Note that if $k_1 = k_2$ in the half-space example, this means that the configuration is a homogeneous medium and therefore the root at k corresponds to plane wave solution which is the only supported mode in this case. For general configurations with more than two layers (even if the top and bottom media are the same) the overall DF will also behave like $f(z)$ in scenario II. This has been carefully considered in the proposed DFs.

From the above discussions we conclude that the double loop integral will not produce a spurious zero according to our DF definition. Another treatment for the double loop integral was given by Smith in [107, 113]. One should note that this result can be generalized for four Riemann sheets. Hence, the loop will cross the four sheets in the manner.